UC San Diego

UC San Diego Electronic Theses and Dissertations

Title

Structurally Dynamic Biosynthetic Polymers for Myocardial Tissue Engineering

Permalink

https://escholarship.org/uc/item/3n06k8vx

Author

Carlini, Andrea Sylvia

Publication Date

2018

Peer reviewed|Thesis/dissertation

eScholarship.org Powered by the California Digital Library
University of California

UNIVERSITY OF CALIFORNIA SAN DIEGO

Structurally Dynamic Biosynthetic Polymers for Myocardial Tissue Engineering

A dissertation submitted in partial satisfaction of the requirements for the degree Doctor of Philosophy

in

Chemistry

by

Andrea Sylvia Carlini

Committee in charge:

Professor Nathan C. Gianneschi, Chair
Professor Neal K. Devaraj, Co-Chair
Professor Michael D. Burkart
Professor Karen L. Christman
Professor Patricia A. Jennings

2018

Copyright

Andrea Sylvia Carlini, 2018

All rights reserved.

The Dissertation of Andrea Sylvia Carlini is approved, and it is acceptable in quality and form for publication on microfilm and electronically.

_____

_____

_____

_____
Co-chair

_____
Chair

University of California San Diego

2018

Dedication

To anyone who actually reads this dissertation.

Epigraph

“The problem with quotes on the internet is you can never be certain they’re authentic.”

-Abraham Lincoln

Table of Contents

Signature Page iii

Dedication iv

Epigraph v

Table of Contents vi

List of Figures ix

List of Tables xiv

Acknowledgements xv

Vita xviii

Abstract of the Dissertation xxi

Chapter 1 1

Introduction 1

1.1 Myocardial Infarction and Left Ventricular Remodeling 1

1.1.1 Pathophysiology of the Heart Post-MI 1
1.1.2 Biomaterials for Therapeutic Tissue Engineering 2
1.1.3 Design of Structurally Dynamic Biosynthetic Polymers and Biopolymers 5
1.1.4 Structurally Dynamic Materials Synthesized via Two Classes of Biosynthetic Materials 7

1.2 Biosynthetic Polymers as Functional Materials 10

1.2.1 Overview of Biosynthetic Materials 10

1.3 Architecture Control 14

1.3.1 Primary Sequence Control 14
1.3.2 Tacticity Control 17
1.3.3 Grafting Control 18
1.3.4 Conclusions for Architecture Control 20

1.4 Structural Dynamics of Polymer Assemblies 22

1.4.1 Dynamic Particle Assemblies 22
1.4.2 Self-Healing Hydrogels via Noncovalent Interactions 25
1.4.3 Conclusions for Structural Dynamics of Polymer Assemblies 29

1.5 Biotherapeutic Stabilization: Storage, Release, and Bioresistance 30

1.5.1 Matrix-Based Assemblies for Biopolymer Storage 30
1.5.2 Controlled Release of Biomaterials from Networks 33
1.5.3 Bioresistance with Biopolymer Conjugates 34
1.5.4 Conclusions for Biostabilization 37

1.6 Perspectives and Outlook 38

1.7 Acknowledgements 39

1.8 References 40

Chapter 2 57

Responsive NPs for Targeted Accumulation and Prolonged Retention 57

2.1 Enzyme-Responsive NPs as Imaging Agents for Disease 57

2.1.1 Advanced Fluorescence Imaging in Tissue with Upregulated MMPs 57

2.2 Targeted Delivery of IV Injectable Responsive NPs Post-MI 61

2.2.1 Introduction 61

2.2.2 Results and Discussion 62

2.2.3 Study Conclusions 75

2.2.4 Experimental Details 76

2.3 Perspectives and Future Outlooks 88

2.3.1 Modifications for Translatability 88

2.3.2 Investigation into Scalable Systems 88

2.3.3 Development of Next Generation Biodegradable and Viscoelastic Constructs 90

2.4 Acknowledgements 92

2.5 References 93

Chapter 3 100

Sterically Constrained Enzyme-Responsive Peptide Progelators 100

3.1 Cyclic Peptides for Minimally Invasive Delivery Post-MI 100

3.1.1 Introduction 100

3.1.2 Results 102

3.1.3 Discussion and Conclusions 137

3.1.4 Experimental Details 140

3.2 Acknowledgements 153

3.3 References 154

Chapter 4 161

Charge-Conversional Peptide Progelators 161

4.1 Polyanionic Maleamic Acid Progelators for Minimally Invasive Delivery to Inflamed Tissue 161

4.1.1 Introduction 161

4.1.2 Results 163

Figure 2.2.1 166

4.1.3 Discussion and Conclusions 188
4.1.1 Experimental Details 190
4.2 Perspectives and Future Outlooks 199

4.1.4 pH Responsiveness by NMR 199
4.1.5 Cell Viability of Progelators and Deprotection Products 199
4.3 Acknowledgements 200

4.4 References 201

Chapter 5 206

Biomimetic Polymer Hydrogel 206

5.1. Architectural Influence on Biosynthetic Polymer Analogues to a Peptide Hydrogel 206

5.1.1 Introduction 206
5.1.2 Results and Discussion 209
5.1.3 Overall Influence of Architecture 228
5.1.4 Conclusions 230
5.1.5 Experimental Details 231
5.2. Acknowledgements 238

5.3. References 239

List of Figures

Figure 1.1.1. Left ventricular (LV) remodeling following myocardial infarction (MI). 2

Figure 1.1.2. Delivery of injectable biomaterials. 4

Figure 1.1.3. Strategy for delivery and targeted accumulation of structurally dynamic biomaterials. .. 6

Figure 1.1.4. Synthetic Scheme for Ring Opening Metathesis Polymerization (ROMP). 8

Figure 1.2.1. Various architectures of functional biosynthetic polymers via the conjugation of natural and synthetic moieties. 11

Figure 1.2.2. Functional biosynthetic polymers. 13

Figure 1.3.1. Strategy for the polymerization of unstrained macrocycles enabling primary sequence control. 16

Figure 1.3.2. IEG-inspired iterative synthesis of sequence and stereo-controlled polymers. 18

Figure 1.4.1. Enzyme-responsive nanoparticles change shape for tumor retention. 24

Figure 1.4.2. Self-assembled hydrogels utilizing polymer−nanoparticle (PNP) interactions. 28

Figure 1.5.1. Trehalose and ethoxylated polyol (EP) hydrogel components for stabilizing model proteins. 32

Figure 1.5.2. A heparin-mimicking polymer conjugate stabilizes bFGF. 35

Figure 1.5.3. Protease-Resistant High Density Brush Peptide-Polymers 36

Figure 2.1.1. Enzyme-responsive NPs with a dense peptide-polymer brush in a tumor model. 59

Figure 2.2.1. Responsive nanoparticles target, accumulate, and are retained within an acute myocardial infarction due to enzyme-induced aggregation. 63

Figure 2.2.2. Spectroscopic and Spectrometric Analysis of MMP-9 Treated Nanoparticles. 64

Figure 2.2.4. Retention of responsive nanoparticles upon localized delivery. 66

Figure 2.2.5. Retention of IV delivered nanoparticles with the infarct. 67

Figure 2.2.6. Effect of reduced permeability on nanoparticle delivery. 68

Figure 2.2.7. *In vivo* TEM of infarct region from rat ischemia reperfusion model. 69

Figure 2.2.8. In vivo TEM of healthy cells incubated with pre-treated nanoparticles. 70

Figure 2.2.9. Macrophage infiltration. 72

Figure 2.2.10. Biodistribution of responsive nanoparticles. 73

Figure 2.2.11. Histology of satellite organs from IV injections. 74

Figure 2.2.12. Animal weight fluctuations. 75

Figure 2.2.13. Preparation of fluorescent MMP-9 responsive nanoparticles. 79

Figure 2.2.14. SEC-MALS intensity plot of homopolymer 1_{20} (black), copolymers 1_{20}-b-2_5 (blue) and 1_{20}-b-2_5-F (red), and PPA-F (green). 80

Figure 2.2.15. Spectroscopic analysis of nanoparticles in 8:1 DMSO:1xDPBS. 81

Figure 2.2.16. Autocorrelation functions. 82

Figure 2.2.17. Dry state TEM micrographs of nanoparticles before and after 24 hr of MMP-9 treatment. 84

Figure 2.3.1. Enzyme-responsive nanoparticles via ROMPISA. 89

Figure 3.1.1. Design of cyclic, enzyme-responsive progelator peptides for activatable gelation. 102

Figure 3.1.2. Chemical structures of KLDL peptides synthesized. 104

Figure 3.1.3. Chemical structures of KFDF peptides synthesized. 105

Figure 3.1.4. ESI mass spectra and sequences of peptides synthesized. 106

Figure 3.1.5. Sequences and design of SAPs and cyclic, enzyme-responsive progelators. 108

Figure 3.1.6. Rheological properties of KLDL and KFDF. 109

Figure 3.1.7. Impact of SAP functionalization on assembly properties. 110

Figure 3.1.8. Strain sweeps of SAPs. 111

Figure 3.1.9. Facile synthesis of sterically constrained and labeled cyclic progelators. 112

Figure 3.1.10. MALDI of labeled progelators before and after cyclization. 113

Figure 3.1.11. HRMS unlabeled and labeled progelators. 114

Figure 3.1.12.Tandem-MS of Rho-$KLDL_{Cyclic}$ and Rho-$KFDF_{Cyclic}$ progelators. 115

Figure 3.1.13. SLS profiles for unlabeled progelator in different buffers. 116

Figure 3.1.14. Effect of cyclic peptide progelator formulation on aggregation. 117

Figure 3.1.15. SLS of cyclic progelator before and after enzyme addition. 118

Figure 3.1.16. Circular dichroism (CD) of $KFDF_{Cyclic}$ progelator. 119

Figure 3.1.17. Enzyme responsiveness of Rho-$KLDL_{Cyclic}$ and Rho-$KFDF_{Cyclic}$ progelators. 120

Figure 3.1.18. Representative enzyme cleavage of unlabeled cyclic progelator. 121

Figure 3.1.20. Simulated control SAPs, $KLDL_{Control}$ and $KFDF_{Control}$, for progelator cleavage. 124

Figure 3.1.21. Frequency sweeps of product analogues and cleavage products. 126

Figure 3.1.22. TCEP reduction of progelator. 127

Figure 3.1.23 *In vitro* catheter injection of low viscosity progelators. 129

Figure 3.1.24. Hemocompatibility in human blood. 130

Figure 3.1.25. Hemostasis kinetics as a response of dosing. 131

Figure 3.1.26. Pro-thrombotic assay statistics. 132

Figure 3.1.27. *In vivo* analysis in a rat ischemia reperfusion model. 134

Figure 3.1.28. Heart slices visualized through IHC staining. 136

Figure 3.1.29. Representative H&E slices of injected heart. 137

Figure 3.1.30. Voltage plots for thermolysin cleavage of labeled progelators by CD. 144

Figure 4.1.1. Schematic of charge-conversional peptide as sensors of inflammation. 162

Figure 4.1.1. Facile synthesis of peptide progelators. 164

Figure 4.1.2. Characterization of progelators by LCMS. 165

Figure 4.1.3. LCMS of KLD control peptide. 166

Figure 4.1.4. Circular dichroism (CD) analysis of self-assembly. 167

Figure 4.1.5. Voltage plots for circular dichroism measurements. 168

Figure 4.1.6. Circular dichroism (CD) of mal-KLD and cit-KLD deprotection over time at pH 3.0 169

Figure 4.1.7. Transmission electron microscopy (TEM) analysis of self-assembly. 170

Figure 4.1.8. Additional TEM of self-assembling peptides and progelators. 171

Figure 4.1.9. Bulk rheological properties of pH-activated hydrogels. 172

Figure 4.1.10. Mass spectrometry of pH-activated hydrogels. 173

Figure 4.1.11. Step-strain oscillations for mal-KLD and cit-KLD treated with acid. 174

Figure 4.1.12. Strain sweeps for LVR identification of soluble progelators and pH activated hydrogels. 175

Figure 4.1.13. Frequency sweeps of mal-KLD Samples. 176

Figure 4.1.14. Frequency sweeps of cit-KLD Samples. 177

Figure 4.1.15. Frequency sweeps of dma-KLD Samples. 178

Figure 4.1.16. Frequency sweep of KLD control hydrogel. 179

Figure 4.1.17. Progelators persist as low viscosity solutions for catheter injection. 180

Figure 4.1.18. Temperature dependent viscoelasticity of soluble progelators and pH activated hydrogels. 181

Figure 4.1.19. Hemocompatibility of peptide progelators in whole blood and red blood cells (RBCs). 182

Figure 4.1.20. Hemocompatibility of peptide progelators in platelet poor plasma (PPP). 185

Figure 4.1.21. Plasma recalcification profiles in platelet poor plasma (PPP). 186

Figure 4.1.22. Excitation and Emission Spectra of ThT in preformed hydrogel. 187

Figure 4.1.23. Serial Addition of ThT to KLD Control at Different pH Values. 188

Figure 5.1.1. Diagram of biomimetic polymer analogue to the KLD-12 peptide hydrogel. 209

Figure 5.1.2. Synthetic routes for ring-opening metathesis polymerization (ROMP) of self-assembling polymers using norbornene-amino acid conjugates (NACs). 210

Figure 5.1.3. Representative examples of polymerization kinetics by NMR and characterization of polymer sizes by SEC-MALS after monomer additions. 212

Figure 5.1.4. Circular dichroism (CD)of representative copolymers and KLD-12 peptide. 213

Figure 5.1.5. The effect of pH and salt on polymer morphology. 215

Figure 5.1.6. TEM morphology of polymers. 217

Figure 5.1.7. Scanning Electron Microscopy (SEM) of peptide and representative polymer hydrogels. 219

Figure 5.1.8. Representative strain sweep plots of polymer and peptide hydrogels. 220

Figure 5.1.9. Viscoelastic properties of bulk polymer assemblies. 221

Figure 5.1.10. Frequency sweep plot of KLD peptide prepared at 108 mM with respect to charged moieties (100 mM NaCl, pH 6.4). 222

Figure 5.1.11. Frequency sweep plots of statistical copolymer samples. 223

Figure 5.1.12. Frequency sweep plots of block copolymer samples. 223

Figure 5.1.13. Shear thinning behavior of formulated hydrogels and non-gelling solutions. 225

Figure 5.1.14. Representative step-strain oscillation profiles. 226

Figure 5.1.15. Strain recovery healing of hydrogels following repeat cycles of excess strain. 227

Figure 5.1.16. Hydrogel stability to clinically relevant temperature changes. 228

Figure 5.1.17. Summary schematic depicting statistical versus block copolymers. 229

Figure 5.1.18. Assembly screen setup. 235

List of Tables

Table 2.2.1. Polymer molecular masses (g/mol) with respect to number (M_n) and weight (M_w), and polydispersity indices ± standard deviation, as measured by SEC-MALS. 80

Table 2.2.2. DLS measurements of particle diameter (nm) before and after incubation with MMP-9. 82

Table 3.1.3. Activated clotting times (ACT) in human blood. 131

Table 3.1.4. Hemolysis of red blood cells (RBCs). 132

Table 3.1.1. FibPredictor experimental setup over three generations. 145

Table 3.1.2. Experimental CD and theoretical modeling of gelators. 145

Table 3.1.3. DisConnect analysis of Rho-KLDL$_{Cyclic}$ progelator. 147

Table 3.1.4. DisConnect analysis of Rho-KFDF$_{Cyclic}$ progelator. 148

Table 4.1.5. Peptide identities by mass spectrometry and visual observation. 166

Table 4.1.6. Hemolysis of red blood cells (RBCs). 183

Table 4.1.7. Activated clotting times (ACT) in human blood. 184

Table 4.1.8. Plasma recalcification clotting extent. 196

Table 4.1.9. Plasma recalcification clotting rate. 197

Table 4.1.10. Plasma recalcification clotting time 197

Table 5.1.11. Polymers prepared with varying primary sequence, degree of polymerization (DP), and hydrophobic content. 211

Acknowledgements

First and foremost, I would like to express my sincere gratitude to my thesis adviser **Professor Nathan Gianneschi**, without whom this thesis work not have been possible. The first time we met to discuss my research project, I walked out of his office feeling like I could solve the world's problems with the piece of paper clutched in my hand, laying out an elaborate map of figures and instructions he had drawn. To my dismay, I looked back down at that sheet a few minutes later and saw an incomprehensible mess of scribbles. Making sense of it forced me to think critically about each idea and carefully consider design of experiments for individual milestone throughout my thesis work.

Nathan's unwavering support of my ambitions and creative input has encouraged me to become a better scientific thinker and innovator. He taught me how to successfully engage the scientific and general community with better presentation skills, grant writing, and conference networking, in ways that stimulate new discussions and future collaborations. He continually impresses me with his expansive knowledge and brilliant creativity that has fostered an environment of research excellence and innovation; this is a standard on which I model my future research endeavors. Nathan will always be a source of guidance and constructive criticism, from which I will continue to better myself as a researcher, educator, and innovator.

It has been a pleasure working with all my colleagues over the years, a few of which deserve special shout-outs: **Dr. Cassi Callmann**, for being the best friend, labmate, and roommate a graduate student could have. Our bond started with Chemistry, Star Trek, and wine, and has only grown stronger since! **Sophie Hirakis**, for the spontaneous adventures and crazy shenanigans on the worst of days, turning them into the best. **Dr. Gina Policastro**, **Dr. Jessica Ungerleider**, and **Dr. Mary Nguyen** for late-night discussions about *in vivo* data and medical procedures. **Dr. Dan Wright**, for keeping me on my toes with simultaneous discouragement and encouragement, ha. **Mollie Touve** for being the best collaborator anyone could have; our project towards the end was the most fun I had in

graduate school! **Dr. Lisa Adamiak**, **Dr. Stephen Nguyen**, **Dr. Swagat Sahu,** and **Dr. Clare LeGuyader** for being the reason why I joined the lab and feel I have a permanent science family.

Prof. Karen Christman, who provided the most helpful feedback and in-depth discussions on translational research of biomaterials, throughout my entire graduate career. **Dr. Matthew Thompson**, for having the answer to every question and going out of his way to help me every time. **Dr. Chris Forman** for being a wonderful roommate and for the insane intellectual debates over a glass (or two) of wine. **Dr. Angela Blum**, for teaching me much of what I know about peptide and polymer chemistry; she is a model educator who cares deeply for her students. To **Dr. Alex Roloff** and **Dr. Julia Michaelis**, for being the life of the party. During the day, we blasted music and danced in lab; At night, it was X-Files and BBQs. To **all my labmates over the years** for the friendship, advice, and fun we had in both San Diego and Chicago.

Most importantly, I need to thank **Kendall Satterfield** and my parents. In the 10 years I have known Kendall, he has provided me unwavering happiness even during the most trying of times. His thoughtful stickie notes on days I pulled all-nighters in lab, and endless patience later when I moved with my lab from San Diego to Chicago, have told me all I need to know about him. Kendall is the most genuine human being I have ever met. I have the most profound level of respect for his intellect, rate of knowledge absorption, and general enthusiasm for science. My education to this point has only been aided with him by my side. Finally, I would like to thank my parents, **Dr. Roger Carlini** and **Margaret Carlini,** for loving me unconditionally and supporting my every decision. They pushed me to challenge myself and always adapt in the face of change and opportunity. For this, I am the most grateful.

The following acknowledgements to my amazing co-authors need to be made:

Chapter 1.2-1.6 is adapted, in part, from material as it appears in Macromolecules 2016. Carlini, Andrea; Adamiak, Lisa; Gianneschi, Nathan. The dissertation author is the first author of this paper.

Chapter 2.1 is adapted, in part, from material as it appears in Journal of the American Chemical Society 2013. Chien, Miao-Ping; Carlini, Andrea; Hu, Dehong; Barback, Christopher; Rush, Anthony, Hall, David; Orr, Galya; Gianneschi, Nathan. The dissertation author is second author of this paper.

Chapter 2.2 is adapted, in part, from material as it appears in Advanced Materials 2015. Carlini, Andrea; Nguyen, Mary; Chien, Miao-Ping; Sonnenberg, Sonya; Luo, Colin; Braden, Rebecca; Osborn, Kent; Li, Yiwen; Gianneschi, Nathan; Christman, Karen. The dissertation author is co-first author of this paper.

Chapter 2.3 is adapted, in part, from material as it appears in Macromolecular Rapid Communications 2018. Wright, Daniel; Thompson, Matthew; Touve, Mollie; Carlini, Andrea; Gianneschi, Nathan. The dissertation author is a contributing author of this paper.

Chapter 3 is adapted, in part, from material currently being prepared as a revised manuscript for resubmission for publication. Carlini, Andrea; Gaetani, Roberto; Braden, Rebecca; Luo, Colin; Christman, Karen; Gianneschi, Nathan. The dissertation author is the first author of this pending manuscript.

Chapter 4 is adapted, in part, from material currently being prepared for submission for publication. Carlini, Andrea; Choi, Wonmin; McCallum, Naneki; Gianneschi, Nathan. The dissertation author is the first author of this pending manuscript.

Chapter 5 is adapted, in part, from material currently being prepared for submission for publication. Crystal, Dustin; Carlini, Andrea; Sahu, Swagat; Hidalgo, Francisco; Blum, Angela; Gianneschi, Nathan. The dissertation author is a co-author of this pending manuscript.

Chapter 6 is adapted, in part, from material currently being prepared for submission for publication. Touve, Mollie; Carlini, Andrea; Gianneschi, Nathan. The dissertation author is co-first author of this pending manuscript.

Vita

2012	Bachelor of Science, Chemistry Virginia Tech, Blacksburg, VA
2012	Bachelor of Science, Biological Sciences Virginia Tech, Blacksburg, VA
2014	Masters of Science, Chemistry University of California San Diego
2018	Doctor of Philosophy, Chemistry University of California San Diego

Patents

N. C. Gianneschi, K. L. Christman, and Carlini, A.S., “Catheter Injectable Cyclic Peptide Pro-Gelators for Myocardial Tissue Engineering.”, Non-Provisional Patent, UCSD Ref. No. SD2017-336.

Publications

Carlini, A.S., Gaetani, R., Braden, R.L., Luo, C., Christman, K.L. and Gianneschi, N.C.*, "Enzyme-Responsive Progelator Cyclic Peptides for Minimally Invasive Delivery to the Heart Post-Myocardial Infarction.", *In revision*.

Wright, D.B., Thompson, M.P., Touve, M.A., **Carlini, A.S.**, and Gianneschi, N.C.*, "Enzyme-Responsive Polymer Nanoparticles via Ring-Opening Metathesis Polymerization-Induced Self-Assembly.", *Macromolecular Rapid Communications*, 2018, *In Press*.

Carlini, A.S., Choi, W., N. McCallum, and Gianneschi, N.C.*, "Charge-Conversion of a Modified KLD-12 Peptide for Inflammation Responsive Hydrogelation.", *Manuscript in preparation*.

Crystal, D., **Carlini, A.S.,** Sahu, S. Hidalgo, F., Blum, A.P.*, and Gianneschi, N.C.,* "Architectural Influence on the Assembly of Biosynthetic Polymer Analogues to a Peptide Hydrogel.", *Manuscript in preparation*.

Carlini, A.S.,† Touve, M.A.,† and Gianneschi, N.C.*, "Direct imaging of structurally dynamic biomaterials by liquid cell transmission electron microscopy with chemical validation by MALDI imaging mass spectrometry.", *Manuscript in preparation*.

Carlini, A.S.,† Touve, M.A.,† and Gianneschi, N.C.*, "Directly observing enzyme-induced fiber formation of Re-labeled peptides.", *Manuscript in preparation*.

Carlini, A.S., Caro, H.F., Touve, M.A., and Gianneschi, N.C.*, "UV Activatable Peptide Bioinks for 4D Nanolithography.", *Manuscript in preparation*.

Wright, D.B., Patterson, J.P. Touve, M.A., **Carlini, A.S.**, and Gianneschi, N.C.*, "Block copolymer morphology switch via colloidal assembly and local reorganization.", *Manuscript in preparation*.

Roloff, A., **Carlini, A.S.**, Callmann, C.E., and Gianneschi, N.C.* "Micellar Thrombin-Binding Aptamers: Reversible Nanoscale Anticoagulants.", *Journal of the American Chemical Society*; 2017, 139(46), 16442-16445.

Carlini, A.S.; Adamiak, L.; Gianneschi, N.C.*, "Biosynthetic Polymers as Functional Materials." *Macromolecules*; 2016, 49(12), 4379-4674.

Carlini, A.S.,† Nguyen, M.M.,† Chien, M.-P., Sonnenberg, S., Luo, C., Braden, R.L., Osborn, K.G., Li, Y., Gianneschi, N.C.*, Christman, K.L.*, "Enzyme-Responsive Nanoparticles for Targeted Accumulation and Prolonged Retention in Heart Tissue after Myocardial Infarction." *Advanced Materials*; 2015, 27(37), 5547-5552.

Chien, M.P., **Carlini, A.S.,** Hu, D., Barback, C., Rush, A., Hall, D., Orr, G., Gianneschi, N.C.*, Enzyme-Directed Assembly of Nanoparticles in Tumors Monitored by In Vivo Whole Animal and Ex Vivo Super Resolution Fluorescence Imaging. *Journal of the American Chemical Society*; 2013, 135(50), 18710-18713.

Carlini, A.S., Electropolishing Copper Substrates for Niobium Thin-Film Coatings in SRF Technologies, *Journal of Undergraduate Research*; 2009, 54(10).

† = equal contribution

ABSTRACT OF THE DISSERTATION

Structurally Dynamic Biosynthetic Polymers for Myocardial Tissue Engineering

by

Andrea Sylvia Carlini

Doctor of Philosophy in Chemistry

University of California San Diego, 2018

Professor Nathan C. Gianneschi, Chair
Professor Neal K. Devaraj, Co-Chair

In recent history, application of macromolecular biomaterials for therapeutic tissue engineering after severe injury has presented a promising strategy to for positive remodeling. Herein, the design of structurally dynamic vehicles for noninvasive delivery and stimuli-responsive self-assembly is investigated. These proof-of-concept platforms were explored for the purpose of expanding the utility of insert biomaterial platforms for practical clinical applications. Ultimately, we envision formulation with biotherapeutics will provide a smart mechanism for treating inflammatory diseases.

First, nanomaterials were designed to respond to matrix metalloproteinases (MMPs) and acutely upregulated at the site of myocardial infarction (MI). Ring opening metathesis polymerization (ROMP) of a brush peptide-polymer amphiphile was explored to generate

intravenous (IV) injectable 20 nm nanoparticles that respond to MMP-2/9 through self-assembly into micron-scale aggregate scaffolds. The *in vivo* targeting efficiency, biodistribution, and toxicity of such constructs was investigated. These materials demonstrate targeted accumulation, nonimmunogenicity, and prolonged retention up to 30 days at the site of MI.

Cyclic peptide progelators were designed as structurally dynamic and biodegradable materials for targeted hydrogelation at the site of myocardial infarction. Self-assembling peptides (SAPs), which stack as β-sheets via intermolecular electrostatic, hydrophobic, and in some cases, π-π interactions were sterically constrained through macrocyclization. This modified construct was sufficient to prevent gelation and lower sample viscosity, enabling delivery via minimally invasive catheter delivery. These peptides respond to MMP-2/9 and elastase upregulated at the MI, as well as to the robust nonspecific protease, thermolysin, through self-assembly into viscoelastic hydrogels. Hemocompatibility and *in vivo* response of one such construct demonstrated the utility of this platform design.

Next, the strategy for generation of catheter-injectable SAPs was expanded into pH-sensitive low viscosity progelators. The pH-responsiveness of the KLD-12 SAP was tuned via temporary modification with substituted maleamic acids to afford polyanionic peptide solutions. The deprotection of these “caps” recapitulates the zwitterionic KLD-12 SAP under physiologically relevant levels of tissue acidosis (pH 6.8). Progelators were catheter injectable and hemocompatible, whereas acid-treated samples produce solid gels that resist material spreading and are reheable. Finally, this platform exhibited acid-induced drug encapsulation, a useful property for targeted therapeutics without complex synthetic manipulation.

Finally, we turned back to nondegradable ROMP co-polymers for studying architectural influence on biomimetic hydrogel assembly. Three amino acid-functionalized monomers were designed to mimic the alternating KLD-12 SAP cationic, neutral hydrophobic, and anionic charges, respectively, that imbue self-assembling behavior. Modification to the degree of polymerization (DP), number of blocks, block lengths, and hydrophobicicity, were explored to investigate their

propensity for hydrogel self-assembly and stability. This investigation provides general insight into physical hydrogel polymer design as well as proteolytic-resistant biomaterials for potential applications as long-term implantable hydrogels.

Chapter 1

Introduction

1.1 Myocardial Infarction and Left Ventricular Remodeling

1.1.1 Pathophysiology of the Heart Post-MI

Heart failure after myocardial infarction (MI) persists as the leading cause of death in the United States and western world.[1-3] Within 5 years after a first MI, >40% of patients over the age of 45 will die. Thus, despite major advancements in health care procedures in the developed world, heart disease remains an overwhelming burden upon modern society.

An MI occurs following blockage of one or more coronary arteries, causing myocardial ischemia due to lack of oxygen-rich blood supply. Subsequent anaerobic respiration leads to tissue acidosis from the buildup of lactic acid, generation of reactive oxygen species (ROS), and significant death of cardiomyocytes (**Figure 2.2.2**). Post-MI, the heart undergoes overlapping phases of healing: the inflammatory, proliferation, and maturation phases.[4,5] Early on, progressive apoptosis and necrosis of cardiomyocytes is accompanied by recruitment and activation of neutrophils and macrophages to remove cellular debris from the infarct area. These inflammatory cells express high levels of extracellular matrix metalloproteinases (MMPs) to digest the supportive collagenous extracellular matrix (ECM).[6] As this LV remodeling process continues, heavy deposition of collagen by fibroblasts forms a scar, which consists of disorganized and electrically compromised myocardial

tissues interspersed in the fibrous mesh.[5,7] This scar impairs cardiac contraction and relaxation profiles, leading to ventricular wall thinning, spherical dilation, and decreased pumping capacity.

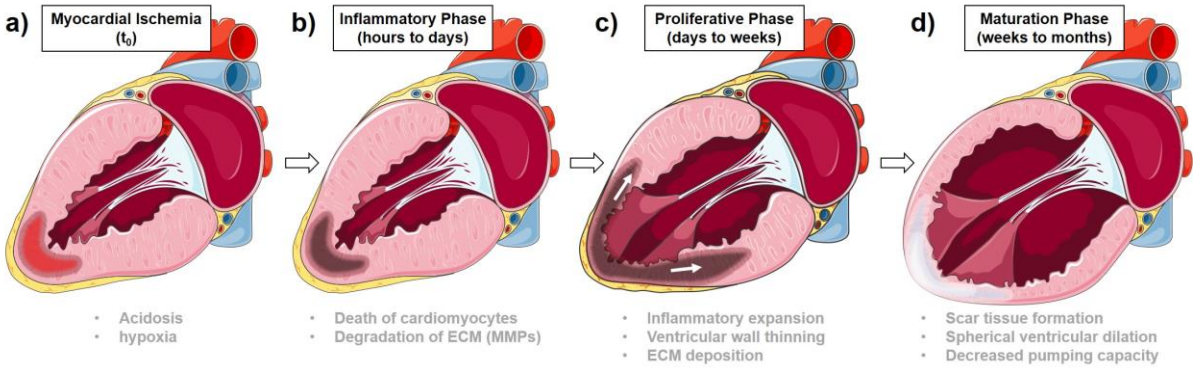


Figure 1.1.1. Left ventricular (LV) remodeling following myocardial infarction (MI). (a) Myocardial ischemia from the blockage of a coronary artery is characterized by lack of blood supply triggering tissue acidosis and generation of reactive oxygen species (ROS). (b) Following reperfusion, the acute inflammatory phase includes apoptosis and necrosis of cardiomyocytes and degradation of the extracellular matrix (ECM) by matrix metalloproteinases (MMPs). (c) The proliferative phase is marked by infarct expansion, and ventricular wall thinning. Myofibroblasts begin to secrete large amounts of collagen for new ECM deposition. (d) During the maturation phase, the new collagenous scar provides a rigid support to prevent ventricular rupture but does not aid with tissue contractility. Ultimately, spherical ventricular dilation and decreased pumping capacity leads to eventual cardiac failure.

1.1.2 Biomaterials for Therapeutic Tissue Engineering

Over the past decade, biomaterials ranging from LV restraints, cardiac patches, and injectable hydrogels or particle formulations, have been investigated to promote positive LV remodeling after MI.[4] These systems are designed to provide increased mechanical support to the compromised tissue, provide a local platform for delivery of therapeutics, and/or aid with adhesion of cellular transplants or promote recruitment of progenitor cells.[8,9] Injectable biomaterials have the advantage of conforming to unique geometries and can be amenable to less invasive delivery methods. Integration of these biomaterials with cell therapies, growth factors, and small molecule drugs has been shown to enhance their therapeutic efficacies. To date, various injectable biomaterials, used either as standalone scaffolds or combined with therapeutic moieties, have been shown to improve tissue viability, promote angiogenesis, enhance cardiomyogenesis, improve LV ejection fraction (LVEF), and reduce infarct size.[10]

Injectable hydrogel-based scaffolds have gained attention as a therapeutic approach to prevent negative LV remodeling by supplementing depleted myocardial ECM, a native hydrogel which provides structural support to surrounding tissue and modulates cellular behavior for regenerative processes.[11] Naturally derived (e.g. alginate, hyaluronic acid, and ECM-based) and synthetic (e.g. peptide and polymer-based) hydrogels have been used with varying levels of success to maintain ventricular wall thickness and decrease LV volume, fibrosis, and infarct size.9 Their chemical functionalization (e.g. signaling peptides) or use with additives (e.g. growth factors and stem cells) have worked to significantly improve therapeutic efficacy.[12] The current hypothesis is that the bioactivity, rather than mechanical stiffness or wall thickness of injected biomaterials, such as inherent cell adhesion domains, angiogenic degradation products, and/or cell infiltration upon degradation of these materials play an important role in preventing adverse LV remodeling.[9,13] Indeed, hydrogel scaffolds ranging in viscoelastic stiffness from ~10 Pa to 20 kPa have been applied to the heart post-MI.[14] Moreover, evidence suggests that early or timed intervention (within the first week) post-MI influences healing.[15-17] However, there are currently no FDA-approved or current clinical trials with injectable biomaterials delivered at early timepoints post-MI, which highlights inherent material property issues. **Figure 1.1.2** outlines advantages and disadvantages of different injectable biomaterials and the avaiable delivery routes.

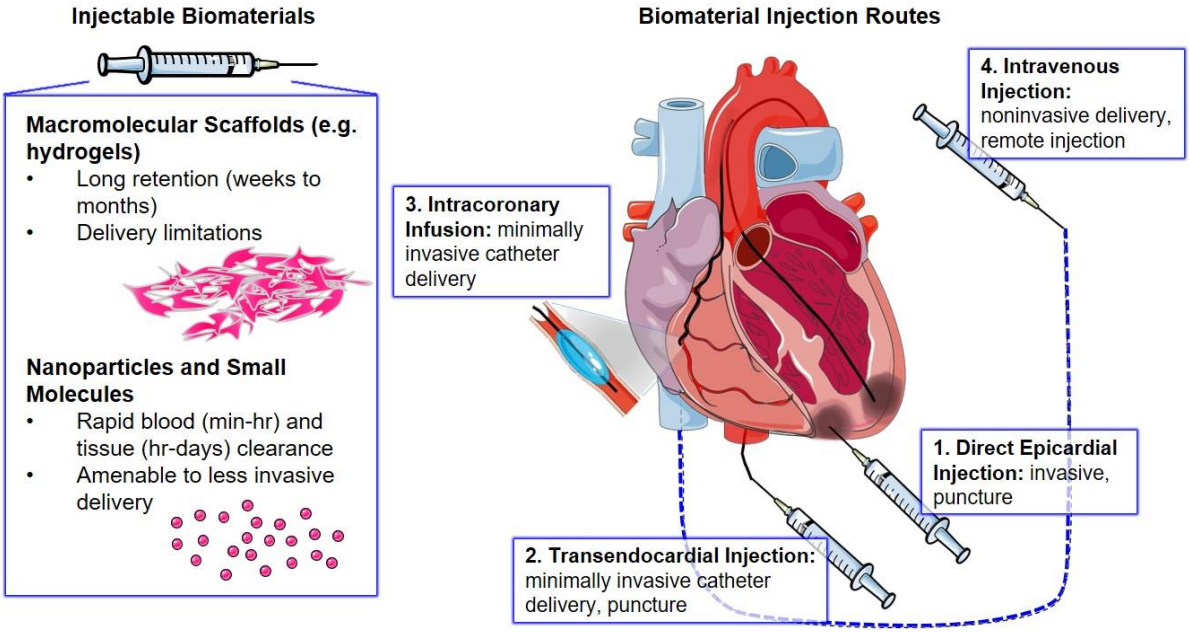


Figure 1.1.2. Delivery of injectable biomaterials. Feasible translation of biomaterials into the clinic requires the least invasive delivery strategies and prolonged retention at the target site (> 1 week post-injection). Delivery routes include 1) direct epicardial injection, 2) transendocardial infarction, 3) intracoronary infusion, and 4) intravenous injection.

Nanoparticles and soluble small molecules (e.g. peptides and polymers) are attractive for minimally invasive delivery because they may be administered via intravenous (IV) and catheter injection. They are used to passively target the heart through the enhanced permeability and retention (EPR) effect which is present in the acute stages of MI due to leaky vasculature.[18] However, spherical nanoparticles within these size ranges (15-350 nm) are often cleared from the target tissue within 24 h, and small molecules can be cleared even faster.[19,20] Both active targeting to the infarcted myocardium and retention of the material for periods longer than one week are current and significant challenges in developing nanoparticle delivery strategies to treat MI.

In contrast, macromolecular hydrogels have demonstrated tissue retention for up to several months. However, current delivery strategies with scaffold materials rely almost exclusively on puncture-based injections (e.g. direct epicardial), which limits clinical application of biologics to >30 days post-MI due to the risk of arrhythmogenesis and ventricular rupture. Paradoxically, extracellular matrix (ECM) degradation by overexpressed matrix metalloproteinases-2 and -9 (MMPs)[21] and

necrotic infarct expansion by acidosis[22,23] begins within the first 24 hr of MI. Therefore, the current protocol allows the heart to undergo significant damage and negative LV remodeling well before a treatment can be given. Minimally invasive catheter delivery can reduce this delivery window significantly. However, most scaffolding materials tested in animal models are not candidates for catheter delivery due to excess material viscosity, catheter clogging, lack of healing capacity, and/or concerns regarding hemocompatibility.[9,11,12] To date, only a handful of biomaterials have demonstrated catheter compatibility. These systems include an oxime cross-linked hydrogel,[24] alginate,[25] decellularized ECM,[26] a pH-sensitive polyacrylic acid (PAA)-based hydrogel,[27] and a pH-sensitive ureido-pyrimidinone (UPy)-modified PEG hydrogel.[28]

Thus, no existing therapy to date meets the above-mentioned criteria. This thesis is therefore devoted to the development of biomaterial scaffolds that can be delivered acutely to the MI (and potentially other forms of severe wound) by simple intravenous (IV) injection or catheter delivery, thereby precluding the risk of ventricular rupture during injection and need for invasive open-chest surgery.

1.1.3 Design of Structurally Dynamic Biosynthetic Polymers and Biopolymers

Given the unique and disparate challenges for effectively delivering biomaterials post-MI, this thesis work focuses on the development of structurally dynamic materials capable of sensing and responding to wounded tissue for scaffold assembly. The overall approach to programmed scaffold assembly specifically in heart tissue post-MI is summarized in **Figure 1.1.3**. A variety of platforms were synthesized, in which the precursor was topologically controlled to prevent self-assembly during delivery as well as when encountering healthy tissue. Biomaterial precursors can be injected IV or by catheter, rather than invasive needle puncture directly into heart tissue. Small biomaterial precursors that circulate in the blood, whether injected systemically, infused locally, or leaked from injection site, assemble into macromolecular scaffolds in response to inflammatory enzymes (e.g. MMP or elastase) or pH gradients present in damaged heart tissue. Therefore, the body's natural

inflammatory response is used to guide these materials *in vivo*. These scaffolds have significantly slowed tissue clearance times relative to the small precursors (e.g. nanoparticles or small molecule peptides) circulating in the blood stream and freely perfusing healthy tissue. Thus, prolonged retention (> 1 week) is possible with these structurally dynamic systems. Ultimately, therapeutic efficacy with these platform strategies (which is beyond the scope of this thesis) would provide any number of self-assembling materials programmed to form a healing scaffold to prevent LV remodeling immediately post-MI.

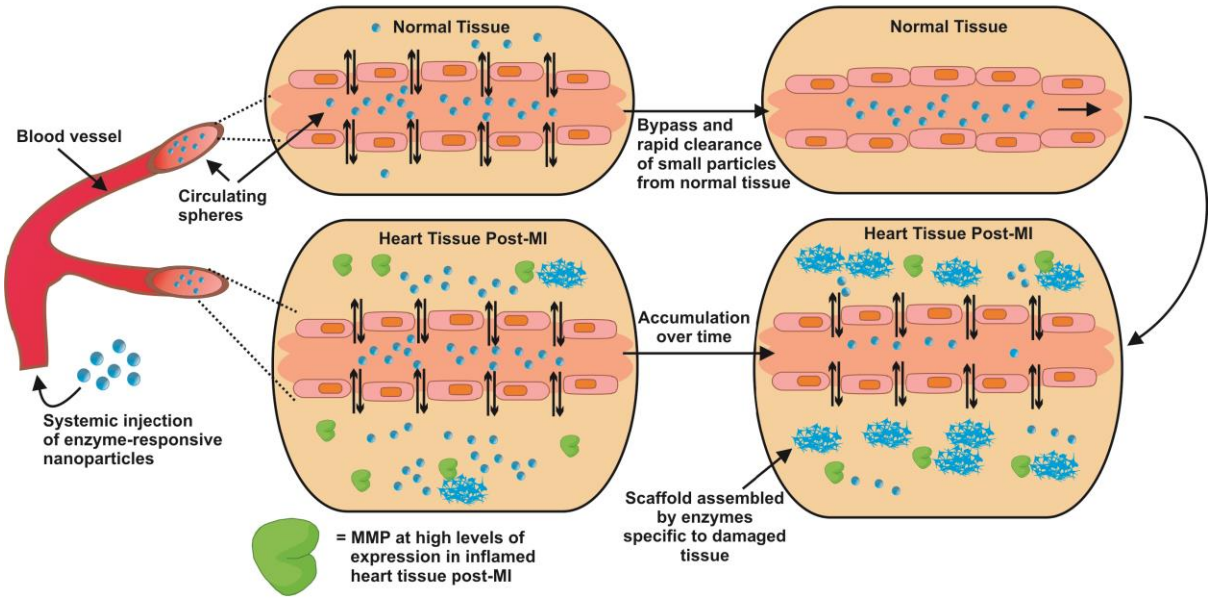


Figure 1.1.3. Strategy for delivery and targeted accumulation of structurally dynamic biomaterials. Polymeric nanoparticles or small molecule (e.g. soluble peptides) act as soluble precursors that form scaffold architectures in response to endogenous signals (e.g. enzymes or acidosis) that are specific to the site of myocardial infarction. Future functionalization of these platform technologies with therapeutic moieties can aid in localized treatment.

The research discussed herein makes critical progress in overcoming persistent translational limitations that are inherent to the inert scaffolds in place today. Platform modularity and simple synthetic manipulation of currently investigated biomaterials is also a recurring theme of this thesis work. Critically, these studies establish a new paradigm for biomaterial delivery to the heart, which could be expanded to additional biomaterials beyond the scope of this dissertation. Future success in combining these strategies with therapeutic biomaterials could have a direct impact on improving

the quality of life of hundreds of thousands of patients each year in the United States alone, as well as significantly reducing health care costs through early treatment. Furthermore, the development of stimuli-induced material assembly from soluble precursors *in vivo* has broad implications in the field of drug delivery in general.

Installing structurally dynamic properties for targeted accumulation and prolonged retention of aggregated scaffolds at the site of disease was the primary goal of **Chapter 2**. **Chapter 3** and **4** expanded upon that work by utilizing biodegradable constructs and viscoelastic hydrogels similar in mechanical properties to the native ECM. Finally, **Chapter 5** provides an in-depth analysis of design criteria for hydrogel self-assembly and performance properties using biosynthetic mimics a peptide explored in the previous two chapters.

1.1.4 Structurally Dynamic Materials Synthesized via Two Classes of Biosynthetic Materials

Two types of structurally dynamic materials were explored in this thesis. **Chapters 2** and **5** utilized peptide-polymer amphiphiles generated via ring-opening metathesis polymerization (ROMP). ROMP offers a high degree of synthetic control, allowing for the rapid preparation of polymers with varying block lengths and sizes in low dispersity.[29-32] This low dispersity is possible through fast monomer initiation kinetics relative to the rate of chain propagation.[33] The synethetic scheme for ROMP with Grubb's 3rd generation catalyst is provided in **Figure 1.1.4**. Relief of ring strain (100 kJ/mol) from incoming norbornene monomers is the driving force for these polymerizations. Importantly, Grubbs' 3rd generation catalyst is a highly functional group tolerant initiator that enables direct polymerization of sugars,[34,35] peptides,[36,37] drugs,[38-40] nucleobases,[41,42] and contrast agents.[43,44]. As such, this a series of proteolytically resistant materials with complex synthetic architectures were generated.

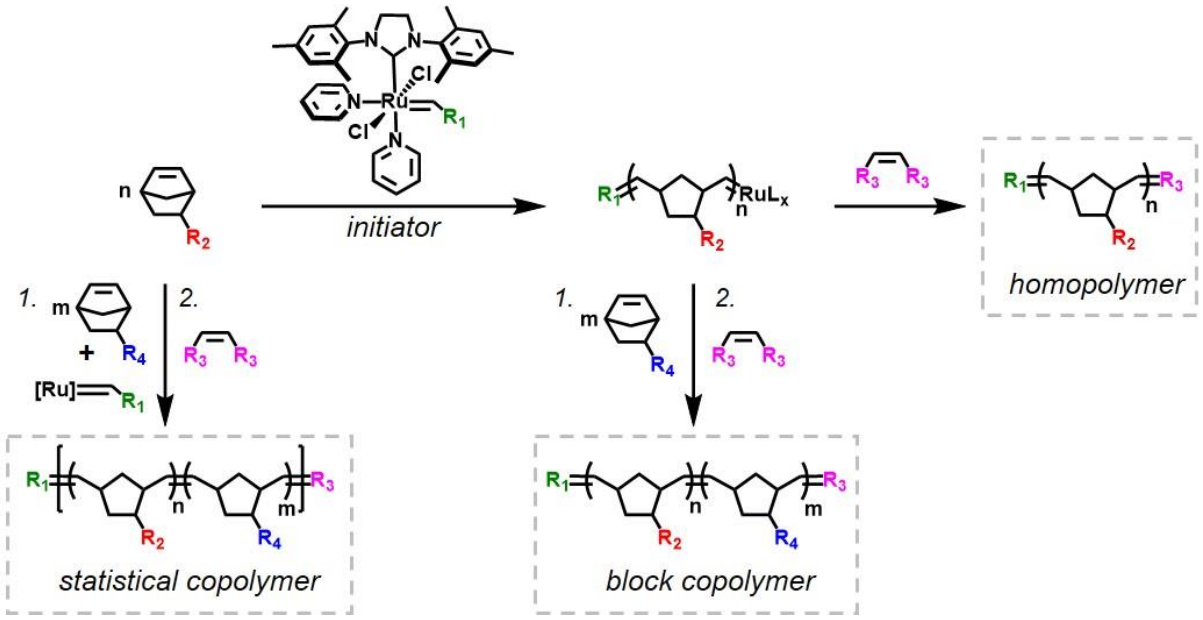


Figure 1.1.4. Synthetic Scheme for Ring Opening Metathesis Polymerization (ROMP). *n* equivalents of a monomer are added to the Ru initiator to afford a living polymer that can be terminated to produce a homopolymer. Addition of a second monomer to the living polymer can be terminated to afford a block copolymer. Mixing of both monomers prior to addition of the Ru initiator, followed by termination, affords a statistical copolymer.

Chapters 3 and **4** utilized primarily peptide-based amphiphiles which were generated via solid phase peptide synthesis (SPPS). SPPS with N-terminal Fmoc protection and acid-sensitive R-group protection is a commonly employed strategy for the preparation of peptides up to 70 amino acids in length,[45] which is possible with the high synthetic yield (>98%) for each amino acid coupling. Synthetic control is possible through step-wise N-terminal resin-bound peptide deprotection with 20% (v/v) piperidine in DMF followed by standard amide bond coupling with an incoming Fmoc-protected amino acid.[46] In addition to the 20 genetically encoded amino acids in the body, hundreds of commercially available amino acids with different functional R-groups, stereochemistries, and different backbone compositions have been introduced to expand the available peptide chemistry toolbox. The resin support provides a stationary platform to retain growing peptides and wash away starting material and reaction byproducts prior to peptide cleavage from the resin, which is generally sensitive to strongly acidic (95% v/v) or weakly acidic (1% v/v) conditions in trifluoroacetic acid (TFA).[47,48] These R-group cleavage conditions may either differ, to allow for complex orthogonal

modifications on and off the resin, or may be identical to general resin cleavage conditions to fully deprotect all amino acid residues when synthesis is complete.[49] Thus SPPS has the advantage of straightfoward synthesis with full control over peptide architecture and reproducibility. Furthermomre, this strategy enabled preparation of biodegradable systems that exhibit complex structural behavior even with simple synthetic architectures.

It is important to note that all materials generated in this thesis can be classified as biosynthetic polymers, whether they are composed of primarily synthetic components (e.g. polynorbornene) or primarily naturally produced components (e.g. oligopeptides). Before discussing these systems, **Chapter 1.2** has been provided to thoroughly introduce biosynthetic polymers, their use as functional materials, and key challenges (architecture control, assembly dynamics, and biostabilization) that must be overcome to embue them with complex behavior.

1.2 Biosynthetic Polymers as Functional Materials

1.2.1 Overview of Biosynthetic Materials

The structure and function of biopolymers found in nature has evolved over the past few billion years to form the underpinnings of life. Biosynthetic polymeric materials exemplify the diversity accessible through synthesis and semisynthesis that is inspired by and utilizes biopolymers (**Figure 1.2.1a**). Hancock and Ludersdorf prepared the first artificial polymer in 1840, through treatment of natural rubber with sulfur to create a tough and elastic material.[50] It was another century before significant advances in polymer chemistry would enable the production of totally synthetic and complex polymeric materials. Within the past few decades, biologically compatible synthetic materials have emerged as one of the most exciting and prolific fields in polymer chemistry due to the widespread adoption of living and controlled polymerization methods (**Figure 1.2.1b**). These materials, herein referred to as biosynthetic polymers, are now used for a multitude of applications such as novel biomolecule stabilizers, drug-delivery vehicles, therapeutics, biosensors, biomedical adhesives, anti-fouling materials, and biomimetic scaffolds.[51-54]

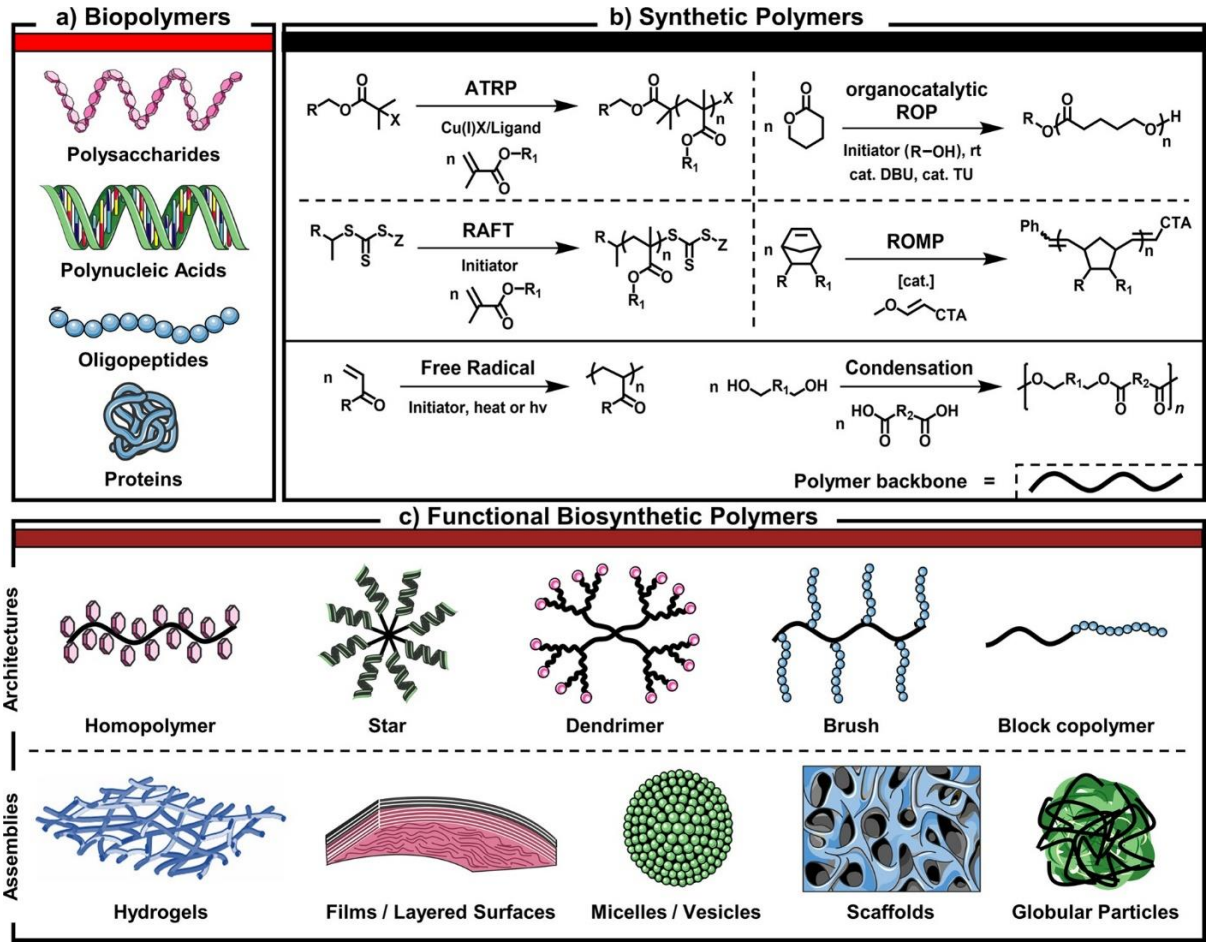


Figure 1.2.1. Various architectures of functional biosynthetic polymers via the conjugation of natural and synthetic moieties. (a) Biopolymers (polysaccharides, polynucleic acids, oligopeptides, and proteins) and their building blocks (nucleotides, monosaccharides, and amino acids) may be combined with (b) synthetic polymers (black) via a variety of polymerization methods. Representative controlled chain growth polymerization methods are depicted above uncontrolled versions. (c) The resulting functional biosynthetic polymers may act as an unstructured conjugate with various architectures or conjugate assemblies.

Biosynthetic polymers are materials that combine synthetic components with biopolymers or moieties prepared as mimics of those found in nature (**Figure 1.2.1c**).[55] These materials consist of (a) synthetically modified biopolymers, such as functionalized hyaluronic acid derivatives[56] or labeled proteins via cell-instruction.[57] In the prior case concerning biopolymers such as polysaccharides or proteins, wherein reactive sites (amine, hydroxyl, thiol, carboxylic acid) are conventionally present as multiple copies, site-specific conjugation (graft-to) and subsequent purification are typically difficult. Other categories of biosynthetic polymers that enable more precise control over advanced architectures, functionalization, and subsequently dynamic function are (b) biomolecules conjugated

to synthetic polymers produced by various grafting strategies[58,59] or (c) bioinspired or fully synthetic polymers that act as biopolymer surrogates, which execute similar functions and occasionally exceed the performance of biopolymers.[60] Considerable effort has been directed toward increasing the precision by which biomolecules are incorporated into polymers in other words, expanding the so-called "bioconjugate toolbox".[61-63] With the advent of "click"-type chemistries, i.e. oxime,[64,65] Staudinger ligation,[66,67] thiol−ene,[68] copper-catalyzed azide−alkyne cycloaddition (CuAAC),[69] and strain-promoted azide/alkyne click (SPAAC),[70] among others,[71,72] biomolecule−polymer conjugates are not only readily attainable but achieve higher fidelity. Though many reports document interesting advancements, the focus of this section is not to catalogue conjugation strategies but to describe paradigm shifts in the development of functional biosynthetic polymers.

As such, the rest of **Chapter 1** discusses exciting and recently published works that address some of the most significant problems which still hinder progress in the field of functional biosynthetic polymers: (1) architecture control of synthetic components, (2) structural dynamics of polymer assemblies, and (3) biostabilization (storage, release, and bioresistance) of therapeutic cargos (**Figure 1.2.2**). Most of the examples discussed herein utilize controlled polymerization methods for addressing previously unmet challenges in architecture control and functional complexity, with some exceptions in which uncontrolled polymerization methods are necessary for simplicity and expense mitigation. **Section 1.3** first section will discuss fundamental advances in polymer chemistry toward controlling primary sequence, tacticity, and functionality via grafting, which are paramount for the execution of complex biological functions, as demonstrated by the precise stereoregularity of biopolymers (i.e., proteins and DNA). **Sections 1.4-1.5** highlight significant progress made in advanced bulk functionality of unstructured and/or assembled biosynthetic polymers.

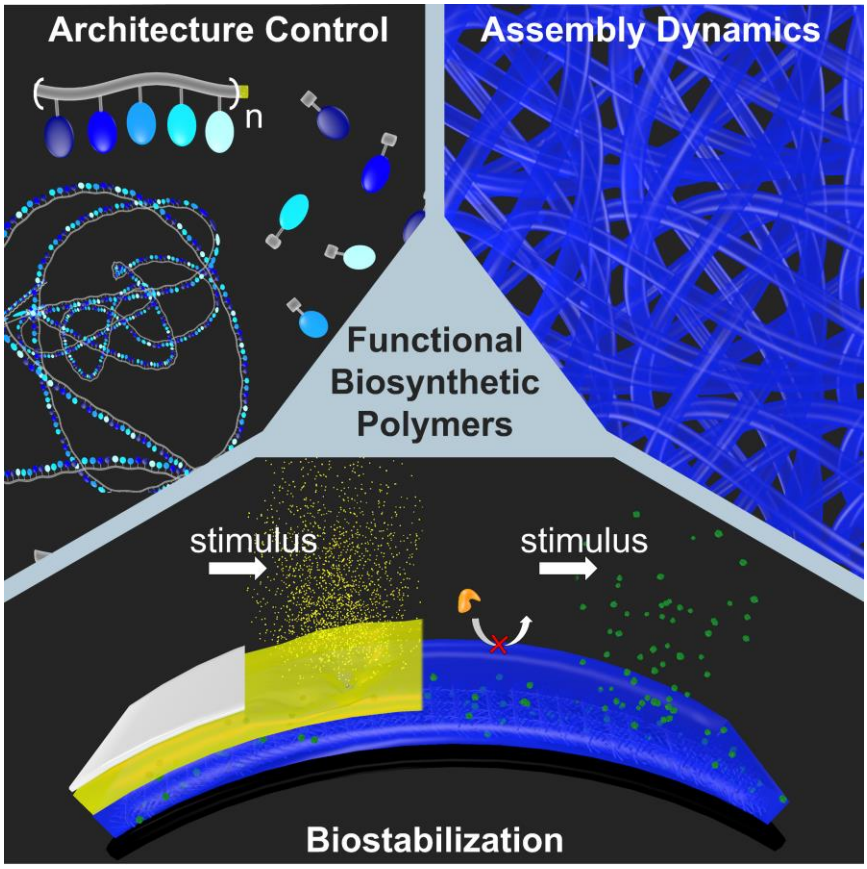


Figure 1.2.2. Functional biosynthetic polymers. The synthesis of functional polymers encoded with biomolecules has been an extensive area of research for decades. As such, a diverse toolbox of polymerization techniques and bioconjugation methods has been developed. The greatest impact of this work has been in biomedicine and biotechnology, where fully synthetic and naturally derived biomolecules are used cooperatively. Despite significant improvements in biocompatible and functionally diverse polymers, our success in the field is constrained by recognized limitations in polymer architecture control, structural dynamics, and biostabilization.

Throughout **Chapter 1**, the merits of simple formulations for designing highly functional biosynthetic polymers are discussed. The conclusion gives a projected outlook on further progress in the field that hinges on the ability to overcome recurring limitations. In this context, our creative efforts to surpass what evolution has perfected are just beginning. In the foreseeable future, further advancements will no longer rely on copying nature for solutions but rather emerge from the limits of our own imagination.

1.3 Architecture Control

The basic informational biopolymers from which all life on earth is built are carbohydrates, nucleic acids, and proteins,[73] with noninformational biogenic polymers including melanins making tremendous functional contributions.[74] Biological organisms are capable of producing biopolymers with extreme complexity and high fidelity and accuracy, while using robust machinery and only a handful of simple monomers including saccharides, nucleotides, amino acids (and their derivatives), other metabolites, and fatty acids.[73] Naturally, our current knowledge and abilities in the field of polymer chemistry pale in comparison to that achieved by billions of years of evolution. Nonetheless, researchers have devoted substantial efforts to synthesize polymers using libraries of novel monomers possessing different physical and chemical properties with diversities far beyond those prevalent in biological systems. Furthermore, strategic organization of these polymeric monomers can enhance the polymer complexity and overall mode of action.[75,76] In this way, semisynthetic or fully synthetic materials may be tailored to mimic the highly versatile and functional properties of biopolymers. The following discussion focuses on current efforts to increase the control of polymer architecture as well as microstructure such as the specific arrangement of monomer sequence and stereoisomers.

1.3.1 Primary Sequence Control

Primary sequence control is vital to reproducible and reliable generation of all biosynthetic materials in this thesis. As such, **Chapters 2** and **5** utilize controlled living polymerization and **Chapters 3-4** utilize SPPS (both of which were discussed earlier in **Section 1.1.4**. Controlled polymerizations may be iterative, step growth, or chain growth in mechanism. In contrast to the others, chain growth strategies generally lack control over primary sequence despite controlled polymerization techniques. The discovery of living polymerizations by Michael Szwarc in 1956 was the first breakthrough in chain growth methods, whereby growth of a polymer chain proceeds at a

constant rate, affording polymers with narrow molecular weight distributions or low dispersity.[77] For the synthesis of precisely controlled polymers, the majority of suitable methods encompass reversible-deactivation radical polymerization (RDRP), including (a) atom transfer radical polymerization (ATRP), Single-Electron Transfer Living Radical Polymerization (SET LRP)[78,79] or Supplemental Activator and Reducing Agent (SARA),[80,81] Activators Regenerated by Electron Transfer (ARGET),[82-84] Electrochemically mediated ATRP (eATRP),[85,86] photoinduced ATRP (Photo-ATRP),[87,88] and Metal-free Photoinduced Electron Transfer ATRP (PETATRP),[89] and (b) reversible addition−fragmentation chain transfer (RAFT) polymerization, with alternatives such as PETRAFT,[90,91] (c) iniferter polymerization,[92] and (d) nitroxide-mediated polymerization (NMP).[93-96] Other well-characterized methods include ring-opening polymerization (ROP), with common variants including organocatalyzed,[97] anionic,[98-100] coordination−insertion,[101] enzymatic,[102,103] N-carboxyanhydride polymerization,[104,105] and ring-opening metathesis polymerization (ROMP),[106] with alternatives such as alternating ROMP (AROMP)[107-109] and metal-free ROMP.[110] With uncontrolled methods, one cannot achieve significant control over primary sequence or advanced architectures. Despite the expansive inventory of controlled polymerization methods available, there is still no equivalent to the kind of sequence control afforded by solid phase peptide synthesis first pioneered by R. B. Merrifield, even with the foremost controlled polymerization methods.[111] Manual or automated iterative strategies have been used to synthesize sequence-controlled polymers;[112] however, these approaches often incur the expenses of unsustainable practices and time. Regardless, stepwise approaches are still advantageous for developing sequence-controlled polymers for tuning properties such as single-chain morphologies.[113] Meanwhile, efforts to develop streamlined chemistries are imperative; the following section describes some recent achievements toward the ability to control primary sequence.

Hawker and co-workers reported a new strategy for ROMP of sequence-controlled polymers using a macrocyclic monomer containing distinct ABCDE-type moieties.[114] Prior to this work, efforts to synthesize sequence-controlled polymers via multi-substituted cyclooctadienes using ROMP have

been limited in number and types of incorporated functionalities.[115,116] During chain extension, the growing polymer sequence obtained ordered repeats of ABCDE units along a polyester backbone. To achieve this, the authors used a small molecule polymerization trigger derived from saccharin to synthesize an unstrained macrocycle. Close proximity of the macrocycle olefin to a terminal alkyne enabled fast intramolecular cyclization and subsequent rapid ROMP with Grubbs' 3rd generation catalyst (G3) (**Figure 1.3.1**). This work demonstrates a general synthetic strategy for ROMP of diverse repeat units such as ester, sulfonamide, heterocyclic, etc., incorporated within the polymer backbone. The strategy also provides one of the few known methods for synthesizing fully biodegradable ROMP polymers,[117] a recurring challenge with highly functionalized biosynthetic polymers. Improvements in the AROMP method were also reported recently. Several examples describe iterative monomer addition by Ru-promoted isomerization of bicyclo[4.2.0]oct-7-ene-7-carboxamides[109] or via living copolymerization of 1,1-disubstituted cyclopropenes with low-strain cyclic olefins.[108] Though there is a great need for further improvement, especially in the context of tailoring these methods toward increased chemical diversity and demonstrated biofunctionality, these approaches chronicle an exciting movement toward efforts to control the primary sequence of copolymers.

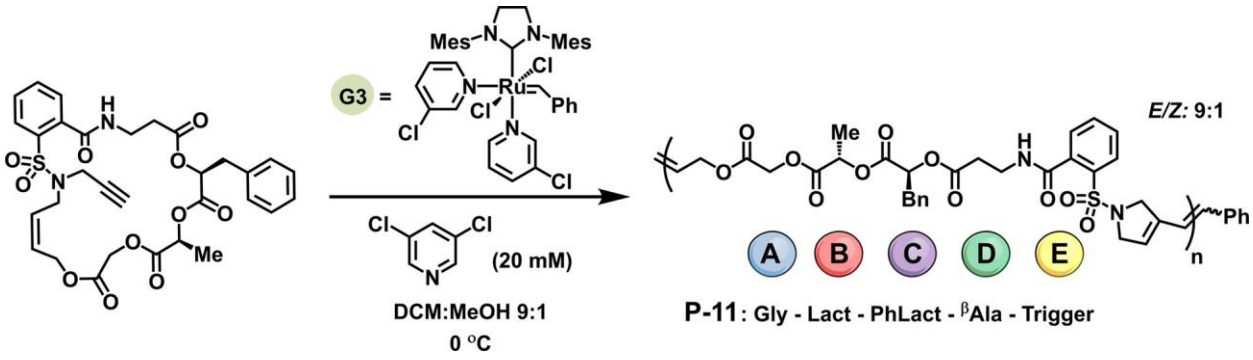


Figure 1.3.1. Strategy for the polymerization of unstrained macrocycles enabling primary sequence control. Monomers are composed of a ROMP polymerization trigger attached to a series of glycolate (Gly), (S)-lactate (Lact), (S)-phenyllactate (PhLact), and β-alanine (βAla). Reproduced with permission from ref [114].

A fascinating example of the use of biological machinery to control sequence selection during copper-mediated ATRP was recently published by Alexander and co-workers.[118] In this example,

GFP-labeled E. coli 539 served as a physical substrate for surface-promoted polymerization of acrylic quaternary amine-containing and sulphobetaine monomers in solution. The reductive environment of bacterial suspensions was utilized to generate catalytically active Cu(I) species, thereby initiating polymerization. This so-called “bacteria-instructed synthesis” produced templated polymers that specifically bound to the cell surface on which they were formed. In contrast, nontemplated polymers that formed in bulk solution had little affinity for the bacterial surface and were readily washed away. To demonstrate these polymers as a diagnostic tool, a presynthesized polymer bearing terminal alkyne groups was incubated with bacteria along with a “clickable” pro-fluorophore. Templated polymers sustained rapid fluorescence in the presence of the metabolically active environment due to copper-mediated cycloaddition. This work presents an innovative semisynthetic method for self-selective polymer sequence control entirely manipulated by bacteria. Its utility in detection and sequestration of matched pathogens is an exciting potential avenue in the field of adaptable diagnostics and antimicrobials.

1.3.2 Tacticity Control

Biopolymers containing tertiary and quaternary structures mediate a wide array of complex biological processes due to the preservation of their stereochemistry. It is known that the stereochemistry of polymers, or tacticity, can impose significant changes in physical and chemical properties of synthetic polymers.[119,120] This is an important consideration in **Chapter 5**, whereby inherent polymer atacticity likely influenced self-assembly control. Even so, stereoregulation remains a barrier for precise control of polymer structure. In a recent example by the Johnson group, an iterative exponential growth (IEG)-inspired approach was demonstrated for the economically scalable synthesis of sequence- and stereocontrolled unimolecular polymers.[121] In this IEG plus side chain functionality strategy, 1R and 1S epoxy alkynes were either subjected to azide substitution followed by functionalization or to deprotection in order to afford species that were coupled efficiently by CuAAC “click” chemistry, generating four different epoxy−alkyne diastereomers (**Figure 1.3.2**). These

"dimers" were then matched appropriately to synthesize macromolecules with the desired tacticity through multiple cycles of azide-instructed epoxide opening, alkyne deprotection, and subsequent CuAAC click conjugation. Comparison of thermogravimetric analysis data for isotactic and syndiotactic hexadecamers revealed subtle differences in thermal properties, namely the glass transition temperatures Tg, suggesting that differences in intermolecular polymer interactions were at play. This method demonstrated the scalable synthesis of a 6300 Da syndiotactic polymer; however, the final product was recovered in approximately 1 week. In order to minimize the length of time required, semiautomated synthesis by Flow-IEG offers a favorable application of this method toward primary sequence and architecture control.[122] With the increasing interest in tacticity control in mind, polymer chemists are actively pursuing advances in conventional chain growth methods. By improving control over primary structure and tacticity, more detailed analyses can be made to understand the correlation between these parameters and macromolecular assembly and function, thus bringing synthetic capabilities closer to the complexity afforded by nature.

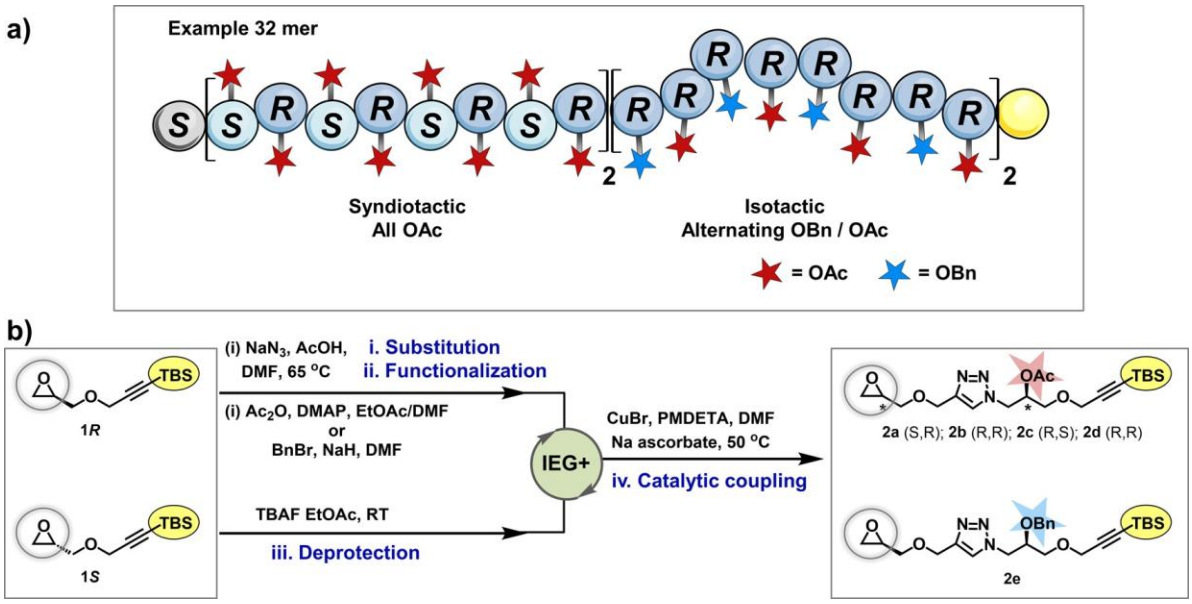


Figure 1.3.2. IEG-inspired iterative synthesis of sequence and stereo-controlled polymers. (a) Example of a 32-mer prepared by (b) orthogonal azidification, functionalization and silyl deprotection of two chiral monomers (1*S*, 1*R*) followed by CuAAC "click" of key stereoisomeric intermediates to generate polymers with precise sequences and stereochemistry. Adapted with permission from ref [121].

1.3.3 Grafting Control

While researchers are investigating novel methods for finely tuning polymer primary sequence, controlled polymerization strategies enable the incorporation of complex biomolecules that in themselves possess absolute sequence control. Therefore, by gaining excellent control over biomolecule graft polymers, materials are generated with 2-dimenional architectural control including the polymer backbone and side chains as a biologically interactive system. In this subsection, impact of 2-dimensional architectures on biological mode of action is highlighted. Moreover, this discussion is important to the design and control over polymer architecutre of several constructs discussed in **Chapters 2** and **5.**

Efforts have been directed at the expansion of graft-through methodologies with ROMP in order to avoid the large kinetic barrier implicit in postpolymerization conjugation of macromolecules. Successful conjugation of macromolecules is limited by steric hindrance, which often results in variable degrees of grafting, difficult purification and low reproducibility of polymer bioconjugates. As such, considerable effort has been devoted toward the direct polymerization of complex peptides,[36] nucleobases,[41] bioderived polyesters,[123] imaging agents,[43] and therapeutic drugs.[38] These biosynthetic polymers possess extreme complexity with rigorous control over polymer assembly and in some cases biofunctionality as tumor targeting[124] and protease resistant materials.[125] In particular, protected and/or deprotected peptide-based monomers, which range in size from 5 to 30 amino acids, can be polymerized into dense brushes as homopolymers[126] or amphiphilic block copolymers that self-assemble into micellar nanoparticles.[127] This modular approach allows very large peptides of any given sequence to be polymerized in the presence of Grubbs‘ 3rd generation catalyst. Attachment of 6-aminohexanoyl spacers to separate the polymerizable norbornene subunit from the peptide sequence further enhances polymerization rates, maintains low dispersity, and enables higher degrees of polymerization of biomacromonomers. Other strategies that incorporate complex functionality may rely on a grafting from approach, such as the preparation of high-chain density cylindrical copolypeptide brushes, via two rounds of N-carboxyanhydride polymerization in a one-pot procedure, with controlled segment lengths.[128] Accompanying the unmistakable advantage that graft-

through and some graft from strategies present for generating highly dense peptide polymers,[129] unique modes of action may be accessed, such as restricted proteolytic degradation.[125]

Regardless of which strategy is utilized, varying polymer architecture via grafting has the potential to modulate biological function. For instance, Sumerlin and co-workers used graft-to polymer bioconjugates in order to improve the therapeutic function of osteoprotegerin (OPG), which is a protein that restricts osteoclast formation and subsequently bone resorption in accelerated bone loss disorders.[130] Specifically, the role of side-chain grafting density was examined for OPG-polymer bioconjugates using linear, loosely branched, and densely branched poly(ethylene glycol) (PEG) architectures. Modest restoration of bone mineral density was achieved for the loosely branched conjugate/analogue in comparison to the other architectures. In another example, Tew and co-workers synthesized bioinspired protein transduction domain mimics with varying degrees of hydrophilic guanidine and hydrophobic phenyl group segregation.[131] Three types of polymers were analyzed for their membrane affinity and cellular internalization characteristics: nonsegregated homopolymers, intermediately segregated gradient copolymers, and strongly segregated block copolymers. Gradient copolymers with intermediate segregation displayed the highest activity and solubility with low cytotoxicity. Insight from this structure−activity survey was used for efficient siRNA delivery and gene knockdown in human T cells.[132] Thus, architecture control via selective grafting strategies can potentially improve efficacy of biosynthetic polymers, depending on the function required.

1.3.4 Conclusions for Architecture Control

Researchers are becoming increasingly aware of the importance of architecture[133] and tacticity[134] in self-assembly. Precise control over both stereo- and regiochemistry may accelerate opportunities for regulating geometries such as polymer tertiary and quaternary structures. Just as nature employs DNA and RNA sequences to encode biological information, and harnesses protein tertiary and quaternary structures to confer specialized activities, so too can researchers aspire to

use semisynthetic or fully synthetic polymers for the preparation of artificial viruses or enzymes, or cofactors in cascade pathways. Further, the ability to directly polymerize large biomolecules has the advantage of loading dense arrays of information. This contrasts with previous synthetic efforts of postpolymerization modification, which have little sequence control, lower grafting densities, and are often difficult to characterize. Achieving complex sequences using simple synthetic methods is paramount; continued efforts in this regard will undoubtedly surpass practically tenuous methods in the movement toward synthetic biological mimics.

1.4 Structural Dynamics of Polymer Assemblies

Complexing biosynthetic polymers into assemblies can increase their versatility and function. For example, nano- and micron-scale particles, vesicles, films, and hydrogels have been developed using self-assembled polymers.[135-137] Polymeric assemblies encompassing these architectures have been developed for various functions including stabilizing internal cargos, slowing clearance within biological systems, performing as supportive scaffolds, and/or serving as vehicles for signaling and detection. Many research groups have sought to develop assemblies with environmentally adaptive characteristics and therefore have devoted efforts to develop stimuli-responsive biomaterials for triggered signaling,[138] drug release,[54] and/or degradation.[71] Motivations for this aim arise from the desire to mimic natural behaviors like blood clotting and wound healing. However, controlling structurally dynamic behaviors within these assemblies is still difficult. Success along this avenue can advance previously unrealized opportunities for functionally diverse materials that surpass the limited utility of structurally inert designs. A notable example in this regard is the enhanced therapeutic efficacy of assemblies with active targeting capabilities compared to ones with passive abilities at low doses.[139] Nonetheless, in the interest of translating these systems for *in vivo* use, increasing functional complexity without forfeiting synthetic simplicity is necessary. The following discussion highlights examples that evaluate these two considerations.

1.4.1 Dynamic Particle Assemblies

The clinical relevance of shape-changing biosynthetic polymers has been demonstrated in a fibrosarcoma tumor model.[38,124,140,141] Specifically, enzyme-directed accumulation and retention of nanoparticle probes in tumor models was demonstrated with dye-labeled peptide-polymer amphiphiles (PPAs) (**Figure 1.4.1**). These PPAs are designed as a hydrophilic peptide brush conjugated to a polynorbornene backbone, and terminally labeled with fluorescent dyes. After proteolytic cleavage by matrix metalloproteinases (MMPs) expressed at elevated levels in the tumor,

the peptide is truncated causing NP aggregation into a larger scaffold assembly. Intratumoral (IT) and intravenous (IV) injection of these materials into tumor-burdened mice shows accumulation in the tumor and prolonged retention up to 8 days, which greatly exceeds insufficient retention times of hours to days observed with other active-targeting nanoparticle formulations.[142,143] These materials are detectable via a FRET signal unique to the newly formed assemblies, which are larger in size and slower to clear than the original nanoparticles. These stationary scaffolds can act as a source of slowly delivered anti-cancer therapeutics.[38,140] These proof-of-concept works demonstrate exceptional utility achieved by the dynamic morphological response of enzyme-responsive micellar assemblies in two ways: first as a discrete vehicle for noninvasive intravenous delivery and second as a stationary scaffold for diagnostics and localized drug release.

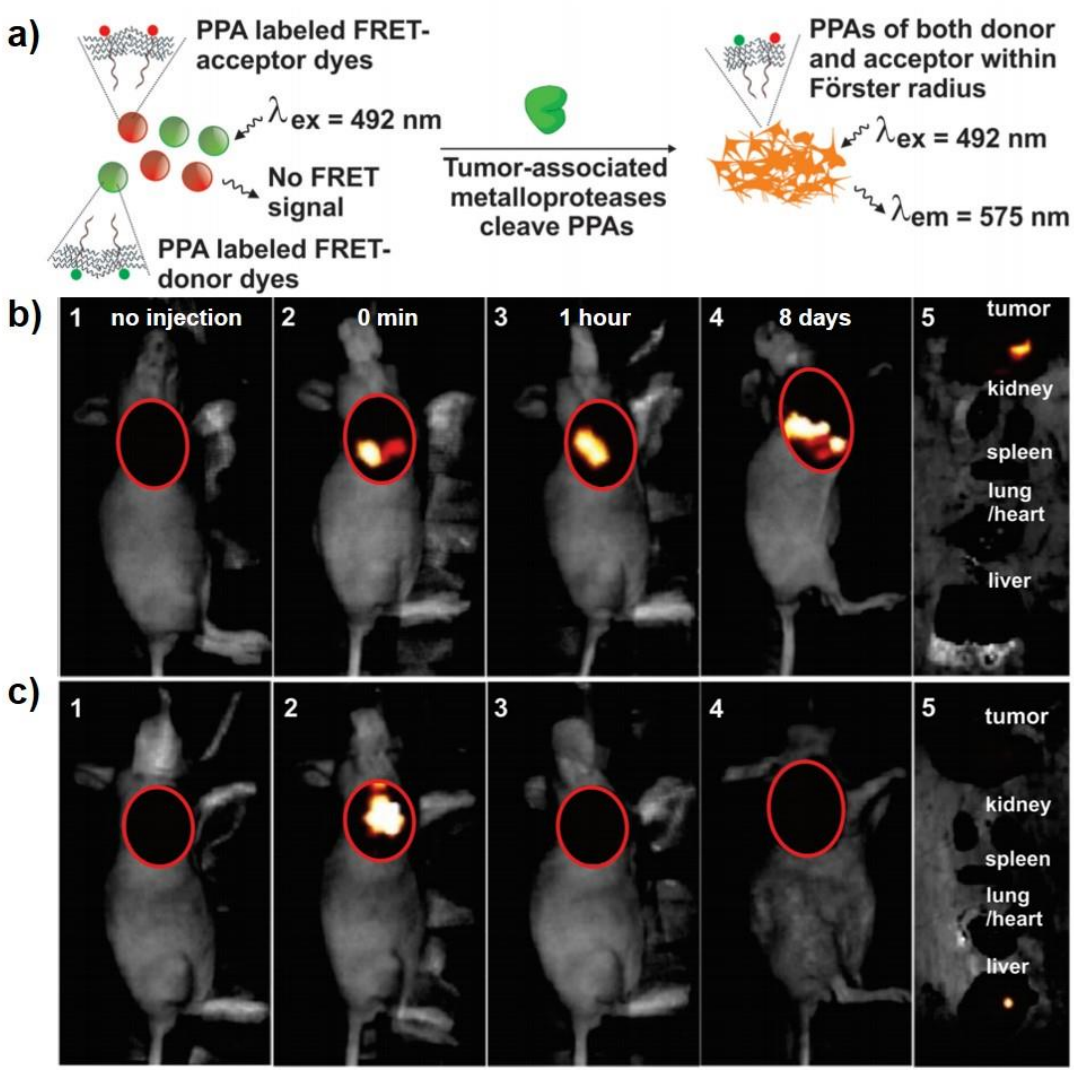


Figure 1.4.1. Enzyme-responsive nanoparticles change shape for tumor retention. (a) Rhodamine (red) or fluorescein (green)-labeled peptide-polymer amphiphiles (PPAs) pack to form enzyme-responsive nanoparticles. Mixture of the particles does not induce FRET signal due to lack of polymer exchange. Activation by MMPs in the tumor microenvironment induce particle aggregation and FRET. (b-c) Intratumoral injection in mice with HT-1080 tumors of (b) responsive L-amino acid-bearing PPAs and (c) nonresponsive D-amino acid-bearing PPAs. FRET signal observed with responsive particles up to 8 days, whereas nonresponsive particles clear from the tumor within 1 hr. Reproduced from ref [124].

Alternative stimuli, such as temperature or pH, have been shown to provoke changes in peptide-based particle assemblies. In one example, researchers developed a “nanopeptifier” system, which relies on thermally triggered self-assembly of elastin-like polypeptide amphiphiles containing a cell-penetrating peptide (CPP) domain on the hydrophilic block.[144] Once assembled into micelles, the high density CPP surface array enhances cellular uptake. To assess therapeutic payload delivery, a

proapoptotic peptide was attached to the hydrophobic domain; the resulting nanopeptifier acts as a dynamic switch, inducing apoptosis only in micellar form above the lower critical solution temperature (LCST). In another example by Savin and co-workers, poly(L-lysine)-*b*-poly(propylene oxide)-*b*-poly(L-lysine) triblock copolymers containing different lysine fractions were found to adopt distinct morphological transitions, either spherical micelle to vesicle or spherical micelle to disk micelle structures, as a function of pH.[145] Dynamic morphologies like this may have the capacity to alter *in vivo* biodistribution and shape-change induced drug release.

Despite increasing efforts for instilling stimuli-responsiveness in polymeric assemblies, some basic questions governing the spatial organization of these assemblies still remain. Specifically, how does conformational fluidity of a biofunctional polymer assembly impact its interaction at biological interfaces, in contrast to inert analogues? For example, amphiphilic block copolymers are promising in their use as artificial biological membranes, which are known to stabilize membrane proteins.[146] An interesting observation emerged from this study by Meier and co-workers, which determined that high flexibility of poly(dimethylsiloxane)-containing block copolymers may be responsible for successful integration of model membrane proteins despite mismatches in their hydrophobic domain sizes. As such, the identity of block copolymers within an assembly must be carefully considered when designing biomimetic membranes and analogous systems.

1.4.2 Self-Healing Hydrogels via Noncovalent Interactions

Polymer hydrogels represent a class of materials well-suited for a range of biological applications such as tissue engineering, regenerative medicines, controlled drug delivery, diagnostics, biological sensors, and microarrays due to their high water content and tunable mechanical properties.[147-149] These viscoelastic materials are achieved via permanent covalent chemical cross-links, through reactions between functional groups or free radicals, or noncovalent physical cross-links, such as hydrogen bonding, electrostatic interactions, metal−ligand coordination, and host−guest recognition. Covalent cross-links form robust and elastic hydrogels for load-bearing

support, whereas noncovalently cross-linked hydrogels have the ability to flow under shear thinning conditions, an important quality for *in vivo* delivery. However, when covalent hydrogels are damaged by breaks or when noncovalent hydrogels resist reassembly after shearing from injection, they inevitably lose their function in biological systems. Thus, many therapeutic hydrogel strategies are not currently viable for noninvasive delivery or prolonged clinical application.[12] In one approach to combat this problem, researchers imparted a permanently crosslinked hydrogel with pH-dependent self-healing by integrating noncovalent physical cross-linking capability, specifically side chains capable of hydrogen bonding.[150] Nevertheless, this combinatorial strategy only enabled healed hydrogels to retain up to 70% of their pristine fracture stress after a single break. Recent accounts using polymer−nanoparticle and host−guest interactions provide simple and adaptable methods for uniform and complete healing via concentrated pockets of strong noncovalent interactions following shear thinning damage; in essence, these interactions act as transient covalent cross-link mimics which provide rapid healing on the order of seconds. These types of composite materials may be a plausible alternative for soft hydrogel-based therapeutic delivery.

Inspired by work with clay particle in polymer dispersions that improve stiffness and elasticity of resulting gels,[151,152] Marcellan, Leibler, and co-workers used TM-50 silicon nanoparticle solutions as adhesives for severed noncovalent gels and biological tissues.[153] This strategy relies on the absorption of nanoparticles onto polymer gels, which then bridge polymer chains. By simply pressing them together in the nanoparticle solutions, separate pieces of poly(dimethylacrylamide) adhered on the order of tens of seconds. Interestingly, glued gels were tougher by lap-shear adhesion tests and resisted further damage at the bonding junction compared to unsevered regions. Within this bonding junction, polymer chains adhered to the nanoparticles reorganized and dissipated energy under stress, thus maintaining flexibility and structural support at the newly repaired tear site. This facile method of noncovalent hydrogel repair contrasts with those that rely on harsher conditions such as chemical, thermal, pH, UV irradiation, or an electric field.

Langer and co-workers tackled a complementary issue with shear-thinning, noncovalently cross-linked hydrogels.[154] Hydroxypropylmethylcellulose derivatives (HPMC-x) were combined with core−shell PEG-*b*-PLA nanoparticles to create shear thinning hydrogels that fully recovered their equilibrium viscoelasticity within 10 s (**Figure 1.4.2**). In contrast, the absence of nanoparticles yielded low-viscosity liquids. Transient and reversible hydrophobic forces between the polymer and nanoparticle chains were responsible for rapid disassembly when traversing the needle under force followed by rapid recovery after exiting. Given this efficient healing process, an encapsulated model therapeutic protein, fluorescein isothiocyanate-labeled bovine serum albumin, remained within the matrix for localized and gradual release over several days following subcutaneous injection into C57BL/6 mice. Another study utilized shear-thinning nanocomposite hydrogels composed of synthetic silicate nanoplatelets and gelatin for the treatment of hermorrhage in a mouse liver bleeding model.[155] Rapid mechanical recovery of the hydrogels and promotion of coagulation enabled sealing of severe incompressible wounds. The results of these studies demonstrate a simple method for minimally invasive delivery of polymeric hydrogels with the capacity for encoding biomolecules.

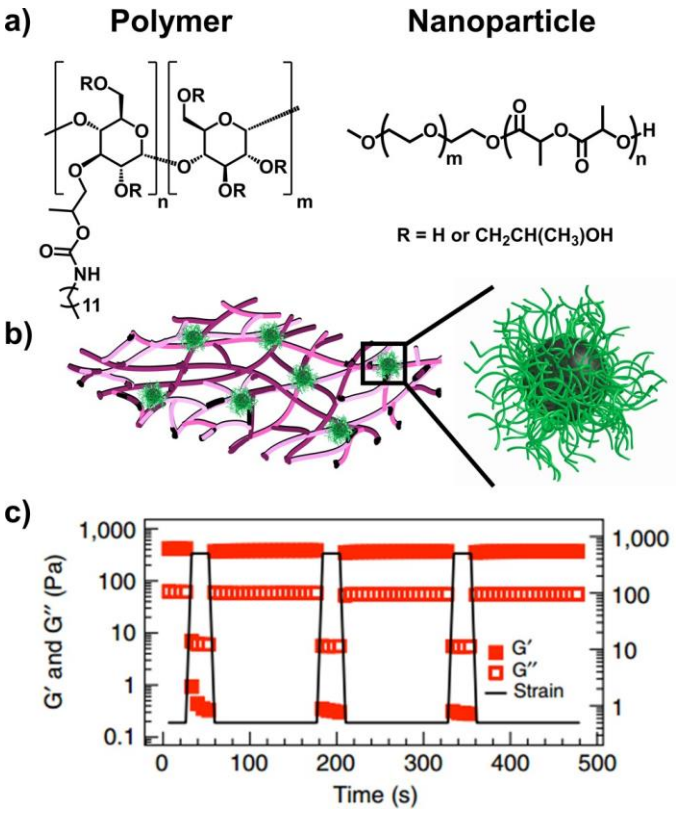


Figure 1.4.2. Self-assembled hydrogels utilizing polymer−nanoparticle (PNP) interactions. (a) Dodecyl-derivatized hydroxypropyl-methylcellulose (HPMC-C12) polymer and core−shell PEG-*b*-PLA based NPs are (b) mixed to form hydrogels where polymer chains adsorb to NPs to create transient noncovalent interactions. (c) These hydrogels shear-thin and self-heal repeatedly as shown by rheology. Adapted with permission from ref [154].

Noncovalent hydrogels utilizing host−guest recognition were first demonstrated in 1994 with cyclodextrins (CDs),[156] which can act as a host for a variety of molecules such as PEG, ferrocene, and adamantine.[137] These interactions have the advantage of providing specificity for selective recognition and stimuli-responsive healing. Yin and co-workers utilized a host−guest complex between β-CD-modified poly(L-glutamic acid) (PLGA-g-β-CD) and cholesterol-modified triblock (PLGA-*b*-PEG-*b*-PLGA)-*g*-Chol to create self-healing and degradable supramolecular hydrogels.[157] A complementary system developed by Scherman and co-workers utilized polysaccharides functionalized with phenylalanine−cysteine dipeptides as a host-responsive biosynthetic progelator.[59] Upon addition of cucurbit[8]uril, strong 1:2 “homoternary” complexes with the pendant phenylalanine residues caused a sol-to-gel transition. Yet another system by Ravoo and co-workers used

amphiphilic β-CD host-bound vesicles and adamantane guest-bound hydroxyethyl cellulose in the formation of supramolecular hydrogels.[158] In contrast to self-healing hydrogels, which rely on nonspecific ionic interactions and hydrogen bonding, these dynamic host−guest interactions mitigated unwanted side reactions leading to passivation of the exposed surface areas;[159] therefore, long-term stability was maintained.

Many polymeric hydrogels possess viscoelastic properties similar to those of soft biological tissues;[160] these materials subsequently make excellent tissue scaffolds for wound repair or delivery vehicles for biomolecules. To ensure durability and/or practical delivery of these polymeric scaffolds in a biological system, however, they must possess dynamic assembly characteristics that enable self-healing despite excess shear stress. New studies on polymer−NP and host−guest interactions in hydrogels can bridge the gap between the discussed disparate advantages of covalently and noncovalently cross-linked polymer hydrogels in biomedical applications. Furthermore, their self-healing properties might address existing issues with injection strategies and prolonged integrity of soft tissue mimics.

1.4.3 Conclusions for Structural Dynamics of Polymer Assemblies

Within the past several decades, interest in dynamic biosynthetic polymers has expanded and with it new approaches to develop materials that encompass both the complex functions intrinsic to natural biomolecules and tunable capabilities like stimuli responsiveness constructed in synthetic polymers. By introducing dynamic complexity into polymeric assemblies such as nanoparticles and hydrogels, we may build a better understanding of biological processes that govern tissue assembly and preservation; ideally, these mimetic polymeric scaffolds could emulate natural soft tissues in complexity to afford wound healing and tissue regeneration.

1.5 Biotherapeutic Stabilization: Storage, Release, and Bioresistance

In **Chapters 2-5**, the mertis of biomaterials with covalently or noncovalently encapsulated drugs are discussed for the future prospect of demonstrating therpauetic efficacy. Namely, how cargos can be stored in self-assemblies or encapsulated as a result of self-assembly, and then be released in a controlled manner, is of paramount interest for the platforms designed herein. Thus a brief discussion on these topics is important to provide context.

The widespread availability of biotherapeutics such as therapeutic peptides and proteins, antibodies, engineered fusion proteins, and conjugates has been used to treat conditions including cardiovascular disease, cancer, inflammation, infectious diseases, and genetic disorders.[161,162] They are advantageous over small molecule drugs due to higher specificity and potency, lower systemic toxicity, and reduced off-target biodistribution. However, the nature of their large sizes and complex structures introduces challenges in the production, storage, and administration of these therapeutics. Functional biosynthetic polymers have been used as vehicles or supports for storing and safely delivering biotherapeutics in formulations such as polymer scaffolds, polymer conjugates, and polymeric and liposomal particles.[136,163,164] In some instances, these approaches are prohibitively expensive or unstable for industrial and agricultural applications.[165] In the following section, efforts to stabilize biotherapeutics are discussed.

1.5.1 Matrix-Based Assemblies for Biopolymer Storage

Hydrogels are one of the most heavily investigated biomaterials for enzyme stabilization and controlled release of small molecule drugs, nanoparticles, and biotherapeutics, due to simple syntheses.[166] However, current hydrogel formulations still remain unsuitable for maintaining prolonged biological activity of many fragile biomacromolecules such as monoclonal antibodies and

therapeutic enzymes.[167] Hydrogels formed through covalent cross-linking or noncovalent interactions can cause denaturation and aggregation, respectively. Recently, however, Maynard and Langer demonstrated the utility of trehalose-based polymeric hydrogels for enhancing long-term functional stability and heat resistance of unstable biotherapeutics.[165,168]

Trehalose is a nonreducing disaccharide which is extremely effective as a protein- and poly(nucleic acid)-stabilizing excipient.[169] Maynard and co-workers analyzed the stabilizing effects of trehalose-based polymeric hydrogels on phytase, a thermally unstable enzyme heavily used in the animal feed industry.[165] Radical polymerization of vinyl-substituted trehalose and simple purification procedures presented a scalable and economical two-step method for preparing trehalose hydrogels for phytase stabilization (**Figure 1.5.1**). Investigators observed 100% phytase activity retention in the presence of trehalose hydrogels even when heated to 90 °C. Interestingly, a noncontrolled polymerization technique still allowed investigators to access highly functional biosynthetic polymers without rigorous control over polymer architecture. In examples such as this, one asks the question, “how vital is discrete polymer architecture for some applications?”

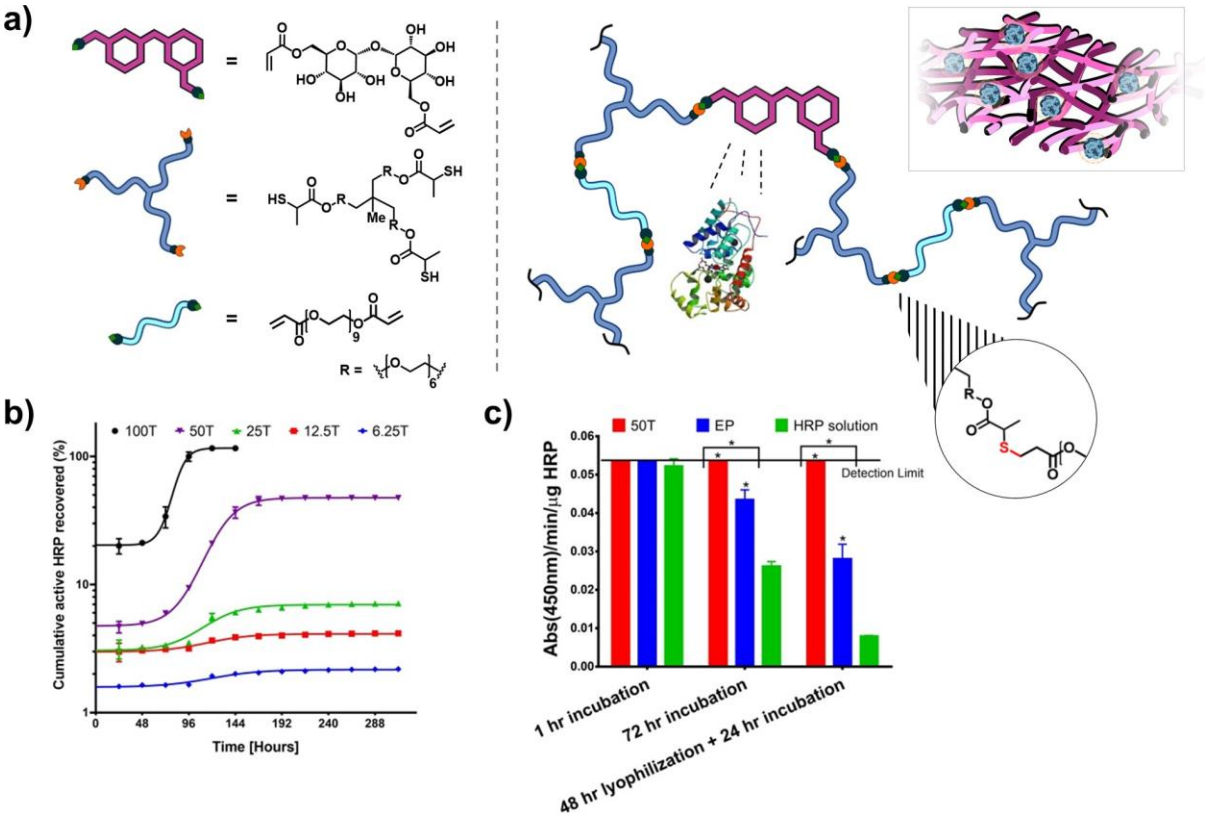


Figure 1.5.1. Trehalose and ethoxylated polyol (EP) hydrogel components for stabilizing model proteins. (a) Thiol−ene cross-linking of diacrylate functionalized trehalose (TDA) with EP, showing hydrogen-bonding interactions between trehalose and horseradish peroxidase (HRP) within the hydrogel network. (b) Increasing trehalose content in the hydrogel correlates with greater percent recovery of active protein during release. (c) Measured stability of HRP within the trehalose gel 1, 72, or 48 h of lyophilization and subsequent rehydration for 24 h. Adapted with permission from ref [168].

In a related study, Langer and co-workers fabricated synthetic trehalose hydrogels through thiol−ene cross-linking of diacrylate-functionalized trehalose (TDA) within a known ethoxylated polyol (EP) hydrogel platform.[168] Horseradish peroxidase (HRP) isoform C, glucose oxidase, and α-chymotrypsin were used as model unstable proteins and into preformed hydrogel disks. Protein stability was directly proportional to trehalose content within EP hydrogel networks, with high levels of biological activity recovery in high trehalose-containing hydrogels. Enhanced stabilization under heat and lyophilization is thought to be attributed in part to uniquely strong hydrogen-bonding character within the trehalose hydrogel network, which is hydration dependent. Furthermore, modular release kinetics was achieved through variable hydrolyzable ester content from trehalose incorporation.

These studies represent new strides in the field of biomolecule-functionalized synthetic polymers for broad utility as biopolymer protectants. Notable are biomimetic polymeric hydrogels containing heparin, hyaluronic acid, and collagen; other native moieties have been used as biotherapeutic storage and release matrices with less impressive stabilization results.[170,171]

1.5.2 Controlled Release of Biomaterials from Networks

A popular tool introduced in 1992 for functionalization of surfaces involves the layer-by-layer (LbL) deposition of polyelectrolyte films,[172] polysaccharides,[173-176] poly(amino acids),[177] poly(acrylic acid),[178] and various other polyelectrolytes.[179,180] The Hammond Lab has made considerable progress with these materials for temporary protection and variable-timed release of therapeutic cargos via diffusion, stimuli-response, and/or network degradation.[181-185] For instance, naturally derived LbL films were assembled through electrostatic complexation between anionic poly(β-L-malic acid) and cationic chitosan in aqueous conditions.[186] By increasing chitosan composition, which stabilized film growth and robustness, protein release kinetics were slowed from total enzyme release in tens of minutes to multiple days to promote burst release or sustain degradative release, respectively. The investigators also noted that release kinetics were unaffected by increasing the total number of surface layers, enabling short-term or prolonged dosing. Application of bFGF-loaded multilayer films in NIH3T3 fibroblast cells demonstrated dose-responsive cell proliferation. Comparison with equal quantities of as-received bFGF showed that film-released bFGF significantly increased proliferative activity. As such, corelease with chitosan was believed to stabilize this liberated bFGF from heat-inactivation and proteolysis.

Rigorous control over biotherapeutic release from a protected state is key for creating personalized medicine. Given the variety of known diseases that affect different physiological pathways and to variable degrees, appropriate dosing is salient for proper treatment. To be seriously considered as a viable system for general application in clinical treatment, biosynthetic polymer assemblies such as those discussed above need to provide rigorously controlled and versatile cargo release profiles.

1.5.3 Bioresistance with Biopolymer Conjugates

Polymer conjugation has been a successful method for prolonging the circulation half-life and activity of unstable biopolymers. Since the late 1970s, protein−polymer conjugates have been widely explored as therapeutics, even gaining FDA approval as PEG conjugates.[187] PEGylation has been widely used because of its solubilizing effect, high biocompatibility, and ability to minimize interactions with blood components. However, recent studies have reported controversial accounts of PEGylation including immunogenicity, degradation under stress, and accumulation in the body above excretion limits. As such, charged zwitterionic polymers,[188] polyglycidols,[189] and biodegradable alternatives[190] like poly(amino acids)s, chitosan mimics, and heparin mimics are currently being explored. A noncytotoxic heparin-mimic polymer PDS-*b*-P(SS-*co*-PEGMA) bearing styrenesulfonate (SS) moieties and a pyridyl disulfide (PDS) functionalizable end group was synthesized via ATRP.[191] Conjugation of this polymer to basic fibroblast growth factor (bFGF), a notoriously unstable protein involved in bone regeneration and wound healing, resulted in superior resistance to extreme temperatures used in storage and delivery, low pH, and proteolysis (**Figure 1.5.2**). Bioactivity of the bFGF-p(SS-*co*-PEGMA) heparin-mimic conjugate was significantly higher than the bFGF-pPEGMA control in which the styrenesulfonate units were omitted. Close proximity of the heparin-mimic polymer to bFGF was shown to protect it from denaturation more so than a simple mixture of heparin and bFGF, the conventional method of stabilizing bFGF for drug delivery. This is the first example of a stabilized bFGF conjugate and may provide an avenue for increasing the scope of biostabilization through polymer conjugates.

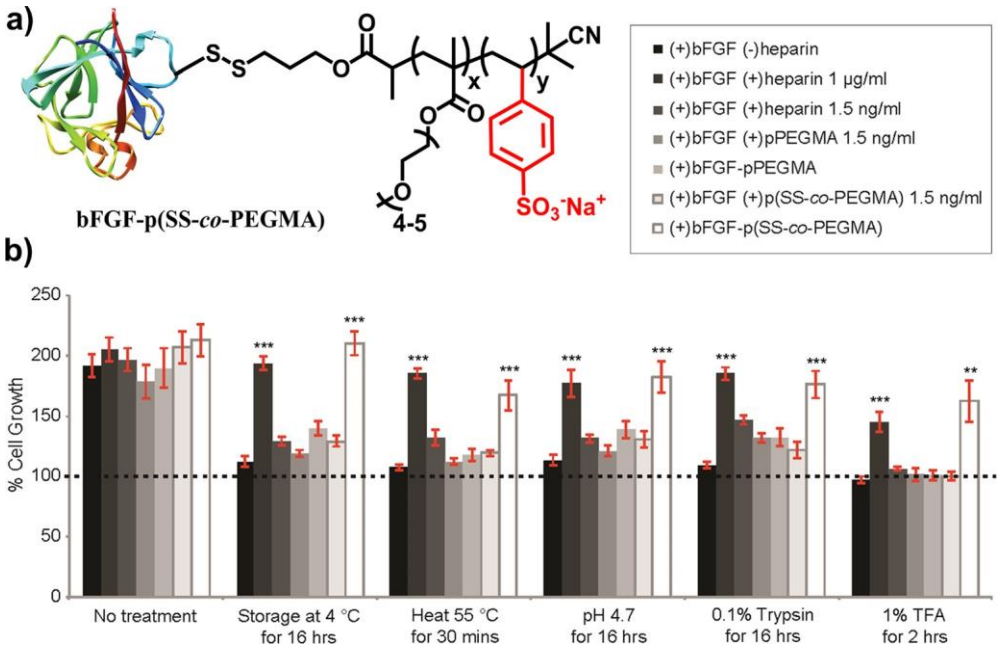


Figure 1.5.2. A heparin-mimicking polymer conjugate stabilizes bFGF. (a) Conjugation of bFGF to a styrenesulfonate and poly(ethylene glycol) bearing methyl methacrylate copolymer (bFGF-p(SS-*co*-PEGMA)) (b) stabilizes the protein to prolonged storage, heat, acidic conditions, and enzymatic degradation. Adapted with permission from ref [191].

In some formulations, polymer conjugates self-assemble into particles.[192,162] Nanoparticle and liposomal formulations with unconjugated cargos have been used as secondary carriers to load and shield biomolecules, but their formulation stability and/ or loading capacities often remain low.[193] This issue is addressed in a study where nucleic acid delivery potency was enhanced through conjugation of DNA with functional synthetic polymers that self-assemble. Inspired by early work from Mirkin and co-workers with spherical nucleic acids on gold nanoparticles[194] and their templated metal-free counterparts,[195] Gianneschi and co-workers directly conjugated DNA to a hydrophobic homopolymer to generate informational amphiphiles.[196] These nucleic acid−polymer conjugates self-assembled into micellar nanoparticles displaying a dense shell of nucleic acids on the surface. The high surface curvature and packing density of the micellar nanoparticle promoted nuclease resistance and rapid cellular uptake for prolonged knockdown of survivin mRNA in HeLa cancer cells.[197] This work shows the utility of simple nucleic acid−polymer conjugates, which protect themselves through spontaneous self-assembly, for targeted biotherapeutic delivery.

A strategy to increase proteolytic resistance of peptides in our lab has been explored in our lab for materials that do not protect themselves by self-assembly, but rather through polymerization of dense peptide-polymer brushes.[125] These peptide-polymer conjugates possess a proteolytically resistant polynorbornene backbone, which is utilized in **Chapter 5**. Furthermore, proteolytic susceptibiliy was tuned by either changing the degree of polymerization (DP) or copolymerization of norbornene-peptide monomers with norbornene-oligoethylene glycol spacer units. Thus, decreasing DP and/or peptide density in these polymer brushes controlled access of various robust proteases (MT1-MMP, thermolysin, pronase, and trypsin) to the peptide substrates.

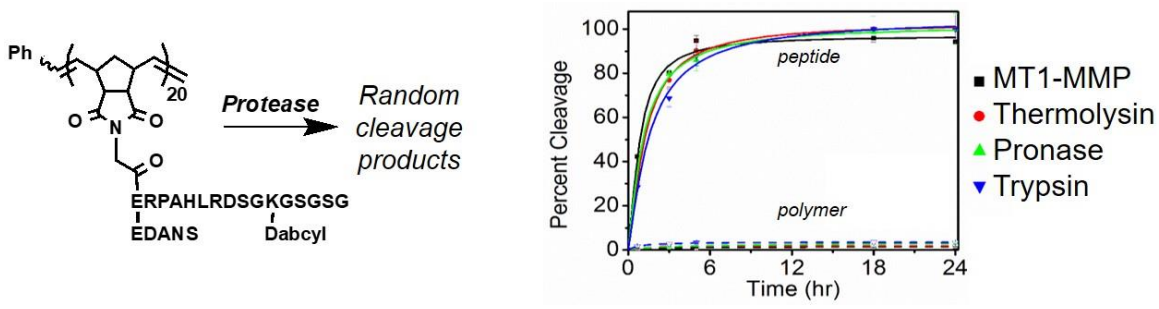


Figure 1.5.3. Protease-Resistant High Density Brush Peptide-Polymers Chemical structure (left) and cleavage kinetics (right) of monomeric and polymeric peptide substrates for thrombin and matrix metalloproteinase (MT1-MMP). Fluorogenic peptide substrates are labeled with an EDANS fluorophore and Dabcyl quencher for detection of peptide cleavage by MT1-MMP, thermolysin, pronase, and trypsin. Homopolymers at DP 20 show no significant cleavage in comparison the monomeric peptides.

Finally, strategies ot improve proteolytic resistance of biopolymer-only constructs can be achieved through simple synthetic modifications such as noncanonical amino acids and topological manipulation. Non-natural amino acids such as D-amino acids, are not recognized by most proteases in the human body, so replacement of some or all L-amino acids with these isomers can prevent their recognition, altogether.[198,199] **Chapter 2** makes use of D-amino acids for the generation of nonresponsive control materials. Synthetic modification of the N-terminal (amine to acetyl functionality)[200] and C-terminal (acid to amide functionality)[201,202] residues of a peptide, is a commonly employed strategy to increase biostability of therapeutic peptides delivered *in vivo*. Importantly, these modifications generally do not impede therapeutic efficacy. Additional noncanonical adducts such as flourinated amino acids,[203] lanthionine rings,[169,204] alkylated histidines,[205], proline-rich domains,[206] and many others[207] have a

profound effect on biopolymer stability. The other strategy for biostabilization, topological manipulation, can be achieved through peptide stapling,[208,209] intramolecular cycliziation,[210] macocyclization,[211] and amphiphilic self-assembly.[212,213] In particular, the unique sequences of self-assembling peptides (SAPs) can induce assembly as macromolecular complexes such as vesicles,[214,215] micelles,[216-218] and nanofibers.[219,220] The dense packing of such constructs limits access of proteases to substrate amino acid residues. We utilize these types of materials in **Chapters 3-4**.

1.5.4 Conclusions for Biostabilization

Expensive biomolecules and biotherapeutics often suffer from instability and rapid degradation or clearance. Thus, the push for stabilization in biotechnology and biomedicine is high. The discussed packaging strategies have the advantage of reduced effective dosages, prolonged treatment, and/or enhanced targeting. Because of the nature of these expensive cargos, however, equally expensive biostabilizing polymers are impractical, as the combined cost would be prohibitive. Therefore, in this field, the necessity for economic viability in the form of adaptability of the technology, scalability, and reproducibility is paramount.

1.6 Perspectives and Outlook

The divide between pure synthetic and natural macromolecules continues to narrow in the pursuit of biologically relevant materials with increasingly complex functionality. Indeed, recent developments in biosynthetic polymer chemistry are allowing scientists to prepare, analyze, and use polymeric systems in unprecedented ways. Synthetic and especially multivalent polymers can partially mimic biopolymers. Conversely, biopolymers can be engineered to generate unnatural materials. Refinements in both controlled polymerization techniques, such as RDRP methods and olefin metathesis reactions, and bioconjugation strategies have enabled chemists to prepare bespoke multifunctional materials with designed architectures. Bioinspired linear polymers with properties similar to natural materials are also now accessible, while new functional materials with biological activity beyond those of natural polymers are in the first stages of development. Perhaps the greatest obstacle still in place is achieving functional complexity through simple design and manufacturing. Several examples presented here are still synthetically challenging and prompt initiatives for modifying existing techniques in order to develop simple and streamlined protocols. Just as personal or hand-held computers were, at worst, not even imagined and, at best, thought to be a near impossibility in the era of large scale computers in the 1960s, functional biosynthetic polymers may in the next few decades become commonplace in numerous industries. Despite great strides being made in this field, a pioneering perspective from 1984 persists as an exciting yet astounding reality to date.[221] Macromolecular chemistry as we know is far from capturing the processes so prevalent and active in living systems. However, we remain inspired by the possibilities that present themselves in the attempt to achieve these lofty heights. The key is an attitude that multidisciplinary approaches and collaborations with neighboring fields will open doors and opportunities for the field itself and for biomedicine alike.

1.7 Acknowledgements

Chapter 1.2-1.6 is adapted, in part, from material as it appears in Macromolecules 2016. Carlini, Andrea; Adamiak, Lisa; Gianneschi, Nathan. The dissertation author is the first author of this paper.

1.8 References

1 Benjamin, E. J., Virani, S. S., Callaway, C. W., Chamberlain, A. M., Chang, A. R., Cheng, S., Chiuve, S. E., Cushman, M., Delling, F. N., Deo, R., Ferranti, S. D. d., Ferguson, J. F., Fornage, M., Gillespie, C., Isasi, C. R., Jiménez, M. C., Jordan, L. C., Judd, S. E., Lackland, D., Lichtman, J. H., Lisabeth, L., Liu, S., Longenecker, C. T., Lutsey, P. L., Mackey, J. S., Matchar, D. B., Matsushita, K., Mussolino, M. E., Nasir, K., O'Flaherty, M., Palaniappan, L. P., Pandey, A., Pandey, D. K., Reeves, M. J., Ritchey, M. D., Rodriguez, C. J., Roth, G. A., Rosamond, W. D., Sampson, U. K. A., Satou, G. M., Shah, S. H., Spartano, N. L., Tirschwell, D. L., Tsao, C. W., Voeks, J. H., Willey, J. Z., Wilkins, J. T., Wu, J. H., Alger, H. M., Wong, S. S. & Muntner, P. Heart Disease and Stroke Statistics--2018 Update: A Report From the American Heart Association. *Circulation* **137**, e67-e492 (2018).

2 Heidenreich, P. A., Trogdon, J. G., Khavjou, O. A., Butler, J., Dracup, K., Ezekowitz, M. D., Finkelstein, E. A., Hong, Y., Johnston, S. C., Khera, A., Lloyd-Jones, D. M., Nelson, S. A., Nichol, G., Orenstein, D., Wilson, P. W. F. & Woo, J. Forecasting the future of cardiovascular disease in the United States: a policy statement from the Americcan Heart Association. *Circulation* **123**, 933-944 (2011).

3 Savarese, G. & Lund, L. H. Global Public Health Burden of Heart Failure. *Cardiac Failure Review* **3**, 7-11, doi:10.15420/cfr.2016:25:2 (2017).

4 Lister, Z., Rayner, K. J. & Suuronen, E. J. How Biomaterials Can Influence Various Cell Types in the Repair and Regeneration of the Heart after Myocardial Infarction. *Frontiers in Bioengineering and Biotechnology* **4**, 62, doi:10.3389/fbioe.2016.00062 (2016).

5 Czubryt, M. P. Common threads in cardiac fibrosis, infarct scar formation, and wound healing. *Fibrogenesis & Tissue Repair* **5**, 19-19, doi:10.1186/1755-1536-5-19 (2012).

6 Spinale, F. G. Myocardial Matrix Remodeling and the Matrix Metalloproteinases: Influence on Cardiac Form and Function. *Physiol. Rev.* **87**, 1285-1342, doi:10.1152/physrev.00012.2007 (2007).

7 Palatinus, J. A., Rhett, J. M. & Gourdie, R. G. Translational Lessons from Scarless Healing of Cutaneous Wounds and Regenerative Repair of the Myocardium. *J. Mol. Cell. Cardiol.* **48**, 550-557, doi:10.1016/j.yjmcc.2009.06.013 (2010).

8 Rane, A. A. & Christman, K. L. Biomaterials for the Treatment of Myocardial Infarction: A 5-Year Update. *J. Am. Coll. Cardiol.* **58**, 2615-2629, doi:https://doi.org/10.1016/j.jacc.2011.11.001 (2011).

9 Hernandez, M. J. & Christman, K. L. Designing Acellular Injectable Biomaterial Therapeutics for Treating Myocardial Infarction and Peripheral Artery Disease. *JACC: Basic to Translational Science* **2**, 212-226, doi:10.1016/j.jacbts.2016.11.008 (2017).

10 Nelson, D. M., Ma, Z., Fujimoto, K. L., Hashizume, R. & Wagner, W. R. Intra-myocardial biomaterial injection therapy in the treatment of heart failure: Materials, outcomes and challenges. *Acta Biomater.* **7**, 1-15, doi:https://doi.org/10.1016/j.actbio.2010.06.039 (2011).

11 Portnov, T., Shulimzon Tiberiu, R. & Zilberman, M. in *Rev. Chem. Eng.* Vol. 33 91 (2017).

12 Ungerleider, J. L. & Christman, K. L. Concise Review: Injectable Biomaterials for the Treatment of Myocardial Infarction and Peripheral Artery Disease: Translational Challenges and Progress. *Stem Cells Translational Medicine* **3**, 1090-1099, doi:10.5966/sctm.2014-0049 (2014).

13 Rane, A. A., Chuang, J. S., Shah, A., Hu, D. P., Dalton, N. D., Gu, Y., Peterson, K. L., Omens, J. H. & Christman, K. L. Increased Infarct Wall Thickness by a Bio-Inert Material Is Insufficient to Prevent Negative Left Ventricular Remodeling after Myocardial Infarction. *PLoS One* **6**, e21571, doi:10.1371/journal.pone.0021571 (2011).

14 Singelyn, J. M. & Christman, K. L. Modulation of material properties of a decellularized myocardial matrix scaffold(). *Macromol. Biosci.* **11**, 731-738, doi:10.1002/mabi.201000423 (2011).

15 Kadner, K., Dobner, S., Franz, T., Bezuidenhout, D., Sirry, M. S., Zilla, P. & Davies, N. H. The beneficial effects of deferred delivery on the efficiency of hydrogel therapy post myocardial infarction. *Biomaterials* **33**, 2060-2066, doi:https://doi.org/10.1016/j.biomaterials.2011.11.031 (2012).

16 Hu, X., Wang, J., Chen, J., Luo, R., He, A., Xie, X. & Li, J. Optimal temporal delivery of bone marrow mesenchymal stem cells in rats with myocardial infarction. *European Journal of Cardio-Thoracic Surgery* **31**, 438-443, doi:10.1016/j.ejcts.2006.11.057 (2007).

17 Yoshizumi, T., Zhu, Y., Jiang, H., D'Amore, A., Sakaguchi, H., Tchao, J., Tobita, K. & Wagner, W. R. Timing effect of intramyocardial hydrogel injection for positively impacting left ventricular remodeling after myocardial infarction. *Biomaterials* **83**, 182-193, doi:10.1016/j.biomaterials.2015.12.002 (2016).

18 Nguyen, M. M., Gianneschi, N. C. & Christman, K. L. Developing injectable nanomaterials to repair the heart. *Curr. Opin. Biotechnol.* **34**, 225-231, doi:https://doi.org/10.1016/j.copbio.2015.03.016 (2015).

19 Alexis, F., Pridgen, E., Molnar, L. K. & Farokhzad, O. C. Factors Affecting the Clearance and Biodistribution of Polymeric Nanoparticles. *Mol. Pharm.* **5**, 505-515, doi:10.1021/mp800051m (2008).

20 Clares, B., Ruiz, M. A., Gallardo, V. & Arias, J. L. Drug Delivery to Inflammation Based on Nanoparticles Surface Decorated with Biomolecules. *Curr. Med. Chem.* **19**, 3203-3211, doi:http://dx.doi.org/10.2174/092986712800784676 (2012).

21 Spinale, F. Myocardial matrix remodeling and the matrix metalloproteinases: influence on cardiac form and function. *Physiol Rev.* **87**, 1285-1342 (2007).

22 Gandhi, A. A. & Akholkar, P. J. Metabolic acidosis in acute myocardial infarction. *2017* **2**, 4, doi:10.18203/2349-3933.ijam20150556 (2017).

23 Kubasiak, L. A., Hernandez, O. M., Bishopric, N. H. & Webster, K. A. Hypoxia and acidosis activate cardiac myocyte death through the Bcl-2 family protein BNIP3. *Proc. Natl. Acad. Sci. U. S. A.* **99**, 12825-12830, doi:10.1073/pnas.202474099 (2002).

24 Grover, G. N., Braden, R. L. & Christman, K. L. Oxime Cross-Linked Injectable Hydrogels for Catheter Delivery. *Adv. Mater.* **25**, 2937-2942, doi:doi:10.1002/adma.201205234 (2013).

25 Leor, J., Tuvia, S., Guetta, V., Manczur, F., Castel, D., Willenz, U., Petneházy, Ö., Landa, N., Feinberg, M. S., Konen, E., Goitein, O., Tsur-Gang, O., Shaul, M., Klapper, L. & Cohen, S. Intracoronary Injection of In Situ Forming Alginate Hydrogel Reverses Left Ventricular Remodeling After Myocardial Infarction in Swine. *Journal of the American College of Cardiology* **54**, 1014-1023, doi:http://dx.doi.org/10.1016/j.jacc.2009.06.010 (2009).

26 Singelyn, J. M., Sundaramurthy, P., Johnson, T. D., Schup-Magoffin, P. J., Hu, D. P., Faulk, D. M., Wang, J., Mayle, K. M., Bartels, K., Salvatore, M., Kinsey, A. M., DeMaria, A. N., Dib, N. & Christman, K. L. Catheter-deliverable hydrogel derived from decellularized ventricular extracellular matrix increases endogenous cardiomyocytes and preserves cardiac function post-myocardial infarction. *Journal of the American College of Cardiology* **59**, 751-763, doi:10.1016/j.jacc.2011.10.888 (2012).

27 Li, Z., Fan, Z., Xu, Y., Lo, W., Wang, X., Niu, H., Li, X., Xie, X., Khan, M. & Guan, J. pH-Sensitive and Thermosensitive Hydrogels as Stem-Cell Carriers for Cardiac Therapy. *ACS Applied Materials & Interfaces* **8**, 10752-10760, doi:10.1021/acsami.6b01374 (2016).

28 Bastings, M. M. C., Koudstaal, S., Kieltyka, R. E., Nakano, Y., Pape, A. C. H., Feyen, D. A. M., van Slochteren, F. J., Doevendans, P. A., Sluijter, J. P. G., Meijer, E. W., Chamuleau, S. A. J. & Dankers, P. Y. W. A Fast pH-Switchable and Self-Healing Supramolecular Hydrogel Carrier for Guided, Local Catheter Injection in the Infarcted Myocardium. *Advanced Healthcare Materials* **3**, 70-78, doi:10.1002/adhm.201300076 (2014).

29 Trnka, T. M. & Grubbs, R. H. The Development of L2X2RuCHR Olefin Metathesis Catalysts: An Organometallic Success Story. *Acc. Chem. Res.* **34**, 18-29, doi:10.1021/ar000114f (2001).

30 Sanford, M. S., Love, J. A. & Grubbs, R. H. A Versatile Precursor for the Synthesis of New Ruthenium Olefin Metathesis Catalysts. *Organometallics* **20**, 5314-5318, doi:10.1021/om010599r (2001).

31 Matson, J. B., Virgil, S. C. & Grubbs, R. H. Pulsed-Addition Ring-Opening Metathesis Polymerization: Catalyst-Economical Syntheses of Homopolymers and Block Copolymers. *J. Am. Chem. Soc.* **131**, 3355-3362, doi:10.1021/ja809081h (2009).

32 Matson, J. B. & Grubbs, R. H. Monotelechelic Poly(oxa)norbornenes by Ring-Opening Metathesis Polymerization Using Direct End-Capping and Cross-Metathesis. *Macromolecules* **43**, 213-221, doi:10.1021/ma9019366 (2010).

33 Love, J. A., Morgan, J. P., Trnka, T. M. & Grubbs, R. H. A Practical and Highly Active Ruthenium-Based Catalyst that Effects the Cross Metathesis of Acrylonitrile. *Angew. Chem. Int. Ed.* **41**, 4035-4037, doi:doi:10.1002/1521-3773(20021104)41:21<4035::AID-ANIE4035>3.0.CO;2-I (2002).

34 Oh, Y. I., Sheng, G. J., Chang, S.-K. & Hsieh-Wilson, L. C. Tailored Glycopolymers as Anticoagulant Heparin Mimetics. *Angewandte Chemie (International ed. in English)* **52**, 11796-11799, doi:10.1002/anie.201306968 (2013).

35 Sletten, E. T., Svec, R. L. & Nguyen, H. M. Synthesis of a polymerizable, bivalent glycan mimetic of the HIV envelope spike gp120. *Tetrahedron Lett.* **56**, 3473-3476, doi:10.1016/j.tetlet.2015.01.016 (2015).

36 Hahn, M. E., Randolph, L. M., Adamiak, L., Thompson, M. P. & Gianneschi, N. C. Polymerization of a peptide-based enzyme substrate. *Chem. Commun.* **49**, 2873-2875, doi:10.1039/C3CC40472B (2013).

37 Kammeyer, J. K., Blum, A. P., Adamiak, L., Hahn, M. E. & Gianneschi, N. C. Polymerization of protecting-group-free peptides via ROMP. *Polymer Chemistry* **4**, 3929-3933, doi:10.1039/C3PY00526G (2013).

38 Callmann, C. E., Barback, C. V., Thompson, M. P., Hall, D. J., Mattrey, R. F. & Gianneschi, N. C. Therapeutic Enzyme-Responsive Nanoparticles for Targeted Delivery and Accumulation in Tumors. *Adv. Mater.* **27**, 4611-4615, doi:10.1002/adma.201501803 (2015).

39 Liao, L., Liu, J., Dreaden, E. C., Morton, S. W., Shopsowitz, K. E., Hammond, P. T. & Johnson, J. A. A Convergent Synthetic Platform for Single-Nanoparticle Combination Cancer Therapy: Ratiometric Loading and Controlled Release of Cisplatin, Doxorubicin, and Camptothecin. *J. Am. Chem. Soc.* **136**, 5896-5899, doi:10.1021/ja502011g (2014).

40 Johnson, J. A., Lu, Y. Y., Burts, A. O., Xia, Y., Durrell, A. C., Tirrell, D. A. & Grubbs, R. H. Drug-Loaded, Bivalent-Bottle-Brush Polymers by Graft-through ROMP. *Macromolecules* **43**, 10326-10335, doi:10.1021/ma1021506 (2010).

41 James, C. R., Rush, A. M., Insley, T., Vuković, L., Adamiak, L., Král, P. & Gianneschi, N. C. Poly(oligonucleotide). *J. Am. Chem. Soc.* **136**, 11216-11219, doi:10.1021/ja503142s (2014).

42 Lo, P. K. & Sleiman, H. F. Nucleobase-Templated Polymerization: Copying the Chain Length and Polydispersity of Living Polymers into Conjugated Polymers. *J. Am. Chem. Soc.* **131**, 4182-4183, doi:10.1021/ja809613n (2009).

43 Thompson, M. P., Randolph, L. M., James, C. R., Davalos, A. N., Hahn, M. E. & Gianneschi, N. C. Labelling Polymers and Micellar Nanoparticles via Initiation, Propagation and Termination with ROMP. *Polymer chemistry* **5**, 1954-1964, doi:10.1039/C3PY01338C (2014).

44 Sowers, M. A., McCombs, J. R., Wang, Y., Paletta, J. T., Morton, S. W., Dreaden, E. C., Boska, M. D., Ottaviani, M. F., Hammond, P. T., Rajca, A. & Johnson, J. A. Redox-responsive branched-bottlebrush polymers for in vivo MRI and fluorescence imaging. *Nature Communications* **5**, 5460, doi:10.1038/ncomms6460

https://www.nature.com/articles/ncomms6460#supplementary-information (2014).

45 Habibi, N., Kamaly, N., Memic, A. & Shafiee, H. Self-assembled peptide-based nanostructures: Smart nanomaterials toward targeted drug delivery. *Nano today* **11**, 41-60, doi:10.1016/j.nantod.2016.02.004 (2016).

46 Stawikowski, M. & Fields, G. B. Introduction to Peptide Synthesis. *Current protocols in protein science / editorial board, John E. Coligan ... [et al.]* **CHAPTER**, Unit-18.11, doi:10.1002/0471140864.ps1801s26 (2002).

47 Behrendt, R., White, P. & Offer, J. Advances in Fmoc solid‐phase peptide synthesis. *J. Pept. Sci.* **22**, 4-27, doi:10.1002/psc.2836 (2016).

48 Coin, I., Beyermann, M. & Bienert, M. Solid-phase peptide synthesis: from standard procedures to the synthesis of difficult sequences. *Nat. Protoc.* **2**, 3247, doi:10.1038/nprot.2007.454 (2007).

49 Paradís-Bas, M., Tulla-Puche, J. & Albericio, F. The road to the synthesis of “difficult peptides”. *Chem. Soc. Rev.* **45**, 631-654, doi:10.1039/C5CS00680E (2016).

50 Günay, K. A., Theato, P. & Klok, H.-A. in *Functional Polymers by Post-Polymerization Modification* 1-44 (Wiley-VCH Verlag GmbH & Co. KGaA, 2012).

51 Khan, F., Tanaka, M. & Ahmad, S. R. Fabrication of polymeric biomaterials: a strategy for tissue engineering and medical devices. *Journal of Materials Chemistry B* **3**, 8224-8249, doi:10.1039/C5TB01370D (2015).

52 Theato, P., Sumerlin, B. S., O'Reilly, R. K. & Epps, I. I. I. T. H. Stimuli responsive materials. *Chemical Society Reviews* **42**, 7055-7056, doi:10.1039/C3CS90057F (2013).

53 Muskovich, M. & Bettinger, C. J. Biomaterials-Based Electronics: Polymers and Interfaces for Biology and Medicine. *Advanced Healthcare Materials* **1**, 248-266, doi:10.1002/adhm.201200071 (2012).

54 Blum, A. P., Kammeyer, J. K., Rush, A. M., Callmann, C. E., Hahn, M. E. & Gianneschi, N. C. Stimuli-Responsive Nanomaterials for Biomedical Applications. *Journal of the American Chemical Society* **137**, 2140-2154, doi:10.1021/ja510147n (2015).

55 Poole-Warren, L. A. & Patton, A. J. in *Biosynthetic Polymers for Medical Applications* (eds L. Poole-Warren, P. Martens, & R. Green) 3-31 (Woodhead Publishing, 2016).

56 Vasi, A.-M., Popa, M. I., Butnaru, M., Dodi, G. & Verestiuc, L. Chemical functionalization of hyaluronic acid for drug delivery applications. *Materials Science and Engineering: C* **38**, 177-185, doi:http://dx.doi.org/10.1016/j.msec.2014.01.052 (2014).

57 Ngo, J. T., Schuman, E. M. & Tirrell, D. A. Mutant methionyl-tRNA synthetase from bacteria enables site-selective N-terminal labeling of proteins expressed in mammalian cells. *Proceedings of the National Academy of Sciences* **110**, 4992-4997, doi:10.1073/pnas.1216375110 (2013).

58 Liu, K., Zheng, L., Liu, Q., de Vries, J. W., Gerasimov, J. Y. & Herrmann, A. Nucleic Acid Chemistry in the Organic Phase: From Functionalized Oligonucleotides to DNA Side Chain Polymers. *Journal of the American Chemical Society* **136**, 14255-14262, doi:10.1021/ja5080486 (2014).

59 Rowland, M. J., Atgie, M., Hoogland, D. & Scherman, O. A. Preparation and Supramolecular Recognition of Multivalent Peptide–Polysaccharide Conjugates by Cucurbit[8]uril in Hydrogel Formation. *Biomacromolecules* **16**, 2436-2443, doi:10.1021/acs.biomac.5b00680 (2015).

60 Bapat, A. P., Roy, D., Ray, J. G., Savin, D. A. & Sumerlin, B. S. Dynamic-Covalent Macromolecular Stars with Boronic Ester Linkages. *Journal of the American Chemical Society* **133**, 19832-19838, doi:10.1021/ja207005z (2011).

61 Cobo, I., Li, M., Sumerlin, B. S. & Perrier, S. Smart hybrid materials by conjugation of responsive polymers to biomacromolecules. *Nat Mater* **14**, 143-159, doi:10.1038/nmat4106 (2015).

62 Espeel, P. & Du Prez, F. E. “Click”-Inspired Chemistry in Macromolecular Science: Matching Recent Progress and User Expectations. *Macromolecules* **48**, 2-14, doi:10.1021/ma501386v (2015).

63 Patterson, D. M., Nazarova, L. A. & Prescher, J. A. Finding the Right (Bioorthogonal) Chemistry. *ACS Chemical Biology* **9**, 592-605, doi:10.1021/cb400828a (2014).

64 Alconcel, S. N. S., Kim, S. H., Tao, L. & Maynard, H. D. Synthesis of Biotinylated Aldehyde Polymers for Biomolecule Conjugation. *Macromolecular Rapid Communications* **34**, 983-989, doi:10.1002/marc.201300205 (2013).

65 Mukherjee, S., Hill, M. R. & Sumerlin, B. S. Self-healing hydrogels containing reversible oxime crosslinks. *Soft Matter* **11**, 6152-6161, doi:10.1039/C5SM00865D (2015).

66 Liu, S. & Edgar, K. J. Staudinger Reactions for Selective Functionalization of Polysaccharides: A Review. *Biomacromolecules* **16**, 2556-2571, doi:10.1021/acs.biomac.5b00855 (2015).

67 Sletten, E. M. & Bertozzi, C. R. From Mechanism to Mouse: A Tale of Two Bioorthogonal Reactions. *Accounts of Chemical Research* **44**, 666-676, doi:10.1021/ar200148z (2011).

68 Stamenović, M. M., Espeel, P., Camp, W. V. & Du Prez, F. E. Norbornenyl-Based RAFT Agents for the Preparation of Functional Polymers via Thiol–Ene Chemistry. *Macromolecules* **44**, 5619-5630, doi:10.1021/ma200799b (2011).

69 Canalle, L. A., van der Knaap, M., Overhand, M. & van Hest, J. C. M. A Comparison of Triazole-forming Bioconjugation Techniques for Constructing Comb-Shaped Peptide–Polymer Bioconjugates. *Macromolecular Rapid Communications* **32**, 203-208, doi:10.1002/marc.201000507 (2011).

70 van Oers, M. C. M., Rutjes, F. P. J. T. & van Hest, J. C. M. Tubular Polymersomes: A Cross-Linker-Induced Shape Transformation. *Journal of the American Chemical Society* **135**, 16308-16311, doi:10.1021/ja408754z (2013).

71 Kharkar, P. M., Kloxin, A. M. & Kiick, K. L. Dually degradable click hydrogels for controlled degradation and protein release. *Journal of Materials Chemistry B* **2**, 5511-5521, doi:10.1039/C4TB00496E (2014).

72 Shih, H.-W. & Prescher, J. A. A Bioorthogonal Ligation of Cyclopropenones Mediated by Triarylphosphines. *Journal of the American Chemical Society* **137**, 10036-10039, doi:10.1021/jacs.5b06969 (2015).

73 Reece, J. B., Urry, L. A., Cain, M. L., Wasserman, S. A., Minorsky, P. V., Jackson, R. & Campbell, N. A. *Campbell biology*. (2014).

74 García-Borrón, J. C. & Olivares Sánchez, M. C. in *Melanins and Melanosomes* 87-116 (Wiley-VCH Verlag GmbH & Co. KGaA, 2011).

75 Noel, A., Borguet, Y. P., Raymond, J. E. & Wooley, K. L. Poly(ferulic acid-co-tyrosine): Effect of the Regiochemistry on the Photophysical and Physical Properties en Route to Biomedical Applications. *Macromolecules* **47**, 7109-7117, doi:10.1021/ma5015534 (2014).

76 Lutz, J.-F., Sumerlin, B. & Matyjaszewski, K. Some More Insights on Precisely Controlled Polymer Architectures. *Macromolecular Rapid Communications* **35**, 377-377, doi:10.1002/marc.201400072 (2014).

77 Szwarc, M. `Living' Polymers. *Nature* **178**, 1168-1169 (1956).

78 Samanta, S. R., Anastasaki, A., Waldron, C., Haddleton, D. M. & Percec, V. SET-LRP of hydrophobic and hydrophilic acrylates in tetrafluoropropanol. *Polymer Chemistry* **4**, 5555-5562, doi:10.1039/C3PY00901G (2013).

79 Zhang, Q., Collins, J., Anastasaki, A., Wallis, R., Mitchell, D. A., Becer, C. R. & Haddleton, D. M. Sequence-Controlled Multi-Block Glycopolymers to Inhibit DC-SIGN-gp120 Binding. *Angewandte Chemie International Edition* **52**, 4435-4439, doi:10.1002/anie.201300068 (2013).

80 Konkolewicz, D., Krys, P., Góis, J. R., Mendonça, P. V., Zhong, M., Wang, Y., Gennaro, A., Isse, A. A., Fantin, M. & Matyjaszewski, K. Aqueous RDRP in the Presence of Cu0: The Exceptional Activity of CuI Confirms the SARA ATRP Mechanism. *Macromolecules* **47**, 560-570, doi:10.1021/ma4022983 (2014).

81 Costa, J. R. C., Mendonça, P. V., Maximiano, P., Serra, A. C., Guliashvili, T. & Coelho, J. F. J. Ambient Temperature “Flash” SARA ATRP of Methyl Acrylate in Water/Ionic Liquid/Glycol Mixtures. *Macromolecules* **48**, 6810-6815, doi:10.1021/acs.macromol.5b01795 (2015).

82 Mendonça, P. V., Averick, S. E., Konkolewicz, D., Serra, A. C., Popov, A. V., Guliashvili, T., Matyjaszewski, K. & Coelho, J. F. J. Straightforward ARGET ATRP for the Synthesis of Primary Amine Polymethacrylate with Improved Chain-End Functionality under Mild Reaction Conditions. *Macromolecules* **47**, 4615-4621, doi:10.1021/ma501007j (2014).

83 Mackenzie, M. C., Shrivats, A. R., Konkolewicz, D., Averick, S. E., McDermott, M. C., Hollinger, J. O. & Matyjaszewski, K. Synthesis of Poly(meth)acrylates with Thioether and Tertiary Sulfonium Groups by ARGET ATRP and Their Use as siRNA Delivery Agents. *Biomacromolecules* **16**, 236-245, doi:10.1021/bm501449a (2015).

84 Simakova, A., Averick, S. E., Konkolewicz, D. & Matyjaszewski, K. Aqueous ARGET ATRP. *Macromolecules* **45**, 6371-6379, doi:10.1021/ma301303b (2012).

85 Magenau, A. J. D., Bortolamei, N., Frick, E., Park, S., Gennaro, A. & Matyjaszewski, K. Investigation of Electrochemically Mediated Atom Transfer Radical Polymerization. *Macromolecules* **46**, 4346-4353, doi:10.1021/ma400869e (2013).

86 Shida, N., Koizumi, Y., Nishiyama, H., Tomita, I. & Inagi, S. Electrochemically Mediated Atom Transfer Radical Polymerization from a Substrate Surface Manipulated by Bipolar Electrolysis: Fabrication of Gradient and Patterned Polymer Brushes. *Angewandte Chemie International Edition* **54**, 3922-3926, doi:10.1002/anie.201412391 (2015).

87 Ribelli, T. G., Konkolewicz, D., Bernhard, S. & Matyjaszewski, K. How are Radicals (Re)Generated in Photochemical ATRP? *Journal of the American Chemical Society* **136**, 13303-13312, doi:10.1021/ja506379s (2014).

88 Ribelli, T. G., Konkolewicz, D., Pan, X. & Matyjaszewski, K. Contribution of Photochemistry to Activator Regeneration in ATRP. *Macromolecules* **47**, 6316-6321, doi:10.1021/ma501384q (2014).

89 Liu, X., Zhang, L., Cheng, Z. & Zhu, X. Metal-free photoinduced electron transfer-atom transfer radical polymerization (PET-ATRP) via a visible light organic photocatalyst. *Polymer Chemistry*, doi:10.1039/C5PY01765C (2016).

90 Xu, J., Shanmugam, S. & Boyer, C. Organic Electron Donor–Acceptor Photoredox Catalysts: Enhanced Catalytic Efficiency toward Controlled Radical Polymerization. *ACS Macro Letters* **4**, 926-932, doi:10.1021/acsmacrolett.5b00460 (2015).

91 Shanmugam, S. & Boyer, C. Stereo-, Temporal and Chemical Control through Photoactivation of Living Radical Polymerization: Synthesis of Block and Gradient Copolymers. *Journal of the American Chemical Society* **137**, 9988-9999, doi:10.1021/jacs.5b05903 (2015).

92 Otsu, T. Iniferter concept and living radical polymerization. *Journal of Polymer Science Part A: Polymer Chemistry* **38**, 2121-2136, doi:10.1002/(SICI)1099-0518(20000615)38:12<2121::AID-POLA10>3.0.CO;2-X (2000).

93 Tesch, M., Hepperle, J. A. M., Klaasen, H., Letzel, M. & Studer, A. Alternating Copolymerization by Nitroxide-Mediated Polymerization and Subsequent Orthogonal Functionalization. *Angewandte Chemie International Edition* **54**, 5054-5059, doi:10.1002/anie.201412206 (2015).

94 Guégain, E., Guillaneuf, Y. & Nicolas, J. Nitroxide-Mediated Polymerization of Methacrylic Esters: Insights and Solutions to a Long-Standing Problem. *Macromolecular Rapid Communications* **36**, 1227-1247, doi:10.1002/marc.201500042 (2015).

95 Garcia-Valdez, O., Champagne-Hartley, R., Saldivar-Guerra, E., Champagne, P. & Cunningham, M. F. Modification of chitosan with polystyrene and poly(n-butyl acrylate) via nitroxide-mediated polymerization and grafting from approach in homogeneous media. *Polymer Chemistry* **6**, 2827-2836, doi:10.1039/C5PY00028A (2015).

96 Delplace, V., Harrisson, S., Ho, H. T., Tardy, A., Guillaneuf, Y., Pascual, S., Fontaine, L. & Nicolas, J. One-Step Synthesis of Azlactone-Functionalized SG1-Based Alkoxyamine for Nitroxide-Mediated Polymerization and Bioconjugation. *Macromolecules* **48**, 2087-2097, doi:10.1021/acs.macromol.5b00178 (2015).

97 Kamber, N. E., Jeong, W., Waymouth, R. M., Pratt, R. C., Lohmeijer, B. G. G. & Hedrick, J. L. Organocatalytic Ring-Opening Polymerization. *Chem. Rev.* **107**, 5813-5840, doi:10.1021/cr068415b (2007).

98 Ito, S., Ishizone, T. & Hirao, A. Precise Synthesis of New Exactly Defined Graft Copolymers Made up of Poly(alkyl methacrylate)s by Iterative Methodology Using Living Anionic Polymerization. *Macromolecules*, doi:10.1021/acs.macromol.5b01908 (2015).

99 McGrath, A. J., Shi, W., Rodriguez, C. G., Kramer, E. J., Hawker, C. J. & Lynd, N. A. Synthetic strategy for preparing chiral double-semicrystalline polyether block copolymers. *Polymer Chemistry* **6**, 1465-1473, doi:10.1039/C4PY01503G (2015).

100 Hirao, A., Goseki, R. & Ishizone, T. Advances in Living Anionic Polymerization: From Functional Monomers, Polymerization Systems, to Macromolecular Architectures. *Macromolecules* **47**, 1883-1905, doi:10.1021/ma401175m (2014).

101 Crawford, K. E. & Sita, L. R. Stereoengineering of Poly(1,3-methylenecyclohexane) via Two-State Living Coordination Polymerization of 1,6-Heptadiene. *Journal of the American Chemical Society* **135**, 8778-8781, doi:10.1021/ja402262x (2013).

102 Castano, M., Zheng, J., Puskas, J. E. & Becker, M. L. Enzyme-catalyzed ring-opening polymerization of e-caprolactone using alkyne functionalized initiators. *Polymer Chemistry* **5**, 1891-1896, doi:10.1039/C3PY01536J (2014).

103 Kundu, S., Bhangale, A. S., Wallace, W. E., Flynn, K. M., Guttman, C. M., Gross, R. A. & Beers, K. L. Continuous Flow Enzyme-Catalyzed Polymerization in a Microreactor. *J. Am. Chem. Soc.* **133**, 6006-6011, doi:10.1021/ja111346c (2011).

104 Cao, J., Hu, P., Lu, L., Chan, B. A., Luo, B.-H. & Zhang, D. Non-ionic water-soluble "clickable" α-helical polypeptides: synthesis, characterization and side chain modification. *Polymer Chemistry* **6**, 1226-1229, doi:10.1039/C4PY01560F (2015).

105 Deming, T. J. Synthesis of Side-Chain Modified Polypeptides. *Chem. Rev.* **116**, 786-808, doi:10.1021/acs.chemrev.5b00292 (2016).

106 Chatterjee, A. K., Toste, F. D., Choi, T.-L. & Grubbs, R. H. Ruthenium-Catalyzed Olefin Cross Metathesis of Styrenes as an Alternative to the Heck and Cross-Coupling Reactions. *Advanced Synthesis & Catalysis* **344**, 634-637, doi:10.1002/1615-4169(200208)344:6/7<634::AID-ADSC634>3.0.CO;2-K (2002).

107 Romulus, J., Tan, L., Weck, M. & Sampson, N. S. Alternating ROMP copolymers containing charge-transfer units. *ACS macro letters* **2**, 749-752, doi:10.1021/mz4002673 (2013).

108 Elling, B. R. & Xia, Y. Living Alternating Ring-Opening Metathesis Polymerization Based on Single Monomer Additions. *Journal of the American Chemical Society* **137**, 9922-9926, doi:10.1021/jacs.5b05497 (2015).

109 Tan, L., Li, G., Parker, K. A. & Sampson, N. S. Ru-Catalyzed Isomerization Provides Access to Alternating Copolymers via Ring-Opening Metathesis Polymerization. *Macromolecules* **48**, 4793-4800, doi:10.1021/acs.macromol.5b01058 (2015).

110 Ogawa, K. A., Goetz, A. E. & Boydston, A. J. Metal-Free Ring-Opening Metathesis Polymerization. *Journal of the American Chemical Society* **137**, 1400-1403, doi:10.1021/ja512073m (2015).

111 Merrifield, R. B. Solid Phase Peptide Synthesis. I. The Synthesis of a Tetrapeptide. *Journal of the American Chemical Society* **85**, 2149-2154, doi:10.1021/ja00897a025 (1963).

112 Ouahabi, A. A., Kotera, M., Charles, L. & Lutz, J.-F. Synthesis of Monodisperse Sequence-Coded Polymers with Chain Lengths above DP100. *ACS Macro Letters* **4**, 1077-1080, doi:10.1021/acsmacrolett.5b00606 (2015).

113 Roy, R. K. & Lutz, J.-F. Compartmentalization of Single Polymer Chains by Stepwise Intramolecular Cross-Linking of Sequence-Controlled Macromolecules. *J. Am. Chem. Soc.* **136**, 12888-12891, doi:10.1021/ja507889x (2014).

114 Gutekunst, W. R. & Hawker, C. J. A General Approach to Sequence-Controlled Polymers Using Macrocyclic Ring Opening Metathesis Polymerization. *Journal of the American Chemical Society* **137**, 8038-8041, doi:10.1021/jacs.5b04940 (2015).

115 Thomas, R. M. & Grubbs, R. H. Synthesis of Telechelic Polyisoprene via Ring-Opening Metathesis Polymerization in the Presence of Chain Transfer Agent. *Macromolecules* **43**, 3705-3709, doi:10.1021/ma902749q (2010).

116 Zhang, J., Matta, M. E. & Hillmyer, M. A. Synthesis of Sequence-Specific Vinyl Copolymers by Regioselective ROMP of Multiply Substituted Cyclooctenes. *ACS Macro Letters* **1**, 1383-1387, doi:10.1021/mz300535r (2012).

117 Fishman, J. M. & Kiessling, L. L. Synthesis of Functionalizable and Degradable Polymers by ROMP. *Angewandte Chemie (International ed. in English)* **52**, 10.1002/anie.201300293, doi:10.1002/anie.201300293 (2013).

118 Magennis, E. P., Fernandez-Trillo, F., Sui, C., Spain, S. G., Bradshaw, D. J., Churchley, D., Mantovani, G., Winzer, K. & Alexander, C. Bacteria-instructed synthesis of polymers for self-selective microbial binding and labelling. *Nat Mater* **13**, 748-755, doi:10.1038/nmat3949

http://www.nature.com/nmat/journal/v13/n7/abs/nmat3949.html#supplementary-information (2014).

119 Cameron, D. J. A. & Shaver, M. P. Control of thermal properties and hydrolytic degradation in poly(lactic acid) polymer stars through control of isospecificity of polymer arms. *Journal of Polymer Science Part A: Polymer Chemistry* **50**, 1477-1484, doi:10.1002/pola.25927 (2012).

120 Biswas, C., Mitra, K., Singh, S., Ramesh, K., Misra, N., Maiti, B., Panda, A., Maiti, P., Kamigaito, M., Okamoto, Y. & Ray, B. Study of the effect of isotacticity on some physical properties of poly(N-isopropylacrylamide). *Colloid Polym Sci* **293**, 1749-1757, doi:10.1007/s00396-015-3562-3 (2015).

121 Barnes, J. C., Ehrlich, D. J. C., Gao, A. X., Leibfarth, F. A., Jiang, Y., Zhou, E., Jamison, T. F. & Johnson, J. A. Iterative exponential growth of stereo- and sequence-controlled polymers. *Nat Chem* **7**, 810-815, doi:10.1038/nchem.2346

http://www.nature.com/nchem/journal/v7/n10/abs/nchem.2346.html#supplementary-information (2015).

122 Leibfarth, F. A., Johnson, J. A. & Jamison, T. F. Scalable synthesis of sequence-defined, unimolecular macromolecules by Flow-IEG. *Proceedings of the National Academy of Sciences* **112**, 10617-10622, doi:10.1073/pnas.1508599112 (2015).

123 Veccharelli, K. M., Tong, V. K., Young, J. L., Yang, J. & Gianneschi, N. C. Dual responsive polymeric nanoparticles prepared by direct functionalization of polylactic acid-based polymers via graft-from ring opening metathesis polymerization. *Chemical Communications* **52**, 567-570, doi:10.1039/C5CC07882B (2016).

124 Chien, M.-P., Thompson, M. P., Barback, C. V., Ku, T.-H., Hall, D. J. & Gianneschi, N. C. Enzyme-Directed Assembly of a Nanoparticle Probe in Tumor Tissue. *Adv. Mater.* **25**, 3599-3604, doi:10.1002/adma.201300823 (2013).

125 Blum, A. P., Kammeyer, J. K., Yin, J., Crystal, D. T., Rush, A. M., Gilson, M. K. & Gianneschi, N. C. Peptides Displayed as High Density Brush Polymers Resist Proteolysis and Retain Bioactivity. *J. Am. Chem. Soc.* **136**, 15422-15437, doi:10.1021/ja5088216 (2014).

126 Kammeyer, J. K., Blum, A. P., Adamiak, L., Hahn, M. E. & Gianneschi, N. C. Polymerization of Protecting-Group-Free Peptides via ROMP. *Polymer chemistry* **41**, 3929-3933, doi:10.1039/C3PY00526G (2013).

127 Chien, M.-P., Carlini, A. S., Hu, D., Barback, C. V., Rush, A. M., Hall, D. J., Orr, G. & Gianneschi, N. C. Enzyme-Directed Assembly of Nanoparticles in Tumors Monitored by in Vivo Whole Animal Imaging and ex Vivo Super-Resolution Fluorescence Imaging. *Journal of the American Chemical Society* **135**, 18710-18713, doi:10.1021/ja408182p (2013).

128 Rhodes, A. J. & Deming, T. J. Tandem Catalysis for the Preparation of Cylindrical Polypeptide Brushes. *Journal of the American Chemical Society* **134**, 19463-19467, doi:10.1021/ja308620h (2012).

129 Lin, E.-W. & Maynard, H. D. Grafting from Small Interfering Ribonucleic Acid (siRNA) as an Alternative Synthesis Route to siRNA–Polymer Conjugates. *Macromolecules* **48**, 5640-5647, doi:10.1021/acs.macromol.5b00846 (2015).

130 Tucker, B. S., Stewart, J. D., Aguirre, J. I., Holliday, L. S., Figg, C. A., Messer, J. G. & Sumerlin, B. S. Role of Polymer Architecture on the Activity of Polymer–Protein Conjugates for the Treatment of Accelerated Bone Loss Disorders. *Biomacromolecules* **16**, 2374-2381, doi:10.1021/acs.biomac.5b00623 (2015).

131 Sgolastra, F., Minter, L. M., Osborne, B. A. & Tew, G. N. Importance of Sequence Specific Hydrophobicity in Synthetic Protein Transduction Domain Mimics. *Biomacromolecules* **15**, 812-820, doi:10.1021/bm401634r (2014).

132 deRonde, B. M., Torres, J. A., Minter, L. M. & Tew, G. N. Development of Guanidinium-Rich Protein Mimics for Efficient siRNA Delivery into Human T Cells. *Biomacromolecules* **16**, 3172-3179, doi:10.1021/acs.biomac.5b00795 (2015).

133 Wright, D. B., Patterson, J. P., Pitto-Barry, A., Lu, A., Kirby, N., Gianneschi, N. C., Chassenieux, C., Colombani, O. & O'Reilly, R. K. The Copolymer Blending Method: A New Approach for Targeted Assembly of Micellar Nanoparticles. *Macromolecules* **48**, 6516-6522, doi:10.1021/acs.macromol.5b01426 (2015).

134 Ren, J. M., Satoh, K., Goh, T. K., Blencowe, A., Nagai, K., Ishitake, K., Christofferson, A. J., Yiapanis, G., Yarovsky, I., Kamigaito, M. & Qiao, G. G. Stereospecific Cyclic Poly(methyl methacrylate) and Its Topology-Guided Hierarchically Controlled Supramolecular Assemblies. *Angewandte Chemie International Edition* **53**, 459-464, doi:10.1002/anie.201308366 (2014).

135 Mai, Y. & Eisenberg, A. Selective Localization of Preformed Nanoparticles in Morphologically Controllable Block Copolymer Aggregates in Solution. *Accounts of Chemical Research* **45**, 1657-1666, doi:10.1021/ar2003144 (2012).

136 De Koker, S., De Cock, L. J., Rivera-Gil, P., Parak, W. J., Auzély Velty, R., Vervaet, C., Remon, J. P., Grooten, J. & De Geest, B. G. Polymeric multilayer capsules delivering biotherapeutics. *Advanced Drug Delivery Reviews* **63**, 748-761, doi:http://dx.doi.org/10.1016/j.addr.2011.03.014 (2011).

137 Buwalda, S. J., Boere, K. W. M., Dijkstra, P. J., Feijen, J., Vermonden, T. & Hennink, W. E. Hydrogels in a historical perspective: From simple networks to smart materials. *Journal of Controlled Release* **190**, 254-273, doi:http://dx.doi.org/10.1016/j.jconrel.2014.03.052 (2014).

138 Kramer, J. R. & Deming, T. J. Multimodal Switching of Conformation and Solubility in Homocysteine Derived Polypeptides. *Journal of the American Chemical Society* **136**, 5547-5550, doi:10.1021/ja500372u (2014).

139 Singh, R., Norret, M., House, M. J., Galabura, Y., Bradshaw, M., Ho, D., Woodward, R. C., Pierre, T. G. S., Luzinov, I., Smith, N. M., Lim, L. Y. & Iyer, K. S. Dose-Dependent Therapeutic Distinction between Active and Passive Targeting Revealed Using Transferrin-Coated PGMA Nanoparticles. *Small* **12**, 351-359, doi:10.1002/smll.201502730 (2016).

140 Daniel, K. B., Callmann, C. E., Gianneschi, N. C. & Cohen, S. M. Dual-responsive nanoparticles release cargo upon exposure to matrix metalloproteinase and reactive oxygen species. *Chem. Commun.* **52**, 2126-2128, doi:10.1039/C5CC09164K (2016).

141 Proetto, M. T., Anderton, C. R., Hu, D., Szymanski, C. J., Zhu, Z., Patterson, J. P., Kammeyer, J. K., Nilewski, L. G., Rush, A. M., Bell, N. C., Evans, J. E., Orr, G., Howell, S. B. & Gianneschi, N. C. Cellular Delivery of Nanoparticles Revealed with Combined Optical and Isotopic Nanoscopy. *ACS Nano* **10**, 4046-4054, doi:10.1021/acsnano.5b06477 (2016).

142 Wang, Y., Lin, T., Zhang, W., Jiang, Y., Jin, H., He, H., Yang, V. C., Chen, Y. & Huang, Y. A Prodrug-type, MMP-2-targeting Nanoprobe for Tumor Detection and Imaging. *Theranostics* **5**, 787-795, doi:10.7150/thno.11139 (2015).

143 Dvir, T., Bauer, M., Schroeder, A., Tsui, J. H., Anderson, D. G., Langer, R., Liao, R. & Kohane, D. S. Nanoparticles Targeting the Infarcted Heart. *Nano Letters* **11**, 4411-4414, doi:10.1021/nl2025882 (2011).

144 MacEwan, S. R. & Chilkoti, A. Controlled Apoptosis by a Thermally Toggled Nanoscale Amplifier of Cellular Uptake. *Nano Letters* **14**, 2058-2064, doi:10.1021/nl5002313 (2014).

145 Ray, J. G., Naik, S. S., Hoff, E. A., Johnson, A. J., Ly, J. T., Easterling, C. P., Patton, D. L. & Savin, D. A. Stimuli-Responsive Peptide-Based ABA-Triblock Copolymers: Unique Morphology Transitions With pH. *Macromol. Rapid Commun.* **33**, 819-826, doi:10.1002/marc.201100881 (2012).

146 Itel, F., Najer, A., Palivan, C. G. & Meier, W. Dynamics of Membrane Proteins within Synthetic Polymer Membranes with Large Hydrophobic Mismatch. *Nano Lett.* **15**, 3871-3878, doi:10.1021/acs.nanolett.5b00699 (2015).

147 Peppas, N. A., Hilt, J. Z., Khademhosseini, A. & Langer, R. Hydrogels in Biology and Medicine: From Molecular Principles to Bionanotechnology. *Advanced Materials* **18**, 1345-1360, doi:10.1002/adma.200501612 (2006).

148 Hunt, J. A., Chen, R., van Veen, T. & Bryan, N. Hydrogels for tissue engineering and regenerative medicine. *Journal of Materials Chemistry B* **2**, 5319-5338, doi:10.1039/C4TB00775A (2014).

149 Ahmed, E. M. Hydrogel: Preparation, characterization, and applications: A review. *Journal of Advanced Research* **6**, 105-121, doi:https://doi.org/10.1016/j.jare.2013.07.006 (2015).

150 Phadke, A., Zhang, C., Arman, B., Hsu, C.-C., Mashelkar, R. A., Lele, A. K., Tauber, M. J., Arya, G. & Varghese, S. Rapid self-healing hydrogels. *Proceedings of the National Academy of Sciences* **109**, 4383-4388, doi:10.1073/pnas.1201122109 (2012).

151 Wang, Q., Mynar, J. L., Yoshida, M., Lee, E., Lee, M., Okuro, K., Kinbara, K. & Aida, T. High-water-content mouldable hydrogels by mixing clay and a dendritic molecular binder. *Nature* **463**, 339-343, doi:http://www.nature.com/nature/journal/v463/n7279/suppinfo/nature08693_S1.html (2010).

152 Jin, Q., Schexnailder, P., Gaharwar, A. K. & Schmidt, G. Silicate Cross-Linked Bio-Nanocomposite Hydrogels from PEO and Chitosan. *Macromolecular Bioscience* **9**, 1028-1035, doi:10.1002/mabi.200900080 (2009).

153 Rose, S., Prevoteau, A., Elziere, P., Hourdet, D., Marcellan, A. & Leibler, L. Nanoparticle solutions as adhesives for gels and biological tissues. *Nature* **505**, 382-385, doi:10.1038/nature12806

http://www.nature.com/nature/journal/v505/n7483/abs/nature12806.html#supplementary-information (2014).

154 Appel, E. A., Tibbitt, M. W., Webber, M. J., Mattix, B. A., Veiseh, O. & Langer, R. Self-assembled hydrogels utilizing polymer–nanoparticle interactions. *Nat Commun* **6**, doi:10.1038/ncomms7295 (2015).

155 Gaharwar, A. K., Avery, R. K., Assmann, A., Paul, A., McKinley, G. H., Khademhosseini, A. & Olsen, B. D. Shear-Thinning Nanocomposite Hydrogels for the Treatment of Hemorrhage. *ACS Nano* **8**, 9833-9842, doi:10.1021/nn503719n (2014).

156 Li, J., Harada, A. & Kamachi, M. Sol-Gel Transition During Inclusion Complex-Formation Between Alpha-Cyclodextrin and High-Molecular Weight Poly(ethylene glycol)s in Aqueous Solution. *Polym. J.* **26**, 1019-1026, doi:10.1295/polymj.26.1019 (1994).

157 Li, G., Wu, J., Wang, B., Yan, S., Zhang, K., Ding, J. & Yin, J. Self-Healing Supramolecular Self-Assembled Hydrogels Based on Poly(l-glutamic acid). *Biomacromolecules* **16**, 3508-3518, doi:10.1021/acs.biomac.5b01287 (2015).

158 Himmelein, S., Lewe, V., Stuart, M. C. A. & Ravoo, B. J. A carbohydrate-based hydrogel containing vesicles as responsive non-covalent cross-linkers. *Chemical Science* **5**, 1054-1058, doi:10.1039/C3SC52964A (2014).

159 McKee, J. R., Appel, E. A., Seitsonen, J., Kontturi, E., Scherman, O. A. & Ikkala, O. Healable, Stable and Stiff Hydrogels: Combining Conflicting Properties Using Dynamic and Selective Three-Component Recognition with Reinforcing Cellulose Nanorods. *Advanced Functional Materials* **24**, 2706-2713, doi:10.1002/adfm.201303699 (2014).

160 Zhu, J. & Marchant, R. E. Design properties of hydrogel tissue-engineering scaffolds. *Expert Rev. Med. Devices* **8**, 607-626, doi:10.1586/erd.11.27 (2011).

161 Walsh, G. Biopharmaceutical benchmarks 2010. *Nature Biotechnology* **28**, 917, doi:10.1038/nbt0910-917 (2010).

162 Hall, M. P. Biotransformation and In Vivo Stability of Protein Biotherapeutics: Impact on Candidate Selection and Pharmacokinetic Profiling. *Drug Metabolism and Disposition* **42**, 1873-1880, doi:10.1124/dmd.114.058347 (2014).

163 Klok, H.-A. Peptide/Protein−Synthetic Polymer Conjugates: Quo Vadis. *Macromolecules* **42**, 7990-8000, doi:10.1021/ma901561t (2009).

164 van Eldijk, M. B., Smits, F. C. M., Vermue, N., Debets, M. F., Schoffelen, S. & van Hest, J. C. M. Synthesis and Self-Assembly of Well-Defined Elastin-Like Polypeptide–Poly(ethylene glycol) Conjugates. *Biomacromolecules* **15**, 2751-2759, doi:10.1021/bm5006195 (2014).

165 Lee, J., Ko, J. H., Lin, E.-W., Wallace, P., Ruch, F. & Maynard, H. D. Trehalose hydrogels for stabilization of enzymes to heat. *Polymer Chemistry* **6**, 3443-3448, doi:10.1039/C5PY00121H (2015).

166 Dong, R., Pang, Y., Su, Y. & Zhu, X. Supramolecular hydrogels: synthesis, properties and their biomedical applications. *Biomaterials Science* **3**, 937-954, doi:10.1039/C4BM00448E (2015).

167 Harding, S. E. Some observations on the effects of bioprocessing on biopolymer stability. *Journal of Drug Targeting* **18**, 732-740, doi:10.3109/1061186X.2010.512470 (2010).

168 O'Shea, T. M., Webber, M. J., Aimetti, A. A. & Langer, R. Covalent Incorporation of Trehalose within Hydrogels for Enhanced Long-Term Functional Stability and Controlled Release of Biomacromolecules. *Advanced Healthcare Materials* **4**, 1802-1812, doi:10.1002/adhm.201500334 (2015).

169 Xue, L., Kelkar, S. S., Wang, X., Ma, J., Madsen, L. A. & Reineke, T. M. A theranostic polycation containing trehalose and lanthanide chelate domains for siRNA delivery and monitoring. *RSC Advances* **5**, 74102-74106, doi:10.1039/C5RA14325J (2015).

170 Vermonden, T., Censi, R. & Hennink, W. E. Hydrogels for Protein Delivery. *Chem. Rev. (Washington, DC, U. S.)* **112**, 2853-2888, doi:10.1021/cr200157d (2012).

171 Vaishya, R., Khurana, V., Patel, S. & Mitra, A. K. Long-term delivery of protein therapeutics. *Expert Opin Drug Deliv* **12**, 415-440 (2015).

172 Decher, G., Hong, J. D. & Schmitt, J. Buildup of ultrathin multilayer films by a self-assembly process: III. Consecutively alternating adsorption of anionic and cationic polyelectrolytes on charged surfaces. *Thin Solid Films* **210–211, Part 2**, 831-835, doi:http://dx.doi.org/10.1016/0040-6090(92)90417-A (1992).

173 Almodóvar, J., Bacon, S., Gogolski, J., Kisiday, J. D. & Kipper, M. J. Polysaccharide-Based Polyelectrolyte Multilayer Surface Coatings can Enhance Mesenchymal Stem Cell Response to Adsorbed Growth Factors. *Biomacromolecules* **11**, 2629-2639, doi:10.1021/bm1005799 (2010).

174 Almodóvar, J., Place, L. W., Gogolski, J., Erickson, K. & Kipper, M. J. Layer-by-Layer Assembly of Polysaccharide-Based Polyelectrolyte Multilayers: A Spectroscopic Study of Hydrophilicity, Composition, and Ion Pairing. *Biomacromolecules* **12**, 2755-2765, doi:10.1021/bm200519y (2011).

175 Cado, G., Kerdjoudj, H., Chassepot, A., Lefort, M., Benmlih, K., Hemmerlé, J., Voegel, J. C., Jierry, L., Schaaf, P., Frère, Y. & Boulmedais, F. Polysaccharide Films Built by Simultaneous or Alternate Spray: A Rapid Way to Engineer Biomaterial Surfaces. *Langmuir* **28**, 8470-8478, doi:10.1021/la300563s (2012).

176 Crouzier, T., Szarpak, A., Boudou, T., Auzély-Velty, R. & Picart, C. Polysaccharide-Blend Multilayers Containing Hyaluronan and Heparin as a Delivery System for rhBMP-2. *Small* **6**, 651-662, doi:10.1002/smll.200901728 (2010).

177 Porcel, C. H., Izquierdo, A., Ball, V., Decher, G., Voegel, J. C. & Schaaf, P. Ultrathin Coatings and (Poly(glutamic acid)/Polyallylamine) Films Deposited by Continuous and Simultaneous Spraying. *Langmuir* **21**, 800-802, doi:10.1021/la047570n (2005).

178 Almquist, B. D., Castleberry, S. A., Sun, J. B., Lu, A. Y. & Hammond, P. T. Combination Growth Factor Therapy via Electrostatically Assembled Wound Dressings Improves Diabetic Ulcer Healing In Vivo. *Advanced Healthcare Materials* **4**, 2090-2099, doi:10.1002/adhm.201500403 (2015).

179 Holmes, C. A. & Tabrizian, M. Enhanced MC3T3 preosteoblast viability and adhesion on polyelectrolyte multilayer films composed of glycol-modified chitosan and hyaluronic acid. *Journal of Biomedical Materials Research Part A* **100A**, 518-526, doi:10.1002/jbm.a.33305 (2012).

180 Hsu, B. B., Park, M.-H., Hagerman, S. R. & Hammond, P. T. Multimonth controlled small molecule release from biodegradable thin films. *Proceedings of the National Academy of Sciences* **111**, 12175-12180, doi:10.1073/pnas.1323829111 (2014).

181 Hsu, B. B., Hagerman, S. R., Jamieson, K., Castleberry, S. A., Wang, W., Holler, E., Ljubimova, J. Y. & Hammond, P. T. Multifunctional Self-Assembled Films for Rapid Hemostat and Sustained Anti-infective Delivery. *ACS Biomaterials Science & Engineering* **1**, 148-156, doi:10.1021/ab500050m (2015).

182 Choi, J.-H., Kim, S.-O., Linardy, E., Dreaden, E. C., Zhdanov, V. P., Hammond, P. T. & Cho, N.-J. Adsorption of hyaluronic acid on solid supports: Role of pH and surface chemistry in thin film self-assembly. *Journal of Colloid and Interface Science* **448**, 197-207, doi:http://dx.doi.org/10.1016/j.jcis.2015.01.060 (2015).

183 Monteiro, I. P., Shukla, A., Marques, A. P., Reis, R. L. & Hammond, P. T. Spray-assisted layer-by-layer assembly on hyaluronic acid scaffolds for skin tissue engineering. *Journal of Biomedical Materials Research Part A* **103**, 330-340, doi:10.1002/jbm.a.35178 (2015).

184 Shah, N. J., Hyder, M. N., Quadir, M. A., Dorval Courchesne, N.-M., Seeherman, H. J., Nevins, M., Spector, M. & Hammond, P. T. Adaptive growth factor delivery from a polyelectrolyte coating promotes synergistic bone tissue repair and reconstruction. *Proceedings of the National Academy of Sciences* **111**, 12847-12852, doi:10.1073/pnas.1408035111 (2014).

185 Min, J., Braatz, R. D. & Hammond, P. T. Tunable staged release of therapeutics from layer-by-layer coatings with clay interlayer barrier. *Biomaterials* **35**, 2507-2517, doi:http://dx.doi.org/10.1016/j.biomaterials.2013.12.009 (2014).

186 Hsu, B. B., Hagerman, S. R., Jamieson, K., Veselinovic, J., O'Neill, N., Holler, E., Ljubimova, J. Y. & Hammond, P. T. Multilayer Films Assembled from Naturally-Derived Materials for Controlled Protein Release. *Biomacromolecules* **15**, 2049-2057, doi:10.1021/bm5001839 (2014).

187 Knop, K., Hoogenboom, R., Fischer, D. & Schubert, U. S. Poly(ethylene glycol) in Drug Delivery: Pros and Cons as Well as Potential Alternatives. *Angewandte Chemie International Edition* **49**, 6288-6308, doi:10.1002/anie.200902672 (2010).

188 Shao, Q. & Jiang, S. Molecular Understanding and Design of Zwitterionic Materials. *Adv. Mater.* **27**, 15-26, doi:10.1002/adma.201404059 (2015).

189 Thomas, A., Müller, S. S. & Frey, H. Beyond Poly(ethylene glycol): Linear Polyglycerol as a Multifunctional Polyether for Biomedical and Pharmaceutical Applications. *Biomacromolecules* **15**, 1935-1954, doi:10.1021/bm5002608 (2014).

190 Kamaly, N., Yameen, B., Wu, J. & Farokhzad, O. C. Degradable Controlled-Release Polymers and Polymeric Nanoparticles: Mechanisms of Controlling Drug Release. *Chem. Rev.* **116**, 2602-2663, doi:10.1021/acs.chemrev.5b00346 (2016).

191 Nguyen, T. H., Kim, S.-H., Decker, C. G., Wong, D. Y., Loo, J. A. & Maynard, H. D. A heparin-mimicking polymer conjugate stabilizes basic fibroblast growth factor. *Nat Chem* **5**, 221-227, doi:http://www.nature.com/nchem/journal/v5/n3/abs/nchem.1573.html#supplementary-information (2013).

192 Ding, K., Alemdaroglu, F. E., Börsch, M., Berger, R. & Herrmann, A. Engineering the Structural Properties of DNA Block Copolymer Micelles by Molecular Recognition. *Angewandte Chemie International Edition* **46**, 1172-1175, doi:10.1002/anie.200603064 (2007).

193 Kim, S., Shi, Y., Kim, J. Y., Park, K. & Cheng, J.-X. Overcoming the barriers in micellar drug delivery: loading efficiency, in vivo stability, and micelle–cell interaction. *Expert Opinion on Drug Delivery* **7**, 49-62, doi:10.1517/17425240903380446 (2010).

194 Mirkin, C. A., Letsinger, R. L., Mucic, R. C. & Storhoff, J. J. A DNA-based method for rationally assembling nanoparticles into macroscopic materials. *Nature* **382**, 607-609 (1996).

195 Cutler, J. I., Zhang, K., Zheng, D., Auyeung, E., Prigodich, A. E. & Mirkin, C. A. Polyvalent Nucleic Acid Nanostructures. *Journal of the American Chemical Society* **133**, 9254-9257, doi:10.1021/ja203375n (2011).

196 Rush, A. M., Thompson, M. P., Tatro, E. T. & Gianneschi, N. C. Nuclease-Resistant DNA via High-Density Packing in Polymeric Micellar Nanoparticle Coronas. *ACS Nano* **7**, 1379-1387, doi:10.1021/nn305030g (2013).

197 Rush, A. M., Nelles, D. A., Blum, A. P., Barnhill, S. A., Tatro, E. T., Yeo, G. W. & Gianneschi, N. C. Intracellular mRNA Regulation with Self-Assembled Locked Nucleic Acid Polymer Nanoparticles. *Journal of the American Chemical Society* **136**, 7615-7618, doi:10.1021/ja503598z (2014).

198 Garton, M., Sayadi, M. & Kim, P. M. A computational approach for designing D-proteins with non-canonical amino acid optimised binding affinity. *PLoS One* **12**, e0187524, doi:10.1371/journal.pone.0187524 (2017).

199 Rink, R., Arkema-Meter, A., Baudoin, I., Post, E., Kuipers, A., Nelemans, S. A., Akanbi, M. H. J. & Moll, G. N. To protect peptide pharmaceuticals against peptidases. *J. Pharmacol. Toxicol. Methods* **61**, 210-218, doi:https://doi.org/10.1016/j.vascn.2010.02.010 (2010).

200 Maillère, B., Mourier, G., Hervé, M. & Ménez, A. Fine chemical modifications at N- and C-termini enhance peptide presentation to T cells, by increasing the lifespan of both free and MHC-complexed peptides. *Mol. Immunol.* **32**, 1377-1385, doi:https://doi.org/10.1016/0161-5890(95)00103-4 (1995).

201 Vlieghe, P., Lisowski, V., Martinez, J. & Khrestchatisky, M. Synthetic therapeutic peptides: science and market. *Drug Discovery Today* **15**, 40-56, doi:https://doi.org/10.1016/j.drudis.2009.10.009 (2010).

202 Kahns, A. H. & Bundgaard, H. Prodrugs of Peptides. 13. Stabilization of Peptide Amides Against α-Chymotrypsin by the Prodrug Approach. *Pharm. Res.* **8**, 1533-1538, doi:10.1023/a:1015854718903 (1991).

203 Meng, H. & Kumar, K. Antimicrobial Activity and Protease Stability of Peptides Containing Fluorinated Amino Acids. *J. Am. Chem. Soc.* **129**, 15615-15622, doi:10.1021/ja075373f (2007).

204 Lubelski, J., Rink, R., Khusainov, R., Moll, G. N. & Kuipers, O. P. Biosynthesis, immunity, regulation, mode of action and engineering of the model lantibiotic nisin. *Cell. Mol. Life Sci.* **65**, 455-476, doi:10.1007/s00018-007-7171-2 (2008).

205 Mittal, S., Kaur, S., Swami, A., Maurya, I. K., Jain, R., Wangoo, N. & Sharma, R. K. Alkylated histidine based short cationic antifungal peptides: synthesis, biological evaluation and mechanistic investigations. *RSC Advances* **6**, 41951-41961, doi:10.1039/C6RA05883C (2016).

206 Kuriakose, J., Hernandez-Gordillo, V., Nepal, M., Brezden, A., Pozzi, V., Seleem, M. N. & Chmielewski, J. Targeting Intracellular Pathogenic Bacteria with Unnatural Proline-Rich Peptides: Coupling Antibacterial Activity with Macrophage Penetration. *Angew. Chem. Int. Ed.* **52**, 9664-9667, doi:doi:10.1002/anie.201302693 (2013).

207 Dumas, A., Lercher, L., Spicer, C. D. & Davis, B. G. Designing logical codon reassignment – Expanding the chemistry in biology. *Chemical Science* **6**, 50-69, doi:10.1039/C4SC01534G (2015).

208 Cromm, P. M., Spiegel, J., Küchler, P., Dietrich, L., Kriegesmann, J., Wendt, M., Goody, R. S., Waldmann, H. & Grossmann, T. N. Protease-Resistant and Cell-Permeable Double-Stapled Peptides Targeting the Rab8a GTPase. *ACS Chem. Biol.* **11**, 2375-2382, doi:10.1021/acschembio.6b00386 (2016).

209 Migoń, D., Neubauer, D. & Kamysz, W. Hydrocarbon Stapled Antimicrobial Peptides. *The Protein Journal* **37**, 2-12, doi:10.1007/s10930-018-9755-0 (2018).

210 Huo, L. & van der Donk, W. A. Discovery and Characterization of Bicereucin, an Unusual d-Amino Acid-Containing Mixed Two-Component Lantibiotic. *J. Am. Chem. Soc.* **138**, 5254-5257, doi:10.1021/jacs.6b02513 (2016).

211 Luca, G., Rossella De, M. & Lucia, C. Chemical Modifications Designed to Improve Peptide Stability: Incorporation of Non-Natural Amino Acids, Pseudo-Peptide Bonds, and Cyclization. *Curr. Pharm. Des.* **16**, 3185-3203, doi:http://dx.doi.org/10.2174/138161210793292555 (2010).

212 Swanekamp, R. J., Welch, J. J. & Nilsson, B. L. Proteolytic stability of amphipathic peptide hydrogels composed of self-assembled pleated β-sheet or coassembled rippled β-sheet fibrils. *Chem. Commun.* **50**, 10133-10136, doi:10.1039/C4CC04644G (2014).

213 Thota, C. K., Yadav, N. & Chauhan, V. S. "A novel highly stable and injectable hydrogel based on a conformationally restricted ultrashort peptide". *Sci. Rep.* **6**, 31167, doi:10.1038/srep31167

https://www.nature.com/articles/srep31167#supplementary-information (2016).

214 Gudlur, S., Sukthankar, P., Gao, J., Avila, L. A., Hiromasa, Y., Chen, J., Iwamoto, T. & Tomich, J. M. Peptide Nanovesicles Formed by the Self-Assembly of Branched Amphiphilic Peptides. *PLoS One* **7**, e45374, doi:10.1371/journal.pone.0045374 (2012).

215 Jeong, W.-j. & Lim, Y.-b. Macrocyclic Peptides Self-Assemble into Robust Vesicles with Molecular Recognition Capabilities. *Bioconjug. Chem.* **25**, 1996-2003, doi:10.1021/bc500367z (2014).

216 Martin, A. D., Wojciechowski, J. P., Robinson, A. B., Heu, C., Garvey, C. J., Ratcliffe, J., Waddington, L. J., Gardiner, J. & Thordarson, P. Controlling self-assembly of diphenylalanine peptides at high pH using heterocyclic capping groups. *Sci. Rep.* **7**, 43947, doi:10.1038/srep43947

https://www.nature.com/articles/srep43947#supplementary-information (2017).

217 Jeong, W.-j., Lee, M. S. & Lim, Y.-b. Helix Stabilized, Thermostable, and Protease-Resistant Self-Assembled Peptide Nanostructures as Potential Inhibitors of Protein–Protein Interactions. *Biomacromolecules* **14**, 2684-2689, doi:10.1021/bm400532y (2013).

218 Kalafatovic, D., Nobis, M., Javid, N., Frederix, P. W. J. M., Anderson, K. I., Saunders, B. R. & Ulijn, R. V. MMP-9 triggered micelle-to-fibre transitions for slow release of doxorubicin. *Biomaterials Science* **3**, 246-249, doi:10.1039/C4BM00297K (2015).

219 Gao, J., Tang, C., Elsawy, M. A., Smith, A. M., Miller, A. F. & Saiani, A. Controlling Self-Assembling Peptide Hydrogel Properties through Network Topology. *Biomacromolecules* **18**, 826-834, doi:10.1021/acs.biomac.6b01693 (2017).

220 Hsieh, P. C. H., Davis, M. E., Gannon, J., MacGillivray, C. & Lee, R. T. Controlled delivery of PDGF-BB for myocardial protection using injectable self-assembling peptide nanofibers. *J. Clin. Invest.* **116**, 237-248, doi:10.1172/JCI25878 (2006).

221 Büschl, R., Folda, T. & Ringsdorf, H. Polymeric monolayers and liposomes as models for biomembranes. How to bridge the gap between polymer science and membrane biology? *Die Makromolekulare Chemie* **6**, 245-258, doi:10.1002/macp.1984.020061984119 (1984).

Chapter 2

Responsive NPs for Targeted Accumulation and Prolonged Retention

2.1 Enzyme-Responsive NPs as Imaging Agents for Disease

2.1.1 Advanced Fluorescence Imaging in Tissue with Chronically Upregulated MMPs

Our lab has a vested interest in understanding how our materials behave and assemble within living systems and do so using advanced imaging and correlative microscopy techniques (TEM, super resolution fluorescence, and isotopic labeling).[1,2] In a preliminary study within a HT1080 fibrosarcoma model, enzyme-responsive particles demonstrated prolonged retention (up to 7 days post-injection) *in vivo* when injected intratumorally (**Figure 2.1.1**). These peptide-polymer amphiphiles (structure provided in **Figure 2.1.1a**) thus behaved similarly to those discussed in **Chapter 1.4.1**. In this new study, however, direct measurements were made inside of the animal to confirm high levels of the endogenously expressed stimulus. To verify that particle activation and subsequent aggregate retention within the MMP-overexpressing HT-1080 tumor **tissue**[3-5] occurs in conjunction with observable expression of MMP-9, tumor tissue samples were measured via enzyme-linked immunosorbent assay (ELISA) (**Figure 2.1.1b**). A time-course study of the tumor tissues after

injection shows constitutive expression of MMP-9. All tissue, whether injected with responsive NPs (L-amino acid containing), nonresponsive NPs (D-amino-acid containing), possessed elevated MMP9 concentrations with no statistical difference from that of control tumor tissue (no injection) ($p > 0.05$). Thus our materials were observed in an environemnt expressing the intended stimulus and the particles did not alter their inflammatory expression.

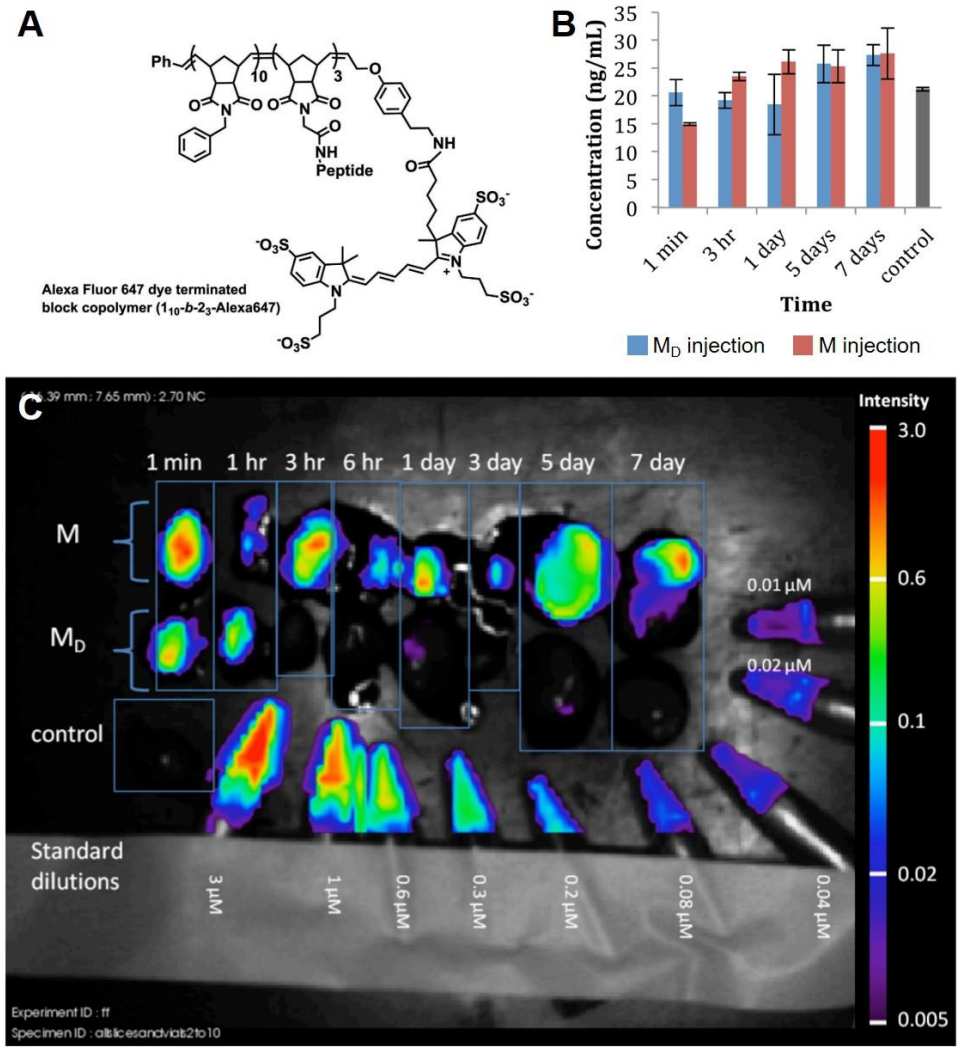


Figure 2.1.1. Enzyme-responsive NPs with a dense peptide-polymer brush in a tumor model. (A-C) Ex-vivo analysis of responsive (M) and nonresponsive (M_D) NPs. (A) Structure of diblock copolymer with dense peptide brush (DP=3), terminally labeled with an NIR dye. (B) MMP-9 ELISA analysis of MMP-9 expression at 1 min (20.6 ± 2.4 ng/mL and 14.9 ± 0.3 ng/mL), 3 hr (19.2 ± 5.4 ng/mL and 23.5 ± 2.2 ng/mL), 1 day (18.5 ± 1.8 ng/mL and 26.1 ± 4.7 ng/mL), 5 days (25.8 ± 4.5 ng/mL and 25.3 ± 4.0 ng/mL), and 7 days (27.4 ± 6.2 ng/mL and 27.6 ± 2.3 ng/mL) post-M and post-M_D NP injection, respectively, and control tumor tissue without injection at day 7 (21.3 ± 3.7 ng/mL). Error bars represent ± standard error. (C) Ex vivo fluorescence intensities of individual tumor slices from M injected (TOP) and M_D NPs injected (MIDDLE) tumor slices from left to right in increasing time course: 1 min, 1 hr, 3 hr, 6 hr, 1 day, 3 day, 5 day, 7 day. Non-injected control tumor slice (BOTTOM) followed by standard M particle concentrations at 50% serial dilutions from left to right: 3 µM, 1 µM, 0.6 µM, 0.3 µM, 0.2 µM, 0.08 µM, 0.04 µM, 0.02 µM, and 0.01 µM. Signal intensities of blanks are included to indicate relative magnitudes being observed between tissue samples. Particle concentrations in tissues are likely present at higher concentrations than indicated by imaged standards due to signal attenuation by quenching within biological tissues. The linear scale bar from 0.005 to 3.0 is given in units of NC x 10^3, where NC is number of counts per second per microwatt. The lower threshold is equal to background intensity from control tissue.

To gain a general feel for cumulative material retention of these polymeric particles in a mouse tumor model, harvested organs were analyzed by *ex vivo* fluorescence. Indeed, the materials are found in the tumor tissue for up to 7 days using responsive NP, or M (**Figure 2.1.1c**). In contrast, nonresponsive NPs, or M_D, clear after 1 hr, demonstratig that recognition of natural peptide substrates are necessary for material retention. Material was not detected in other clearance organs such as the kidnes, spleen, lungs, heart, or liver, which is the ideal scenerio. With this basic construct for structurally dyanmic nanoparticles in mind, we sought to apply a similar system in a myocardial ischemia-reperfusion model, in which the acute expression and activity levels of MMP-2/9 are drastically upregulated, as discussed in **Chapter 1.1**

An important consideration is that these materials were directly injected to the site of interest, so NPs were given the greatest opportunity for recognition by MMPs expressed at the tumor site. However, when moving away from the target tissue, as is the ultimate goal for noninvasive delivery via remotely intravenous (IV) injection, NPs are likely to spend even less time at the target diseased tissue site before perfusing out of the tissue again and reentering the circulatory system. Thus we aimed to develop a system with even faster MMP-responsiveness to offset potential issues with lack of targeted accumulation. To achieve this goal without completely redesigning the structually dynamic peptide-polymer NPs, we reassessed the current polymer architecture (**Figure 2.1.1a**).

The polymers in this study were generated through direct polymerization of a peptide monomer to create a dense peptide brush with a degree of polymerization (DP) of 3, which is known to increase increased proteolytic resistance of the peptide substrate through increased steric hindrance.[6] These observations influenced the design of polymers that were developed for application in a rat myocardial ischemia model in **Section 2.2.2**. Namely, we made efforts to reduce peptide brush density by post-polymerization functionalization with peptide substrates, in order to improve responsiveness.

2.2 Targeted Delivery of IV Injectable Responsive NPs Post-MI

2.2.1 Introduction

Heart failure following a myocardial infarction (MI) continues to be one of the leading causes of death.[7] Immediately after MI, there is an initial inflammatory response with cardiomyocyte death and degradation of the extracellular matrix.[8,9] This results in negative left ventricular (LV) remodeling leading to wall thinning, LV dilation, and depressed cardiac function.[10-12] Several experimental approaches have been examined to inhibit this negative remodeling process; one promising approach is the use of injectable biomaterials,[13] which can be used as stand-alone scaffolds to encourage endogenous repair or for delivering therapeutics such as cells, growth factors, or small molecules.[13,14] Ideally a therapeutic should be delivered in a minimally invasive procedure as acutely as possible to prevent continued cardiomyocyte apoptosis and initiation of negative LV remodeling. Local intramyocardial delivery of biomaterials to the injured myocardium can be performed minimally invasively via catheter when the material is designed appropriately;[14] however, needle-based injection during the acute phase post-MI is unlikely to translate to the clinic given safety concerns with the weakened acute MI wall and unstable patient population.[14,15]

Nanoparticles are attractive for minimally invasive delivery because they may be administered via intravenous (IV) injection and target the heart through the enhanced permeability and retention (EPR) effect that is present in the acute stages of MI due to leaky vasculature.[16] Nanoparticle systems are unique in that they may be prepared with relatively small diameters ranging from 6 – 200 nm, making them ideal for systemic transport. Particles with diameters from 10-100 nm have demonstrated improved circulation times,[17,18] and nanoparticles possessing diameters from 15-350 nm have been injected IV and delivered to the infarct via the leaky post-MI vasculature.[19-21] However, spherical nanoparticles within these size ranges are often cleared from the target tissue within 24 hours.[21-23] Targeted nanoparticle systems are likely to increase retention within the myocardium, but many of these studies lack long-term evaluation beyond a few hours to days.[19,22,24] Both active

targeting to the infarcted myocardium and retention of the material for periods longer than 1 week are current and significant challenges in developing nanoparticle delivery strategies to treat MI.

2.2.2 Results and Discussion

We present a novel approach for targeting the MI as well for achieving prolonged retention of a material in an acute MI via IV injection. The nanoparticles were designed to respond to enzymatic stimuli (matrix metalloproteinases, MMPs) present in the acute MI resulting in a morphological transition from discrete micellular nanoparticles into network-like scaffolds (**Figure**). The fluorescent nanoparticle is composed of brush peptide-polymer amphiphiles (PPAs)[25] based on a polynorbornene backbone with peptide sequences specific for recognition of MMP-2 and MMP-9 (methods and characterization provided in Supplemental Information). IV delivery allows the enzyme-responsive nanoparticles to freely circulate in the bloodstream until reaching the infarct through the leaky post-MI vasculature,[16] where they assemble and remain within the injured site for up to 28 days post-injection.

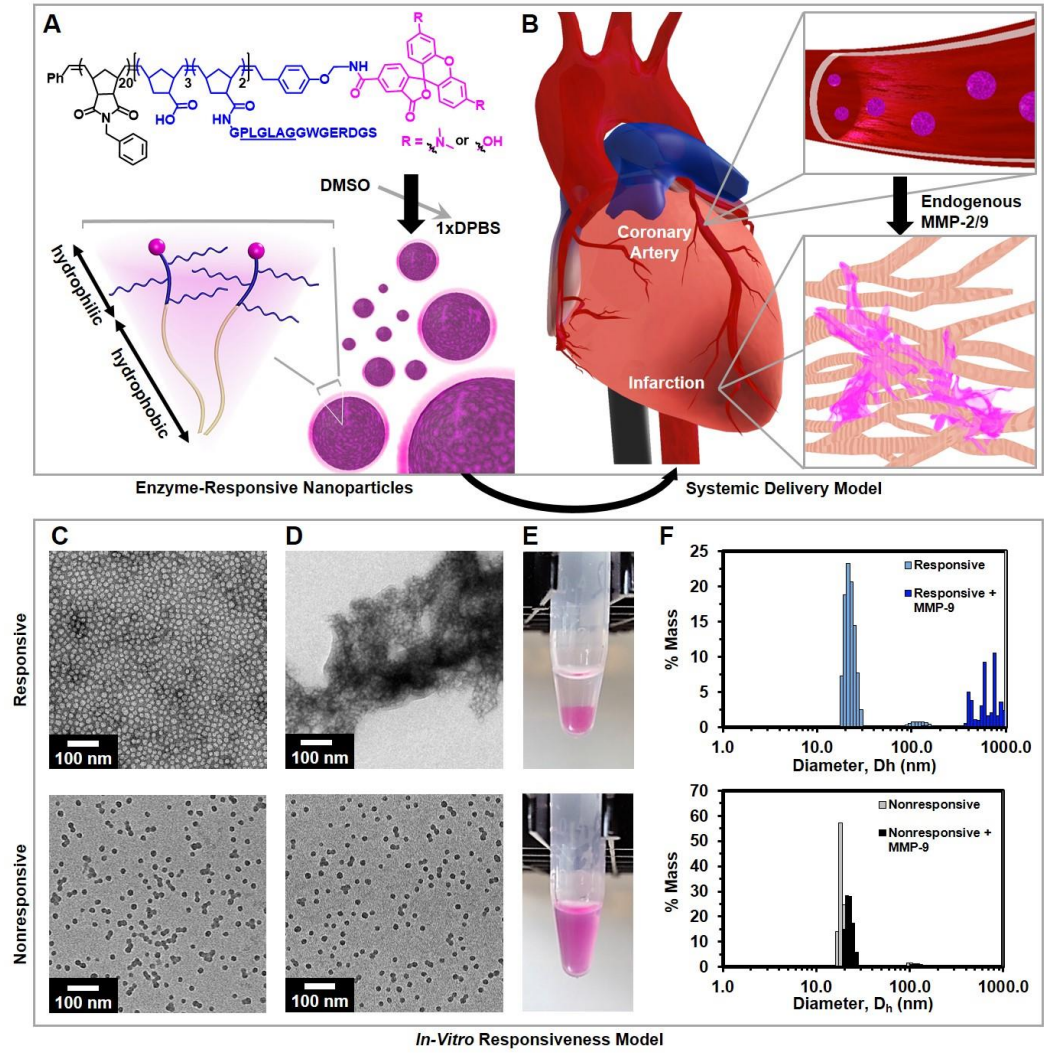


Figure 2.2.1. Responsive nanoparticles target, accumulate, and are retained within an acute myocardial infarction due to enzyme-induced aggregation. (A) Diagram of a dye-labeled brush peptide-polymer amphiphile (PPA) containing an MMP-2 and MMP-9 specific recognition sequence, shown underlined. PPAs self-assemble into nanoparticles through hydrophobic-hydrophilic interactions when dialyzed into aqueous buffer. (B) Schematic of nanoparticles freely circulating in the bloodstream (not to scale) upon systemic delivery. Nanoparticles enter the infarct tissue through the leaky acute MI vasculature, and upregulated MMPs within the infarct induce the formation of an aggregate-like scaffold. (C) *In vitro*, responsive (top) and nonresponsive (bottom) nanoparticles are monodisperse micelles with diameters of 15-20 nm, and (D) upon activation, only responsive nanoparticles form an aggregate-like scaffold. (E) Corresponding images of nanoparticle solutions following activation. (F) Dynamic light scattering of nanoparticles before and after MMP activation.

Previously, similar enzyme-responsive nanoparticles were shown to successfully accumulate after IV delivery in murine tumors that chronically overexpressed MMP-2 and MMP-9.[25] For the MI application, the polymer design was modified to optimize net polymer amphiphilicity. We reduced the degree of polymerization of the hydrophilic block and degree of conjugation of hydrophilic peptide

such that the hydrophilic weight fraction was 0.45 instead of 0.55, which increased the responsiveness of the system (**Figure 2.2.2**) by decreasing the peptide brush density within formulated micelles of the same size. In this study, we demonstrate proof-of-concept that these enzyme-responsive nanoparticles target, assemble, and are retained in an acute MI, thereby providing a promising approach for delivery of therapeutics immediately post-MI and obviating the need for risky intramyocardial injections.

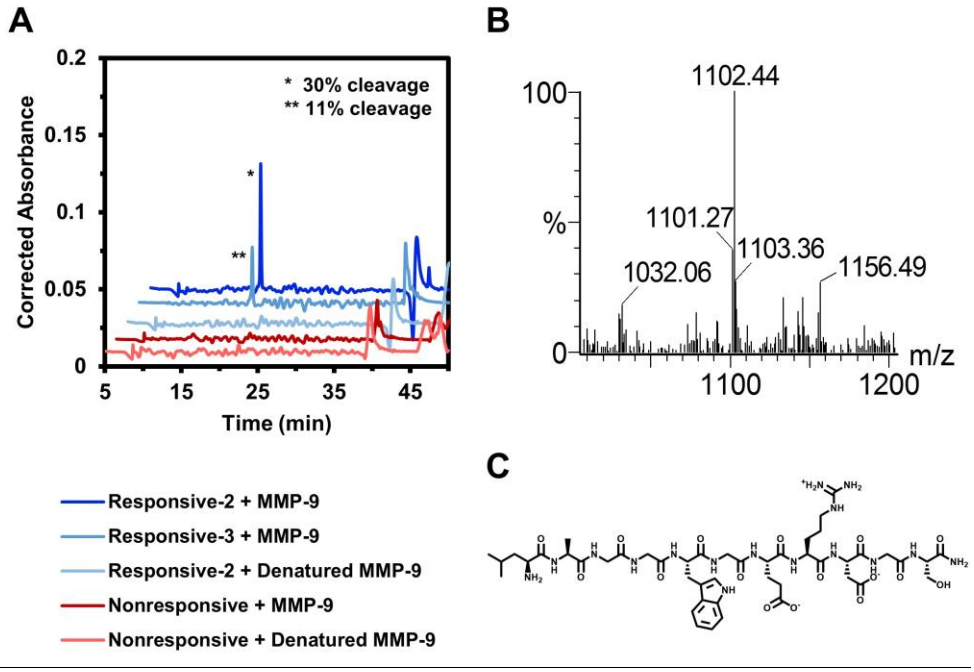


Figure 2.2.2. Spectroscopic and Spectrometric Analysis of MMP-9 Treated Nanoparticles. (A) Analytical HPLC of responsive and nonresponsive nanoparticles treated with either active or denatured MMP-9. A linear elution gradient of 0 - 30% buffer B over 30 min, then 30 – 50% buffer B over 10 min measured at 214nm (flow rate: 1 mL/min) was used to resolve peaks. The cleavage fragment for enzyme treated responsive nanoparticles are indicated by asterisks at R_t = 19 min (16% buffer B). Responsive-2, corresponding to particles containing 2 peptides per PPA, were used throughout this study. Responsive-3, corresponding to particles containing 3 peptides per PPA, were previously reported nanoparticles used in a tumor model, as discussed in the main text. Comparison of cleavage fragments after 24 hr of enzyme treatment shows that Responsive-2 particles are much more responsive to MMP-9 than Responsive-2, with percent peptide cleavages of 30% and 11%, respectively. Cleavage fragments were measured by (B) ESI MS using the negative ion mode. Observed: $[M-H]^-$ 1102.44 m/z. Calculated: $[M-H]^-$ 1102.15 m/z. (C) The cleaved peptide product, LAGGWGERDGS, chemical structure is indicated.

We hypothesized that enzyme-responsive nanoparticles could respond to the upregulation of MMP-2 and MMP-9 that occurs in an acute MI,[26] creating a scaffold that would be retained in the tissue. In a previous report, super resolution fluorescence microscopy was used to detect a particle

size increase from a similarly responsive particle system within tumor tissue.[27] To first evaluate whether the aggregated particles would remain in the infarct over time, we pretreated responsive (containing *L*-amino acids) and nonresponsive (containing *D*-amino acids) particles with MMP-9 for 24 hours to cause pre-aggregation of the responsive particles *in vitro*, and then injected the resulting material into healthy rat myocardium (*in vivo* methods provided in Supplemental Information). The results indicated that pretreated, responsive particles remain in the tissue up to 7 days post-injection, while nonresponsive particles were cleared after 1 hour (**Figure 2.2.3**). These data suggest that responsive particles are activated by MMP-9 to induce a morphological change into an assembled scaffold, which is retained at the injection site. By contrast, nonresponsive particles remain inert in the presence of MMP-9 and are cleared quickly.

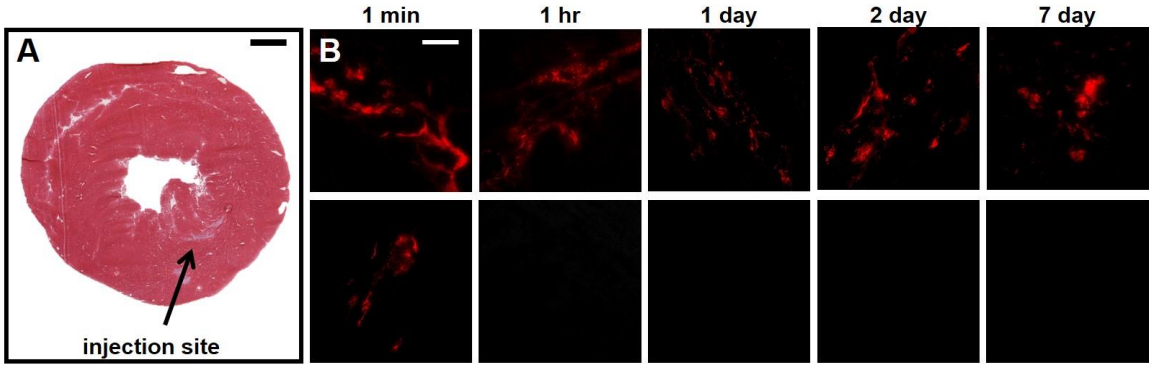


Figure 2.2.3 Retention of MMP pretreated responsive nanoparticles and clearance of nonresponsive nanoparticles in healthy myocardium. MMP pretreated particles were injected into healthy rat myocardium (A) and tissue was evaluated 1 minute, 1 hour, 1 day, 2 days, and 7 days post-injection for presence of the fluorescent aggregates (B). Rhodamine labeled, responsive particles (B, top row) were observed at the site of injection up to 7 days post-injection, while the nonresponsive particles (B, bottom row) were cleared after 1 hour. Scale bar: 1 mm (A); 50 μm (B).

Next, we evaluated our system in a rat MI model to determine whether upregulated MMPs in the infarct were sufficient to cause particle aggregation. Responsive and nonresponsive particles were delivered via intramyocardial injection 7 days post-MI, and rats were euthanized 6 days post-injection. Aggregation was observed in hearts that received responsive particles compared to minimal accumulation of the nonresponsive particles (**Figure 2.2.4**), demonstrating that the increased expression of MMPs post-MI activates the morphological transition of our responsive particles. The

responsive particles were observed up to 6 days post-injection, suggesting that the network-like scaffold remains in the infarct zone over time, compared to the minimal aggregation observed for nonresponsive particles.

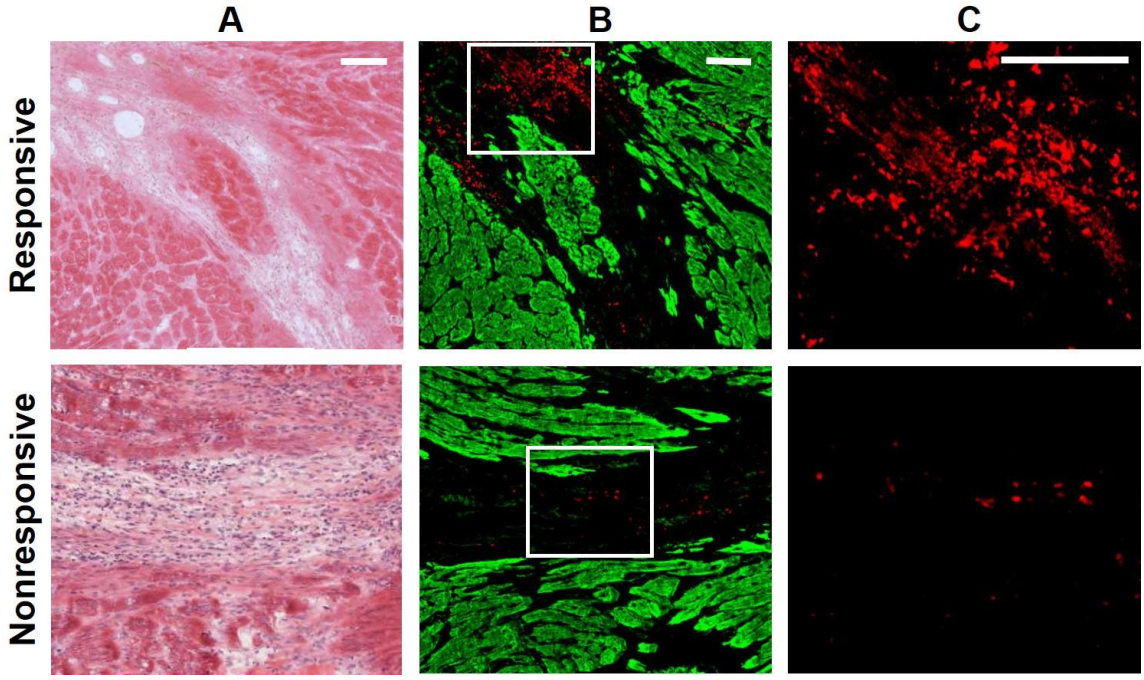


Figure 2.2.4. Retention of responsive nanoparticles upon localized delivery. Particles were injected intramyocardially 7 days post-MI and assessed 6 days post-injection. H&E images display the infarct area in A, and neighboring fluorescent sections are shown in B. Particles are shown in red and myocardium, which was labeled with an anti-α-actinin antibody, is shown in green. Selected regions from B (white outline) were magnified to highlight particle aggregation in C. Scale bar: 100 μm.

Next, we tested whether the nanoparticle system could be delivered IV and accumulate in the infarct. Responsive and nonresponsive nanoparticles (300 nmol) were injected into the tail vein of rats 24 hours post-MI (*in vivo* methods provided in Supplemental Information). After 2 days, greater accumulation was observed in the hearts of animals that received the responsive particles, compared to the nonresponsive particles (**Figure 2.2.5**). Responsive particles were found in the infarct and adjacent borderzone, but not in the remote, viable myocardium. This pattern of accumulation continued to be observed in the tissue at 7, 14, and 28 days post-injection, demonstrating that this unique targeting approach provides for long-term retention in the tissue. When responsive particles

were injected into healthy, non-infarcted rats, no aggregates were observed in the heart (**Figure 2.2.5**).

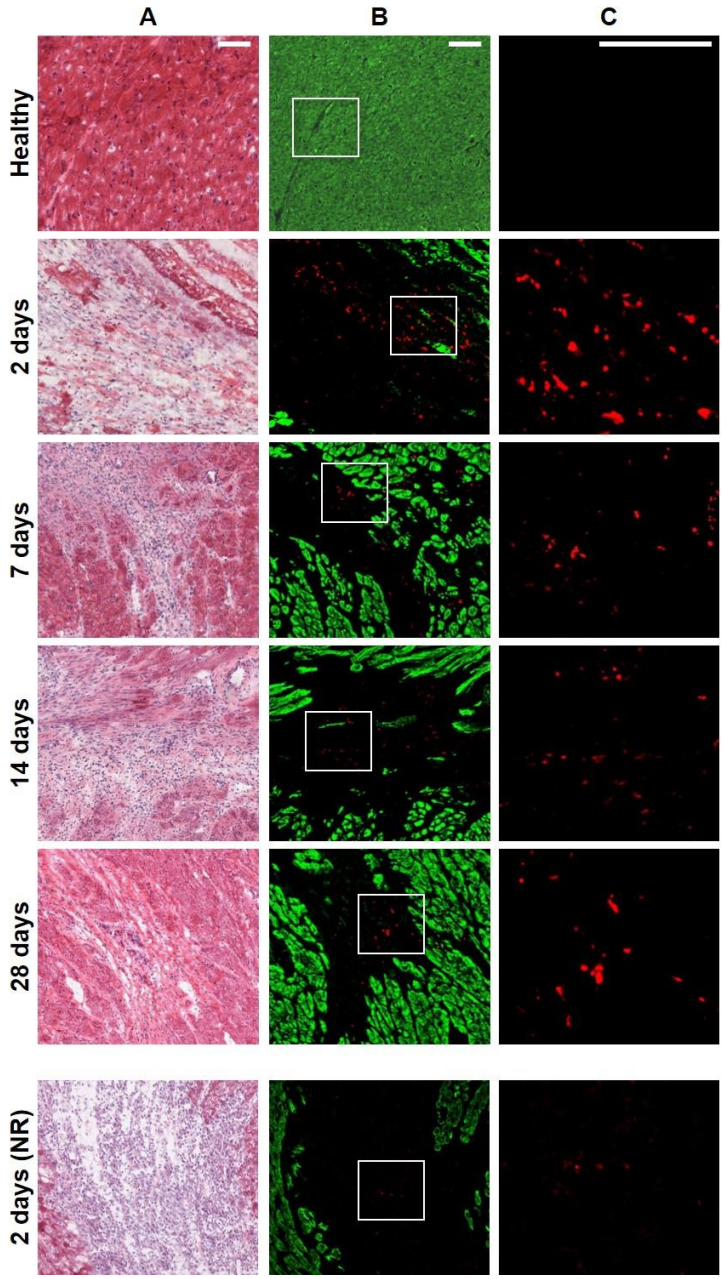


Figure 2.2.5. Retention of IV delivered nanoparticles with the infarct. H&E images are shown in A, and neighboring fluorescent sections are shown in B. Particles are shown in red and myocardium, which was labeled with an anti-α-actinin antibody, is shown in green. Selected magnified regions from B (white outline) are shown in C. In the absence of an infarct, IV injected responsive particles do not accumulate in healthy myocardium. Very few nonresponsive particles (NR) particles, which were IV injected 24 hours post-MI, were observed in the infarct 2 days post-injection. In contrast, aggregates of responsive particles were observed in the infarct 2, 7, 14, or 28 days post-injection. Scale bar: 100 μm.

To test whether the leaky post-MI vasculature was necessary for particle accumulation in the infarct, we injected responsive particles (IV route) 30 days post-MI. The EPR effect, which occurs acutely post-MI,[8,28] is less prevalent over time.[16] For example, in other studies, less accumulation of liposomes has been observed when injected IV 7 days post-MI compared to both 1 and 4 days post-MI.[20] In our system, minimal accumulation was observed when delivered in the presence of a chronic MI (**Figure 2.2.6**), suggesting that the EPR effect is necessary for particles to initially enter the tissue.

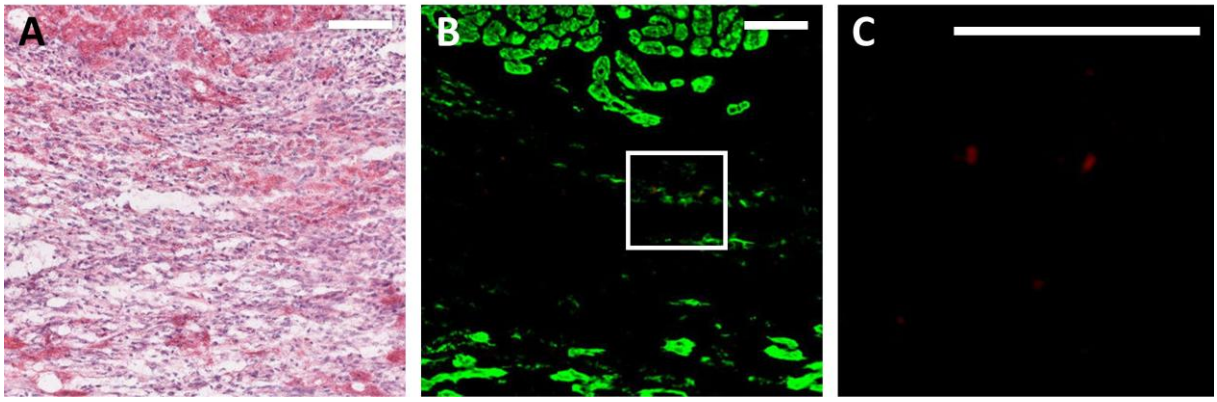


Figure 2.2.6. Effect of reduced permeability on nanoparticle delivery. Responsive nanoparticles were injected IV 30 days post-MI, and the animals survived for 2 days post-injection. H&E image is shown in A, and the neighboring fluorescent section, with particles in red and the myocardium in green, is shown in B. Selected magnified region from B (white outline) is shown in C. Scale bar: 100 μm

Other nanoparticle systems have exploited the EPR effect for passive targeting including polymeric micelles[29], liposome based nanoparticles[30], and vascular endothelial growth factor (VEGF)-encapsulated liposomes[31]. While these systems showed promise in treating MI by demonstrating increased cardiac function or decrease in infarct size compared to their saline or non-treated controls, they are limited by their lack of long-term retention. The MMP responsive nanoparticles reported here likewise use the EPR effect for initial passive targeting. However, in contrast, these particles undergo a morphological switch in response to upregulated MMPs, due to incorporation of the MMP-cleavable peptide sequence, which results in long-term retention (up to 28 days) at the site of infarction.

Our enzyme-responsive morphological switch was demonstrated *in vitro* and from evidence that nonresponsive, but not responsive, nanoparticles, rapidly clear from infarct tissue. Given the complex microenvironment of MI tissue *in vivo*, comprised of various cells, proteins, signaling

molecules, and salts, enzyme-aggregated polymer scaffolds may exhibit different shapes and sizes. The morphology of injected particles was investigated with *in vivo* TEM of heart tissue slices (**Figure 2.2.7**). At the infarct site, myocardium is observed as a dense array of myofilaments (**Figure 2.2.7A**). The interstitial space at the zone of cell death is covered by cellular debris and collagen at 8 days post-MI (**Figure 2.2.7B**). Injected nanoparticles assemble as large and low contrast scaffolds within this region of zone death, as indicated with red arrows (**Figure 2.2.7C-D**).

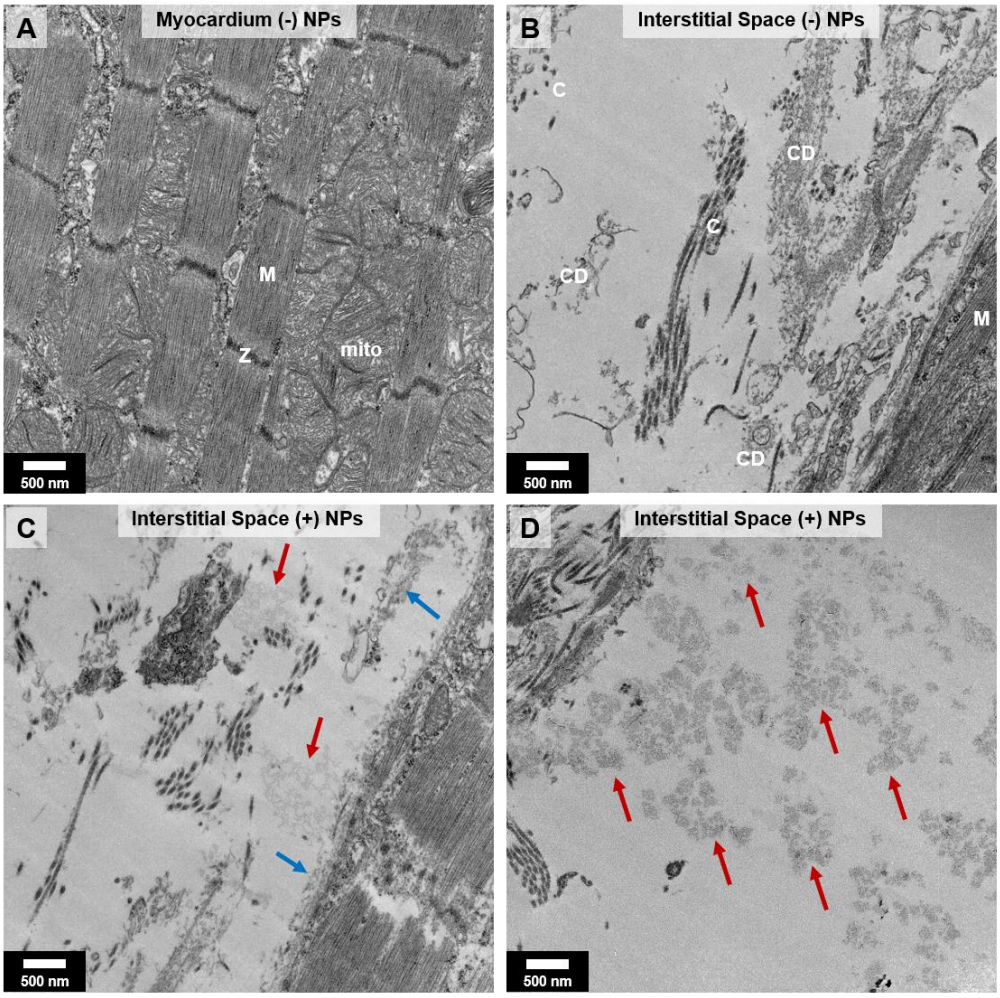


Figure 2.2.7. *In vivo* TEM of infarct region from rat ischemia reperfusion model. (A-B) Infarct tissue without nanoparticle (NP) injection and harvested at 8 days post-MI. (A) Intact myocardial cells outside of the immediate infarct region. (B) Interstitial space at the site of infarct showing cellular debris and collagen. (C-D) Infarct tissue with direct injection of NPs at 7 days post-MI and harvested 1 day post-injection. (C) Interstitial space at the site of infarct showing low contrast aggregate assemblies (red arrows) mixed with cellular debris (blue arrows). (D) Infarct more concentrated region of aggregated scaffolds. Magnification 3000x. Myofilament (M), Z-line (Z), mitochondria (mito), collagen (C), and cellular debris (CD).

To confirm that these structures do indeed correspond to our aggregated polymeric materials, we incubated HEKa cells with pre-treated nanoparticles, and performed the same sample fixation, staining, and sectioning steps for *in vivo* TEM (**Figure 2.2.8**). Control cells without pre-treated particles showed no material in the extracellular space (**Figure 2.2.8A**). However, aggregated scaffolds with similar morphologies and contrast to that found *in vivo* were observed when incubated at 0.02 mg/mL for 1 and 24 hr (**Figure 2.2.8B-D**). Notably, in both studies *in vivo* and with cell, scaffolds were not internalized. Thus, we believe these materials accumulate within the extracellular matrix, where MMP expression is high in an acute MI. This conclusion is further supported by the large negative zeta potential of responsive nanoparticles (**Figure 2.2.8E**), which likely prevents cellular penetration and internalization.

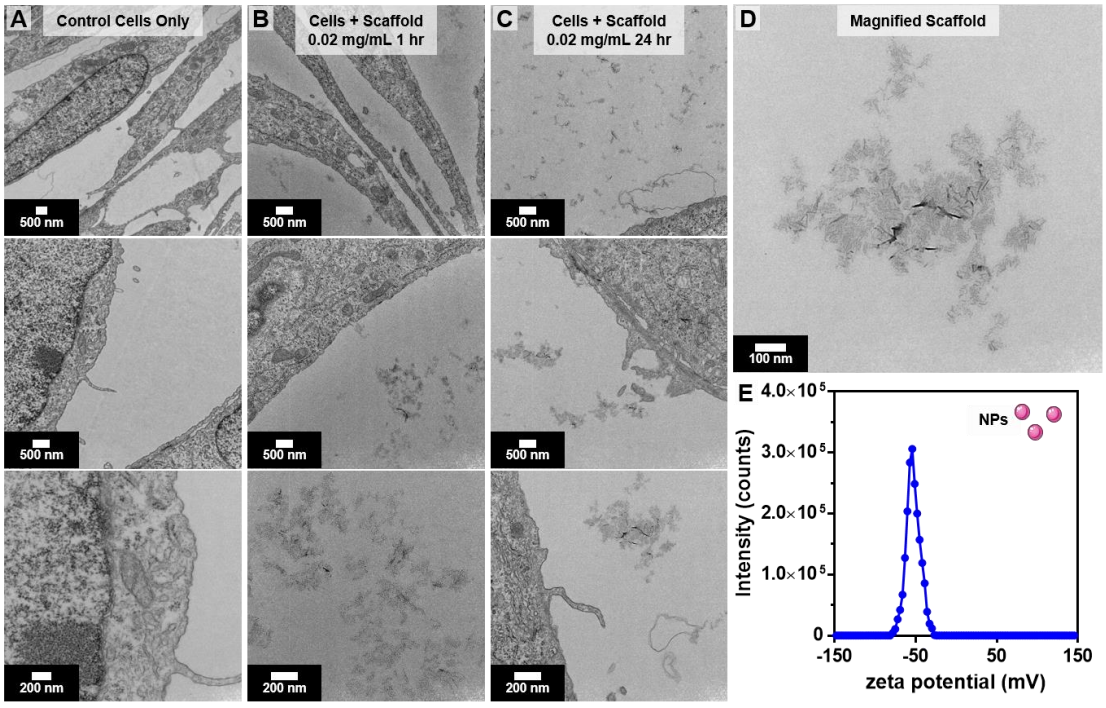


Figure 2.2.8. In vivo TEM of healthy cells incubated with pre-treated nanoparticles. Responsive nanoparticles were incubated with thermolysin to initiate aggregation prior to incubation with HEKa cells. (A) Control cells only. (B-D) Cells incubated with 0.02 mg/mL pre-treated scaffolds for (B) 1 hr and (C) 24 hr. (D) Magnified view of pre-aggregated scaffolds in cells at 24 hr. (E) Zeta potential of responsive nanoparticles. ZP = -56 ± 2 mV (n = 12 samples). 30 μM nanoparticles in H2O (pH 7.4), 37 ℃.

A therapeutic material should remain in the infarcted tissue for a prolonged period (>1 week to several weeks) to adequately prevent negative LV remodeling. This places a substantial burden on nanoparticle design and delivery strategies. Surprisingly, only a limited number of studies have looked at long-term retention of nanoparticles, but of those that have, nanoparticles relying solely on passive targeting mechanisms (i.e. via the EPR effect) are rapidly cleared from target tissue.[8,23,32-34] Nanoparticles relying on active targeting mechanisms involving receptor recognition, such as MMP-2 and MMP-9 targeting peptides,[35] have demonstrated efficient targeting in ischemic zones and shown somewhat improved retention times from 24 hr to 7 days.[23,33] Despite these improvements, current receptor binding strategies to target ligands in the infarct post-MI are not sufficient for prolonged retention.[20,36-38] Data for target tissue retention of receptor binding nanoparticles within other disease models (e.g. ischemic hindlimb or cancer) beyond hours or days is similarly lacking.[39-42] Our results demonstrate that a localized morphology change from nanoscale spherical micelles to microscale network-like materials drastically enhances retention within the infarct as compared with non-responsive particles, providing a unique tactic for overcoming rapid tissue clearance. Unlike other systems, we utilize an active targeting mechanism reliant on the activity of an enzyme, rather than a receptor binding event. Furthermore, our system is maintained in the infarct zone as suggested by visualization of the rhodamine dye up to 28 days post-injection. Given that free dye would be rapidly cleared and that the nonresponsive particles also have the same tag, yet do not show the same degree of aggregation and retention, this suggests that fluorescently labeled aggregates remain in the tissue.

In addition to infarct targeting, off-site accumulation and safety are important to assess with any nanoparticle therapy. Histopathologic evaluation of heart sections showed expected inflammatory responses associated with MI remodeling.[8] No differences were observed between infarcted myocardium containing aggregated particles and the time matched infarct controls, which received no injections. Furthermore, at 28 days post-injection, there was no observed difference in macrophage infiltration (as identified by CD68+ cells) compared to the infarct control (**Figure 2.2.9**).

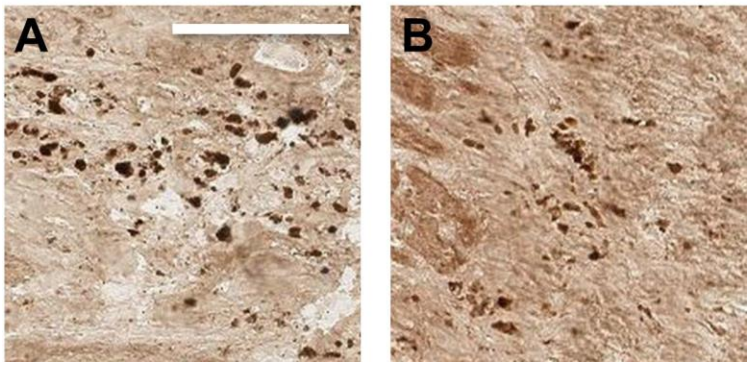


Figure 2.2.9. Macrophage infiltration. CD68+ macrophages (brown staining) were observed in both the infarct control animal 29 days post-MI (A), and the infarct with responsive particles 28 days-post-injection (B). Scale bar: 100 μm.

We also evaluated the biodistribution of responsive particles to satellite organs. Particles were observed in the liver, spleen, and lung, with minimal presence seen in the kidneys (**Figure 2.2.10**). The biodistribution of nanoparticles when delivered IV has been described for a number of different systems, and it is generally accepted that larger particles are internalized by the reticuloendothelial system (RES), while smaller particles are more widely distributed in the body.[18,43-46] Despite these observations, the toxicity and biodistribution of nanoparticles when delivered IV is not well understood.[44,47] For example, similarly sized nanoparticles composed of silver, gold, and poly(ethylene glycol) have shown different distribution trends.[43,45,46] Among polymeric nanoparticles, toxicity has been evidenced by acute liver inflammation and apoptosis.[43]

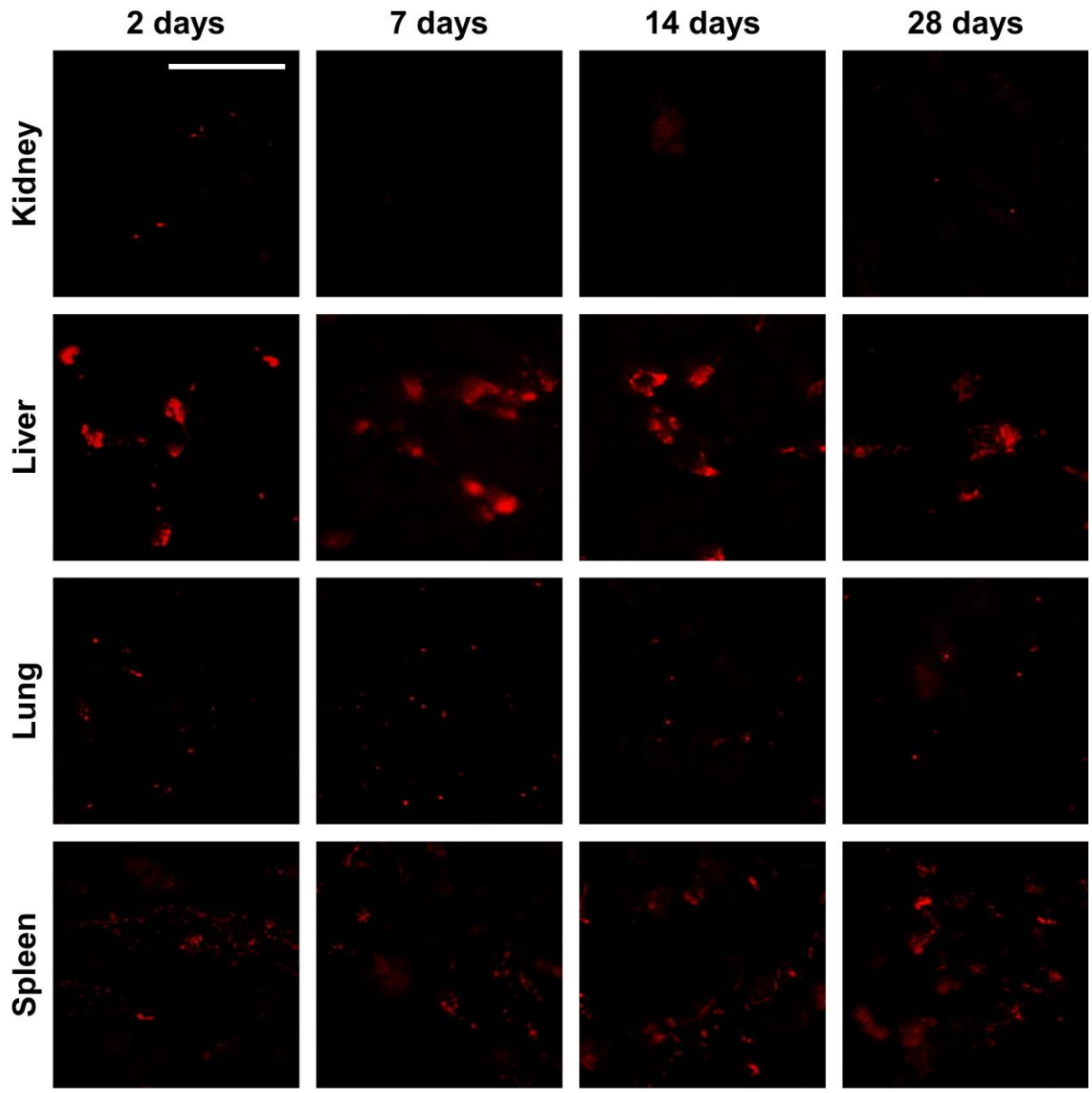


Figure 2.2.10. Biodistribution of responsive nanoparticles. Fluorescent micrographs of satellite organs from animals that received responsive particles 24 hours post-MI over 2, 7, 14, and 28 days post-injection. Scale bar: 20 μm

To assess the potential toxicity of our responsive particles, satellite organs from rats, 2 and 28 days post-IV injection (3 and 29 days post-MI, respectively) were evaluated and compared to those from both healthy and infarcted rats that received no injections (**Figure 2.2.11**). Satellite organ histopathologic evaluation revealed essentially normal tissues, when scrutinized by a trained histopathologist blinded to the study.

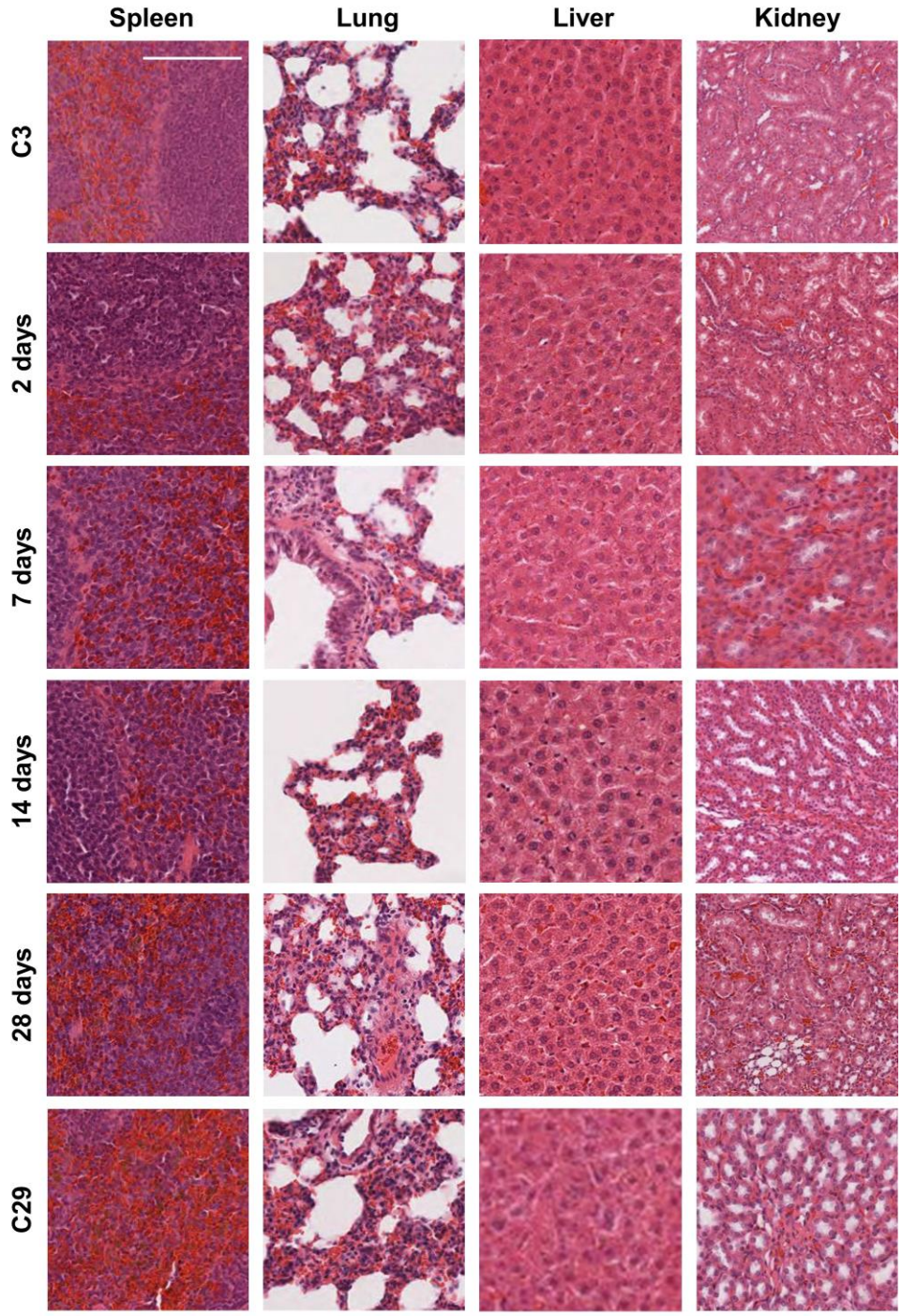


Figure 2.2.11. Histology of satellite organs from IV injections. H&E stained images of satellite organs from animals that received responsive particles 24 hours post-MI over 2, 7, 14, and 28 days post-injection. Respective organs from non-injected, infarcted animals 3 days (C3) and 29 days (C29) post-MI were used as controls. Scale bar: 100 μm

In addition, no signs of weight loss (**Figure 2.2.12**) or changes in behavior were observed within both groups for up to 5 days post-injection and upon euthanasia 28 days post-injection. These results indicate that there were no signs of toxicity from these nanoparticles. It will however be important to perform more rigorous toxicity studies prior to translation. The responsive particles were fluorescently labeled for easy detection ex vivo; however, this label would not be necessary for human application. While ROMP polymers containing polynorbornene backbones have similarly shown to be non-toxic in the presence of mammalian cell lines,[48,49] several additional toxicity and biocompatibility studies will be necessary to prove the safety of this polymer and nanoparticle formulations.

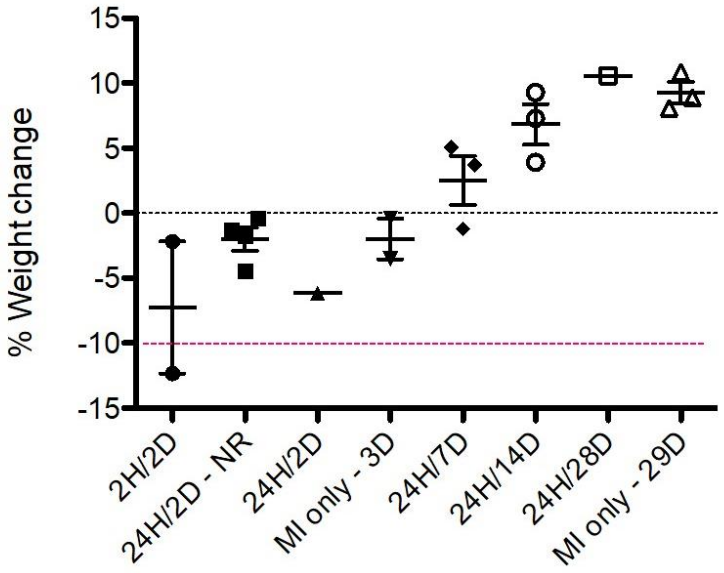


Figure 2.2.12. Animal weight fluctuations. Average % weight change between the time of injection post-MI and the time of euthanasia post-injection. H (hours), D (days), NR (nonresponsive nanoparticles). Unless otherwise stated, injections were performed with responsive nanoparticles. The Animal Care Program (ACP) considers a 10% loss in weight as statistically significant (red line).

2.2.3 Study Conclusions

Early intervention of MI has the potential to slow or inhibit the progression of negative LV remodeling. To date, most therapeutic delivery strategies have involved intramyocardial biomaterial injections,[15] although translation to acute MI patients is unlikely given the increased risk of ventricular rupture immediately post-MI.[14,15] One promising, minimally invasive strategy is the systemic injection of nanoparticles. However, many of the investigated systems lack long-term retention within the

MI.[20,29,30] The enzyme-responsive nanoparticles described here provide an efficient template for targeting the acute MI and remain in the infarct for up to 28 days post-injection. We have shown that the responsive nanoparticles are enzyme-responsive, accumulate due to upregulation of MMPs after MI, and are deliverable through both intramyocardial and IV injection. In summary, this unique approach constitutes a minimally invasive method for the delivery of a material scaffold to acutely infarcted myocardium, providing a promising approach for prolonged therapeutic delivery. Future studies will explore the conjugation of different small molecule or peptide therapeutics, and their efficacy in the heart balanced with potential side effects from off target nanoparticle retention.

2.2.4 Experimental Details

General Methods: All reagents were purchased from Sigma-Aldrich and used without further purification. (N-Benzyl)-5-norbornene-exo-2,3-dicarboximide (1) was prepared as described previously.[50] 1-{[(2S)-bicyclo[2.2.1]hept-5-en-2-ylcarbonyl]oxy}-2,5-pyrrolidinedione (2) was prepared as described by Pontrello et al.[51] Dye-termination agents (3) were prepared as described previously.[52] (IMesH2)(C5H5N)2(Cl)2Ru=CHPh was prepared as described by Sanford et al.[53] Polymerizations were performed under dry nitrogen atmospheres with anhydrous N,N-dimethylformamide (DMF). MMP-9 (human catalytic domain) (BML-SE360) was acquired from Enzo Life Sciences, as a 0.5 mg/mL solution at 24 U/µg in 50 mM TRIS (pH 7.5), 1 mM $CaCl_2$, 300 mM NaCl, 5 µM ZnCl, 0.1% BRIJ-35, and 15% glycerol.

Peptides were synthesized on an AAPPTec Focus XC peptide synthesizer. Analytical HPLC analysis of peptides was performed on a Jupiter 4u Proteo 90A Phenomenex column (150 x 4.60 mm) using a Hitachi-Elite LaChrom L-2130 pump equipped with UV-Vis detector (Hitachi- Elite LaChrom L-2420). Peptides were purified on a Armen Glider CPC preparatory HPLC. The solvent system for both HPLC instruments consist of (A) 0.1% TFA in water and (B) 0.1% TFA in acetonitrile. Mass spectra were obtained at the UCSD Chemistry and Biochemistry Molecular Mass Spectrometry Facility using a Micromass Quattro Ultima Electrospray Ionization (ESI) mass spectrometer. Polymer

polydispersities and molecular weights were determined by size-exclusion chromatography on a Phenomenex Phenogel 5u, 1K-75K, 300 x 7.80 mm in series with a Phenomex Phenogel 5u, 10K-1000K, 300 x 7.80 mm (0.05 M LiBr in DMF) using a Shimatzu pump equipped with a Wyatt Technology DAWN-HELIOS multi-angle light scattering detector and a Hitachi L-2490 refractive index detector. Detectors were normalized with a 30,000 MW polystyrene standard. The hydrodynamic diameter (D_h) of particles was measured by DLS using a Wyatt Dynapro NanoStar. Zeta potential was measured with a Zetasizer Nano ZS90. TEM images were acquired on an FEI Tecnai G2 Sphera at 200 KV. Particle concentration measurements were conducted on an EnSpire Multimode Plate Reader.

Preparation of Peptide Substrates: Peptides containing the amino acid sequence, GPLGLAGGWGERDGS, were synthesized, containing an MMP-2 and -9 recognition sequence (underlined). Peptides were synthesized on rink amide 4-methyl benzylhydrylamine (MBHA) resin via standard Fmoc-based solid phase peptide synthesis. Fmoc deprotection was performed by agitating resin in 20% 4-methylpiperidine in DMF for 5, draining, and repeating this procedure for another 15 min. Amino acid couplings were carried out for 45 min per amino acid using N,N,N,N',N'-Tetramethyl-O-(1H-benzotriazol-1-yl)uranium hexafluorophosphate (HBTU) and N,N-diisopropylethylamine (DIPEA) (resin/amino acid/HATU/DIPEA 1:3:3:6). Final peptides were cleaved from resin by treatment with trifluoracetic acid (TFA), triisopropyl silane (TIPS), dithiothreitol (DTT), and water (TFA/TIPS/DTT/H_2O 88% v/v:2% v/v:5% w/v: 5% w/w) for 2 hr. Peptides were then precipitated in cold ethyl ether and centrifuged at 4500 rpm for 15 min; this procedure was repeated twice. The precipitated peptide products were evaporated in vacuo to give an off white crude solid. Peptides were purified by reverse phase prep HPLC (0-15% Buffer B over 35 min, retention time = 25 min), evaluated by negative-mode ESI MS (mass calculated $[M-H]^-$ =1425.69 m/z; mass observed $[M-H]^-$ = 1425.58 m/z) and lyophilized to afford a pure white solid. L-amino acid responsive peptides and D-amino acid non-responsive controls were both synthesized by this method.

Synthesis of Block Copolymer (1_{20}-b-2_5-F and 1_{20}-b-2_5-R) (**Figure 2.2.13**): To a stirred solution of i) (100 mg, 394.3 µmol) in dry DMF (2.0 mL) was added a solution of ii) the catalyst ((IMesH2)(C5H5N)2(Cl)2Ru=CHPh) (14.3 mg, 19.7 µmol) in dry DMF (2 mL) under N_2 atmosphere. The reaction was left to stir under nitrogen for 45 min, after which an aliquot (20 µL) was removed and quenched with v) ethyl vinyl ether. After 15 min the quenched polymer was precipitated in anhydrous ethyl ether to give the homopolymer 1_{20} as a solid. To the remaining reaction mixture, a solution of iii) (46.5 mg, 197.2 µmol) in dry DMF (2 mL) was added immediately following aliquot removal. The mixture was left to stir under nitrogen for 45 min, after which an aliquot (20 µL) was removed and quenched with v) ethyl vinyl ether. After 15 min the polymer was precipitated in anhydrous ethyl ether to give the block copolymer 1_{20}-b-2_5 as an off-white solid. The remaining bulk reaction mixture was split into two portions and a solution of iv) dye termination agent (16.3 mg Dye_1 or 13.6 mg Dye_2, 11.8 µmole) in dry DMF (1.0 mL) was added. The mixtures were left to stir under nitrogen for 2 hr then v) ethyl vinyl ether (30 µL) was added to quench the catalyst. After 15 min the solutions were precipitated by dropwise addition to cold anhydrous ethyl ether to give the two copolymers, 1_{20}-b-2_5-F and 1_{20}-b-2_5-R.

Synthesis of Peptide-Polymer Amphiphiles, PPA-F and PPA-R: To a stirred solution of copolymer 1_{20}-b-2_5-F or 1_{20}-b-2_5-R (18.7 mg, 2.896 µmol) dissolved in a dry mixture of 4:1 DMF:DMSO (370 µL) at 50 mg/mL was added L-amino acid peptide and DIPEA (copolymer:peptide:DIPEA 1:4:16). The reaction was stirred at room temperature for 27 hrs. For 1_{20}-b-2_5-F, NH_4OH (460 µL, 160 µL/µmol polymer) was added and stirred for 45 min at room temperature to deprotect the fluorescein pivalate groups, followed by evaporative removal of NH4OH. Solutions were then precipitated in cold anhydrous ether and washed with cold methanol (2 x 4 mL),collected by centrifugation at 13,000 rpm for 3 min, decanted, and dried to obtain the peptide conjugated systems, PPA-F and PPA-R. This notation is used to distinguish inactive copolymers from peptide-activated amphiphilic materials, which no longer contain NHS conjugatable moieties. This same procedure was followed for D-amino acid analogues.

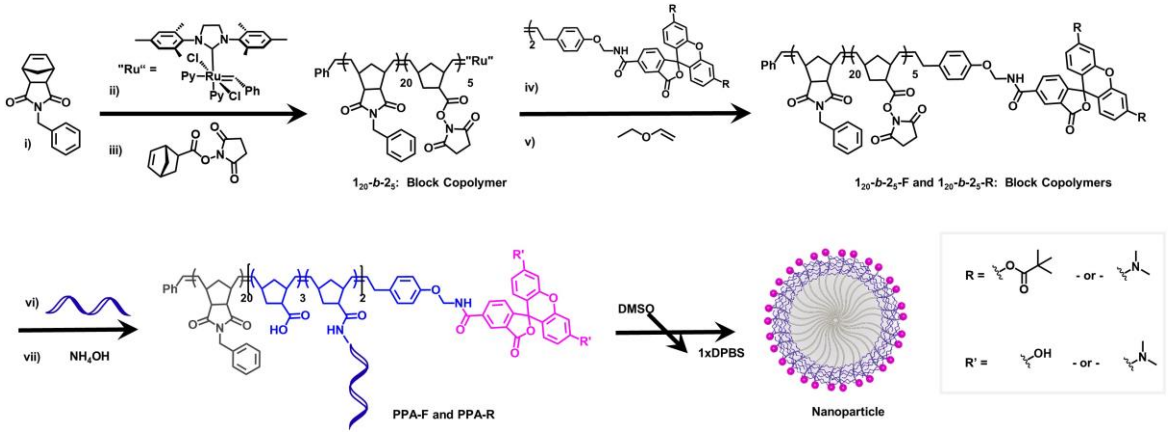


Figure 2.2.13. Preparation of fluorescent MMP-9 responsive nanoparticles. Block copolymers were synthesized with a hydrophobic phenyl-moiety and a conjugatable N-hydroxy succinimide-ester prepared via ring-opening metathesis polymerization.[54] The living polymer was modified either with a fluorescein or rhodamine (pink)-labeled termination agent and further modified with a peptide sequence (blue) consisting of either L-amino acids as a cleavable substrate or D-amino acids as a nonresponsive substrate. Peptide polymer amphiphiles (PPA) were combined in a 1:1 molar ratio and dialyzed into 1x DPBS to create micellar nanoparticles.

SEC-MALS Analysis (**Figure 2.2.14**, **Table 2.2.1**) of Polymers: Representative SEC-MALS data for the 1_{20} homopolymer, 1_{20}-b-$2_5$and 1_{20}-b-2_5-F copolymers, and PPA-F are provided (**Figure 2.2.14**). dn/dc for these polymers is 0.179. Calculations of polymer sizes, their PDI, and block size or conjugation number, are provided in Supplemental Table 1. Calculations for 1_{20}-b-2_5-R and PPA-R are not provided due to interference of the dye at λ=657 nm when measuring the differential refractive index (dRI). The degree of peptide conjugation for PPA-R is assumed to be the identical to that of PPA-F .

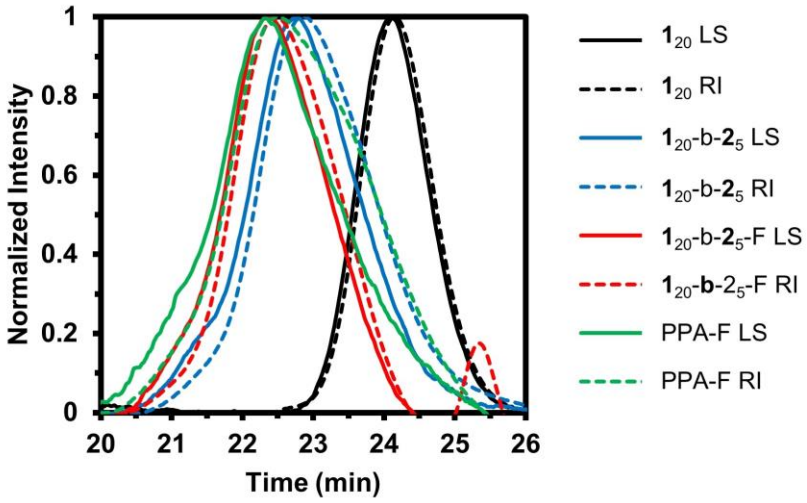


Figure 2.2.14. SEC-MALS intensity plot of homopolymer 1_{20} (black), copolymers 1_{20}-b-2_5 (blue) and 1_{20}-b-2_5-F (red), and PPA-F (green). Light scattering (LS) and differential refractive index (RI) traces are show as solid and dashed lines, respectively.

Table 2.2.1. Polymer molecular masses (g/mol) with respect to number (M_n) and weight (M_w), and polydispersity indices ± standard deviation, as measured by SEC-MALS. Calculated block sizes or peptide conjugation numbers are shown.

	1_{20}	1_{20}-b-2_5	1_{20}-b-2_5-F	PPA-F
M_n	5253 (± 1.512%)	6461 (±1.829%)	7192 (±1.833%)	8663 (± 1.919%)
M_w	5310 (±1.447%)	6873 (±1.543%)	7465 (±1.833%)	9583 (±1.726%)
PDI	1.011 (±2.093%)	1.064 (±2.393%)	1.038 (±2.533%)	1.106 (±2.581%)
size or number	20	5	n/a	2

Spherical Micelle Formulation: Responsive particles were prepared using equal parts PPA-F and PPA-R containing L-amino acid peptides whereas nonresponsive particles were prepared using equal parts PPA-F and PPA-R containing D-amino acid peptides. PPA-F (25 mg, 2.89 μmol) and PPA-R (25 mg each, 2.89 μmol each) were dissolved in DMSO (50 mL, 1mg/mL) and stirred as H_2O was slowly added via syringe pump at 0.75 mL/hr until the solution was 30% v/v aqueous (critical water concentration) and left to stir for 2 days. H_2O was then added at 5 mL/hr until reaching 50% v/v aqueous concentration. This solution was transferred to 3,500 MWCO SnakeSkin dialysis tubing and placed in water (pH 8.0). The buffer was changed three times per day for 2 days. The solvent was then switched to 1x DPBS using the same buffer exchange conditions listed above.

Stock Solution Preparation and Concentration Characterization (**Figure 2.2.15**): Particles were concentrated using EMD Millipore Amiccon Ultra-15 centrifugal filter units (10K Nominal Molecular Weight Limit, NMWL). Filters were centrifuged at 3000 rcf for 8 min at 21 ℃. Final stock solutions were sterilized through 0.2 µm EMD Millipore Steriflip sterile disposable vacuum filter units. Stock solution concentrations were determined by disrupting and diluting nanoparticles 7-fold in DMSO and recording absorbance values for fluorescein and rhodamine. Plate reader measurements for standards and stock solutions were performed with 150 uL of sample in clear bottom 96-well plates. Nanoparticle concentrations are reported in this chapter with respect to calculated total dye concentration.

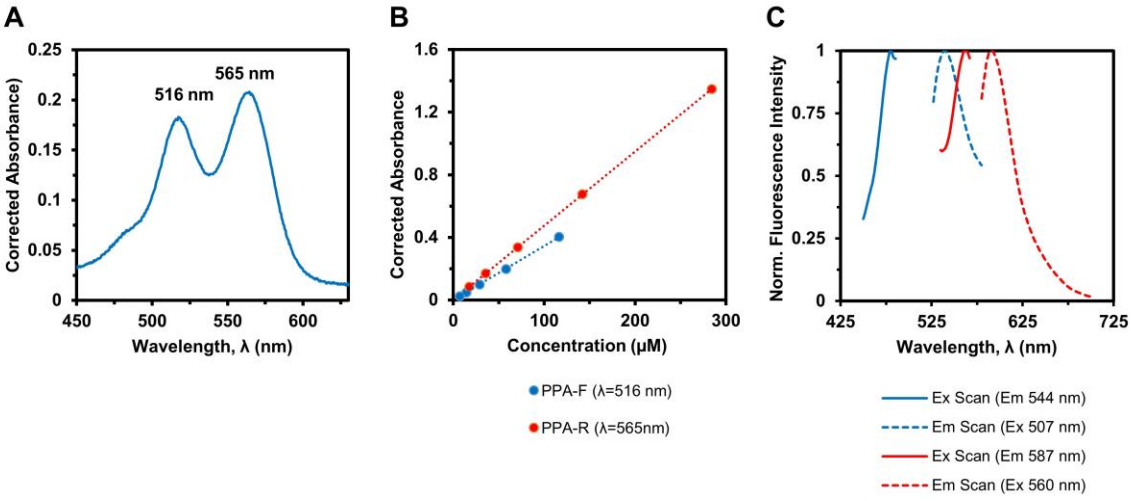


Figure 2.2.15. Spectroscopic analysis of nanoparticles in 8:1 DMSO:1xDPBS. (A) Absorbance spectrum of nanoparticles labeled with fluorescein (λ_{max} = 516 nm) and rhodamine (λ_{max} = 565 nm). (B) Absorbance calibration curves as a function of PPA, or total dye, concentration (µM). Trendline slopes 3.44851×10^{-3} (PPA-F) and 4.74505×10^{-3} (PPA-R). R_2 values 0.99803 (PPA-F) and 0.99995 (PPA-R). (n=2) (C) Normalized fluorescence intensity of excitation and emission scans for nanoparticles.

Dynamic Light Scattering (DLS) and Zeta Potential (Figure 2.2.16, Table 2.2.2): The hydrodynamic diameter (D_h) of responsive and nonresponsive particles with and without MMP-9 treatment was calculated by DLS (Figure **Figure 2.2.16**). Only responsive particles exhibit a morphology switch from monodisperse micellar nanoparticles (15-20 nm) to multi-micron-scale scaffolded aggregates. Scaffolds are larger than the reported detection limit of 1 µm in diameter. A significant shift occurs in the normalized autocorrelation function for responsive particles incubated

with MMP-9, while no discernable change is observed for nonresponsive particles treated with MMP-9. (**Figure 2.2.16**). Visible aggregation at 24 hr MMP-9 treatment for responsive particles can be seen with the eye (**Figure 2.2.1**). In contrast, nonresponsive particles remain intact by DLS and fully dispersed in solution. Supplemental Table 2 below provides quantitative data on particle diameter with respect to calculated % mass and % intensity, as well as the measured % polydispersity (Pd). Zeta potential of 30 μM (with respect to polymer) solutions of nanoparticles was measured in H_2O (pH 7.4) at 37 ℃ and found to be -56 ± 2 mV (n = 12 samples).

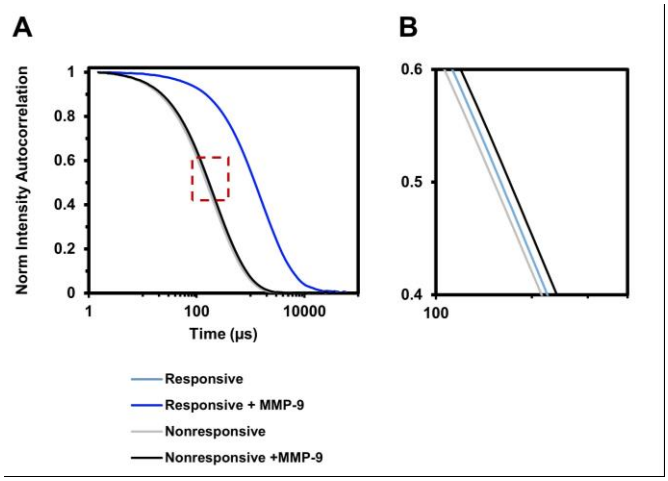


Figure 2.2.16. Autocorrelation functions. (A) Normalized autocorrelation functions for responsive and nonresponsive particles before and after 24 hr MMP-9 treatment. Highlighted region is replotted in (B) to demonstrate nearly identical autocorrelation functions for all conditions except responsive particles after MMP-9 treatment. These functions correspond to DLS data from **Figure 1F** in the main text.

Table 2.2.2. DLS measurements of particle diameter (nm) before and after incubation with MMP-9. Provided are % mass, % intensity, and % polydispersity of particle sizes

	Diameter (nm)	% Mass	% Intensity	% Pd
Responsive	23.0	94.6	26.4	12.1
	127.0	5.4	73.6	17.9
Responsive + MMP-9	615.0 to > 1000	99.2	80.5	n/a
Nonresponsive	18.5	96.1	23.3	5.0
	104.0	3.9	77.7	6.1
Nonresponsive + MMP-9	22.8	97.9	24.8	9.1
	117.7	2.1	75.2	10.6

Transmission Electron Microscopy (TEM) (Figure 2.2.17. Dry state TEM micrographs of nanoparticles before and after 24 hr of MMP-9 treatment.**Figure 2.2.17**): Small aliquots (3.5 μL) of sample were utilized for dry state TEM via standard procedures. Briefly, the sample was applied onto

400 mesh carbon grids (Ted Pella, INC.) that had previously been glow discharged using an Emitech K350 glow discharge unit and plasma-cleaned for 90 s in an E.A. Fischione 1020 unit. After 3-5 min, samples were rinsed with water and stained with 1% (w/v) uranyl acetate briefly and wicked dry. The sample grid was then transferred into a grid holder in the FEI Sphera microscope. Micrographs were recorded on a 2K X 2K Gatan CCD camera. Only responsive nanoparticles that were treated with MMP-9 exhibited a morphology switch from discrete micellar nanoparticles to micron-scale scaffold aggregates.

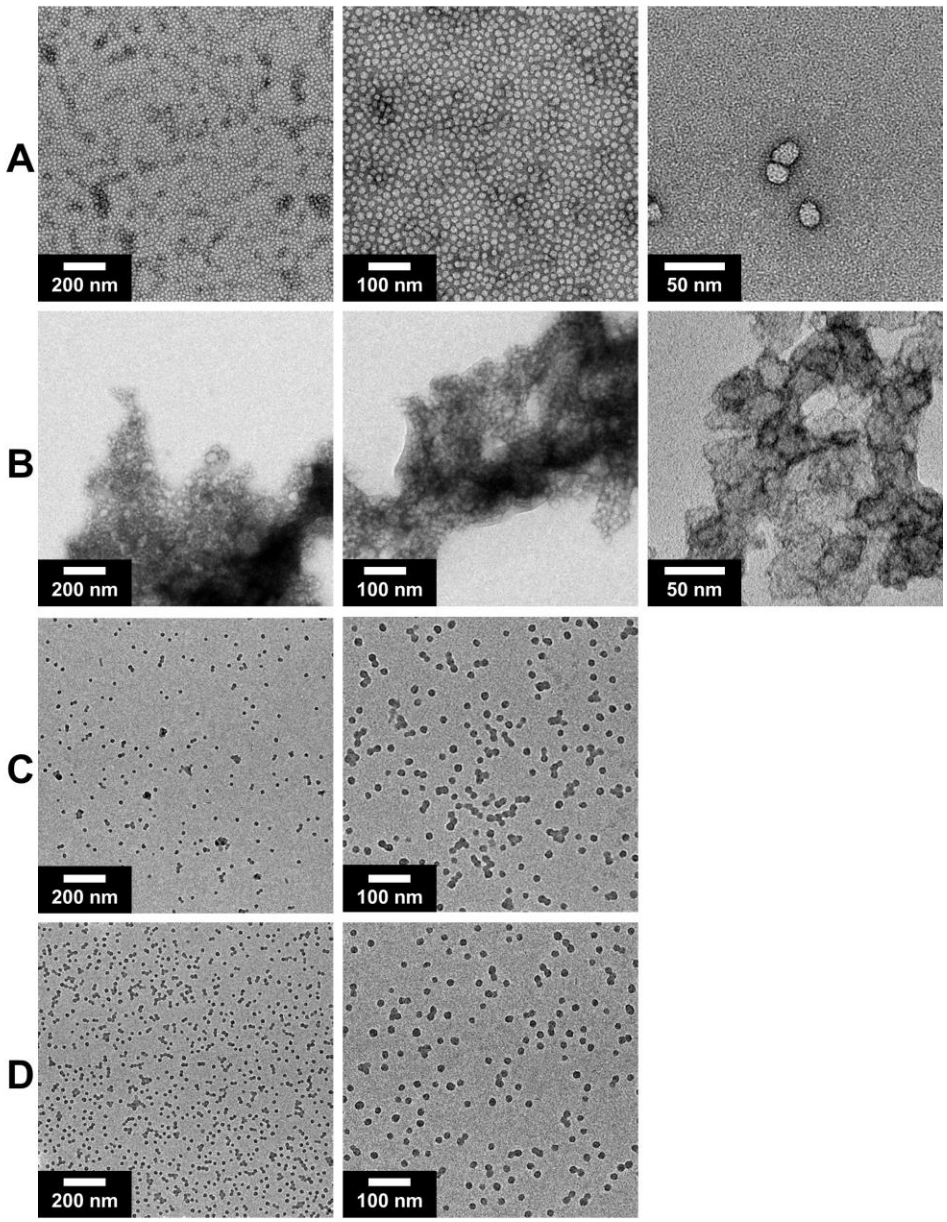


Figure 2.2.17. Dry state TEM micrographs of nanoparticles before and after 24 hr of MMP-9 treatment. (A) responsive particles before MMP-9 treatment, (B) responsive particles after MMP-9 treatment, (C) nonresponsive nanoparticles before MMP-9 treatment, (D) nonresponsive nanoparticles after MMP-9 treatment. Images are provided with scale bars from left to right measuring 200 nm, 100 nm, and 50 nm, respectively.

In Vitro MMP-9 Cleavage Assay (**Figure 2.2.2**): Micellar nanoparticles (100 μM, with respect to total dye) were treated with MMP-9 (1 μM, 36 U) for 24 hr at 37 ℃ in cleavage buffer (200 mM NaCl, 50 mM TRIS, 5 mM $CaCl_2$, and 1 mM $ZnCl_2$, pH 7.5). Reactions performed at 100 μL. Denatured enzyme controls were prepared by heating the enzyme solution to 65 ˚C for 30 min before

adding to the substrate. Analytical HPLC was used to monitor enzymatic cleavage of peptide substrate within nanoparticles. The expected cleavage product at R_t = 19 min (red trace) is produced when responsive nanoparticles are treated with MMP-9. The cleavage product mass-to-charge ratio was measured by ESI in negative ion mode to be $[M-H]^-$ 1102.44 m/z (calculated 1102.15 m/z) (**Figure 2.2.2B**) which corresponds to the predicted peptide sequence when cleaved between the G and L amino acid residues of our substrate.

In Vivo Studies: All animal experiments were conducted in accordance with the guidelines established by the Institutional Animal Care and Use Committee at the University of California San Diego and the Association for the Assessment and Accreditation of Laboratory Animal Care and approved by the Institutional Animal Care and Use Committee at UCSD (A3033-01). Female Sprague Dawley rats (225 – 250 g) were used in all studies.

Intramyocardial Injection of Particles into Healthy Rats: An intramyocardial injection was performed under isofluorane, using a previously described procedure.[55,56] To investigate the clearance of responsive and nonresponsive particles, particles (2.8 nmol, 70 µL) were pre-treated with MMP-9 catalytic domain (1 nmol) for 24 hours at 37°C prior to injection. Aggregated responsive particles and unchanged, nonresponsive particles were injected into the left ventricular free wall of female Sprague Dawley rats with a 27 G needle. Animals were euthanized with an overdose of pentobarbital (200 mg/kg) 1 minute, 1 hour, 1 day, 2 days, or 7 days post-injection (n=3 per group).

Intramyocardial Injection of Particles into Infarcted Rats: MI was performed via 25-min ischemia-reperfusion, as previous described.[55,57] The intramyocardial injections were performed 7 days post-MI, as described above. The particles were prepared in sterile saline (75 nmol, 75 µL) and injected into the infarct with a 27 G needle. Animals were euthanized with an overdose of pentobarbital (200 mg/kg), and the hearts were collected for histological analysis.

Tail Vein Injections of Particles in Infarcted and Healthy Rats: MI was performed via 25-min ischemia-reperfusion, as previous described.[55,57] Tail vein injections were performed either 24 hours or 30 days post-MI, and animals were anesthetized with 5% isoflurane and maintained at 2.5%

isoflurane during the procedure. Animals received 1 mL of responsive or nonresponsive nanoparticles (n=3 per group, 300 nmol) and were monitored daily for 5 days. All animals were visually examined and weighed prior to intravenous injection and euthanasia. Animals were euthanized with an overdose of pentobarbital (200 mg/kg), and the heart, lung, liver, spleen, and kidneys were collected for histological analysis.

Histology and Immunohistochemistry: After euthanasia, hearts were resected, fresh frozen in OCT, and cryosectioned. Other organs were formalin fixed, paraffin embedded and sectioned. Sections were stained with hematoxylin and eosin (H&E) to identify the infarct region or mounted with FluoroMount for fluorescent imaging using a Leica Ariol Platform. Given the strong autofluorescence in the infarcts in the green channel, only rhodamine was used to visualize the particles. H&E stained slides were examined by an experienced histopathologist who was blinded to the groups. Organs from healthy, untreated rats and infarcted rats receiving no injections were used as controls. Myocardium was identified using anti-α-actinin antibody (1:800 dilution, Sigma-Aldrich), and an Alexa Fluor 488 goat anti-mouse IgG secondary (1:500 dilution, Life Technologies). Macrophages were identified with an anti-CD68 antibody (1:100 dilution, AbD Serotec), followed by a horseradish peroxidase (HRP) conjugated goat anti-mouse IgG (1:100 dilution, Abcam), and visualized with diaminobenzidine (DAB) (Vector Laboratories).

Preparation of heart tissue with injected nanoparticles for *in vivo* TEM: Heart tissue from frozen OCT blocks were cut into 1 mm thick slices and carefully rinsed with 1xDPBS at 4 ℃ (5 x 10min) to remove OCT. Tissue sections were fixed with 2% paraformaldehyde in 0.1 M sodium cacodylate buffer at pH = 7.4 (SC buffer) for 3 days at 4 ℃.

Preparation of HEKa cells incubated with pre-aggregated scaffolds for *in vivo* TEM: HEKa cells were plated in 35 mm round plastic dishes and incubated in a 5% CO2 atmosphere at 37 ℃ using EpiLife medium with HKGS growth supplement (Life Technologies) until reaching 95% confluency, then rinsed with 1xDPBS prior to material incubation. Responsive nanoparticles were

treated with thermolysin (1:500 enzyme and polymer) in 1xDPBS for 48 hours to initiate rapid and complete peptide cleavage. Pre-treated polymer aggregates were incubated at 0.02 mg/mL in cell cultures for 1 hr and 24 hr. Media was carefully removed, and cells were fixed with 2% paraformaldehyde in 0.1 M sodium cacodylate buffer at pH = 7.4 (SC buffer) overnight at 4 ℃.

Tissue staining and sectioning for In vivo TEM: Fixed tissue was washed three times with 0.1 M SC buffer for 5 min, the cells were post-fixed with 1% osmium tetroxide in 0.1 M SC buffer for 1 hour on ice. The cell pellets were washed 3 times with 0.1 M SC buffer for 5 min, followed by a quick rinse in distilled H2O. Cell pellets were stained with 2% uranyl acetate (UA) for 1 hour on ice, then dehydrated in a graded series of ethanol (50%, 70%, 90% and 2 times 100%) for 5-8 min, and dried in acetone at room temperature. The cell pellets were infiltrated by a 50:50 dry acetone/Durcupan solution for 1-2 hours on a shaker, followed by 100% Durcupan overnight and two further treatments of 100% durcupan the next day. Finally, cell pellets were embedded in durcupan and incubated at 60 o C for 36-48 hours. Ultrathin sections (around 50 nm) were cut for TEM.

2.3 Perspectives and Future Outlooks

2.3.1 Modifications for Translatability

Chapter 2 encompasses the use of enzyme-responsive nanoparticle systems for use in diseased tissue targeting. **Chapter 2.2**, in particular, details the first studies that utilize a responsive and structurally dynamic biomaterial that is IV deliverable and targets the infarct post-MI. This work presents a major advancement for traditionally structurally inert biomaterials, namely in overcoming disadvantages exhibited as lack of targeting and rapid tissue clearance (small moelcules and particle systems) or incompatibility with minimally invasive delivery strategies (macrmolecular networks). Next generation constructs of these structurally dynamic materials have three major components that must be addressed for feasible translation into the clinic: 1) scalability, 2) degradability, and 3) therapeutic drug loading. A method for increasing scale, whilst decreasing the number of synthetic steps and harsh solvents, is discussed in **Section 2.3.2**.

2.3.2 Investigation into Scalable Systems

The ability to form well-defined nanoscale polymeric assemblies has implications in an extensive array of applications, ranging from drug or gene delivery to catalysis.[58-60] However, in many cases the synthetic processes are limited in their ability to generate polymeric particles at high weight percentage solids. Classical amphiphilic polymer assembly via the solvent switch method is often conducted at less than 5 wt% solids, which renders scale-up difficult.[61-64] In contrast, polymerization-induced self-assembly (PISA)[65-79] can provide an efficient route to high concentrations of well-defined polymeric nanomaterials. The process works when an initial, soluble polymer is extended, with a second block growing and gradually becoming incompatible with the solvent, leading to the aggregation of polymer chains into defined structures. One of the attractive qualities of this approach is the ability to conduct these polymerization reactions at high weight percentage solids; in some cases, up to 50 wt% solids.[74,80]

Ring-opening metathesis polymerization (ROMP) allows for the polymerization of a wide range of functional monomers, and utilization in PISA should in turn yield functionalized, well- defined nanostructures in situ. ROMPISA was used to prepare enzyme-responsive nanoparticles in pure water, open-to-air, and in one step, which offers a great tool for robust scale-up. This approach is critical for robust scale-up, and for facile generation of structurally dynamic materials. Their responsiveness to the proteolytic enzyme thermolysin was demonstrated in **Figure 2.3.1**.

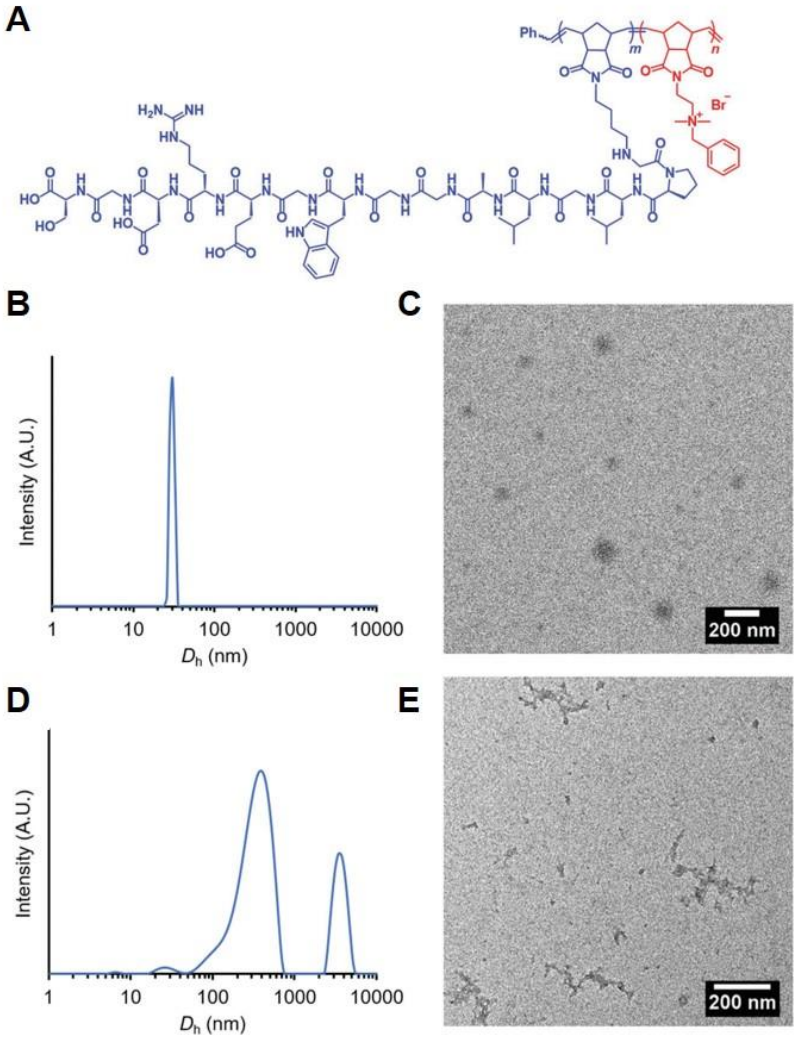


Figure 2.3.1. Enzyme-responsive nanoparticles via ROMPISA. A) Structure of the polymer peptide amphiphile synthesized via open-to-air ROMPISA. m=20, n=20. Blue and red coloring identify hydrophilic and hydrophobic units, respectively. (B-C) Micellar nanoparticles prior to enzyme activation possess (B) low dispersity hydrodynamic diameter, D_h, in the nanometer scale and (C) spherical morphology by TEM (D-E) Thermolysin-treated nanoparticles possess (D) high dispersity D_h in the sub-micron and micron scale and (E) aggregated morphologies.

The peptide stabilizer block was synthesized in situ via ROMP of the (L)-amino acid-based norbornene dicarboximide peptide substrate with sequence GPLGLAGGWGERDGS, in aqueous media open-to-air using a fully water-soluble quaternary amine-based Hoveyda-Grubbs type second generation initiator, as previously reported;[73] this peptide acts as a substrate for the proteolytic enzyme thermolysin (recognition sequence underlined). A diblock copolymer, consisting of the peptide and a quaternary amine-based phenyl norbornene dicarboximide, was synthesized with a target architecture of peptide$_{20}$-*b*-phenyl$_{20}$. Polymerization at 10 wt% solids provided a balance of high solid concentrations and good morphology control as micellar nanoparticles.

Nanoparticle were incubated with thermolysin and underwent a similar phase transition to large aggregate scaffolds, as seen with enzyme-responsive nanoparticles discussed throughout **Chapter 2**. This morphology switch is the result of a change in the packing parameter that governs block copolymer assemblies,[81] where the cleavage results in an increase in the packing parameter fraction and the polymers must reorganize into a new structure. The ability to prepare materials under these conditions greatly improves the practicality of the enzyme-responsive materials for scale-up and translation.

2.3.3 Development of Next Generation Biodegradable, Viscoelastic, and Drug-Loaded Constructs

Two methods in our lab are being explored for converting these platform materials into biodegradable systems. In ongoing studies, the nondegradable polynorbornene backbone, which has thus far been used throughout **Chapter 2**, is replaced with degrable polymer backbones such as poly(caprolactone) (PCL), which breaks down through simple ester hydrolysis. Another strategy that will be discussed throughout **Chapters 3 and 4** utilzes peptide-only constructs. In these systems, biodegradation products lead to biocompatible amino acid residues that are naturally found within the body. Furthermore, the materials discussed in these next two chapters utilize structurally dyanmic responsiveness to generate viscoelastic hydrogels, as opposed to unordered aggregates, that mimic the native extracellullar matrix (ECM). This is particularly important for biomaterials that are used in

tissue engineering to replace or supplement degrading ECM as a result of MI and extreme inflammation.

Finally, constructs that incorporate small molecule drugs within the platforms discussed in **Chapter 2** are currently being designed. One might envision any number of small molecule hydrophobic drugs that replace the inert phenyl group lining the hydrophobic block within these polymers. This has already been explored with cancer models in our lab.[59] Furthermore, replacement of the proteolytically discarded hydrophilic peptide with a therapeutic peptide sequence can provide a secondary means of treatment from a localized scaffold. As the purpose of this thesis focuses on designing platforms for introducing complex structural behavior into delivery vehicles composed of biosynthetic polymers and biopolymers, their therapeutic efficacy is not explored. Rather, discussions are in place to emphasize the modularity of all constructs, such that simple synthetic modification or formulaic incorporate of any number of therapeutics can be achieved.

2.4 Acknowledgements

Chapter 2.1 is adapted, in part, from material as it appears in Journal of the American Chemical Society 2013. Chien, Miao-Ping; Carlini, Andrea; Hu, Dehong; Barback, Christopher; Rush, Anthony, Hall, David; Orr, Galya; Gianneschi, Nathan. The dissertation author is second author of this paper.

Chapter 2.2 is adapted, in part, from material as it appears in Advanced Materials 2015. Carlini, Andrea; Nguyen, Mary; Chien, Miao-Ping; Sonnenberg, Sonya; Luo, Colin; Braden, Rebecca; Osborn, Kent; Li, Yiwen; Gianneschi, Nathan; Christman, Karen. The dissertation author is co-first author of this paper.

Chapter 2.3 is adapted, in part, from material as it appears in Macromolecular Rapid Communications 2018. Wright, Daniel; Thompson, Matthew; Touve, Mollie; Carlini, Andrea; Gianneschi, Nathan. The dissertation author is a contributing author of this paper.

2.5 References

1 Chien, M.-P., Carlini, A. S., Hu, D., Barback, C. V., Rush, A. M., Hall, D. J., Orr, G. & Gianneschi, N. C. Enzyme-Directed Assembly of Nanoparticles in Tumors Monitored by in Vivo Whole Animal Imaging and ex Vivo Super-Resolution Fluorescence Imaging. *Journal of the American Chemical Society* **135**, 18710-18713, doi:10.1021/ja408182p (2013).

2 Proetto, M. T., Anderton, C. R., Hu, D., Szymanski, C. J., Zhu, Z., Patterson, J. P., Kammeyer, J. K., Nilewski, L. G., Rush, A. M., Bell, N. C., Evans, J. E., Orr, G., Howell, S. B. & Gianneschi, N. C. Cellular Delivery of Nanoparticles Revealed with Combined Optical and Isotopic Nanoscopy. *ACS Nano* **10**, 4046-4054, doi:10.1021/acsnano.5b06477 (2016).

3 Galande, A. K., Hilderbrand, S. A., Weissleder, R. & Tung, C.-H. Enzyme-Targeted Fluorescent Imaging Probes on a Multiple Antigenic Peptide Core. *J. Med. Chem.* **49**, 4715-4720, doi:10.1021/jm051001a (2006).

4 Jiang, T., Olson, E. S., Nguyen, Q. T., Roy, M., Jennings, P. A. & Tsien, R. Y. Tumor imaging by means of proteolytic activation of cell-penetrating peptides. *Proc. Natl. Acad. Sci. U. S. A.* **101**, 17867-17872, doi:10.1073/pnas.0408191101 (2004).

5 Querol, M., Chen, J. W. & Bogdanov, J. A. A. A paramagnetic contrast agent with myeloperoxidase-sensing properties. *Org. Biomol. Chem.* **4**, 1887-1895, doi:10.1039/B601540A (2006).

6 Blum, A. P., Kammeyer, J. K., Yin, J., Crystal, D. T., Rush, A. M., Gilson, M. K. & Gianneschi, N. C. Peptides Displayed as High Density Brush Polymers Resist Proteolysis and Retain Bioactivity. *J. Am. Chem. Soc.* **136**, 15422-15437, doi:10.1021/ja5088216 (2014).

7 Mozaffarian, D., Benjamin, E. J., Go, A. S., Arnett, D. K., Blaha, M. J., Cushman, M., de Ferranti, S., Despres, J. P., Fullerton, H. J., Howard, V. J., Huffman, M. D., Judd, S. E., Kissela, B. M., Lackland, D. T., Lichtman, J. H., Lisabeth, L. D., Liu, S., Mackey, R. H., Matchar, D. B., McGuire, D. K., Mohler, E. R., 3rd, Moy, C. S., Muntner, P., Mussolino, M. E., Nasir, K., Neumar, R. W., Nichol, G., Palaniappan, L., Pandey, D. K., Reeves, M. J., Rodriguez, C. J., Sorlie, P. D., Stein, J., Towfighi, A., Turan, T. N., Virani, S. S., Willey, J. Z., Woo, D., Yeh, R. W., Turner, M. B., American Heart Association Statistics, C. & Stroke Statistics, S. Heart disease and stroke statistics-2015 update: a report from the american heart association. *Circulation* **131**, e29-e322, doi:10.1161/CIR.0000000000000152 (2015).

8 Frangogiannis, N. G., Smith, C. W. & Entman, M. L. The inflammatory response in myocardial infarction. *Cardiovascular research* **53**, 31-47, doi:Pii S0008-6363(01)00434-5

Doi 10.1016/S0008-6363(01)00434-5 (2002).

9 Dobaczewski, M., Gonzalez-Quesada, C. & Frangogiannis, N. G. The extracellular matrix as a modulator of the inflammatory and reparative response following myocardial infarction. *Journal of molecular and cellular cardiology* **48**, 504-511, doi:10.1016/j.yjmcc.2009.07.015 (2010).

10 Sun, Y. & Weber, K. T. Infarct scar: a dynamic tissue. *Cardiovascular research* **46**, 250-256, doi:Doi 10.1016/S0008-6363(00)00032-8 (2000).

11 Mann, D. L. Mechanisms and models in heart failure: A combinatorial approach. *Circulation* **100**, 999-1008 (1999).

12 Yang, F., Liu, Y. H., Yang, X. P., Xu, J., Kapke, A. & Carretero, O. A. Myocardial infarction and cardiac remodelling in mice. *Exp Physiol* **87**, 547-555 (2002).

13 Rane, A. A. & Christman, K. L. Biomaterials for the Treatment of Myocardial Infarction. *Journal of the American College of Cardiology* **58**, 2615-2629, doi:Doi 10.1016/J.Jacc.2011.11.001 (2011).

14 Johnson, T. D. & Christman, K. L. Injectable hydrogel therapies and their delivery strategies for treating myocardial infarction. *Expert Opinion on Drug Delivery* **10**, 59-72, doi:Doi 10.1517/17425247.2013.739156 (2013).

15 Ungerleider, J. L. & Christman, K. L. Concise review: injectable biomaterials for the treatment of myocardial infarction and peripheral artery disease: translational challenges and progress. *Stem Cells Transl Med* **3**, 1090-1099, doi:10.5966/sctm.2014-0049 (2014).

16 Horwitz, L. D., Kaufman, D., Keller, M. W. & Kong, Y. O. Time-Course of Coronary Endothelial Healing after Injury Due to Ischemia and Reperfusion. *Circulation* **90**, 2439-2447 (1994).

17 Longmire, M., Choyke, P. L. & Kobayashi, H. Clearance Properties of Nano-sized Particles and Molecules as Imaging Agents: Considerations and Caveats. *Nanomedicine (London, England)* **3**, 703-717, doi:10.2217/17435889.3.5.703 (2008).

18 Alexis, F., Pridgen, E., Molnar, L. K. & Farokhzad, O. C. Factors affecting the clearance and biodistribution of polymeric nanoparticles. *Mol. Pharmaceutics* **5**, 505-515 (2008).

19 Won, Y. W., McGinn, A. N., Lee, M., Bull, D. A. & Kim, S. W. Targeted Gene Delivery to Ischemic Myocardium by Homing Peptide-Guided Polymeric Carrier. *Molecular Pharmaceutics* **10**, 378-385, doi:10.1021/mp300500y (2013).

20 Dvir, T., Bauer, M., Schroeder, A., Tsui, J. H., Anderson, D. G., Langer, R., Liao, R. & Kohane, D. S. Nanoparticles targeting the infarcted heart. *Nano Lett.* **11**, 4411-4414 (2011).

21 Paulis, L. E., Geelen, T., Kuhlmann, M. T., Coolen, B. F., Schaefers, M., Nicolay, K. & Strijkers, G. J. Distribution of lipid-based nanoparticles to infarcted myocardium with potential application for MRI-monitored drug delivery. *Journal of Controlled Release* **162**, 276-285, doi:10.1016/j.jconrel.2012.06.035 (2012).

22 Suarez, S., Almutairi, A. & Christman, K. L. Micro- and nanoparticles for treating cardiovascular disease. *Biomaterials Science* **3**, 564-580, doi:10.1039/C4BM00441H (2015).

23 Chang, M. Y., Yang, Y. J., Chang, C. H., Tang, A. C. L., Liao, W. Y., Cheng, F. Y., Yeh, C. S., Lai, J. J., Stayton, P. S. & Hsieh, P. C. H. Functionalized nanoparticles provide early cardioprotection after acute myocardial infarction. *Journal of Controlled Release* **170**, 287-294, doi:Doi 10.1016/J.Jconrel.2013.04.022 (2013).

24 Liu, X., Chen, Y., Li, H., Huang, N., Jin, Q., Ren, K. & Ji, J. Enhanced Retention and Cellular Uptake of Nanoparticles in Tumors by Controlling Their Aggregation Behavior. *ACS Nano* **7**, 6244-6257, doi:10.1021/nn402201w (2013).

25 Chien, M.-P., Thompson, M. P., Barback, C. V., Ku, T.-H., Hall, D. J. & Gianneschi, N. C. Enzyme-directed assembly of a nanoparticle probe in tumor tissue. *Adv. Mater. Weinheim* **25**, 3599-3604 (2013).

26 Spinale, F. G. Myocardial Matrix Remodeling and the Matrix Metalloproteinases: Influence on Cardiac Form and Function. *Physiol. Rev.* **87**, 1285-1342 (2007).

27 Chien, M.-P., Carlini, A. S., Hu, D., Barback, C. V., Rush, A. M. & Hall, D. J. Enzyme-Directed Assembly of Nanoparticles in Tumors Monitored by In Vivo Whole Animal and Ex Vivo Super Resolution Fluorescence Imaging. *JACS* **135**, 18710–18713, doi:doi:10.1021/ja408182p (2013).

28 Galaup, A., Gomez, E., Souktani, R., Durand, M., Cazes, A., Monnot, C., Teillon, J., Le Jan, S., Bouleti, C., Briois, G., Philippe, J., Pons, S., Martin, V., Assaly, R., Bonnin, P., Ratajczak, P., Janin, A., Thurston, G., Valenzuela, D. M., Murphy, A. J., Yancopoulos, G. D., Tissier, R., Berdeaux, A., Ghaleh, B. & Germain, S. Protection Against Myocardial Infarction and No-Reflow Through Preservation of Vascular Integrity by Angiopoietin-Like 4. *Circulation* **125**, 140-U557, doi:Doi 10.1161/Circulationaha.111.049072 (2012).

29 Lukyanov, A. N., Hartner, W. C. & Torchilin, V. P. Increased accumulation of PEG-PE micelles in the area of experimental myocardial infarction in rabbits. *J Control Release* **94**, 187-193 (2004).

30 Geelen, T., Paulis, L. E., Coolen, B. F., Nicolay, K. & Strijkers, G. J. Passive targeting of lipid-based nanoparticles to mouse cardiac ischemia-reperfusion injury. *Contrast Media Mol Imaging* **8**, 117-126 (2013).

31 Scott, R. C., Rosano, J. M., Ivanov, Z., Wang, B., Chong, P. L.-G., Issekutz, A. C., Crabbe, D. L. & Kiani, M. F. Targeting VEGF-encapsulated immunoliposomes to MI heart improves vascularity and cardiac function. *Faseb Journal* **23**, 3361-3367, doi:10.1096/fj.08-127373 (2009).

32 Mizrahy, S., Goldsmith, M., Leviatan-Ben-Arye, S., Kisin-Finfer, E., Redy, O., Srinivasan, S., Shabat, D., Godin, B. & Peer, D. Tumor targeting profiling of hyaluronan-coated lipid based-nanoparticles. *Nanoscale* **6**, 3742-3752 (2014).

33 Zhang, C., Li, C., Liu, Y., Zhang, J., Bao, C., Liang, S., Wang, Q., Yang, Y., Fu, H., Wang, K. & Cui, D. Gold Nanoclusters-Based Nanoprobes for Simultaneous Fluorescence Imaging and Targeted Photodynamic Therapy with Superior Penetration and Retention Behavior in Tumors. *Adv. Funct. Mater.* **25**, 1314-1325 (2015).

34 Zhong, Y., Meng, F., Deng, C. & Zhong, Z. Ligand-Directed Active Tumor-Targeting Polymeric Nanoparticles for Cancer Chemotherapy. *Biomacromolecules* **15**, 1955-1969 (2014).

35 Nguyen, J., Sievers, R., Motion, J. P., Kivimae, S., Fang, Q. & Lee, R. J. Delivery of lipid micelles into infarcted myocardium using a lipid-linked matrix metalloproteinase targeting Peptide. *Mol Pharm* **12**, 1150-1157, doi:10.1021/mp500653y (2015).

36 Wang, Y., Lin, T., Zhang, W., Jiang, Y., Jin, H., He, H., Yang, V. C., Chen, Y. & Huang, Y. A Prodrug-type, MMP-2-targeting Nanoprobe for Tumor Detection and Imaging. *Theranostics* **5**, 787-795, doi:10.7150/thno.11139 (2015).

37 Scott, R. C., Wang, B., Nallamothu, R., Pattillo, C. B., Perez-Liz, G., Issekutz, A., Del Valle, L., Wood, G. C. & Kiani, M. F. Targeted delivery of antibody conjugated liposomal drug carriers to rat myocardial infarction. *Biotechnol. Bioeng.* **96**, 795-802 (2007).

38 Yan, P., Chen, K.-J., Wu, J., Sun, L., Sung, H.-W., Weisel, R. D., Xie, J. & Li, R.-K. The use of MMP2 antibody-conjugated cationic microbubble to target the ischemic myocardium, enhance Timp3 gene transfection and improve cardiac function. *Biomaterials* **35**, 1063-1073, doi:http://dx.doi.org/10.1016/j.biomaterials.2013.10.043 (2014).

39 Wang, Y., Zhou, K., Huang, G., Hensley, C., Huang, X., Ma, X., Zhao, T., Sumer, B. D., DeBerardinis, R. J. & Gao, J. A nanoparticle-based strategy for the imaging of a broad range of

tumours by nonlinear amplification of microenvironment signals. *Nat Mater* **13**, 204-212, doi:10.1038/nmat3819

http://www.nature.com/nmat/journal/v13/n2/abs/nmat3819.html#supplementary-information (2014).

40 Kim, J., Cao, L., Shvartsman, D., Silva, E. A. & Mooney, D. J. Targeted Delivery of Nanoparticles to Ischemic Muscle for Imaging and Therapeutic Angiogenesis. *Nano Lett.* **11**, 694-700 (2011).

41 Mizrahy, S., Goldsmith, M., Leviatan-Ben-Arye, S., Kisin-Finfer, E., Redy, O., Srinivasan, S., Shabat, D., Godin, B. & Peer, D. Tumor targeting profiling of hyaluronan-coated lipid based-nanoparticles. *Nanoscale* **6**, 3742-3752 (2014).

42 Arosio, P., Orsini, F., Piras, A. M., Sandreschi, S., Chiellini, F., Corti, M., Masa, M., Muckova, M., Schmidtova, L., Ravagli, C., Baldi, G., Nicolato, E., Conti, G., Marzola, P. & Lascialfari, A. MR imaging and targeting of human breast cancer cells with folate decorated nanoparticles. *RSC Advances* **5**, 39760-39770, doi:10.1039/C5RA04880J (2015).

43 Cho, W.-S., Cho, M., Jeong, J., Choi, M., Cho, H.-Y., Han, B. S., Kim, S. H., Kim, H. O., Lim, Y. T., Chung, B. H. & Jeong, J. Acute toxicity and pharmacokinetics of 13 nm-sized PEG-coated gold nanoparticles. *Toxicology and Applied Pharmacology* **236**, 16-24, doi:http://dx.doi.org/10.1016/j.taap.2008.12.023 (2009).

44 Johnston, H. J., Hutchison, G., Christensen, F. M., Peters, S., Hankin, S. & Stone, V. A review of the in vivo and in vitro toxicity of silver and gold particulates: Particle attributes and biological mechanisms responsible for the observed toxicity. *Critical Reviews in Toxicology* **40**, 328-346, doi:doi:10.3109/10408440903453074 (2010).

45 Lankveld, D. P. K., Oomen, A. G., Krystek, P., Neigh, A., Troost-de Jong, A., Noorlander, C. W., Van Eijkeren, J. C. H., Geertsma, R. E. & De Jong, W. H. The kinetics of the tissue distribution of silver nanoparticles of different sizes. *Biomaterials* **31**, 8350-8361, doi:Doi 10.1016/J.Biomaterials.2010.07.045 (2010).

46 Sonavane, G., Tomoda, K. & Makino, K. Biodistribution of colloidal gold nanoparticles after intravenous administration: Effect of particle size. *Colloids and Surfaces B-Biointerfaces* **66**, 274-280, doi:Doi 10.1016/J.Colsurfb.2008.07.004 (2008).

47 Fischer, H. C. & Chan, W. C. W. Nanotoxicity: the growing need for in vivo study. *Current Opinion in Biotechnology* **18**, 565-571, doi:http://dx.doi.org/10.1016/j.copbio.2007.11.008 (2007).

48 Gestwicki, J. E., Strong, L. E., Cairo, C. W., Boehm, F. J. & Kiessling, L. L. Cell Aggregation by Scaffolded Receptor Clusters. *Chem. Biol.* **9**, 163-169, doi:https://doi.org/10.1016/S1074-5521(02)00102-3 (2002).

49 Kolonko, E. M., Pontrello, J. K., Mangold, S. L. & Kiessling, L. L. General synthetic route to cell-permeable block copolymers via ROMP. *Journal of the American Chemical Society* **131**, 7327-7333, doi:10.1021/ja809284s (2009).

50 Ku, T.-H., Chien, M.-P., Thompson, M. P., Sinkovits, R. S., Olson, N. H., Baker, T. S. & Gianneschi, N. C. Controlling and Switching the Morphology of Micellar Nanoparticles with Enzymes. *J. Am. Chem. Soc.* **133**, 8392-8395, doi:10.1021/ja2004736 (2011).

51 Pontrello, J. K., Allen, M. J., Underbakke, E. S. & Kiessling, L. L. Solid-Phase Synthesis of Polymers Using the Ring-Opening Metathesis Polymerization. *Journal of the American Chemical Society* **127**, 14536-14537, doi:10.1021/ja053931p (2005).

52 Thompson, M. P., Randolph, L. M., James, C. R., Davalos, A. N., Hahn, M. E. & Gianneschi, N. C. Labelling Polymers and Micellar Nanoparticles via Initiation, Propagation and Termination with ROMP. *Polymer chemistry* **5**, 1954-1964, doi:10.1039/C3PY01338C (2014).

53 Sanford, M. S., Love, J. A. & Grubbs, R. H. A Versatile Precursor for the Synthesis of New Ruthenium Olefin Metathesis Catalysts. *Organometallics* **20**, 5314-5318, doi:10.1021/om010599r (2001).

54 Bielawski, C. W. & Grubbs, R. H. Living ring-opening metathesis polymerization. *Progress in Polymer Science* **32**, 1-29, doi:http://dx.doi.org/10.1016/j.progpolymsci.2006.08.006 (2007).

55 Seif-Naraghi, S. B., Horn, D., Schup-Magoffin, P. J. & Christman, K. L. Injectable extracellular matrix derived hydrogel provides a platform for enhanced retention and delivery of a heparin-binding growth factor. *Acta Biomaterialia* **8**, 3695-3703, doi:http://dx.doi.org/10.1016/j.actbio.2012.06.030 (2012).

56 Johnson, T. D., Braden, R. L. & Christman, K. L. Injectable ECM scaffolds for cardiac repair. *Methods in molecular biology* **1181**, 109-120, doi:10.1007/978-1-4939-1047-2_10 (2014).

57 Singelyn, J. M., Sundaramurthy, P., Johnson, T. D., Schup-Magoffin, P. J., Hu, D. P., Faulk, D. M., Wang, J., Mayle, K. M., Bartels, K., Salvatore, M., Kinsey, A. M., DeMaria, A. N., Dib, N. & Christman, K. L. Catheter-Deliverable Hydrogel Derived From Decellularized Ventricular Extracellular Matrix Increases Endogenous Cardiomyocytes and Preserves Cardiac Function Post-Myocardial Infarction. *J Am Coll Cardiol* **59**, 751-763, doi:Doi 10.1016/J.Jacc.2011.10.888 (2012).

58 Lu, A. & O'Reilly, R. K. Advances in nanoreactor technology using polymeric nanostructures. *Current Opinion in Biotechnology* **24**, 639-645, doi:https://doi.org/10.1016/j.copbio.2012.11.013 (2013).

59 Callmann, C. E., Barback, C. V., Thompson, M. P., Hall, D. J., Mattrey, R. F. & Gianneschi, N. C. Therapeutic Enzyme-Responsive Nanoparticles for Targeted Delivery and Accumulation in Tumors. *Advanced Materials* **27**, 4611-4615, doi:10.1002/adma.201501803 (2015).

60 Saraiva, C., Praça, C., Ferreira, R., Santos, T., Ferreira, L. & Bernardino, L. Nanoparticle-mediated brain drug delivery: Overcoming blood–brain barrier to treat neurodegenerative diseases. *Journal of Controlled Release* **235**, 34-47, doi:https://doi.org/10.1016/j.jconrel.2016.05.044 (2016).

61 Nicolai, T., Colombani, O. & Chassenieux, C. Dynamic polymeric micelles versus frozen nanoparticles formed by block copolymers. *Soft Matter* **6**, 3111-3118, doi:10.1039/B925666K (2010).

62 Jain, S. & Bates, F. S. Consequences of Nonergodicity in Aqueous Binary PEO−PB Micellar Dispersions. *Macromolecules* **37**, 1511-1523, doi:10.1021/ma035467j (2004).

63 Jain, S. & Bates, F. S. On the Origins of Morphological Complexity in Block Copolymer Surfactants. *Science* **300**, 460-464, doi:10.1126/science.1082193 (2003).

64 Hayward, R. C. & Pochan, D. J. Tailored Assemblies of Block Copolymers in Solution: It Is All about the Process. *Macromolecules* **43**, 3577-3584, doi:10.1021/ma9026806 (2010).

65 Jones, E. R., Semsarilar, M., Wyman, P., Boerakker, M. & Armes, S. P. Addition of water to an alcoholic RAFT PISA formulation leads to faster kinetics but limits the evolution of copolymer morphology. *Polymer Chemistry* **7**, 851-859, doi:10.1039/C5PY01795E (2016).

66 Karagoz, B., Esser, L., Duong, H. T., Basuki, J. S., Boyer, C. & Davis, T. P. Polymerization-Induced Self-Assembly (PISA) – control over the morphology of nanoparticles for drug delivery applications. *Polymer Chemistry* **5**, 350-355, doi:10.1039/C3PY01306E (2014).

67 Tan, J., Liu, D., Bai, Y., Huang, C., Li, X., He, J., Xu, Q., Zhang, X. & Zhang, L. An insight into aqueous photoinitiated polymerization-induced self-assembly (photo-PISA) for the preparation of diblock copolymer nano-objects. *Polymer Chemistry* **8**, 1315-1327, doi:10.1039/C6PY02135B (2017).

68 Tan, J., Sun, H., Yu, M., Sumerlin, B. S. & Zhang, L. Photo-PISA: Shedding Light on Polymerization-Induced Self-Assembly. *ACS Macro Letters* **4**, 1249-1253, doi:10.1021/acsmacrolett.5b00748 (2015).

69 Tan, J., Zhang, X., Liu, D., Bai, Y., Huang, C., Li, X. & Zhang, L. Facile Preparation of CO2-Responsive Polymer Nano-Objects via Aqueous Photoinitiated Polymerization-Induced Self-Assembly (Photo-PISA). *Macromolecular Rapid Communications* **38**, 1600508, doi:doi:10.1002/marc.201600508 (2017).

70 Wright, D. B., Touve, M. A., Adamiak, L. & Gianneschi, N. C. ROMPISA: Ring-Opening Metathesis Polymerization-Induced Self-Assembly. *ACS Macro Letters* **6**, 925-929, doi:10.1021/acsmacrolett.7b00408 (2017).

71 Yeow, J. & Boyer, C. Photoinitiated Polymerization‐Induced Self‐Assembly (Photo‐PISA): New Insights and Opportunities. *Advanced Science* **4**, 1700137, doi:10.1002/advs.201700137 (2017).

72 Touve, M. A., Figg, C. A., Wright, D. B., Park, C., Cantlon, J., Sumerlin, B. S. & Gianneschi, N. C. Polymerization-Induced Self-Assembly of Micelles Observed by Liquid Cell Transmission Electron Microscopy. *ACS Central Science* **4**, 543-547, doi:10.1021/acscentsci.8b00148 (2018).

73 Wright, D. B., Touve, M. A., Thompson, M. P. & Gianneschi, N. C. Aqueous-Phase Ring-Opening Metathesis Polymerization-Induced Self-Assembly. *ACS Macro Letters* **7**, 401-405, doi:10.1021/acsmacrolett.8b00091 (2018).

74 Canning, S. L., Smith, G. N. & Armes, S. P. A Critical Appraisal of RAFT-Mediated Polymerization-Induced Self-Assembly. *Macromolecules* **49**, 1985-2001, doi:10.1021/acs.macromol.5b02602 (2016).

75 Fielding, L. A., Derry, M. J., Ladmiral, V., Rosselgong, J., Rodrigues, A. M., Ratcliffe, L. P. D., Sugihara, S. & Armes, S. P. RAFT dispersion polymerization in non-polar solvents: facile production of block copolymer spheres, worms and vesicles in n-alkanes. *Chemical Science* **4**, 2081-2087, doi:10.1039/C3SC50305D (2013).

76 Warren, N. J., Mykhaylyk, O. O., Mahmood, D., Ryan, A. J. & Armes, S. P. RAFT Aqueous Dispersion Polymerization Yields Poly(ethylene glycol)-Based Diblock Copolymer Nano-Objects with Predictable Single Phase Morphologies. *Journal of the American Chemical Society* **136**, 1023-1033, doi:10.1021/ja410593n (2014).

77 Warren, N. J., Mykhaylyk, O. O., Ryan, A. J., Williams, M., Doussineau, T., Dugourd, P., Antoine, R., Portale, G. & Armes, S. P. Testing the Vesicular Morphology to Destruction: Birth and Death of Diblock Copolymer Vesicles Prepared via Polymerization-Induced Self-Assembly. *Journal of the American Chemical Society* **137**, 1929-1937, doi:10.1021/ja511423m (2015).

78 Williams, M., Penfold, N. J. W., Lovett, J. R., Warren, N. J., Douglas, C. W. I., Doroshenko, N., Verstraete, P., Smets, J. & Armes, S. P. Bespoke cationic nano-objects via RAFT aqueous dispersion polymerisation. *Polymer Chemistry* **7**, 3864-3873, doi:10.1039/C6PY00696E (2016).

79 Williams, M., Penfold, N. J. W. & Armes, S. P. Cationic and reactive primary amine-stabilised nanoparticles via RAFT aqueous dispersion polymerisation. *Polymer Chemistry* **7**, 384-393, doi:10.1039/C5PY01577D (2016).

80 Figg, C. A., Carmean, R. N., Bentz, K. C., Mukherjee, S., Savin, D. A. & Sumerlin, B. S. Tuning Hydrophobicity To Program Block Copolymer Assemblies from the Inside Out. *Macromolecules* **50**, 935-943, doi:10.1021/acs.macromol.6b02754 (2017).

81 Mai, Y. & Eisenberg, A. Self-assembly of block copolymers. *Chemical Society Reviews* **41**, 5969-5985, doi:10.1039/C2CS35115C (2012).

Chapter 3

Sterically Constrained Enzyme-Responsive Peptide Progelators

3.1 Cyclic Peptides for Minimally Invasive Delivery Post-MI

3.1.1 Introduction

Myocardial infarction (MI) accounts for 46% of all deaths attributed to cardiovascular disease.[1] Within the first few days post-MI, an inflammatory response causes cardiomyocyte death and degradation of the native extracellular matrix (ECM) by secreted matrix metalloproteinases (MMPs).[2] This in turn can lead to aneurysmal thinning and negative left ventricular (LV) remodeling within days to weeks. Left untreated, heart failure results as one of the leading causes of death in the western world.

Injectable hydrogel-based scaffolds have gained attention as a therapeutic approach to prevent negative LV remodeling by utilizing materials to stimulate cardiac repair. Materials for this purpose have included myocardial ECM,[3] alginate,[4] and hyaluronic acid hydrogels,[5] or employing biomaterials as therapeutic delivery scaffolds such as naturally derived polymeric hydrogels (e.g.

collagen,[6] fibrin,[7] heparin,[8] and gelatin[9]), synthetic polymeric hydrogels (e.g. PNIPAAm,[10] ureido-pyrimidinone-modified PEG,[11] and chitosan[12]) and microparticles (e.g. PLGA[13] and dextran[14]). Despite many successful preclinical studies, wide spread translation and initiation of clinical trials has been slow, with current studies limited to a myocardial ECM hydrogel (clinicaltrials.gov identifier NCT02305602) and alginate (NCT3082508 and NCT01311791). One reason for this lack of translation is that the majority of these hydrogels are not candidates for minimally invasive catheter delivery because of excess material viscosity, their quick gelling nature that can lead to catheter clogging, and concerns regarding hemocompatibility since materials can leak into the blood stream upon injection into a beating heart.[15-17] One versatile class of materials that has been successfully tested in several preclinical MI models using surgical epicardial injections is self-assembling peptides (SAPs).[18-21] SAP hydrogels are attractive as they are: (1) mimetic of resemble native ECM, (2) require no additive reagents to induce gelation, (3) are biodegradable, (4) are biocompatible, (5) have pore sizes (~5-200 nm) conducive to promote endothelial cell adhesion and capillary formation, (6) allow rapid cellular migration because of their flexibility, (7) are rehealable, (8) do not suffer from batch-to-batch chemical variability, and (9) are amenable to sequence modification.[22,23] However, SAPs have not demonstrated amenability to cardiac injection catheter delivery.

Inspired by recent efforts with enzyme-responsive peptides[24-26] and a study by Nilsson and coworkers utilizing reductively triggered cyclic peptides as progelators,[27] we focused on developing a cyclic, enzyme triggered, responsive peptide platform that would enable minimally invasive delivery of SAPs to the heart. Previously, we demonstrated that soluble peptide-polymer based nanoparticles can aggregate into macromolecular scaffolds in diseased tissue through the action of endogenously expressed inflammatory-related enzymes, matrix metalloproteinases (MMPs), providing a viable method for targeted accumulation,[28] prolonged tissue retention,[29] and therapeutic delivery.[30] However, these materials employed a non-biodegradable functionalized polynorbornene backbone and did not possess viscoelastic properties. In this work, we engineered cyclic peptide progelators that flow freely in solution and resists assembly into hydrogel until acted upon by an endogenous

signal (**Figure 3.1.1**), namely MMP-2/9[2,31] and elastase,[32,33] which are expressed at the site of MI during the acute inflammatory (days) and fibrotic (weeks) phases. These enzymes play key roles in the healing process through degradation of extracellular matrix (ECM) and fibrinogen.[2]

SAP sequences were prepared as water soluble, dispersed cyclic progelators (green rings, **Figure 3.1.1a**) that contain a substrate recognition sequence for MMP-2/9 and elastase (red). Two different cyclic progelators were prepared; one without a fluorescent label and one with a rhodamine label (pink ellipse) located adjacent to the substrate sequence. We show that enzymatic cleavage of these sterically constrained cyclic progelators results in linearization to generate SAPs (**Figure 3.1.1b**) which subsequently assemble into rehealable viscoelastic hydrogels (**Figure 3.1.1c**). Their low viscosity, ability to gel at the site of MI, and hemocompatible nature of the concentrated progelator are demonstrated. In addition, we show that the progelators are amenable to minimally invasive catheter injection using an *in vitro* model system. This opens up the possibility of delivering SAPs to the heart via catheter.

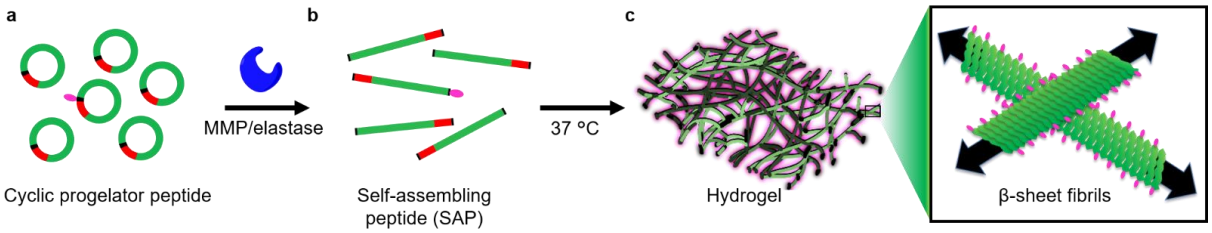


Figure 3.1.1. Design of cyclic, enzyme-responsive progelator peptides for activatable gelation. a, cyclic progelator peptides, containing gelling sequence (green), MMP/elastase enzyme-cleavage recognition sequence (red), and disulfide bridge (black) resist assembly due to conformational constraint. Rhodamine labeled (pink ellipse) SAPs were employed for *in vivo* studies as a 5 mol% additive to provide a means for imaging the hydrogels in *ex vivo* microscopy analyses. **b**, Enzymatic cleavage results in linearization into SAPs. **c**, SAPs assemble into viscoelastic hydrogels composed of β-sheets fibrils.

3.1.2 Results

Design of stimuli-responsive SAPs for activatable gelation *in vivo*. SAPs undergo spontaneous assembly through electrostatic and amphiphilic interactions into ordered nanostructures.[34,35] In many instances, variation of sequence and charge distribution in SAPs can influence properties such as secondary structure,[36] fiber diameter,[37] and bulk viscoelasticity[38]. In our

design, we began with a gellable core based on a SAP consisting of the repeat sequence $(KLDL)_3$ (referred to in this study as KLDL), which has been studied as a non-immunogenic, non-hemolytic, and antimicrobial scaffold for tissue engineering applications.[39-41] This peptide self-assembles spontaneously into β-sheets through cationic and anionic crosslinking of the Lys and Asp residues and hydrophobic interactions along the Leu residues. As a proof-of-concept for sequence control, we chose to employ an analogue of KLDL hypothesized to alter secondary structural assembly and achieve modified gel properties. For this purpose, we designed $(KFDF)_3$ (referred to as KFDF), in which the incorporation of aromatic Phe residues introduce π-π interactions. From the KLDL and KFDF SAPs, we engineered a small library of functionalized SAPs and progelators for studying assembly within a biological relevant environment (**Figure 3.1.2, Figure 3.1.3,** and **Figure 3.1.4**).

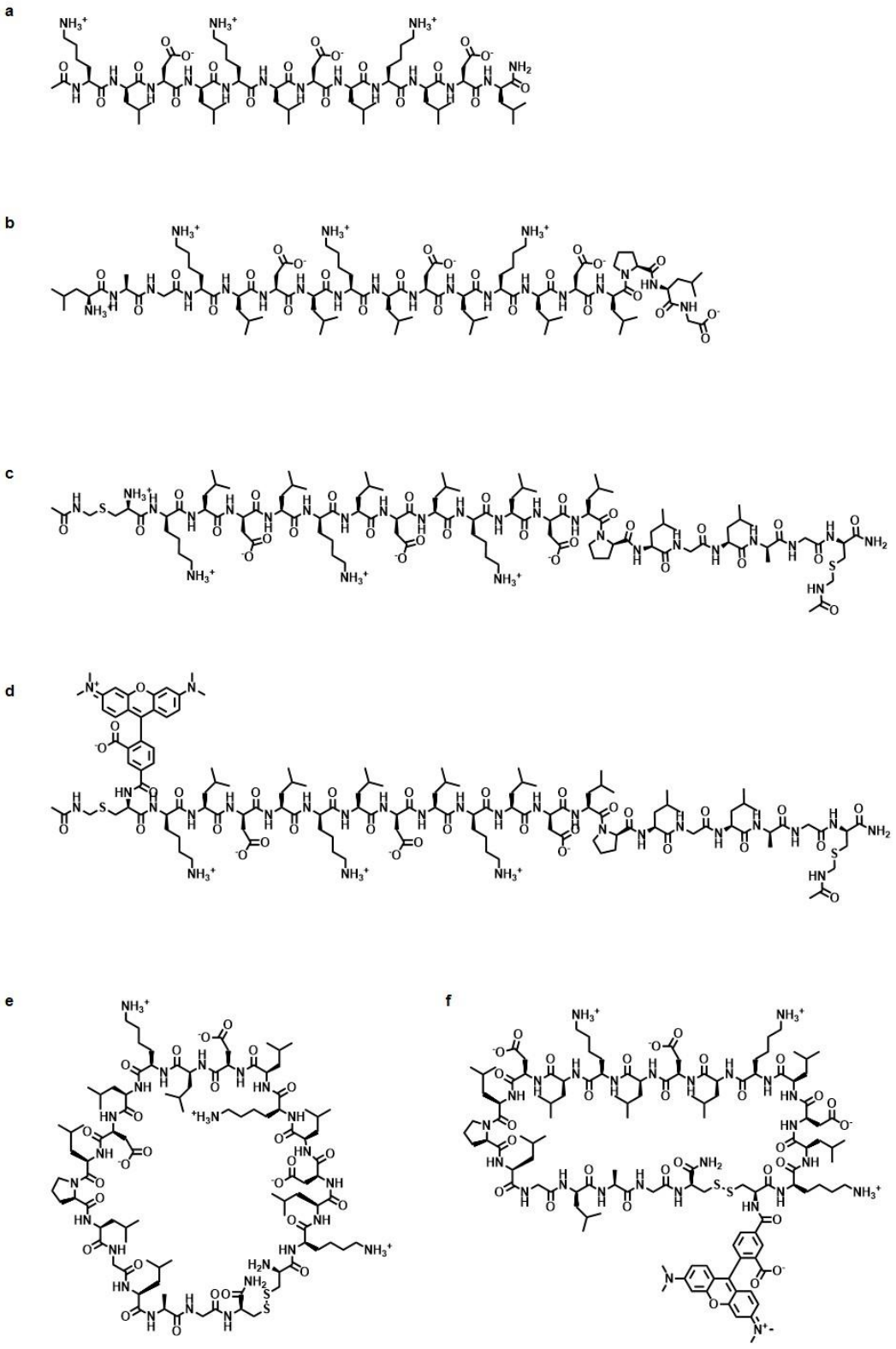


Figure 3.1.2. Chemical structures of KLDL peptides synthesized. a-f, KLDL (**a**), $KLDL_{Control}$ (**b**), $KLDL_{Linear}$ (**c**), Rho-$KLDL_{Linear}$ (**d**), $KLDL_{Cyclic}$ (**e**), and Rho-$KLDL_{Cyclic}$ (**f**).

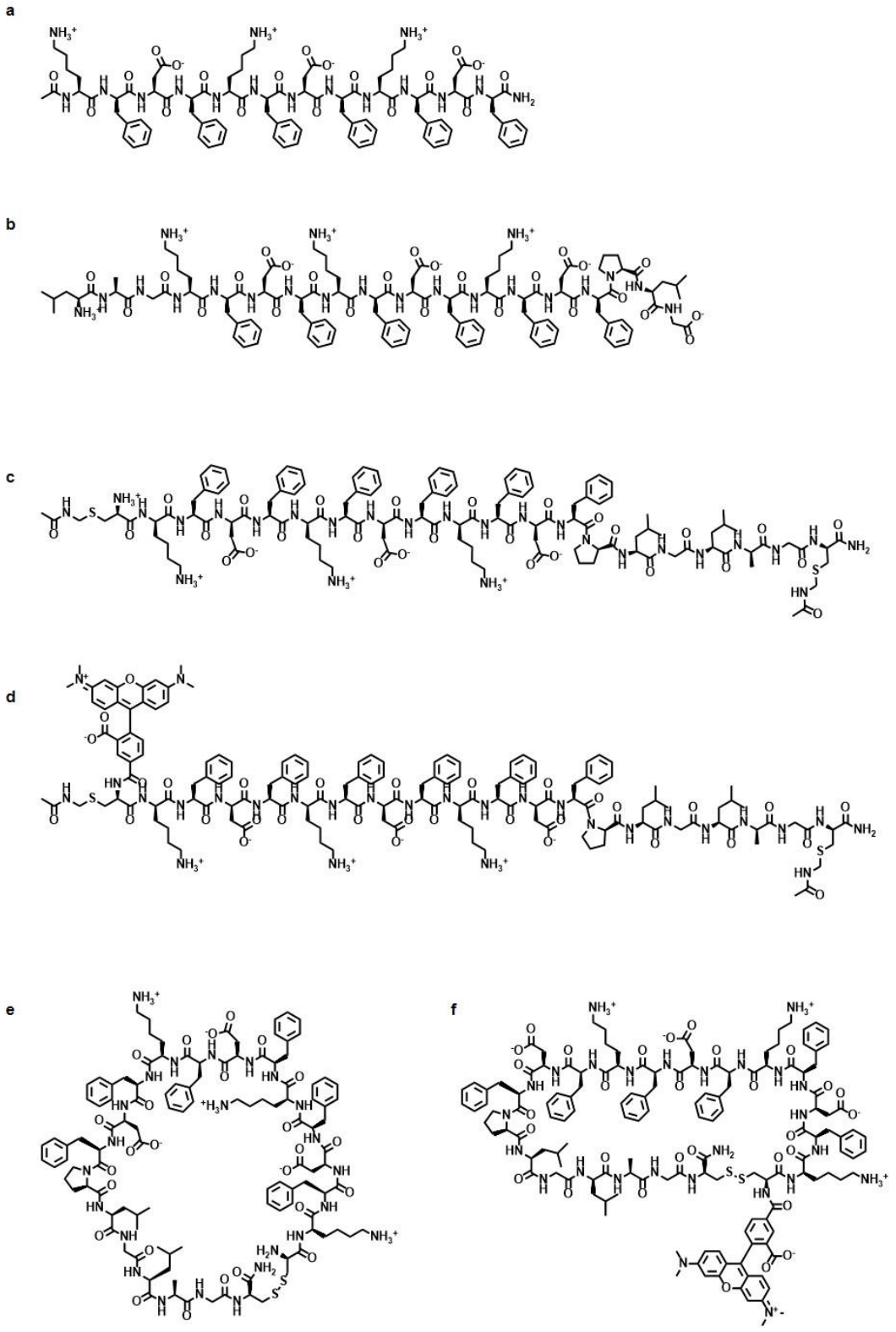
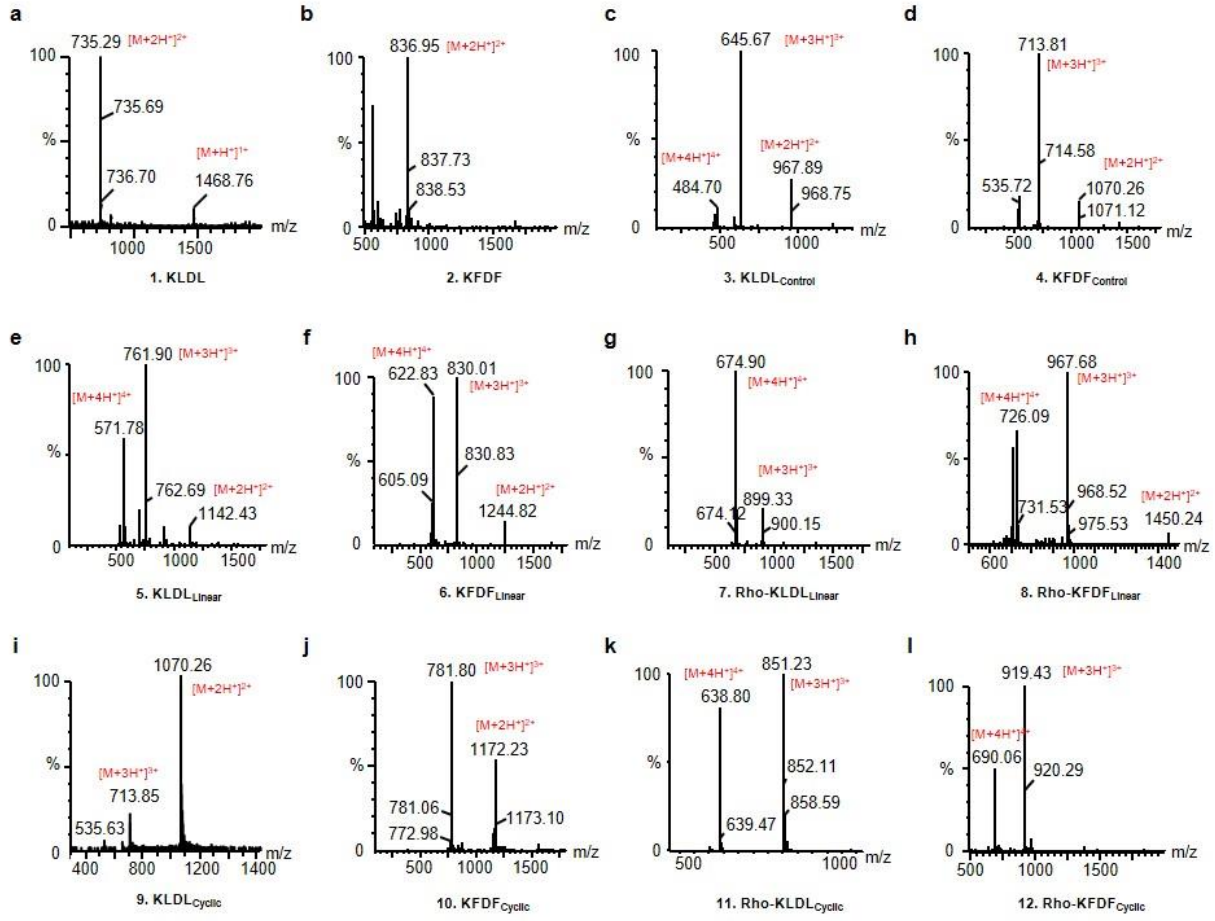


Figure 3.1.3. Chemical structures of KFDF peptides synthesized. a-f, KFDF (**a**), $KFDF_{Control}$ (**b**), $KFDF_{Linear}$ (**c**), Rho-$KFDF_{Linear}$ (**d**), $KFDF_{Cyclic}$ (**e**), and Rho-$KFDF_{Cyclic}$ (**f**).



m

	Peptide Name	Peptide Sequence	Expected MW (pH < 3)	Observed m/z
1	KLDL	Ac-KLDLKLDLKLDL-conh$_2$	1470.84 g/mol	735.29 m/z $[M+2H^+]^{2+}$
2	KFDF	Ac-KFDFKFDFKFDF-conh$_2$	1674.94 g/mol	836.95 m/z $[M+2H^+]^{2+}$
3	$KLDL_{Control}$	H_2n-LAGKLDLKLDLKLDLPLG-cooh	1938.4064 g/mol	645.67 m/z $[M+3H^+]^{3+}$
4	$KFDF_{Control}$	h$_2$n-LAGKFDFKFDFKFDFPLG-cooh	2143.52 g/mol	713.81 m/z $[M+3H^+]^{3+}$
5	$KLDL_{Linear}$	h$_2$n -C(acm)LAGKLDLKLDLKLDLPLGC(acm)-conh$_2$	2286.87 g/mol	761.90 m/z $[M+3H^+]^{3+}$
6	$KFDF_{Linear}$	h$_2$n -C(acm)LAGKFDFKFDFKFDFPLGC(acm)-conh$_2$	2490.97 g/mol	830.01 m/z $[M+3H^+]^{3+}$
7	Rho-$KLDL_{Linear}$	Rho-C(acm)LAGKLDLKLDLKLDLPLGC(acm)-conh$_2$	2698.30 g/mol	674.90 m/z $[M+4H^+]^{4+}$
8	Rho-$KFDF_{Linear}$	Rho-C(acm)LAGKFDFKFDFKFDFPLGC(acm)-conh$_2$	2902.41 g/mol	967.68 m/z $[M+3H^+]^{3+}$
9	$KLDL_{Cyclic}$	h$_2$n-*CKLDLKLDLKLDLPLGLAGC*-conh$_2$	2141.68 g/mol	713.85 m/z $[M+3H^+]^{3+}$
10	$KFDF_{Cyclic}$	*CKFDFKFDFKFDFPLGLAGC*-conh$_2$	2345.79 g/mol	781.80 m/z $[M+3H^+]^{3+}$
11	Rho-$KLDL_{Cyclic}$	Rho-*CKLDLKLDLKLDLDFPLGLAGC*-conh$_2$	2555.14 g/mol	851.23 m/z $[M+3H^+]^{3+}$
12	Rho-$KFDF_{Cyclic}$	Rho-*CKFDFKFDFKFDFPLGLAGC*-conh$_2$	2759.24 g/mol	919.43 m/z $[M+3H^+]^{3+}$

Figure 3.1.4. ESI mass spectra and sequences of peptides synthesized. a-l, Spectra with accompanied m/z species identifications (shown in red) for unmodified SAPs, functionalized SAPs, and progelators in study. (**a**) KLDL, (**b**) KFDF, (**c**) $KLDL_{Control}$, (**d**) $KFDF_{Control}$, (**e**) $KLDL_{Linear}$, (**f**) $KFDF_{Linear}$, (**g**) Rho-$KLDL_{Linear}$, (**h**) Rho-$KFDF_{Linear}$, (**i**) $KLDL_{Cyclic}$, (**j**) $KFDF_{Cyclic}$, (**k**) Rho-$KLDL_{Cyclic}$, and (**l**) Rho-$KFDF_{Cyclic}$. **m**, Corresponding sequences with expected molecular weight (MW) and observed m/z values. * indicates a disulfide bond between neighboring cysteines.

SAPs and progelators synthesized in this study are summaried in **Figure 3.1.5.** We first evaluated whether the addition of non-gelling amino acids from the MMP-2/9 recognition sequence (PLG|LAG) and cysteine residues used for macrocyclization into the SAP sequences would interfere with their ability to self-assemble (**Figure 3.1.5a**). Predictive computational modeling with open-access FibPredictor software[42] provided initial evidence that functionalized $KLDL_{Linear}$ and $KFDF_{Linear}$ SAPs would experience a switch in self-assembly orientation from antiparallel to parallel β-sheets. Regardless, such a design would retain the capacity to form fibrillar bilayers (**Figure 3.1.5b-c** and see **Experimental Detail**). Notably in $KFDF_{Linear}$, Phe residues on each strand are sandwiched with analogous residues on neighboring strands, which facilitate π-π stacking and stronger hydrophobic interactions than those of Leu-containing peptides.

Indeed, with the design validated *in silico*, synthetic preparation of the KFDF SAP resulted in materials with increased mechanical strength without sacrificing re-healing capacity or fibrous morphology, inherent to the known KLDL system[43] (**Figure 3.1.6**).

a

KLDL SAPs and Progelators		KFDF SAPs and Progelators		Diagrammatical Representation
Name	Sequence	Name	Sequence	
KLDL	Ac-KLDLKLDLKLDL-$CONH_2$	KFDF	Ac-KFDFKFDFKFDF-$CONH_2$	
$KLDL_{Linear}$	NH_2-C(acm)KLDLKLDLKLDLPLGLAGC(acm)-$CONH_2$	$KFDF_{Linear}$	NH_2-C(acm)KFDFKFDFKFDFPLGLAGC(acm)-$CONH_2$	
Rho-$KLDL_{Linear}$	Rho-C(acm)KLDLKLDLKLDLPLGLAGC(acm)-$CONH_2$	Rho-$KFDF_{Linear}$	Rho-C(acm)KFDFKFDFKFDFPLGLAGC(acm)-$CONH_2$	
$KLDL_{Cyclic}$	NH_2-CKLDLKLDLKLDLPLGLAGC-$CONH_2$ (S-S)	$KFDF_{Cyclic}$	NH_2-CKFDFKFDFKFDFPLGLAGC-$CONH_2$ (S-S)	
Rho-$KLDL_{Cyclic}$	Rho-CKLDLKLDLKLDLPLGLAGC-$CONH_2$ (S-S)	Rho-$KFDF_{Cyclic}$	Rho-CKFDFKFDFKFDFPLGLAGC-$CONH_2$ (S-S)	

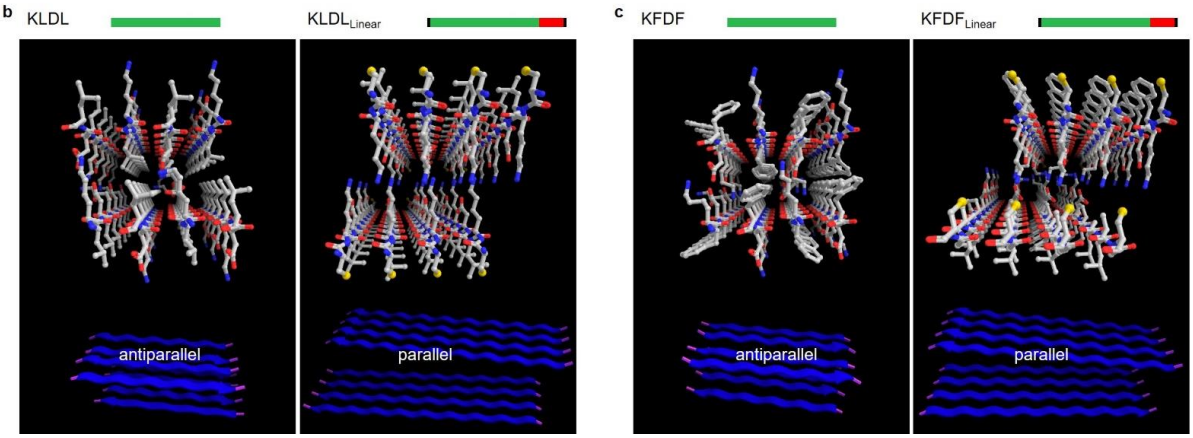


Figure 3.1.5. Sequences and design of SAPs and cyclic, enzyme-responsive progelators. **a**, Table of SAPs and progelators based on the $(KLDL)_3$ and $(KFDF)_3$ amino acid gelling sequence with corresponding diagrammatical representations. Sequences are shown for the base, unmodified SAPs (KLDL and KFDF) and modified SAPs ($KLDL_{Linear}$ and $KFDF_{Linear}$) primed for cyclization but lacking fluorescent labels, together with the corresponding cyclized versions (progelators, $KLDL_{Cyclic}$ and $KFDF_{Cyclic}$). In addition, rhodamine labeled modified SAPs (Rho-$KLDL_{Linear}$ and Rho-$KFDF_{Linear}$) are shown, together with their corresponding labeled cyclized progelators (Rho-$KLDL_{Cyclic}$ and Rho-$KFDF_{Cyclic}$). "acm" denotes the acetamidomethyl protecting group on Cysteine residues. "Rho" designates the 5(6)-carboxytetramethyl rhodamine label. **b-c**, Modeling predicts β-sheet re-orientation, rather than self-assembly disruption, following significant SAP functionalization. **b**, Predicted structures and ribbon diagrams (bottom) of KLDL and $KLDL_{Linear}$ SAPs from FibPredictor simulations revealing antiparallel and parallel β-sheet orientations, respectively. **c**, Predicted structures and ribbon diagrams (bottom) of KFDF and $KFDF_{Linear}$ SAPs from FibPredictor simulations revealing antiparallel and parallel β-sheet orientations, respectively (see **Experimental Details**). Ball & stick models of interacting peptides are displayed with carbon, oxygen, and nitrogen atoms in white, red, and blue, respectively.

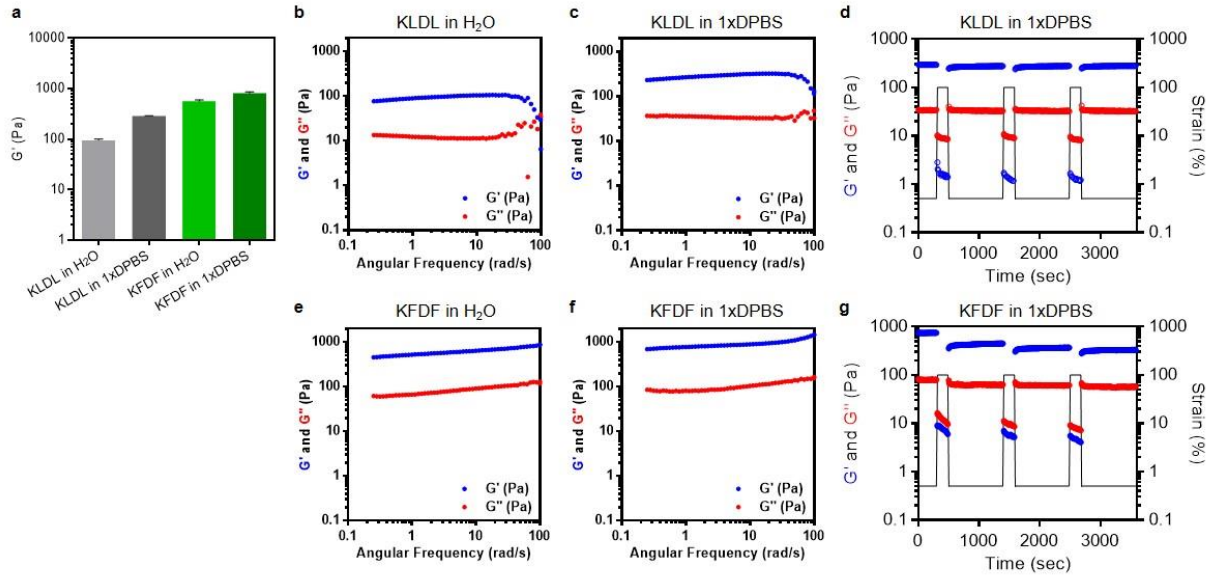


Figure 3.1.6. Rheological properties of KLDL and KFDF. Unmodified linear SAP compared with respect to molar concentration (10 mM) present as porous networks hydrogel networks with rehealable properties. Stiffer gels obtained when Phe substituted for Leu in the KFDF SAP. **a**, Storage moduli (G') for KLDL and KFDF SAPs in H_2O or 1xDPBS show increasing stiffness with increasing saline content and peptide hydrophobicity. Angular frequency 2.5 rad/s, 0.5% strain. **b-c**, Frequency sweeps (100-0.25 rad/s, 0.5% strain) of KLDL in H_2O and 1xDPBS. **d**, Step-strain oscillation analysis of KLDL in 1xDPBS. **e-f**, Frequency sweeps (100-0.25 rad/s, 0.5% strain) of KFDF in H_2O and 1xDPBS. **g**, Step-strain oscillation analysis of KFDF in 1xDPBS. KLDL and KFDF SAPs show rapid and repeat healing capacity of hydrogels (G'>G'') following complete network disruption (G''>G') at high strains. Viscoelastic storage (G') and loss (G'') moduli are plotted as a function of time with step cycles at 100 % destructive strain (t=3 min) followed by 0.5% recovery strain (t=15 min) to monitor healing. Hydrogels prepared at 10 mM in 1x DPBS. Angular frequency 2.5 rad/s.

In practice, modified SAPs capable of going on to form the cyclic progelators, namely $KLDL_{Linear}$ and $KFDF_{Linear}$, retained the capacity to self-assemble (both experimentally and predicted) despite modest changes in secondary structure and viscoelastic properties (**Figure 3.1.7**). Experimental CD demonstrated that $KLDL_{Linear}$ and $KFDF_{Linear}$ retained β-sheet conformations (n→π* transition at 215 nm). However, the positive peak at ~200 nm (π→π* transition) found in KLDL and KFDF is blue-shifted to ~195 nm, indicative of a parallel to antiparallel orientation switch (**Figure 3.1.7a-b**).[44] Additionally, $KFDF_{Linear}$ reveals a new high energy minimum at 203 nm corresponding to π-π* effects resulting from aromatic π-π interactions in the hydrophobic interior of the bilayer structure (**Figure 3.1.7b**).[27] This transition is predicted in theoretical spectra from DichroCalc[45] for $KFDF_{Linear}$ (202 nm) and not for $KLDL_{Linear}$, which contains no aromatic residues. (**Figure 3.1.7c-d**). Regardless of altered secondary structure, fiber morphology and bulk viscoelastic properties exhibited minimal

changes to that of unmodified KLDL and KFDF (**Figure 3.1.7e-h**). Slight drops in storage moduli for $KLDL_{Linear}$ and $KFDF_{Linear}$ are attributed to the decreasing molar concentration of amino acids (hydrogels prepared with respect to weight at 15 mg/mL) contributing to β-sheet formation.

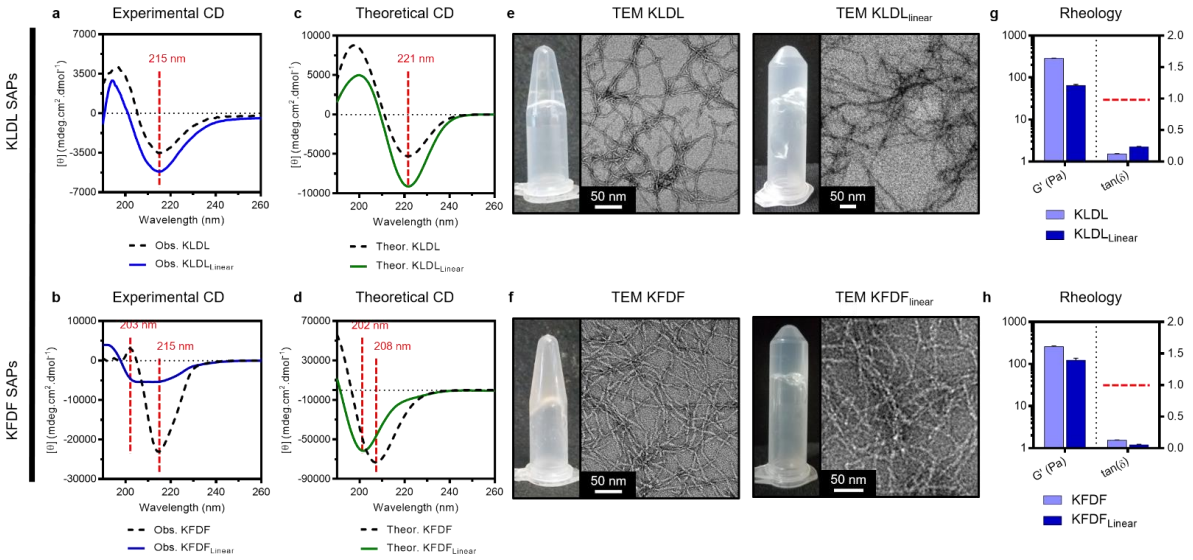


Figure 3.1.7. Impact of SAP functionalization on assembly properties. **a**, Experimental circular dichroism (CD) spectra of KLDL and $KLDL_{Linear}$ SAPs, with labeled minimum at 215 nm (n→π*). **b**, Experimental circular dichroism (CD) spectra of KFDF and $KFDF_{Linear}$ SAPs, with labeled minima at 215 nm (n→π*) and 203 nm (π→π*). **c**, Theoretical CD spectra of KLDL and $KLDL_{Linear}$ SAPs from DichroCalc simulations using FibPredictor models. **d**, Theoretical CD spectra of KFDF and $KFDF_{Linear}$ SAPs from DichroCalc simulations using FibPredictor models (**Table 3.1.** and **Table 3.1.2**). CD spectra minima denoted with dashed lines. **e**, Assembled hydrogel photographs and corresponding TEM images of the KLDL (left) and $KLDL_{Linear}$ (right) SAPs. **f**, Assembled hydrogel photographs and corresponding TEM images of the KFDF (left) and $KFDF_{Linear}$ (right) SAPs. **g**, Viscoelastic measurements of storage moduli, G' (Pa), and damping factor, tan δ, for KLDL and $KLDL_{Linear}$. **h**, Viscoelastic measurements of storage moduli, G' (Pa), and damping factor, tanδ, for KFDF and $KFDF_{Linear}$. Gel capacity is defined as tanδ < 1 (dashed line). CD measurements performed at 500 μM SAP in 10 mM Tris buffer, pH 7.4. (n=3 repeats) SAPs for TEM and rheology prepared at 100 μM and 15 mg/mL in 1xDPBS (pH 7.4), respectively. Rheological measurements reported for angular frequency of 2.5 rads/s. (n=3 repeats) Values are mean ± SEM.

Regardless, no significant disruptive effects to gelling capacity, as defined by tanδ < 1 (**Figure 3.1.7g-h**) or strain tolerance (**Figure 3.1.8**) were observed through the introduction of over 66% more amino acid residues to the SAP sequence. This exemplifies the robustness of these linear SAPs to sequence modification and potential capacity to tolerate functional moieties such as fluorescent tags or small molecule drugs.

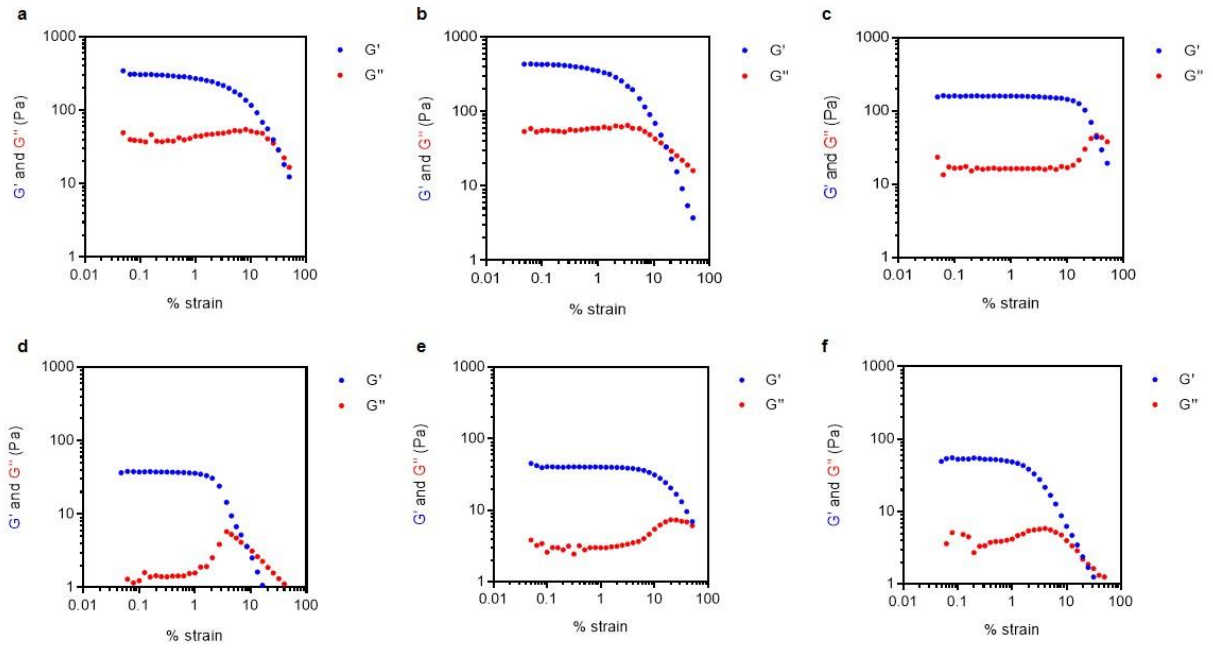


Figure 3.1.8. Strain sweeps of SAPs. a-e, Storage (G') and loss (G'') moduli were measured as a function of strain (0.5 – 50%) to identify the linear viscoelastic region (LVR) and appropriate rheological measurement conditions for all SAPs. Corresponding plots of (**a**) KLDL, (**b**) KFDF, (**c**) $KFDF_{Control}$, (**d**) $KFDF_{Linear}$, (**e**) $KFDF_{Cyclic}$ + thermolysin, and (**f**) $KLDL_{Cyclic}$ + thermolysin. A strain of 0.5% lies within the LVR for these strain sweeps and was chosen for all rheological measurements in this study. SAPs were prepared at 15 mg/mL in 1x DPBS. Angular frequency 2.5 rad/s.

Cyclization and progelator formulation. SAP steric constraint provides a simple and versatile engineering approach for preventing network assembly in a biological environment (**Figure 3.1.9**). Functionalized SAP analogues containing an Fmoc protecting group or rhodamine dye on the N-terminus were cyclized through oxidation of terminal cysteine residues to generate unlabeled and labeled progelators (**Figure 3.1.9a-e**). Fmoc was temporarily used for unlabeled progelators to improve peak separation during purification and to monitor cyclization by HPLC and ESI (**Figure 3.1.9b-e**). Dilute solution phase macrocyclization was complete within 125 min by LCMS (**Figure 3.1.9f,h**).

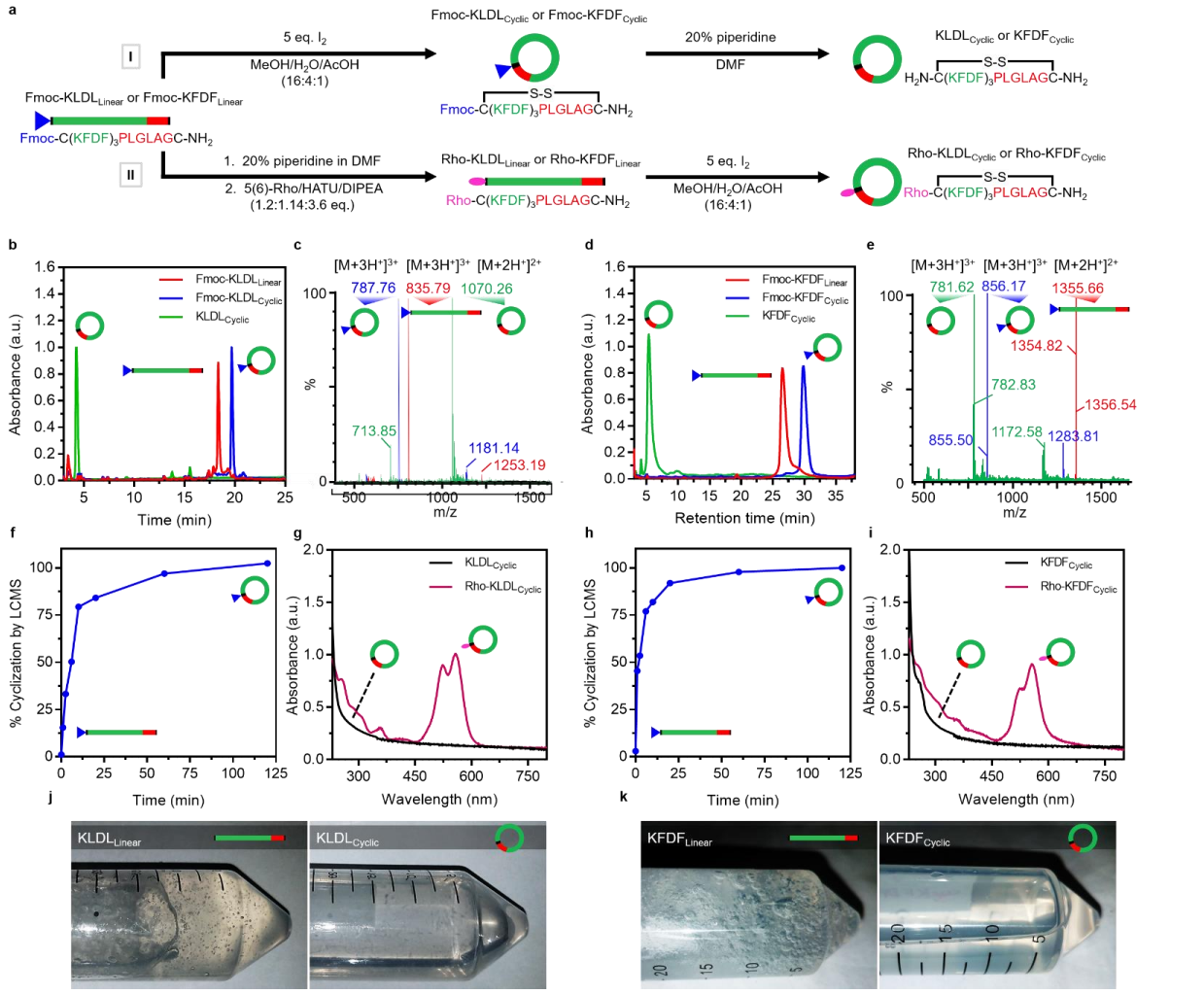


Figure 3.1.9. Facile synthesis of sterically constrained and labeled cyclic progelators. **a**, Synthetic scheme for unlabeled (route I) and labeled (route II) $KLDL_{Cyclic}$ and $KFDF_{Cyclic}$ progelators. All SAPs were cyclized under dilute conditions (500 µM) with 5 eq I_2 in a mixture of AcOH/MeOH/H_2O to create a soluble progelator. Route I uses N-terminal Fmoc-protected SAPs to improve material separation during chromatographic purification. Fmoc-removal generates the intended unlabeled progelators $KLDL_{Cyclic}$ and $KFDF_{Cyclic}$. Route II depicts the synthesis of labeled progelators through N-terminal modification with 5(6)-carboxytetramethyl rhodamine prior to cyclization. **b-c**, HPLC (b) monitored at 214nm and corresponding ESI spectra (c) of Fmoc-$KLDL_{Linear}$, Fmoc-$KLDL_{Cyclic}$, and $KLDL_{Cyclic}$ (835.79 m/z, 787.76 m/z, and 1070.26 m/z, respectively) verify purity and mass of synthetic modifications to KLDL peptides. **d-e**, HPLC (d) monitored at 214nm and corresponding ESI spectra (e) of Fmoc-$KFDF_{Linear}$, Fmoc-$KFDF_{Cyclic}$, and $KFDF_{Cyclic}$ (781.862 m/z, 856.17 m/z, and 1355.66 m/z, respectively) verify purity and mass of synthetic modifications to KFDF peptides. In both KLDL and KFDF systems, macrocyclization causes a slight decrease in polarity and Fmoc-deprotection increases progelator polarity **f**, $KLDL_{Linear}$ SAP macrocyclization kinetics monitored by LCMS at 214 nm reveal complete cyclization after 120 min. **g**, Absorbance spectra of unlabeled and labeled KLDL progelators (λ_{max} = 565 nm for rhodamine signal). **h**, $KFDF_{Linear}$ SAP macrocyclization kinetics monitored by LCMS at 214 nm reveal complete cyclization after 120 min. **i**, Absorbance spectra of unlabeled and labeled KFDF progelators (λ_{max} = 565 nm for rhodamine signal). **j**, $KLDL_{Linear}$ precursor assembles as a hydrogel (left) and the resulting $KLDL_{Cyclic}$ progelator exists a soluble solution (right). **k**, $KLDL_{Linear}$ precursor assembles as a hydrogel (left) and the resulting $KLDL_{Cyclic}$ progelator exists as a soluble solution (right).

UV spectra confirm the presence of rhodamine absorbance in Rho-KLDL$_{Cyclic}$ and Rho-KFDF$_{Cyclic}$ progelators (**Figure 3.1.9g,i**). Nonviscous progelators (**Figure 3.1.9j-k**) were dialyzed into milliQ H_2O, sterile filtered (0.2 µm PES), and lyophilized for storage prior to use *in vitro* and *in vivo*. Combined, matrix assisted laser desorption ionization (MALDI) (**Figure 3.1.10**), high resolution mass spectrometry (HRMS) (**Figure 3.1.11**)**,** and Tandem-MS (**Figure 3.1.12**) confirm synthesis of the cyclic peptides. This analysis was important as linear peptide from reduction of disulfide bonds would have a mass difference of Δ-2 Da and macrocyclic dimerization would present an $[M+2H^+]^{2+}$ m/z identical to that of the macrocyclic unimer $[M+H^+]^+$ m/z.

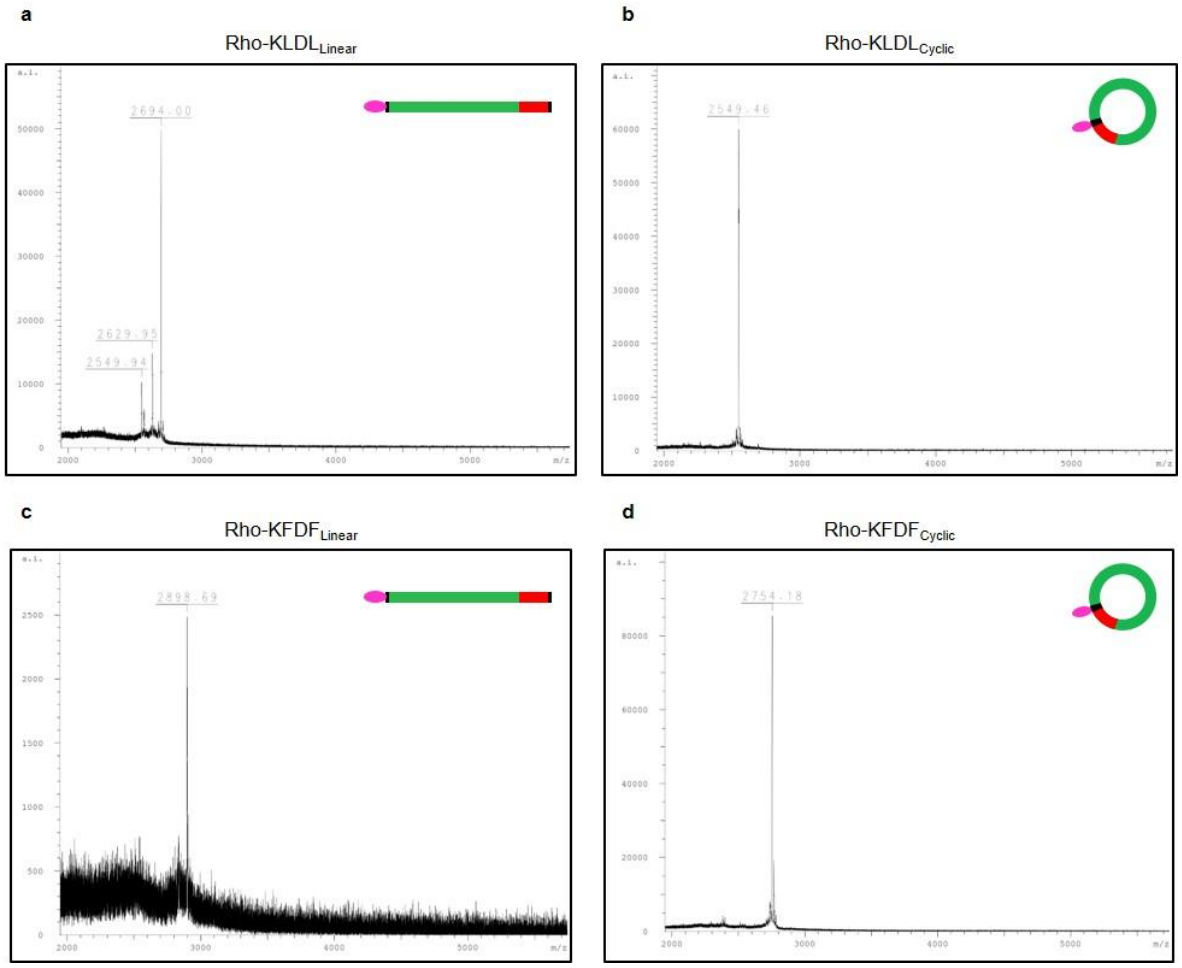
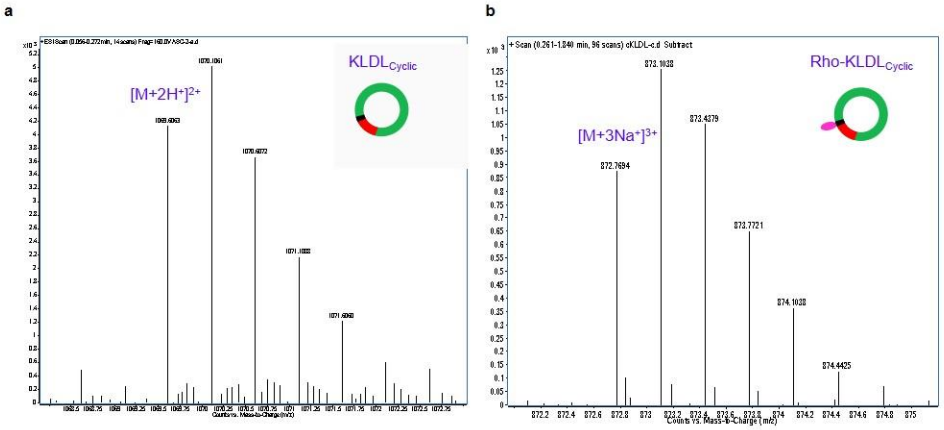


Figure 3.1.10. MALDI of labeled progelators before and after cyclization. **a-b**, Rho-KLDL$_{Linear}$ (**a**) and resulting cyclization product (**b**)Rho-KLDL$_{Cyclic}$. Masses are 2694.00 m/z $[M+H^+]^{1+}$ and 2549.46 m/z $[M+H^+]^{1+}$, respectively. **c-d**, Rho-KFDF$_{Linear}$ (**c**) and resulting cyclization product (**d**)Rho-KFDF$_{Cyclic}$. Masses are 2989.69 m/z $[M+H^+]^{1+}$ and 2754.18 m/z $[M+H^+]^{1+}$, respectively.



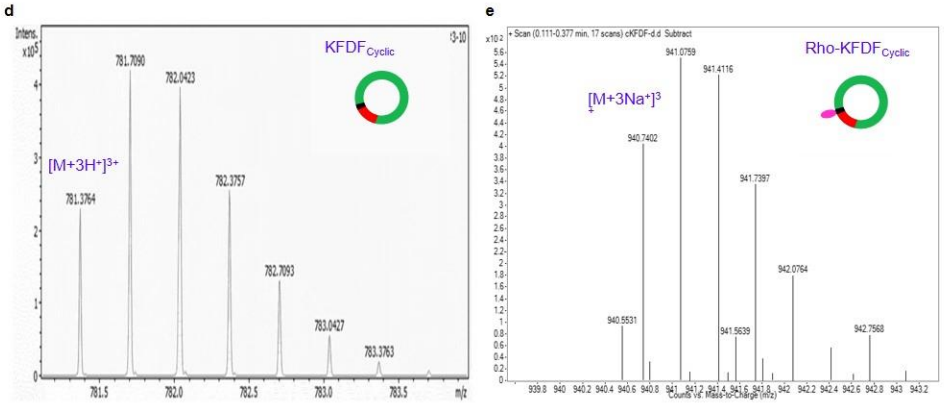
c

Unlabeled

Conformation	Theo. Mass (m/z)	Mass Measured (m/z)	Delta (ppm)	Composition
open	1070.6153			$[C_{96}H_{172}N_{24}O_{26}S_2]^{2+}$
closed	1069.6074	1069.6063	-1.0	$[C_{96}H_{170}N_{24}O_{26}S_2]^{2+}$

Labeled

Conformation	Theo. Mass (m/z)	Mass Measured (m/z)	Delta (ppm)	Composition
open	873.4420			$[C_{121}H_{190}N_{26}O_{30}S_2Na_3]^{3+}$
closed	872.7701	872.7694	-0.8	$[C_{121}H_{188}N_{26}O_{30}S_2Na_3]^{3+}$



f

Unlabeled

Conformation	Theo. Mass (m/z)	Mass Measured (m/z)	Delta (ppm)	Composition
open	782.0480			$[C_{114}H_{161}N_{24}O_{26}S_2]^{3+}$
closed	781.3761	781.3764	0.4	$[C_{114}H_{159}N_{24}O_{26}S_2]^{3+}$

Labeled

Conformation	Theo. Mass (m/z)	Mass Measured (m/z)	Delta (ppm)	Composition
open	941.4107			$[C_{139}H_{178}N_{26}O_{30}S_2Na_3]^{3+}$
closed	940.7387	940.7402	1.5	$[C_{139}H_{176}N_{26}O_{30}S_2Na_3]^{3+}$

Figure 3.1.11. HRMS unlabeled and labeled progelators. Analysis conducted to identify whether final progelator peptides were in closed cyclic or open linear conformations. **a-b**, HRMS spectra for (**a**) KLDL$_{Cyclic}$ and (**b**) Rho-KLDL$_{Cyclic}$. **c**, Corresponding summary of theoretical m/z, measured m/z, measurement error, and elemental compositions for opened and closed conformations. **d-e**, HRMS spectra for (**d**) KFDF$_{Cyclic}$ and (**e**) Rho-KFDF$_{Cyclic}$. **f**, Corresponding summary of theoretical m/z, measured m/z, measurement error, and elemental compositions for opened and closed conformations. All measurements reveal closed conformation in contrast to open linear peptide.

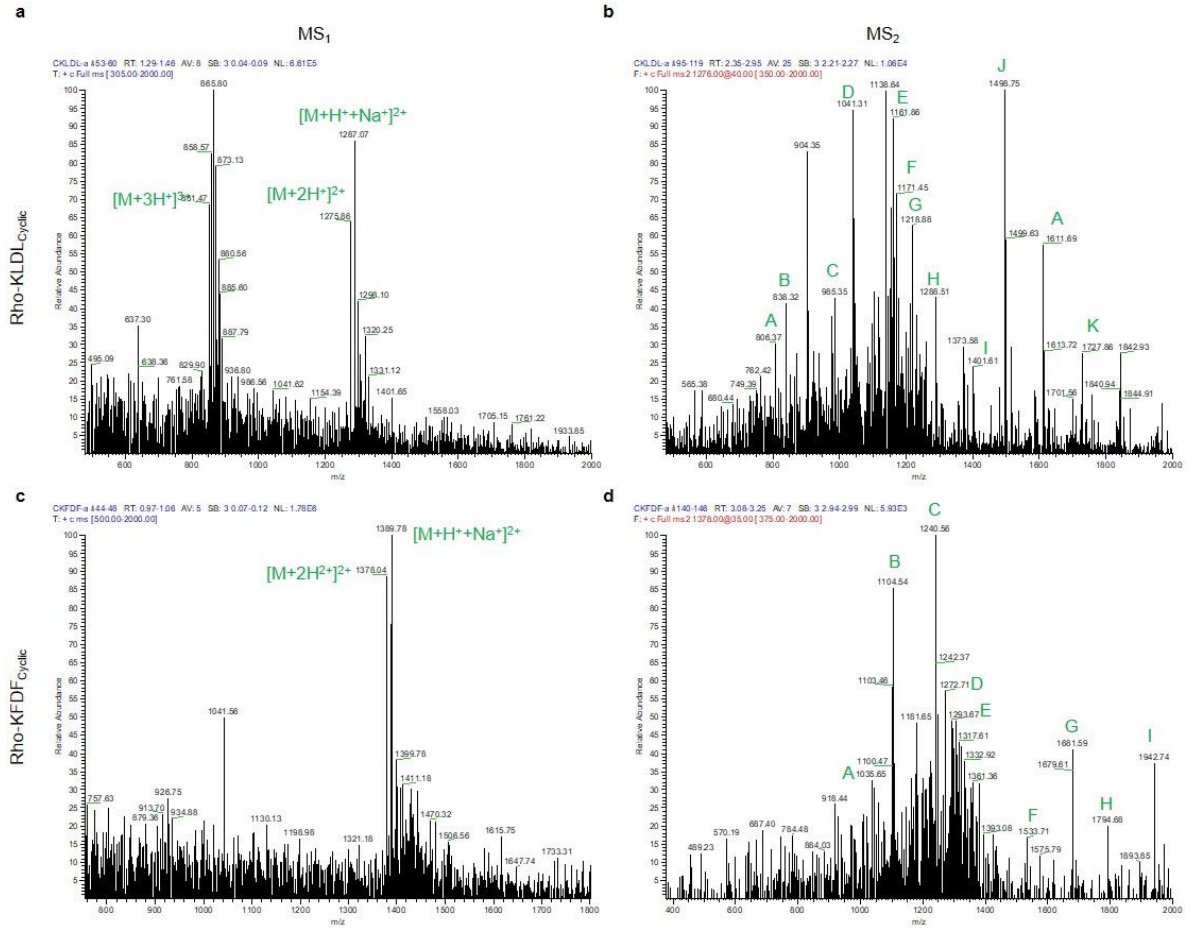


Figure 3.1.12.Tandem-MS of Rho-KLDL$_{Cyclic}$ and Rho-KFDF$_{Cyclic}$ progelators. Fragmentation of the peptide sequence enables identification of the peptide sequence, notably those that contain the less labile covalent disulfide bond. **a**, MS^1 spectrum for Rho-KLDL$_{Cyclic}$ with peak identities labeled in green. **b**, Corresponding MS^2 fragmentation spectrum filtered for the 1276 m/z ion. Peak identities, as determined by DisConnect software, are displayed in Error! Reference source not found.. **c**, MS^1 spectrum for Rho-KLDL$_{Cyclic}$ with peak identities l abeled in green. **d**, Corresponding MS^2 fragmentation spectrum filtered for the 1378 m/z ion. Peak identities, as determined by DisConnect software, are displayed in Error! Reference source not found.. Note that only normal fragmentation peaks (no H2O, NH3, or CO losses) are identified

To ensure synthetic reproducibility and appropriate biological analysis in this study, our cyclic progelators were structurally characterized and formulated by first dissolving in aqueous solution under basic conditions, followed by neutralization to give final solutions in 1xDPBS, pH 7.4 (10 mM peptide). This formulation was determined by searching for conditions that minimized aggregation in different solvents and pH. Reports of SAPs injected into the heart post-MI often involve formulation in sucrose[19,46,47] or PBS[48]. Timecourse static light scattering (SLS) measurements of progelator

suspended in H_2O, 1xDPBS, and 295 mM sucrose (intensity of solvents only subtracted) showed that 1xDPBS minimizes the size of aggregate assemblies (**Figure 3.1.13**). This is verified with corresponding TEM images.

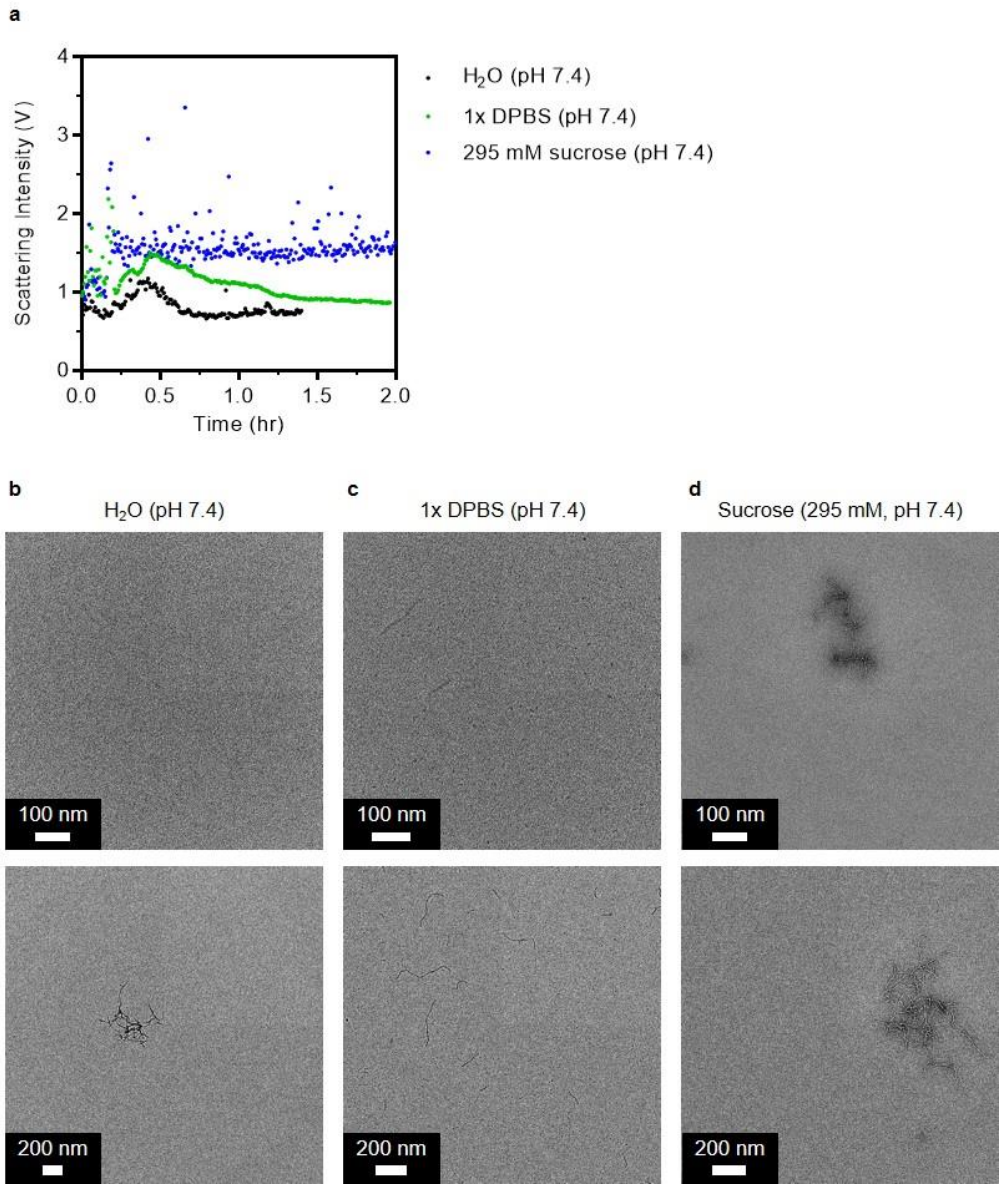


Figure 3.1.13. SLS profiles for unlabeled progelator in different buffers. **S**oluions of $KFDF_{Cyclic}$ were formulated in solvents commonly used for formulating SAPs to identify optimal solvents that minimize the occurrence of large assemblies in solution. **a**, $KFDF_{Cyclic}$ was pre-dissolved at 10 mg/mL in H_2O at pH 9 and added to solvent in the DLS cuvette such that final concentrations were 1 mg/mL in H_2O, 1x DPBS, or 295 mM sucrose (pH 7.4). Scattering was highest for sucrose solutions and equivalent in H_2O and 1x DPBS after 2 hr incubation indicating smaller assemblies in the later solvent. Intensities were corrected for background solvent scattering. Scattering intensities were normalized to individual solvents. **b-d**, TEM analysis in H_2O (**b**), 1x DPBS (**c**), and 295 mM sucrose (**d**), diluted to 100 µM. Large structures were absent in H_2O and 1x DPBS with some small clusters of fibrils in sucrose.

Next the effect of pH, prior to the addition of 1xDPBS (pH 7.4), was investigated (**Figure 3.1.14**). TEM and dynamic light scattering reveal that minimal aggregation was observed when using a pH switch from pH 9 to neutral conditions prior to addtion of 1xDPBS.

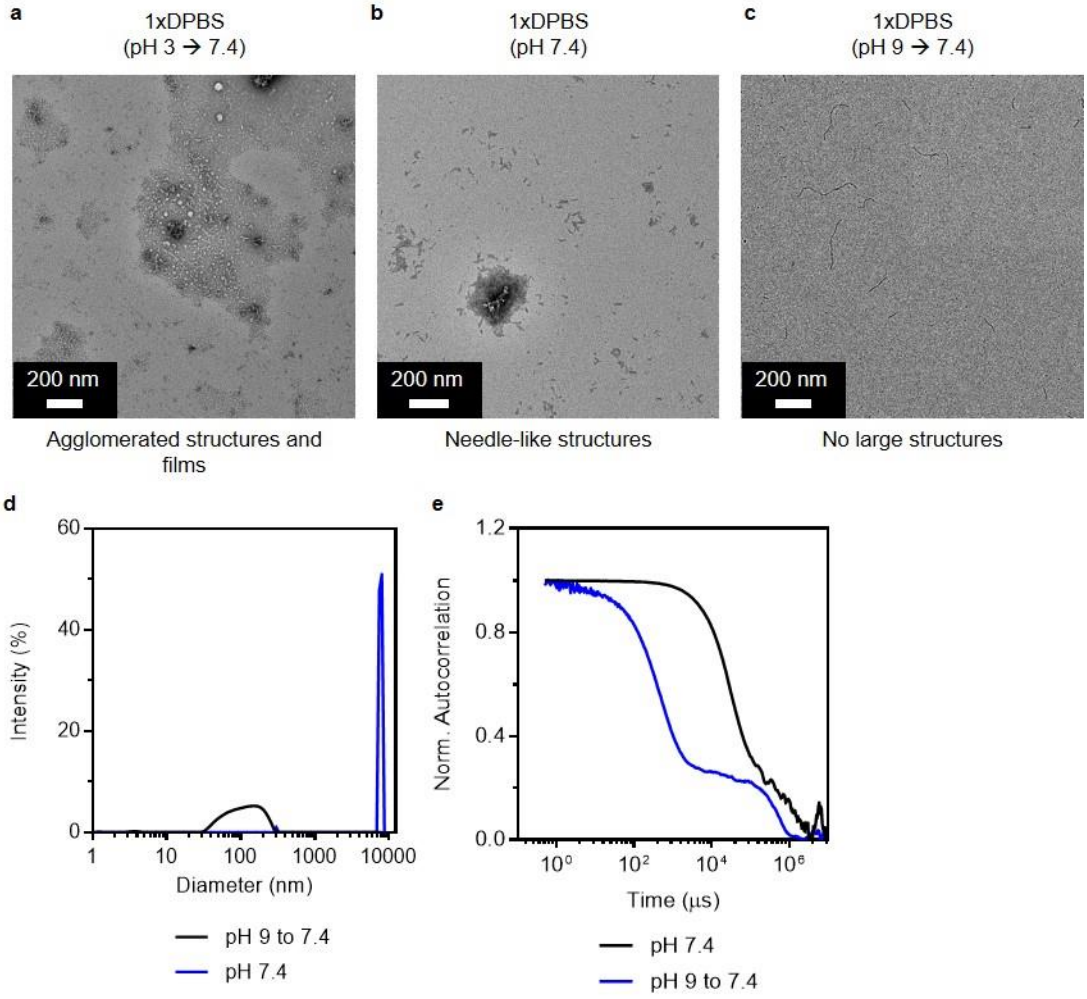


Figure 3.1.14. Effect of cyclic peptide progelator formulation on aggregation. Solutions of $KFDF_{Cyclic}$ and $KFDF_{Linear}$ (data not shown) were optimally formulated in 1x DPBS using a pH switch from basic (pH 9.0) to neutral (pH 7.4) conditions prior to addition of saline to limit aggregation. These formulations in 1x DPBS are stable over prolonged incubation periods (up to 3 days) under dilute (100 µM) and concentrated (10 mM) conditions. a-c, TEM (100 µM) micrographs of progelator formulated in 1x DPBS after solvent switch from acidic to neutral pH (a), no pH switch (b), or switch from basic to neutral pH (c). d-e, DLS (1 mg/mL) (d) and the corresponding normalized autocorrelation functions (e) depict the influence of different formulation conditions on aggregation.

Finally, a quick test was conducted to verify that cyclic progelator linearization does still indeed lead to an increase in light scattering, due to self-assembly into macromoelcular structures (**Figure 3.1.15**). SLS signal of the progelator formulation remained stable over 1 hr prior to addition of enzyme, and increased signal was observed after enzyme addition. Thus, these optimized formulation conditions do not interfere with the designed reactivity of our progelator. Furthermore, these final formulations in 1x DPBS were stable over prolonged incubation periods (up to 3 days) under dilute (100 μM) and concentrated (10 mM) conditions.

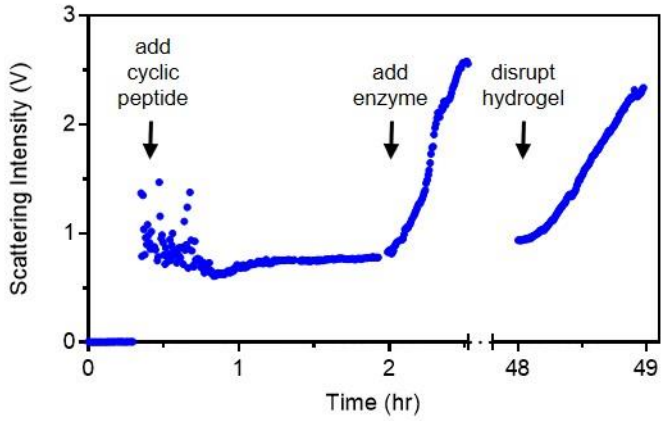


Figure 3.1.15. SLS of cyclic progelator before and after enzyme addition. This scattering profile demonstrates that progelator in solution is stable to flocculation for hours until addition of thermolysin induces a steep increase in scattering intensity as self-assembly occurs. Complete disruption of macromolecular structures via sonication at 48 hr post-activation results in a return to nominal scattering intensity like that of the cyclic progelator. Reassembly is observed by a gradual increase in scattering intensity of this dilute solution. Final peptide concentration is 1 mg/mL in 1xDPBS at 37 ˚C. Hydrogel disruption was achieved with 10 min sonication.

By CD under formulation conditions, the magnitude of the high energy minimum at 204 nm is increased significantly following cyclization, which is attributed to aromatic π-π* effects achieved through vertically stacked macrocycles (**Figure 3.1.16**). Conformational rigidification via macrocyclization is suspected to have induced limited oligomerization via intermolecular stacking of cyclic constructs into transient nanotubes, as has been reported in the literature.[49-51] Despite this

observed secondary structure, large assemblies were absent by TEM (**Figure 3.1.14c**). Thus, our formulated cyclic progelators persist as free-flowing solutions for easy injection *in vivo*.

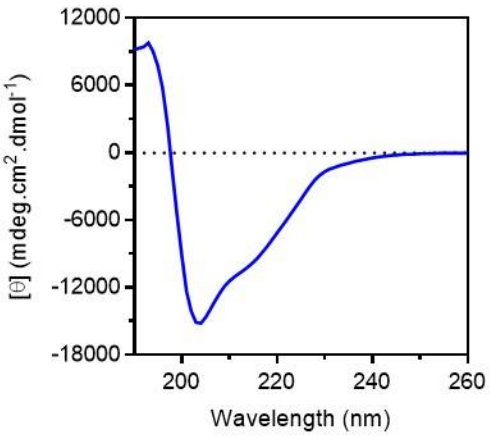


Figure 3.1.16. Circular dichroism (CD) of KFDF$_{Cyclic}$ progelator. a, CD spectrum of KFDF$_{Cyclic}$ progelator (500 µM, pH 7.4) formulated with basic to neutral pH solvent switch. (n=3 repeats). The magnitude of the high energy minimum at 204 nm is increased significantly following cyclization of KFDF$_{Linear}$ (from **Figure 3.1.7b**), which is attributed to aromatic π-π* effects achieved through vertically stacked macrocycles

Cyclic progelators are responsive to inflammation associated enzymes. Labeled cyclic peptide progelators were tested for their responsiveness to inflammatory-related proteases overexpressed post-MI (**Figure 3.1.17**). The initial inflammatory response is marked by the recruitment of abundant neutrophils, which contribute to the release of proteases such as matrix metalloproteinases (MMPs) and elastase in the first days post-MI.[31,52] The fibrotic phase (weeks post-MI) is notable for residually high MMP concentrations[2,31] and elevated sources of elastase from neutrophil extracellular traps (NETs), remaining weeks after neutrophil apoptosis.[32,33] Rho-KLDL$_{Cyclic}$ and Rho-KFDF$_{Cyclic}$ were incubated with MMP-9 catalytic domain and porcine elastase to cleave at preferential cut sites (**Figure 3.1.17a,d).** Enzymatic cleavage by active MMP-9 and elastase induced visible aggregation in reaction vials and entangled fibrous meshes by TEM (**Figure 3.1.17b,e**), whereas denatured enzymes elicited no response.

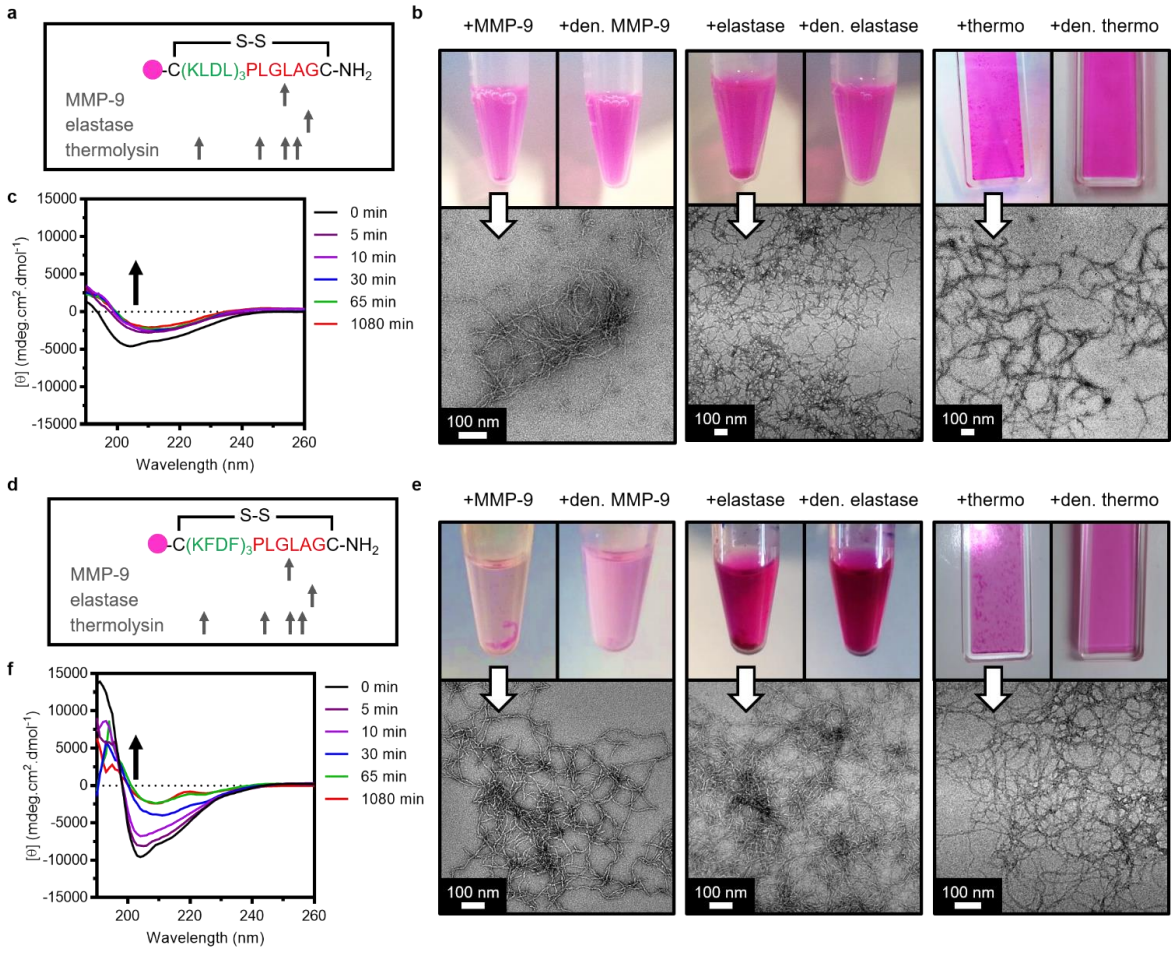


Figure 3.1.17. Enzyme responsiveness of Rho-KLDL$_{Cyclic}$ and Rho-KFDF$_{Cyclic}$ progelators. a-c, Analysis of Rho-KLDL$_{Cyclic}$ responsiveness to MMP-9, elastase, and thermolysin. (**a**) Peptide sequence and indicated enzymatic cuts sites. (**b**), Progelator incubated with active enzymes (left insets) shows material aggregation and settling from solution, and progelator incubated with denatured enzymes (right insets) show fully dispersed peptide solutions. Corresponding TEM images (bottom) of active enzyme cleavage products show fiber formation. (**c**), CD spectra of cleavage kinetics with thermolysin. Disappearance of signal at 204 nm (black arrow), corresponds to ring-opening. **d-f,** Analysis of Rho-KFDF$_{Cyclic}$ to responsiveness MMP-9, elastase, and thermolysin. (**d**) Peptide sequence and indicated enzymatic cuts sites. (**e**), Progelator incubated with active enzymes (left insets) shows material aggregation and settling from solution, and progelator incubated with denatured enzymes (right insets) show fully dispersed peptide solutions. Corresponding TEM images (bottom) of active enzyme cleavage products show fiber formation. (**f**) CD spectra of cleavage kinetics with thermolysin. Disappearance of signal at 204 nm (black arrow), corresponds to ring-opening. CD of 500 µM progelator in 10 mM Tris buffer, pH 7.4. Enzyme cleavages performed at 500µM progelator with 1:1000, 1:250, and 1:4500 enzyme/substrate molar ratio in 1x cleavage buffers (see Methods). Samples diluted to 100 µM for TEM.

Liquid chromatography (LC) reveals the appearance of peptide cleavage product in response to incubation with both MMP-9 catalytic domain and porcine elastase, which cleave at a single location and produce a single product (**Figure 3.1.18**). As the final peptide product is nearly identical,

the cleavage product for both reactions is observed at the same elution time. Furthermore, this agrees well with the actual elution time for the representative linear product analogue.

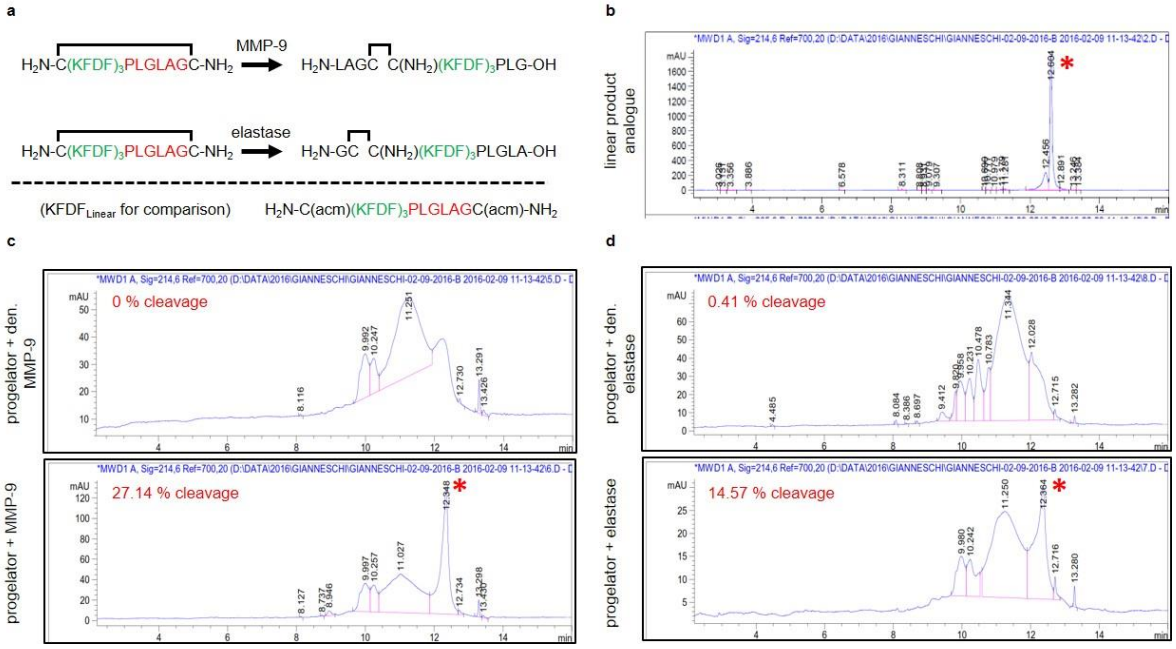


Figure 3.1.18. Representative enzyme cleavage of unlabeled cyclic progelator. $KFDF_{Cyclic}$ and $KLDL_{Cyclic}$ (data not shown) were treated with MI-associated enzymes, MMP-9 and elastase to confirm enzyme responsiveness. a, Sequences of the $KFDF_{Cyclic}$ progelator cleavage reactions and $KFDF_{Linear}$ analogue for comparison. b, LCMS spectrum of $KFDF_{Linear}$ analogue (R_t = 12.5 min) as a positive control. c, LCMS spectra of $KFDF_{Cyclic}$ progelator treated with denatured (top) and active (bottom) MMP-9 catalytic domain for 5 hr. d, LC spectra of $KFDF_{Cyclic}$ progelator treated with denatured (top) and active (bottom) porcine elastase for 5 hr. Calculated percent cleavages are reported in the spectra. Cleavage products are indicated with red asterixis. Due to the large number of cis/trans configurational isomers and amphiphilic self-assembling nature of our cyclic peptides, our pure $KFDF_{Cyclic}$ progelator eluted within an R_t range between 9.7-12.5 min. Cleaved peptide peaks (R_t ~ 12.4 min) have better resolution likely due to increased molecular flexibility. Cleavage reactions are described in the Methods section of the main text.

At the site of MI, the presence of very high MMP and elastase concentrations is expected to induce rapid cleavage, forcing the peptide progelator to assemble and solidify at the target site. However, other inflammation-associated enzymes or constitutively expressed extracellular proteases could play a role in nonspecific degradation. Thus, thermolysin was used as a robust nonspecific enzyme to assess general stability of our material to excess proteolysis and subsequent hydrogel disassembly *in vivo*.[53] Despite the promiscuous activity of thermolysin, incubation with Rho-$KLDL_{Cyclic}$ and Rho-$KFDF_{Cyclic}$ induced fiber formation by TEM (**Figure 3.1.17b,e**). CD revealed structural rearrangements during this linearization process (**Figure 3.1.17c,f**). Potential

intramolecular[54] and intermolecular[55,56] steric hindrance from these labeled progelators might explain differences in the CD cleavage kinetics. The similar responsiveness of both unlabeled progelators to inflammatory enzymes and resistance to dissolution by thermolysin demonstrate the versatility of our general platform for conformational control.

Progelators assemble as viscoelastic and rehealable hydrogels despite robust proteolysis. The concept behind our cyclic progelator platform relies on upregulated enzymes to initiate assembly and ultimately viscoelastic gel formation at the site of MI. However, excess proteolysis *in vivo* from the 'soup' of proteases at the MI may prevent gelation or retention of hydrogels at the site of injury. To simulate this environment, we treated our material at 10 mM with a large quantity of the robust and non-specific enzyme, thermolysin . Hydrogel assembly kinetics and resulting mechanical properties were then measured rheologically (**Figure 3.1.19**).

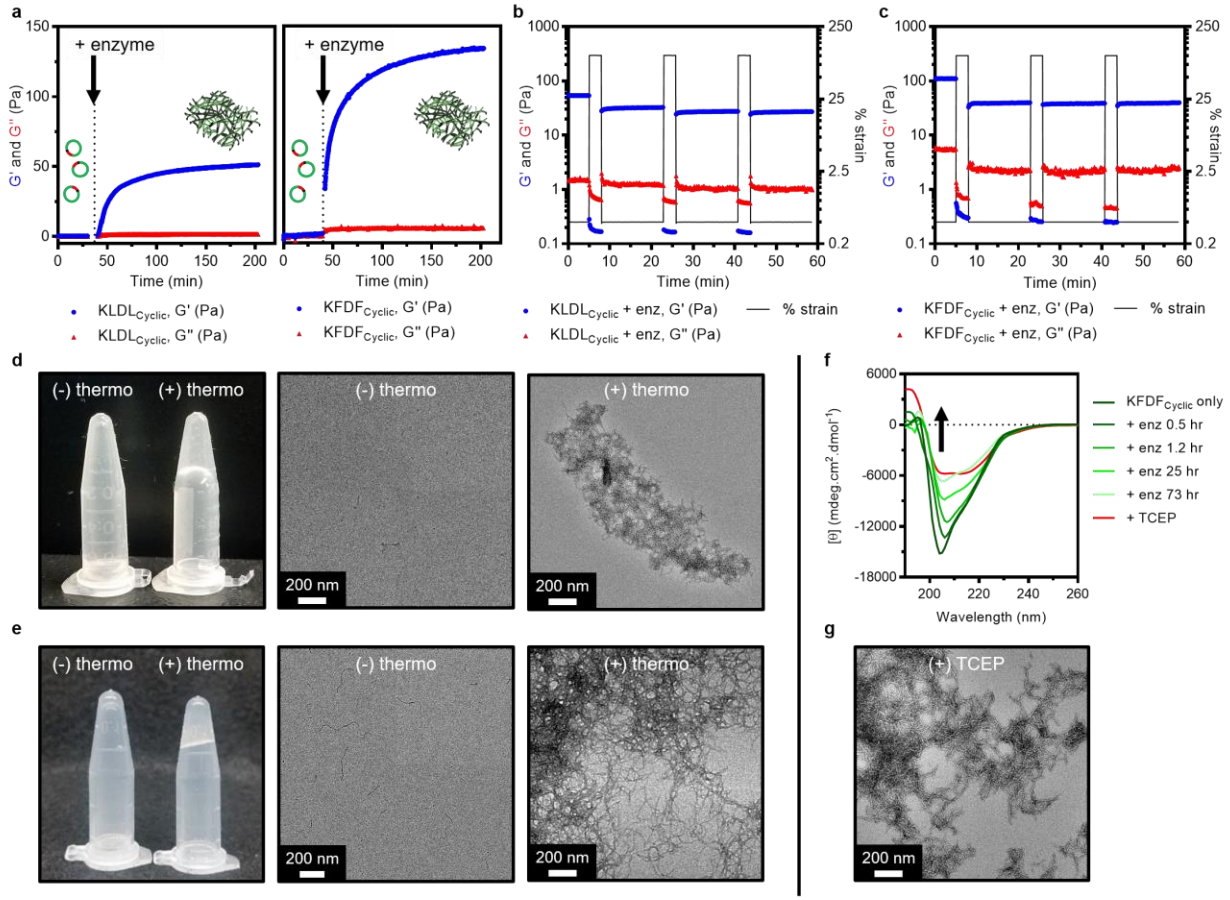


Figure 3.1.19 Bulk Scale Gelation of Unlabeled Cyclic Progelators. a, Time course rheological analysis of KLDL$_{Cyclic}$ (left) and KFDF$_{Cyclic}$ (right) progelators before and after addition of thermolysin (t=~40 min). Divergence of G' from G'' (G'>G'') indicates formation of crosslinked hydrogel. **b-c**, Step-strain oscillation plots of resulting (**b**) linearized KLDL and (**c**) linearized KFDF SAP hydrogels at 9 hr post-enzyme-activation reveal repeat healing (3 min at 100 % strain, 15 min at 0.5% strain, n=3 cycles). Angular frequency 2.5 rad/s, 0.5% strain. **d-e**, Images of (**d**) KLDL$_{Cyclic}$ and (**e**) KFDF$_{Cyclic}$ progelators in the absence (-) and presence (+) of thermolysin with corresponding TEM. Enzyme cleavages at 10 mM in 1xDPBS with 1:4500 enzyme/substrate molar ratio. TEM of samples diluted to 100 µM. **f**, CD of KFDF$_{Cyclic}$ before and after subsequent additions of thermolysin at 0.5, 1.2, 25, and 73 hr shows gradual disappearance of minimum around 204 nm from π- π* interactions between stacked cyclic peptides. 500 µM peptide in 10 mM Tris, pH 7.4. **g**, TCEP (1.2 eq) induced reduction of progelator disulfide bond shows ideal assembly of linearized progelators. Two minima at 204 nm (π→π*) and 215 nm (n→π*) reveal weak aromatic π-π* interactions and β-sheets assembly, respectively. 500 µM peptide in H_2O, pH 7.4.

Initially, KLDL$_{Cyclic}$ and KFDF$_{Cyclic}$ displayed overlapping storage (G') and loss (G'') moduli, indicative of solutions lacking significant crosslinks or chemical interactions (**Figure 3.1.19a-b**). Incubation with thermolysin initiates rapid increase in G' and divergence from G'' shows the formation of viscoelastic hydrogels. A steady state was reached at 200 min and continuous measurement of viscoelastic properties revealed no change for up to 3 days in the presence of

thermolysin. The tightly entangled macromolecular scaffolds are suspected to confer some degree of resistance to further proteolysis. Furthermore, the resulting gels displayed rapid healing capacity when subjected to repeat cycles of excess strain (100%) (**Figure 3.1.19b-c**). Morphological changes from rheology samples before and after enzyme incubation are illustrated in **Figure 3.1.19d-e.** Synthetic product analogue SAPs in which the gelator sequence contained flanking substrate residues ($KLDL_{Control}$ and $KFDF_{Control}$) were used for simple comparison with enzyme-induced gelation (**Figure 3.1.20**).

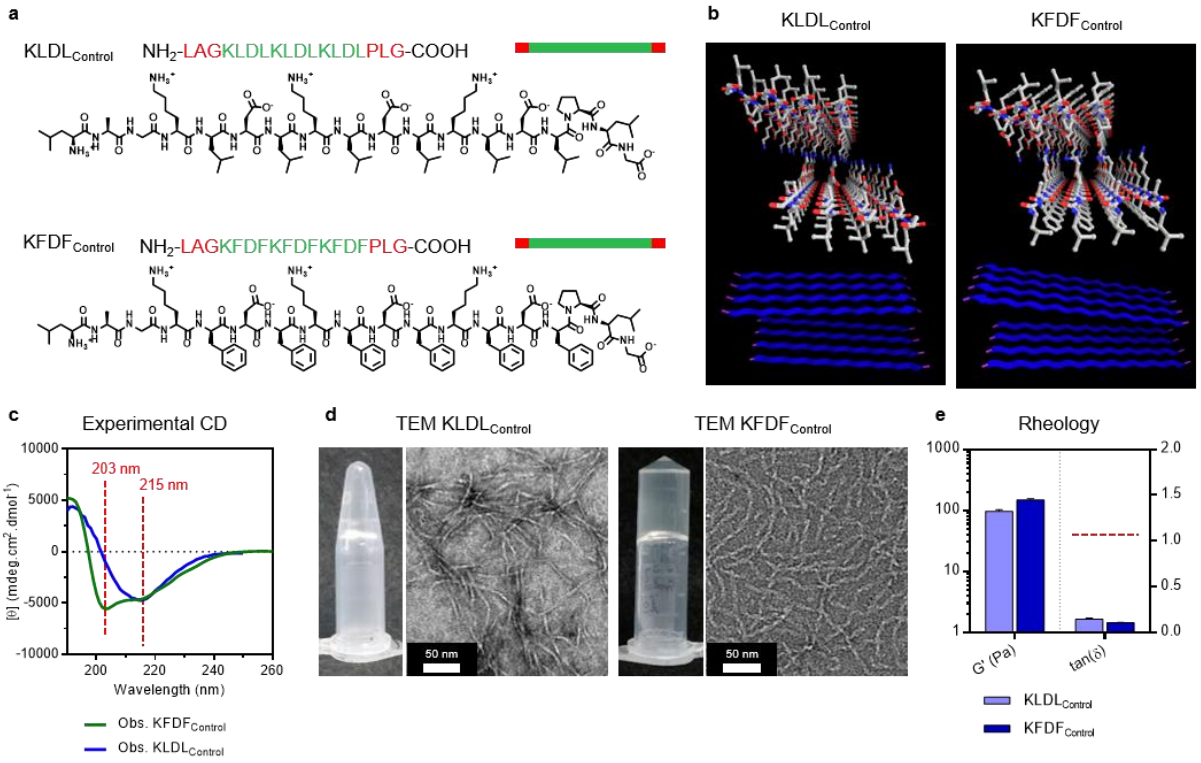


Figure 3.1.20. Simulated control SAPs, $KLDL_{Control}$ and $KFDF_{Control}$, for progelator cleavage. $KLDL_{Control}$ and $KFDF_{Control}$ SAPs were used to represent the enzymatically cleaved progelators containing flanking substrate residues on the gelling sequences. **a**, Sequences, chemical structures, and corresponding diagrammatical representations of peptides, with green denoting gelator sequence and red denoting cleaved substrate recognition sequences. **b**, Predicted structures and ribbon diagrams (bottom) of $KLDL_{Control}$ and $KFDF_{Control}$ SAPs from FibPredictor simulations revealing parallel β-sheet orientations (see Supplementary Tables 1-2). **c**, Experimental circular dichroism (CD) spectra of $KLDL_{Control}$ and $KFDF_{Control}$ SAPs, with labeled minima at 215 nm (n→π*) and 203 nm (π→π*). **d**, Assembled hydrogel photographs and corresponding TEM images of $KLDL_{Control}$ (left) and $KFDF_{Control}$ (right) SAPs. **e**, Viscoelastic measurements of storage moduli, G' (Pa), and damping factor, tanδ, for $KLDL_{Control}$ and $KFDF_{Control}$. Gel capacity is defined as tanδ < 1 (dashed line). CD measurements performed at 500 μM SAP in 10 mM Tris buffer, pH 7.4. (n=3 repeats) SAPs for TEM and rheology prepared at 100 μM and 15 mg/mL in 1xDPBS (pH 7.4), respectively. Rheological measurements reported for angular frequency of 2.5 rads/s. (n=3 repeats) Values are mean ± SEM.

Indeed, secondary assembly characteristics (CD), fibril morphology (TEM), and viscoelastic properties (rheology) of $KFDF_{Control}$ match closely to that of enzymatically cleaved $KFDF_{Cyclic}$ in **Figure 3.1.19**. However, $KLDL_{Control}$ SAP produced a viscoelastically stronger gel than that demonstrated by $KLDL_{Cyclic}$ following enzyme directed linearization. We suspect that the slowed kinetics of gel formation for enzyme-treated $KLDL_{Cyclic}$ vs $KFDF_{Cyclic}$ is caused by lower specificity of thermolysin for Leu vs Phe at the P1 position.[57,58] With hydrogel assembly following close behind, increased proteolytic resistance of tightly packed fibers and limited enzyme diffusion within the porous network[56,59] likely has a restrictive effect on further progelator linearization and subsequent gel stiffening for all samples.

Angular frequency sweeps of hydrogels measured with product analogues ($KLDL_{Control}$ and $KFDF_{Control}$) as well as enzyme treated progelators ($KLDL_{Cyclic + enz}$ and $KFDF_{Cyclic + enz}$) reveal frequency independent viscoelastic properties (**Figure 3.1.21**). Thus these hydrogels behave more as a stiff gel rather than extremely viscous liquid which flows over time. This property is especially important for biomaterials used in tissue engineering, where the assembled hydrogel is expected to remain in place throughout the duration of its lifetime *in vivo*.

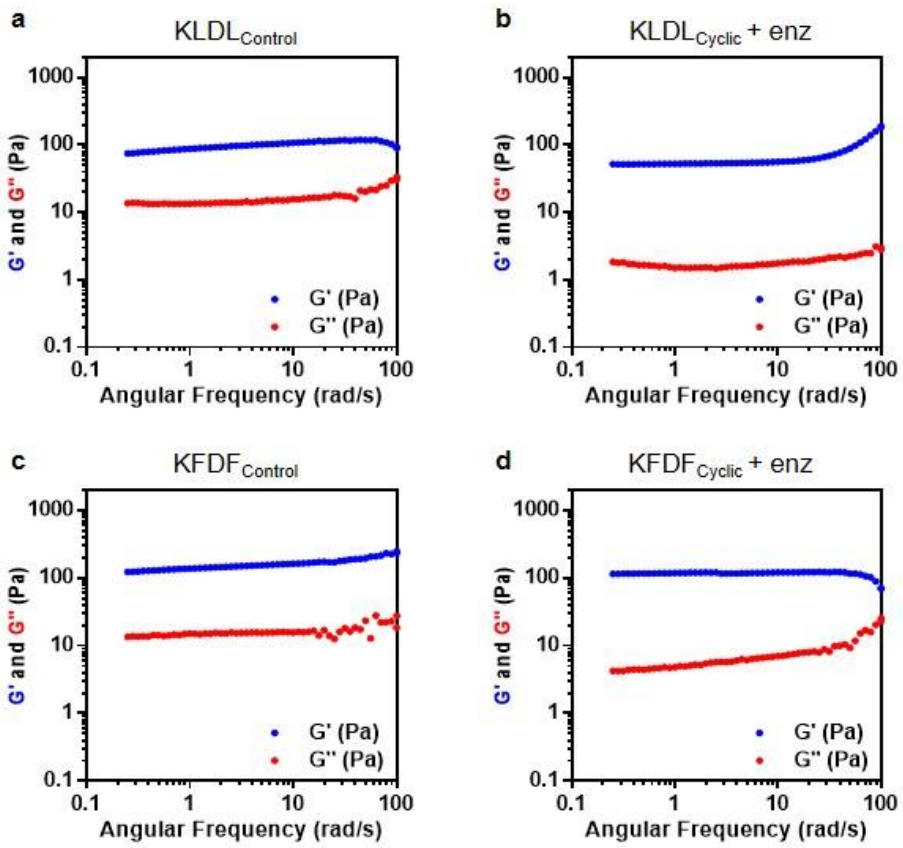


Figure 3.1.21. Frequency sweeps of product analogues and cleavage products. Product analogues (KLDL$_{Control}$ and KFDF$_{Control}$) and enzymatically cleavage progelators (KLDL$_{Cyclic}$ + enz and KFDF$_{Cyclic}$ + enz) were analyzed for frequency dependence of the viscoelastic moduli across low and high frequency. **a-b**, Frequency sweeps for (**a**) KLDL$_{Control}$ and (**b)** KLDL$_{Cyclic}$ + enz hydrogels. **c-d**, Frequency sweeps for (**a**) KFDF$_{Control}$ and (**b)** KFDF$_{Cyclic}$ + enz hydrogels. Hydrogels at 10 mM in 1xDPBS (pH 7.4). Angular frequency sweeps (100-0.25 rad/s) at 0.5% strain (n=3 repeats). Values are mean ± SEM.

To understand the initial stages of self-assembly when progelators first encounter their target protease *in vivo*, slow step-wise cleavage of KFDF$_{Cyclic}$ progelator was achieved through serial additions of dilute thermolysin (**Figure 3.1.19f**). CD reveals that linearization by enzyme cleavage causes an increase in peptide flexibility, shown by a steep decrease in the signal at 204nm, and unchanged β-sheet signal from lateral alignment at 215 nm. Tris(2-carboxyethyl)phosphine (TCEP) was used as a positive control to represent ideal assemblies of linearized peptides through complete reduction of the disulfide bond **(Figure 3.1.22)**. By TEM,

reduced peptides assemble as tangled fibrils, similarly to enzymatically cleaved peptides (**Figure 3.1.19 g**). Thus, the enzyme-induced gels observed in **Figure 3.1.19** are likely forming through the same self-assembly mechanisms predicted with $KFDF_{Control}$. The rheological and spectroscopic results presented here indicate that our system has to potential to tolerate excess proteolytic degradation *in vivo*.

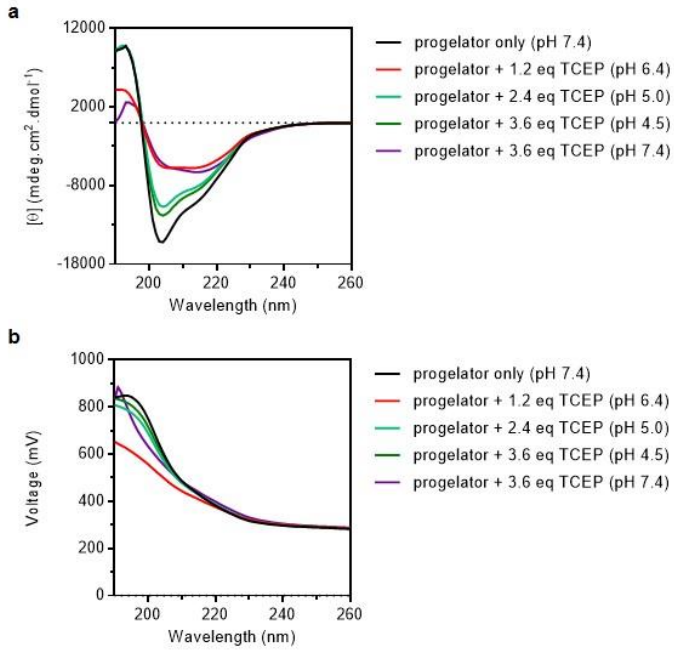


Figure 3.1.22. TCEP reduction of progelator. TCEP reduction indicates ideal assemblies from when cleavage of cyclic progelators is complete. TCEP reduction is shown to be reversible through TCEP inactivation at lower pH a, Progelator treated with 1.2, 2.4, and 3.6 eq of TCEP. Gradual decrease in pH (pH 7.4 to 4.5) occurs from successive TCEP additions. Neutralization to pH 7.4 with NaOH revives TCEP reductive potential. b, Corresponding high tension (HT) voltage plots. Concentration 500 μM progelator. (n=3 repeats).

Catheter compatibility of cyclic peptide progelators. Minimally invasive injection of hydrogels into the heart is typically performed through transendocardial injections. Unlike direct epicardial injections performed in small animal models, transendocardial delivery has certain constraints that are not amenable to most hydrogel systems, namely materials should be able to reside within the catheter for up to hour-long procedures, yet still flow over multiple injections during this time, and finally only form a solid gel once it has entered the tissue.[17,60] Rapid gelation and/or high viscosity prohibit many injectable hydrogels from being considered for this minimally invasive

delivery route. $KLDL_{Cyclic}$ and $KFDF_{Cyclic}$ progelators were amenable to cardiac catheter injection (**Figure 3.1.23**). As shown in **Figure 3.1.23a**, both unmodified SAPs and cyclic progelators exhibit shear-thinning behavior, but the viscosities for the latter are over 20x lower for both $KLDL_{Cyclic}$ and $KFDF_{Cyclic}$. Thus, conformational constraint of β-sheet forming SAPs was sufficient to disrupt favorable unimer alignment and weakened structural interactions. We reasoned that SAP cyclization would be sufficient to prevent clogging during catheter injection (**Figure 3.1.23b**).

To mimic cardiac catheter injection *in vivo,* both cyclic progelators (2 mol% labeled for visualization) were flowed through the inner nitinol tubing of a 27G (0.21 mm inner diameter) MyoStar transendocardial injection catheter at 37 ˚C using a syringe pump **(Figure 3.1.23c)**. No excess resistance was detected by manual operation following incubation of cyclic progelator within the catheter loop for 60 min for either peptide. In contrast, unmodified KLDL and KFDF SAPs caused immediate catheter clogging. Excess resistance from high viscosity and tendency to rapidly self-assemble during shearing injection could explain why there are no previous reports of SAPs for cardiac catheter delivery. To ensure that the shear forces upon cyclic progelators during injection do not inhibit enzyme activation, and prevent gelation *in vivo*, the cyclic peptides were injected through the catheter into a vial containing thermolysin and incubated for 3 hr (37 ˚C), resulting in hydrogel formation (**Figure 3.1.23e**)**.**

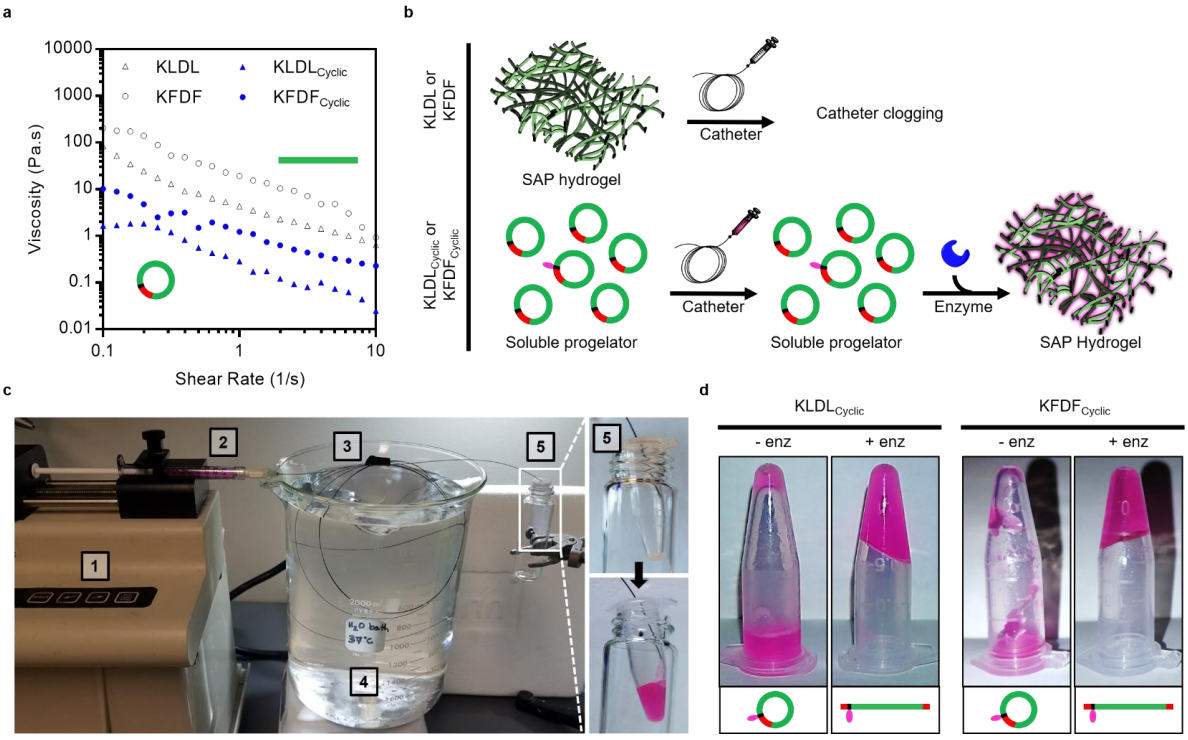


Figure 3.1.23 ***In vitro*** **catheter injection of low viscosity progelators.** **a**, Complex viscosity of KLDL$_{Cyclic}$ and KFDF$_{Cyclic}$ progelators reveal >20x decrease in comparison to corresponding unmodified KLDL and KFDF SAPs. **b**, Schematic illustrating catheter applicability of KLDL and KFDF SAPs vs that of enzyme-responsive KLDL$_{Cyclic}$ and KFDF$_{Cylic}$ progelators. Injection of SAP hydrogels causes clogging. **c**, Experimental setup of progelator (2 mol% labeled) catheter injection test. Peptide was (1) loaded in a 1mL syringe, (2) mounted on a syringe pump, and (3) flowed at 0.6 mL/min through the inner nitinol tubing (27G) of a MyoStar transendocardial injection catheter. The catheter was (4) submerged in a circulating water bath heated to 37 °C. The collection tube (5) before (top) and after (bottom) injection show successful injection. **d**, Image of KLDL$_{Cyclic}$ and KFDF$_{Cyclic}$ progelators (2 mol% labeled) after catheter injection into an empty vial (left) or a vial containing thermolysin (right), demonstrating that injection does not disrupt enzyme-responsiveness. Progelator formulated as 10 mM in 1xDPBS (pH 7.4) and treated with 1:4500 enzyme/substrate molar ratio.

Hemocompatibility and intramyocardial injections in a rat myocardial infarction model.

For proof-of-concept analyses in biological systems, we examined the KFDF$_{Cyclic}$ progelator in hemocompatibility studies and assessed *in vivo* gelation (**Figure 3.1.24**). Biomaterial leakage is a concern with transendocardial injection since injections are performed into a beating heart.[61] Therefore, we assessed hemocompatibility of the cyclic progelator to ensure that modification and cyclization of the SAPs would not generate a thrombogenic response. Whole human blood clotting times, hemostasis kinetics, red blood cell (RBC) hemolysis, and pro-thrombotic profiles were evaluated in the presence of increasing cyclic peptide progelators concentrations in blood.

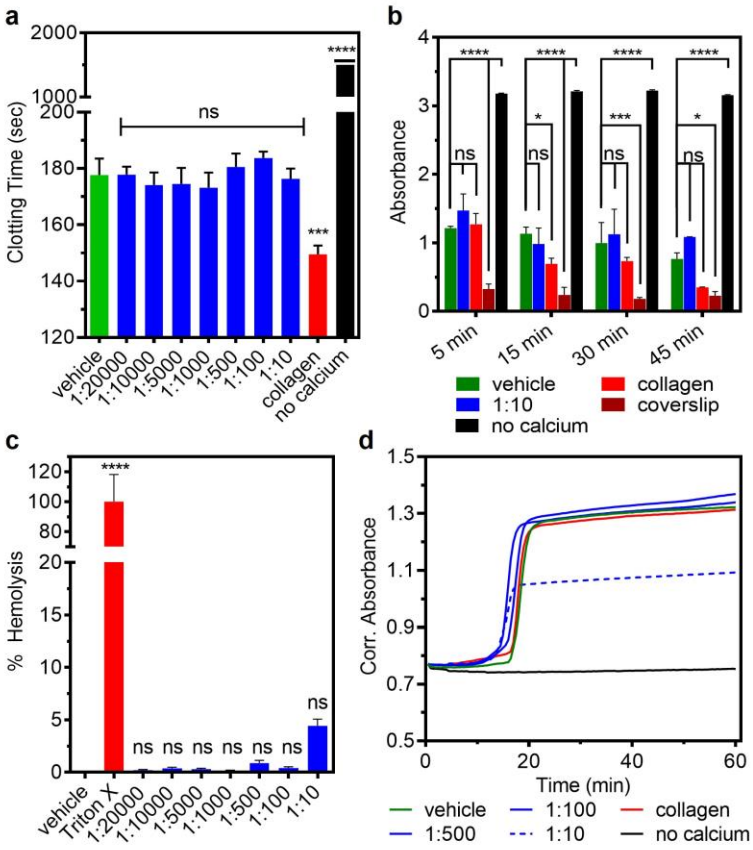


Figure 3.1.24. Hemocompatibility in human blood. a-d, Hemocompatibility analysis of progelator in human blood. **a**, Activated clotting time (ACT) in whole human blood. Collagen (pos) and blood without calcium (neg) controls. Samples without calcium exceed instrument maximum time range (>1500 sec). (n=6 per group) **b**, Whole blood hemostasis kinetics monitored at 5, 15, 30, and 45 min in recalcified human blood. Collagen (pos), glass coverslip (pos), and blood without calcium (neg) controls. (n=4 per group) **c**, Hemolysis of isolated RBCs after 1 hr incubation. 1% Triton X-100 (pos) and vehicle only (neg) normalization controls. (n=4 per group) **d**, Pro-thrombotic profile in platelet poor plasma (PPP) plotted with respect to time. Onset of coagulation is accompanied by an increase in absorbance. Collagen (pos) and no calcium (neg) controls. (n=6 per group) Vehicle in all samples contain biological fluid without progelator. Progelator concentrations are 1:20000, 1:10000, 1:5000, 1:1000, 1:500, 1:100, and 1:10 blood volume dilution of injected dosage. ns ($p > 0.05$), *** ($p \leq 0.001$), **** ($p \leq 0.0001$). Ordinary one-way ANOVA for comparison with vehicle standard for **a** and **c.** Two-way ANOVA at each timepoint for comparison with vehicle standard for **b**. Values are mean ± SEM.

Activated clotting times (ACT) were used as a standard method[62] that encompasses intrinsic and common coagulation pathways to assess thrombogenicity. Furthermore, as this method is influenced by increased sample viscosity due to clot formation, potential peptide cleavage by blood proteases and resulting self-assembly would decrease clotting times. No adverse effects were observed for up to 1:10 peptide:blood concentrations (**Figure 3.1.24a** and **Table 3.1.3**). In contrast, collagen showed a significant clot time reduction, and chelation of calcium prevented clotting

altogether. Whole blood clotting kinetics were also measured in the absence of an activator to monitor the influence of progelator on hemostasis. Similarly, no statistical difference in clotting was observed between the vehicle and the highest progelator concentration (1:10) at any timepoint (**Figure 3.1.24b**). A progelator doping analysis in **Figure 3.1.25** is consistent with these results**.** In contrast, collagen and glass controls increased the clot rate.

Table 3.1.3. Activated clotting times (ACT) in human blood. Supplemental data corresponding to **Figure 3.1.24a**. Average times reported ± standard error of mean (n=6 per group). Ordinary one-way ANOVA for comparison with vehicle standard. Values are mean ± SEM.

	standard	peptide in blood dilutions							positive control	negative control
	vehicle	1:20000	1:10000	1:5000	1:1000	1:500	1:100	1:10	collagen	no calcium
Average Time (sec)	178	178	174	175	173	181	184	176	150	>1500
SEM	(± 6)	(± 3)	(± 4)	(± 6)	(± 5)	(± 5)	(±2)	(±3)	(± 3)	n/a
P Value		> 0.9999	0.9941	0.9969	0.9787	0.9975	0.8982	0.9997	0.0002	< 0.0001
Summary		ns	ns	ns	ns	ns	ns	ns	***	****

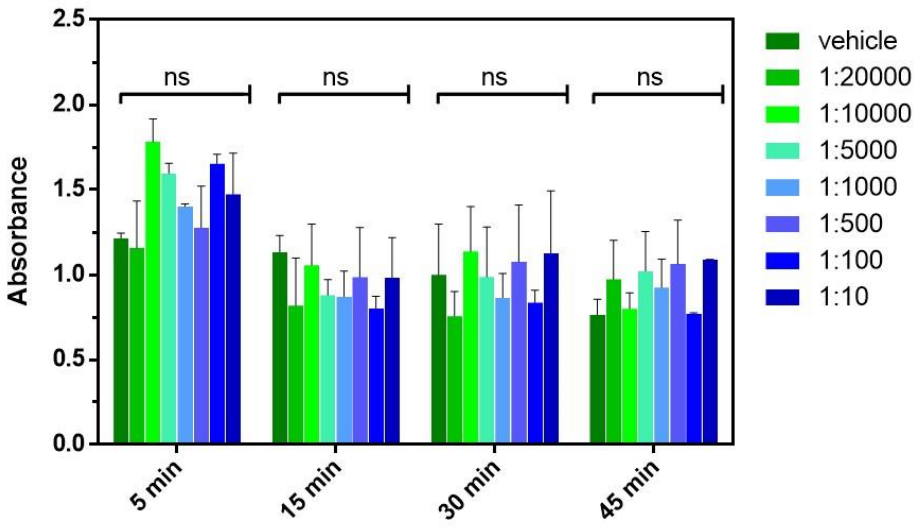


Figure 3.1.25. Hemostasis kinetics as a response of dosing. Supplementary data corresponding to **Figure 3.1.24b** in main text. Extent of clotting measured as absorbance at 405 nm as a function of dosing at 5, 15, 30, and 45 min in whole human blood. ns ($p > 0.05$). (n=4 per group). Two-way ANOVA at each timepoint for comparison with vehicle standard. Values are mean ± SEM.

Red blood cell (RBC) hemolysis in the presence of progelator was used to assess acute toxicity (**Figure 3.1.24c** and **Table 3.1.4**). Doses up to 1:10 revealed <5% hemolysis, which is below

the limit for consideration as a hemolytic biomaterial.[63] Finally, a pro-thrombotic assay using platelet poor plasma (PPP) was used to monitor non-platelet and phospholipid-specific effects on blood (**Figure 3.1.24d**), such as potential to inhibit thrombin activity, prevent crosslinking of fibrinogen, or sequestration of calcium for decreased platelet activation. This assay has the advantage of monitoring the intrinsic pathway only, which is useful for studying surface contact activation in blood-biomaterial interactions. The onset of coagulation is indicated by a steep rise in the absorbance vs time curve. A plateau in absorbance was reached within a few minutes and maintained over time, indicating a fully formed, stable clot. No changes to coagulation rate (slope), half-maximal coagulation time, and extent of coagulation (**Figure 3.1.26**) were observed in samples incubated with progelator up to doses of 1:100 peptide/blood.

Table 3.1.4. Hemolysis of red blood cells (RBCs). Supplemental data corresponding to **Figure 3.1.24c** in the main text. Nonhemolytic biomaterials classified by < 5% hemolysis. (n=4 per group). ns ($p > 0.05$), *** ($p \leq 0.001$), **** ($p \leq 0.0001$). Ordinary one-way ANOVA for comparison with vehicle standard. Values are mean ± SEM.

	standard	peptide in blood dilutions							positive control
	vehicle	1:20000	1:10000	1:5000	1:1000	1:500	1:100	1:10	1% Triton X-100
%Hemolysis	0.00	0.20	0.37	0.30	0.13	0.26	0.40	4.43	100.00
SEM	(± 0.07)	(± 0.06)	(± 0.12)	(± 0.08)	(± 0.07)	(± 0.26)	(± 0.12)	(±0.64)	(± 18.17)
P Value		> 0.9999	> 0.9999	> 0.9999	> 0.9999	0.9999	> 0.9999	0.9968	< 0.0001
Summary		ns	ns	ns	ns	ns	ns	ns	****

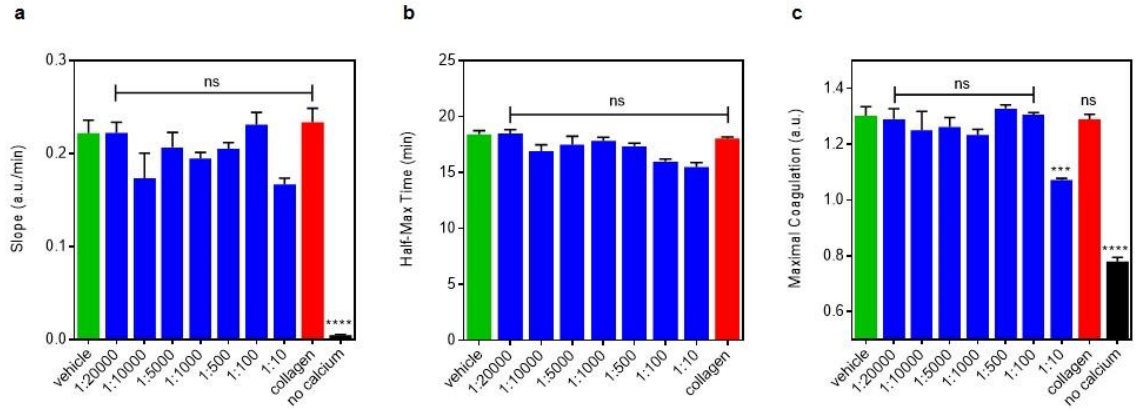


Figure 3.1.26. Pro-thrombotic assay statistics. Supplementary data corresponding to **Figure 3.1.24d** in main text. **a**, Coagulation rate measured as the maximal first derivative, or slope, of coagulation. **b**, Time at which coagulation is at half maximal completion. **c**, Extent of coagulation measured as the plateau absorbance. (n=6 group). Progelator concentrations are 1:20000, 1:10000, 1:5000, 1:1000, 1:500, 1:100, and 1:10 volume dilution in PPP. ns ($p > 0.05$), *** ($p \leq 0.001$), **** ($p \leq 0.0001$). Ordinary one-way ANOVA for comparison with vehicle standard. Values are mean ± SEM.

With hemocompatibility verified, we applied the progelator in an initial proof-of-concept study *in vivo* (**Figure 3.1.27)**. Enzyme-responsive progelator, $KFDF_{Cyclic,}$ doped with a small amount of Rho-$KFDF_{Cyclic}$ (5 mol%) for imaging, was injected into the infarct region 7 days post-MI in a rat ischemia-reperfusion model (**Figure 3.1.27a**). Assessment of hearts at 24 hr post-injection confirmed that progelator effectively gelled at the heart (**Figure 3.1.27b**). Histological and fluorescence analysis of heart sections revealed hydrogel assembly occurred at the site of MI in all rats (**Figure 3.1.27b-c)**.

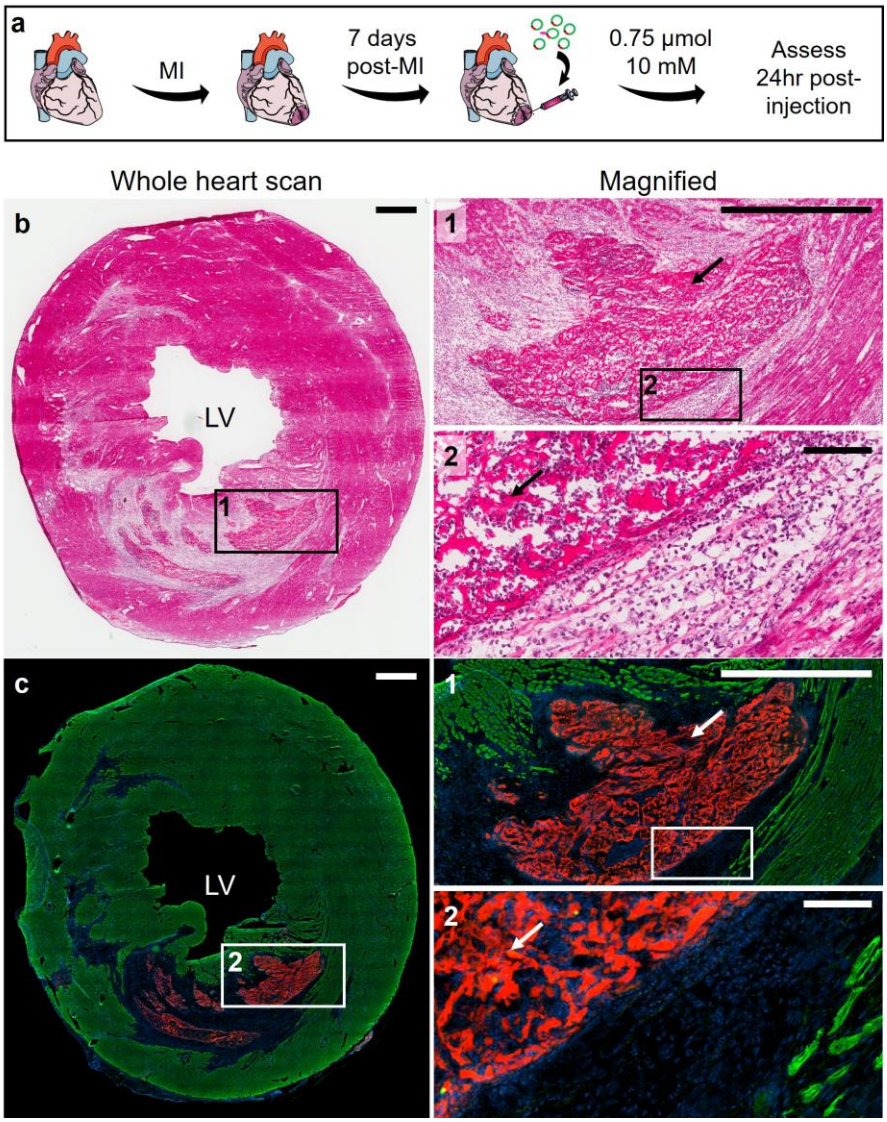


Figure 3.1.27. *In vivo* analysis in a rat ischemia reperfusion model. a, *In vivo* study timeline. Female Sprague-Dawley rats that received ischemic reperfusion surgery (35 min occlusion) were provided a single 75 µL intramyocardial injected of $KFDF_{Cyclic}$ progelator (5 mol% Rho-$KFDF_{Cyclic}$) at 7 days post-MI, to simulate a local injection. Animals were euthanized at 24 hr post-injection, and hearts were collected. Progelator formulated at 10 mM peptide in 1xDPBS (pH 7.4) (n=5 animals). **b**, H&E stained representative heart section. Selected regions at 10x magnification (inset **1**) and 40x magnification (inset **2**) illustrate hydrogel assembly in the infarct. Arrows point to peptide material. **c,** Corresponding fluorescence images of the neighboring section, stained for nuclei (blue) and α-actinin (green), with rhodamine-labeled peptide gels in red. LV is left ventricle. Scale bars are 1 mm (**b**, **c**, and inset **1**) and 100 µm (inset **2**), respectively.

Additional fluorescene images of heart sections from 5 rat hearts, along with a saline injected control, are displayed in **Figure 3.1.28** to emphasize localization of the peptide hydrogel preferentially

within the infarct tissue. Magnification of H&E stains show peptide hydrogel (bright pink) located within the infarct tissue (**Figure 3.1.29**). No excess immunogenic response is detected for infarct regions containing gel vs infarct only areas. Combined, these experiments demonstrate the activation and subsequent gelation of enzyme-responsive progelators to inflamed biological tissue.

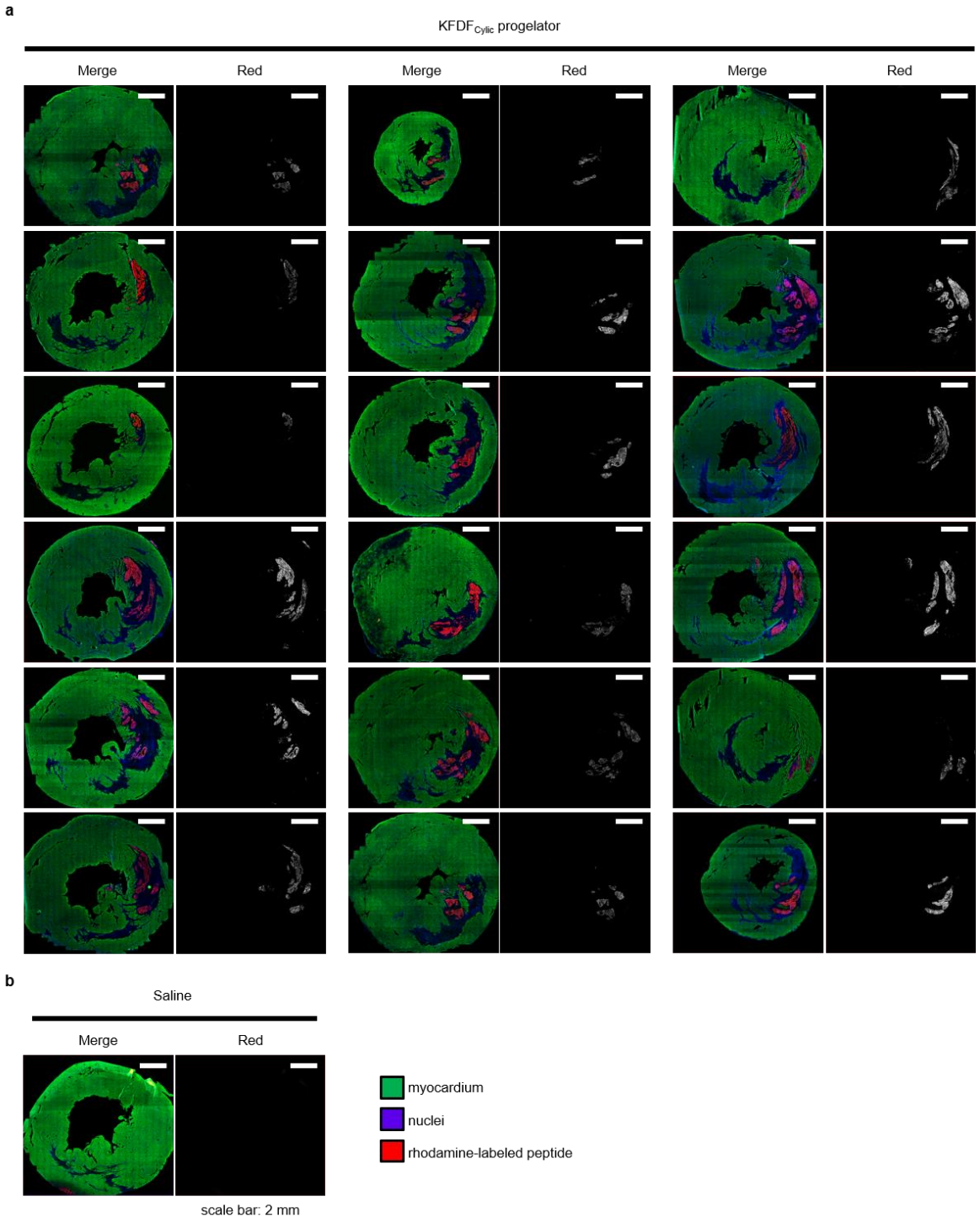


Figure 3.1.28. Heart slices visualized through IHC staining. **a**, Merged (left) and red channel-only (right) fluorescence images of 18 slices from 5 rat hearts that received intramyocardial injections of KFDF$_{Cyclic}$ progelator at 7 days post-MI and harvested 24 hr later. Images correlate with main text Fig. 6. Tissue is stained for myocardium with anti-α-actinin antibody (green) and nuclei with Hoechst (blue), and peptides are visualized through the rhodamine tag (red). Peptide is localized within the MI region (+blue-green). **b**, Representative slice of heart receiving saline injection at 7 days post-MI and harvested 24 hr later. Scale bar = 2 mm

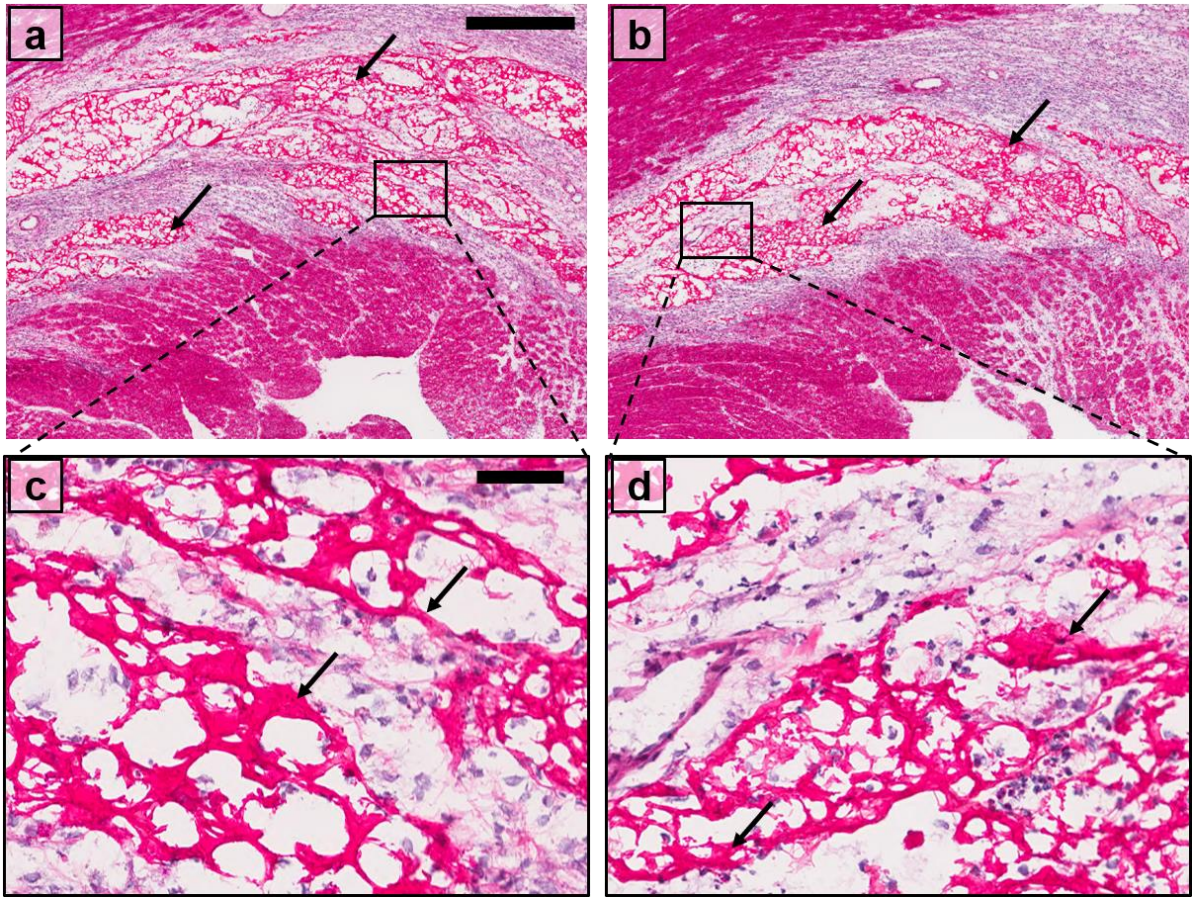


Figure 3.1.29. Representative H&E slices of injected heart. **a-d**, Intramyocardial injection of $KFDF_{Cyclic}$ progelator (75 µL, 10 mM in 1x DPBS) at 7 days post-MI and harvested 24 hr later. **a-b**, Infarct tissue at 5x magnification shown as blue stained cellular nuclei. Intact tissue is stained pink/blue. Eosinophilic peptide from progelator injection stains bright pink as indicated by black arrows. Scale bar 0.5 mm. **c-d**, Corresponding 40x magnified images. Scale bar 50 µm.

3.1.3 Discussion and Conclusions

The number of candidate biomaterials amenable to minimally invasive cardiac catheter delivery to the heart post-MI is limited. Consequently, translation of promising scaffolds from preclinical to clinical trials has been rare. In this study, we examined a platform modification strategy to enable one promising class of hydrogels, SAPs, to be injectable via a cardiac injection catheter by conformationally constraining linear SAPs into macrocyclic progelators which resist self-assembly (**Figure 3.1.1**). These progelators were further modified with a substrate recognition sequence for

endogenously expressed MI-associated proteases. We took the approach of designing peptide sequences based on a known SAP, and then utilizing *in silico* modeling to provide preliminary insight into any modifications that may cause disruption of gelation (**Figure 3.1.5**). These modified sequences were then prepared synthetically for testing. Subsequent experimental analysis of self-assembly characteristics and mechanical properties agreed well with these predictions, namely that sequence modifications did not interfere with self-assembly as β-sheets into fibrils and viscoelastic hydrogels (**Figure 3.1.7**). It is hypothesized that any number of other SAP sequences used in biomedical applications could similarly be adapted to our structurally dynamic platform.[64,65]

The versatility of our platform is demonstrated through the functionalization of two different SAPs sequences, which exhibit disparate self-assembly mechanisms, and yet form progelators with identical responsiveness. Cyclic progelators synthesized in **Figure 3.1.9** lacked the capacity to gel when sterically constrained. However, they exhibited responsiveness to enzymes that are inherently active in the MI during both the acute inflammatory phase and fibrotic phase (**Figure 3.1.17**). Despite the different cut sites recognized by MMP-9 catalytic domain, elastase, and thermolysin, similar secondary structure and nanoscale morphology changes were observed. Bulk cleavage of these sterically constrained materials resulted in healable viscoelastic hydrogels that were stable against excess proteolysis (**Figure 3.1.19**).

The development of smart structurally dynamic and responsive materials for tissue engineering post-MI is a relatively untapped field. With many scaffolds, the common issue remains that chemical modification (e.g. crosslinks, binding moieties, targeting motifs, or therapeutics drugs) can negatively impact material properties such as sample viscosity and gelation kinetics, which would preclude their use in catheters. With our design, mechanical differences (e.g. stiffness or healing kinetics) in the resulting hydrogel would not affect the initial progelator formulation. Importantly, we provide the first demonstration of low viscosity peptide-based progelators for use in a cardiac injection catheter with little resistance to flow (**Figure 3.1.23**). The results of these experiments demonstrate that the cyclic progelator acts as a non-Newtonian fluid for smooth catheter-based injection and still

retains the capacity to solidify when acted upon by endogenously expressed inflammatory enzymes in the heart, suggesting this could provide a useful strategy for cardiac catheter delivery *in vivo.*

With the potential for tissue leakage into the bloodstream, thrombogenicity of transendocardially injected biomaterials is a concern. Synthetic modifications to the KFDF SAP were shown to be hemocompatible and non-thrombogenic through a comprehensive assessment of whole blood clotting times, hemostatic kinetics, RBC hemolysis, and pro-thrombotic assays (**Figure 3.1.24**A dosing analysis shows no statistically significant difference in hemostasis due to increasing progelator concentration in whole blood. The extent of coagulation in platelet poor plasma was only altered at the highest peptide dose which indicates that local high concentrations of peptide have an minor anti-coagulative effect on the intrinsic coagulation (contact-based) pathway; furthermore, the impact that our peptide does have on coagulation was shown to be independent of platelet-dependent thrombus formation, a key player in the pathogenesis of acute MI.[66] This conclusion is supported by the lack of change in pro-thrombotic profiles when incubated with collagen, which increases clotting rates only through the activation of platelet aggregation.[67] Given a “standard” clinical concentration of 1:10,000,[68] which assumes that no material was injected into the heart wall and instead escaped into the bloodstream, we observed no adverse effects on coagulation at this clinically relevant dose. These results indicate that this platform for generating an inert cyclic adduct of known SAPs should not result in unwanted blood interactions during delivery. Critically, this result expands the scope of our progelator design for even less invasive and technically challenging delivery via intracoronary infusion cardiac catheter.[69,70]

Our platform enables facile delivery of a free-flowing progelator, and on-demand gelation at the site of inflammation (**Figure 3.1.27**). *In vivo* analysis of $KFDF_{Cyclic}$ progelator revealed successful gelation of activated hydrogel scaffolds in a rat MI model. As such, we have demonstrated a simplistic strategy that uses the naturally complex MI microenvironment for delivery and smart assembly in tissue. This proof-of-concept test paves the way for exploring the amenability of various other SAP systems (e.g. RAD16-II) with our progelator system for cardiac catheterization *in vivo*. Additionally,

there exists the potential to use this platform in conjunction with various therapeutics. Herein, we observed that covalent conjugation of a rhodamine dye to cyclic progelators did not disrupt gelation. We envision a modular system to deliver and sustain any number of covalently bound therapeutics (e.g. small molecule drugs or short peptides). For larger therapeutics (e.g. cell therapiesor growth factors), formulation as a nonviscous mixture for delivery, and subsequent encapsulation within locally activated networks, might provide a means for targeted cardiac regeneration without the need for complex synthetic chemistries. Ultimately, our simple strategy for structural control of self-assembling peptides could be employed for minimally invasive delivery of promising therapeutic peptides to other forms of injury or disease where MMPs are upgregulated, including osteoarthritis,[71] cartilage tissue repair,[41] nerve damage,[72,73] and acute brain injury.[74]

3.1.4 Experimental Details

General information**.** Amino acids used in Fmoc SPPS were purchased from AAPPTec and NovaBiochem. All other synthetic materials were obtained from Sigma-Aldrich and used without further purification unless otherwise noted. MMP-9 (recombinant human catalytic domain) (BML-SEro360) was acquired from Enzo Life Sciences, as a 1.0 mg/mL solution at 40 U/µL in 50mM TRIS, pH 7.5, 1mM $CaCl_2$, 300mM NaCl, 5µM $ZnCl_2$, 0.1% Brij-35, and 15% glycerol. Porcine pancreatic elastase (3246821000U) was acquired from EMD Millipore, as a lyophilized powder (22 U/mg). Thermolysin (V400A) was acquired from Promega, as a lyophilized powder. Unspun whole human blood (citrated, non-heparinized) was obtained from Biological Specialty Corporation (LS23 95099) and stored at 1-6 °C.

Peptide synthesis**.** Peptides were synthesized in an AAPPTec Focus XC peptide synthesizer. Peptides with C terminal amides were synthesized on rink amide MBHA resin and peptides with C-terminal carboxylic acids were synthesized on Wang-OH resin using double coupling conditions for the first amino acid. HBTU (*N*,*N*,*N*′,*N*′-tetramethyl-O-(1H-benzotriazol-1-yl) uronium hexafluorophosphate) was used as the general coupling agent. When included, rhodamine was

incorporated during the synthesis at the N-terminus of the sequence as 5(6)-carboxytetramethyl rhodamine using HATU (1-[Bis(dimethylamino)methylene]-1H-1,2,3-triazolo[4,5-b]pyridinium 3-oxid hexafluorophosphate) as the coupling agent. 5(6)-carboxytetramethyl rhodamine was synthesized as previously described.[75] General peptide cleavage and deprotection was performed in 95:2.5:2.5 (%v/v) trifluoroacetic acid (TFA), triisopropyl silane (TIPS), and H_2O, respectively, for 2 hr. Cleaved peptides were precipitated in cold anhydrous ether (3x) to yield solid crude. Semi-protected peptides containing Cys(acm) were purified prior to cyclization. To synthesize cyclic progelators, iodine was used to simultaneously deprotect Cys(acm) and initiate disulfide bond formation under dilute conditions to favor intramolecular macrocyclization.[76] To a solution of semi-protected peptides (500 µM) in a mixture of acetic acid/methanol/H_2O (1:16:4) was slowly added 0.1 M methanolic iodide until the yellow color persisted (~4-5 eq). The reaction was vigorously stirred at room temperature for 2 h and reaction completion was confirmed by LCMS. After 2 hr reaction, Amberlite IRA-400 Resin (chloride form) was stirred in the solution for 1 hr to quench excess iodine and absorb reacted iodide ions. Filtrated was placed on a rotary evaporator to remove acetic acid and methanol. The remaining solution was diluted with H_2O and lyophilized to a white powder. By HPLC no dimerization was observed. For cyclization kinetics analysis (**Figure 3.1.92c-e**), the N-terminal Fmoc was temporarily left on unlabeled peptides for improved peak separation during purification.

Peptide purification and analysis**.** Analytical scale RP-HPLC analysis of peptides was performed on a Jupiter Proteo90A Phenomenex column (150 x 4.60 mm) using a Hitachi-Elite LaChrom L2130 pump with a UV-Vis detector (Hitachi-Elite LaChrom L-2420) monitoring at 214 nm, 256 nm, 290 nm, and 565 nm. Gradients performed over 30 min. LCMS was performed with a Waters AQUITY UPLC System using a C-18 column over a 4 or 10 min gradient. Peptides were purified with a Jupiter Proteo90A Phenomenex column (2050 x 25.0 mm) on an Armen Glider CPC preparatory phase HPLC over a 43 min gradient to yield 90-95% purity. For all RP-HPLC assays and purifications, gradient solvent systems utilized Buffer A (H_2O with 0.1% TFA) and Buffer B (acetonitrile with 0.1% TFA). For all LCMS assays, gradient solvent systems used Buffer A (H_2O) and Buffer B (acetonitrile

with 0.1% formic acid). Crude peptide was prepared for purification in 5:25:70 acetic acid/Buffer A/Buffer B via initial dissolution in acetic acid with sonication, followed by addition of ACN then H_2O. Unless otherwise stated, peptides were purified using a gradient of 25-45% Buffer B over 30 min and 50 min for analytical HPLC and preparatory phase HPLC, respectively. Following purification, product was analyzed by ESI to verify identity (see **Figure 3.1.4**). Due to the large number of cis/trans configurational isomers that our cyclic progelators could adopt,[77,78] and amphiphilic self-assembling nature of our peptides, peak resolution via HPLC was low in many instances. We relied on various mass spectrometry techniques (ESI, MALDI, HRMS, and Tandem-MS) to verify purity of isolated materials.

Mass spectrometric (MS) analysis of peptides**.** General mass spectra were obtained at the UCSD Chemistry and Biochemistry Molecular Mass Spectrometry Facility using a Micromass Quattro Ultima Triple Quadrupole Electrospray Ionization (ESI) mass spectrometer or Bruker Biflex IV MALDI-TOFMS using HCCA (1:1 v/v) as the matrix. HRMS on a Thermo LTQ Orbitrap XL MS and Tandem-MS on a Thermo LCQdeca-MS were collected for cyclic progelators to discern conformation as cyclic or linear. DisConnect software[79] was used to unambiguously characterize disulfide connectivity. The following settings were used: MS^2 fragmentation ions, monoisotopic mass calculations, tolerance ± 3Da, normal peptide fragments (no losses), and calculations based on ion-trap filtering.

UV Absorbance Spectra**.** UV absorbance spectra of peptide labeling was measured on a ThermoScientific Nanodrop 2000c.

Progelator sterilization and formulation for *in vivo* analysis HPLC purified peptides were dialyzed with 1 kDa MW cutoff tubing into milliQ H_2O, sterile filtered through a 0.2 µm PES filter, and lyophilized to a powder. Peptide was reconstituted prior to injection with sterile pH 9 H_2O to form a clear solution (11.11 mM) then diluted further with sterile 10x DPBS to a final concentration of 10 mM peptide in 1x DPBS (pH 7.4). Solutions for *in vivo* analysis contained 5 mol% rhodamine labeled progelator (0.5 mM labeled + 9.5 mM unlabeled) for fluorescence imaging purposes.

Transmission electron microscopy (TEM). Formvar/Carbon-coated 400 mesh Cu grids (Ted Paella, Inc.) were glow discharged for 90 s and spotted with 4-5 µL peptide sample (100 µM) and set for 5 min. Grids were washed with distilled H_2O (10 drops), stained with 1% w/w uranyl acetate (3 drops), and wicked dry with filter paper. TEM images were acquired on an FEI Tecnai G2 Sphera at 200 kV.

Static and dynamic light scattering (SLS and DLS). Light scattering measurements were performed on a Wyatt DynaPro NanoStar at 37 °C (λ = 657 nm). For each DLS measurement, 10 acquisitions for 10 sec were taken. Samples were prepared at 1 mg/mL in either H_2O, 1x DPBS, or 295 mM sucrose (pH 7.4). Experiments with enzyme activation used 1:4500 enzyme/substrate molar ratio.

Experimental circular dichroism (CD). Peptides were dissolved at a final concentration of 125 µM (labeled peptides) or 500 µM (unlabeled peptides) in 10 mM Tris buffer or H_2O (for TCEP reduction only) at pH 7.4, to reduce signal interference seen with DPBS at lower wavelengths. UV-Vis circular dichroism (CD) was measured on a Jasco J-810 Spectropolarimeter to evaluate the secondary structure of peptide samples. Measurements were taken using the following settings: wavelength range = 190-260 nm, scanning speed = 50 nm/min, response time = 2 s, data pitch = 1 nm, band width = 1 nm, accumulations = 3, pathlength = 1 mm, and temperature = 37 °C. Spectra are presented as an average of all accumulations. Sample voltage was monitored to verify the signal intensity did not exceed 800 mV within the wavelength range (**Figure 3.1.30**). Spectra were converted from units of millidegrees (mdeg) to molar ellipticity [θ] using the following equation:

$$[\theta] = \frac{mdeg * M}{C * L * 10}$$

, where mdeg is the measured absorbance of circularly polarized light, C is concentration in g/L, M is the mean residual weight in g/mol, and L is the cell pathlength in cm.

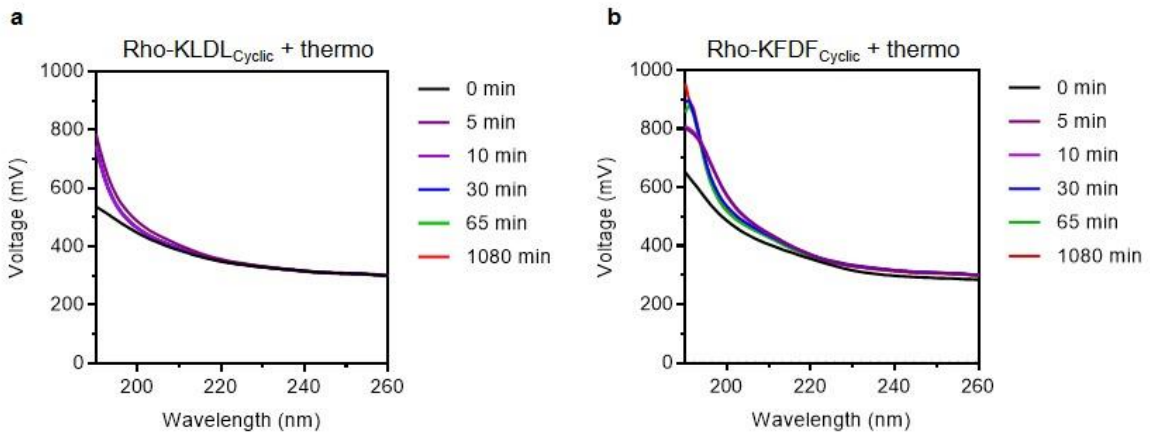


Figure 3.1.30. Voltage plots for thermolysin cleavage of labeled progelators by CD. Corresponding data for **Figure 3.1.17c,f** CD spectra of time-course analysis of thermolysin cleavage. **a**, High tension (HT) voltage plot of thermolysin cleavage of Rho-KLDL$_{Cyclic}$ over time. **b**, High tension (HT) voltage plot of thermolysin cleavage of Rho-KFDF$_{Cyclic}$ over time. Detector saturation at wavelengths where HT voltage > 800 mV. Peptide concentration 125 μM. [substrate:enzyme] = 4500:1.

Computational modeling with FibPredictor**.** FibPredictor was utilized as a commercially available software for generating native-like amyloid fibril structures.[42] This software was chosen for our study due to its unique ability to reliably model all classes of amyloid fibrils starting from sequence-only input. The algorithm combines β-sheet model building, β-sheet replication, and symmetry operations with side-chain prediction and statistical scoring functions, for computational predictions on amyloid fibril structures of self-assembling peptides utilized in this study. From each random model generated, a SCRWL internal scoring function was used by SCWRL4 to predict the energetically lowest side chain orientations. This scoring function was used to calculate the minimal total energy of the entire model and outputs coordinates for the structure as a PDB file with predicted side chains using the same residue numbering and chain identifiers as the input structure. To identify the most energetically favorable candidate structures in the ensemble, both Amb_3b (computationally more efficient)[80] and GOAP (more accurate)[81] statistical scoring functions were used to calculate total energies of the protein structure. Reported energies are unitless as they are empirically derived scores, thus it is not advisable to interpret results as kcal/mol. Normalized GOPA scores are useful for comparing fibrils of different sizes. Three generations of modeling were performed with literature-recommended parameters shown in **Table 3.1.1**. Results of top model for each peptide sequence

from the third-generation analysis are reported in **Table 3.1.2**. Corresponding structures displayed in **Figure 3.1.5**. Output PDB files, containing the atomic coordinates of the chromophores, from top models were used to generate theoretical CD spectra with DichroCalc.[45]

Table 3.1.1. FibPredictor experimental setup over three generations. Input included the peptide sequence, number of strands per sheet (x 2 sheets total) to model, and selection criterion about scoring functions, and rotation operations performed on the second β-spine relative to the first β-spine for generating all classes of amyloid fibrils. The number of random models, and distances angle variation between sheets, were also selected to improve modeling conditions. Changes to parameters with each future generation were a result of model analysis from the (n-1) generation.

	Generation 1	Generation 2	Generation 3
Number of strands per sheet	2	4	4
Sense of β-sheet orientation	Both	Antiparallel or parallel	Selected in Gen 2
Scoring function(s)	Amb_3b_score only	Amb_3b and GOAP score	Amb_3b and GOAP score
Rotations	x,z,zx,no rotation	x,z,zx,no rotation	x,z,zx,no rotation
Random models	30	60	200
Distance variation between the sheets	7 Å	7 Å	6 Å
Minimum distance between the sheets	3 Å	3 Å	4 Å
Angle variation between the sheets	45˚	45˚	10˚

Table 3.1.2. Experimental CD and theoretical modeling of gelators. Corresponds to **Figure 3.1.5** and **Figure 3.1.7**. Observed shift in high energy minimum in CD spectra indicate reorientation in 2˚ structure. Calculated orientations for minimal total energy structures generated in FibPredictor agree with observed inferences. Internal scoring SCWRL4 energies and corresponding empirical (Amber_3b) and statistical (SCWRL4) scores for minimal energy models are displayed for the top model of each sequence. Normalized GOAP scores are provided for comparison of fibrils of different sizes. Scores are unitless.

Peptide	Sequence	Obs. CD π→π* Peak	Obs. CD Inference	Theor. CD Orientation	SCWRL4 energy	Amb_3b score	GOAP score	GOAP normalized
KLDL	$(KLDL)_3$	---	antiparallel	antiparallel	353.796	-96.984	-7271.93	-75.7493
$KLDL_{Control}$	$LAG(KLDL)_3PLG$	Blue-shifted	Parallel	Parallel	351.78	-112.363	-7675.04	-53.2989
$KLDL_{Linear}$	$C(KLDL)_3PLGLAGC$	Blue-shifted	Parallel	Parallel	370.407	-128.576	-8610.19	-53.8137
KFDF	$(KFDF)_3$	----	Antiparallel	Antiparallel	621.622	-53.771	-7179.08	-74.7821
$KFDF_{Control}$	$LAG(KFDF)_3PLG$	Blue-shifted	Parallel	Parallel	262.448	-158.008	-7755.24	-53.8558
$KFDF_{Linear}$	$C(KFDF)_3PLGLAGC$	Blue-shifted	parallel	parallel	340.488	-158.782	-11096.7	-69.3543

Theoretical CD spectra with DichroCalc**.** DichroCalc was used to calculate CD spectra using predicted PDB from FibPredictor. This web interface predicts secondary structure type using a variety of matrix method parameters, which have been derived from *ab initio* calculations.[45] These

parameters include the peptide chromophore in the far-UV, charge-transfer between neighboring peptide groups in the deep-UV, and aromatic side chain chromophores with transitions in the near-UV. Full analysis CD spectra were output in units of molar ellipticity [θ] vs wavelength.

Table 3.1.3. DisConnect analysis of Rho-KLDL$_{Cyclic}$ progelator. Data from DisConnect software displayed in tables with peak labels corresponding to **Figure 3.1.12a-b**. MS^2 fragmentation sequences, mass and charge values, and conclusions about cysteine connectivity. B is Rhodamine (413.15 m/z), | indicates separate peptides linked through a cysteine disulfide bond.

Peak	Sequence	m/z	Z (+)	Conclusion
A	BC1 | KLDLPLGLAGC2	806.36 / 1612.72	1 and 2	All Cys connected
A	BC1K | LDLPLGLAGC2	806.36 / 1612.72	1 and 2	All Cys connected
A	BC1KL | DLPLGLAGC2	806.36 / 1612.72	1 and 2	All Cys connected
A	BC1KLD | LPLGLAGC2	806.36 / 1612.72	1 and 2	All Cys connected
A	BC1KLDL | PLGLAGC2	806.36 / 1612.72	1 and 2	All Cys connected
B	DLKLDLKLDLPLGLAG	837.98	2	0|0|0|0
B	KLDLKLDLKLDLPLG	837.995	2	0|0|0|0
C	BC1K | DLKLDLPLGLAGC2	984.46	2	All Cys connected
C	BC1KLD | KLDLPLGLAGC2	984.46	2	All Cys connected
C	BC1KLDLK | DLPLGLAGC2	984.46	2	All Cys connected
C	BC1KLDLKLD | PLGLAGC2	984.46	2	All Cys connected
D	BC1 | KLDLKLDLPLGLAGC2	1041	2	All Cys connected
D	BC1K | LDLKLDLPLGLAGC2	1041	2	All Cys connected
D	BC1KL | DLKLDLPLGLAGC2	1041	2	All Cys connected
D	BC1KLD | LKLDLPLGLAGC2	1041	2	All Cys connected
D	BC1KLDL | KLDLPLGLAGC2	1041	2	All Cys connected
D	BC1KLDLK | LDLPLGLAGC2	1041	2	All Cys connected
D	BC1KLDLKL | DLPLGLAGC2	1041	2	All Cys connected
D	BC1KLDLKLD | LPLGLAGC2	1041	2	All Cys connected
D	BC1KLDLKLDL | PLGLAGC2	1041	2	All Cys connected
E	BC1K | LKLDLKLDLPLGLAGC2	1161.59	2	All Cys connected
E	BC1KL | KLDLKLDLPLGLAGC2	1161.59	2	All Cys connected
E	BC1KLDLK | LKLDLPLGLAGC2	1161.59	2	All Cys connected
E	BC1KLDLKL | KLDLPLGLAGC2	1161.59	2	All Cys connected
E	BC1KLDLKLDLK | LPLGLAGC2	1161.59	2	All Cys connected
E	BC1KLDLKLDLKL | PLGLAGC2	1161.59	2	All Cys connected
F	BC1KLDLKLDLKLD | LGLAGC2	1170.58	2	All Cys connected
F	BC1KLDLKLDLKLDL | GLAGC2	1170.58	2	All Cys connected
G	BC1KL | LKLDLKLDLPLGLAGC2	1218.13	2	All Cys connected
G	BC1KLDLKL | LKLDLPLGLAGC2	1218.13	2	All Cys connected
G	BC1KLDLKLDLKL | LPLGLAGC2	1218.13	2	All Cys connected
H	BC1KL | LGLAGC2	1287.56	1	All Cys connected
H	BC1KLD | GLAGC2	1289.51	1	All Cys connected
H	BC1KLDLK | GC2	1289.54	1	All Cys connected
I	BC1KLD | LGLAGC2	1402.59	1	All Cys connected
I	BC1KLDL | GLAGC2	1402.59	1	All Cys connected
I	BC1KLDLKL | GC2	1402.62	1	All Cys connected
J	BC1KL | LPLGLAGC2	1497.69	1	All Cys connected
J	BC1K | DLPLGLAGC2	1499.64	1	All Cys connected
J	BC1KLD | PLGLAGC2	1499.64	1	All Cys connected
K	BC1KLD | DLPLGLAGC2	1727.75	1	All Cys connected

Table 3.1.4. DisConnect analysis of Rho-KFDF$_{Cyclic}$ progelator. . Data from DisConnect software displayed in tables with peak labels corresponding to **Figure 3.1.12c-d**, MS^2 fragmentation sequences, mass and charge values, and conclusions about cysteine connectivity. B is Rhodamine (413.15 m/z), | indicates separate peptides linked through a cysteine disulfide bond

Peak	Sequence	m/z	Z (+)	Conclusion
A	BC1K | DFKFDFPLGLAGC2	1035.445	2	All Cys connected
A	BC1KFD | KFDFPLGLAGC2	1035.445	2	All Cys connected
A	BC1KFDFK | DFPLGLAGC2	1035.445	2	All Cys connected
A	BC1KFDFKFD | PLGLAGC2	1035.445	2	All Cys connected
B	KFDFKFDFKFDFPLGLAGC2	1104.035	2	69|0|0|0
C	BC1 | DFKFDFKFDFPLGLAGC2	1240.03	2	All Cys connected
C	BC1KFD | FDFKFDFPLGLAGC2	1240.03	2	All Cys connected
C	BC1KFDF | DFKFDFPLGLAGC2	1240.03	2	All Cys connected
C	BC1KFDFKFD | FDFPLGLAGC2	1240.03	2	All Cys connected
C	BC1KFDFKFDF | DFPLGLAGC2	1240.03	2	All Cys connected
D	BC1KFDFKFDFKFDF | GLAGC2	1272.545	2	All Cys connected
E	BC1KFDFKFDFKFDFP | LAGC2	1292.56	2	All Cys connected
E	BC1KFDFKFDFKFDFPL | AGC2	1292.56	2	All Cys connected
F	BC1K | DFPLGLAGC2	1533.63	1	All Cys connected
F	BC1KFD | PLGLAGC2	1533.63	1	All Cys connected
G	BC1 | KFDFPLGLAGC2	1680.7	1	All Cys connected
G	BC1K | FDFPLGLAGC2	1680.7	1	All Cys connected
G	BC1KF | DFPLGLAGC2	1680.7	1	All Cys connected
G	BC1KFD | FPLGLAGC2	1680.7	1	All Cys connected
G	BC1KFDF | PLGLAGC2	1680.7	1	All Cys connected
H	BC1KFD | DFPLGLAGC2	1795.73	1	All Cys connected
I	BC1 | DFKFDFPLGLAGC2	1942.8	1	All Cys connected
I	BC1KFD | FDFPLGLAGC2	1942.8	1	All Cys connected
I	BC1KFDF | DFPLGLAGC2	1942.8	1	All Cys connected

In vitro enzyme cleavage of cyclic peptide progelator**.** Unless otherwise stated, enzyme cleavage experiments were performed on progelator at a final concentration of 500 µM in 1x enzyme cleavage buffers. MMP-9 cleavages were performed at 1:1000 enzyme/substrate molar ratio in 1x buffer (50 mM Tris-HCl, 200 mM NaCl, 5 mM $CaCl_2$, 1 mM $ZnCl_2$, pH 7.5) for 5 hr. Elastase cleavages were performed at 1:250 enzyme/substrate molar ratio in 1x buffer (100 mM Tris-HCl, 0.2 mM NaN_3, pH 8.0), and thermolysin (50 mM Tris-HCl, 0.5 mM $CaCl_2$) for 5 hr. Thermolysin cleavages were

performed at 1:4500 enzyme/substrate molar ratio in 1x buffer (1x DPBS, pH 7.4) for 15 min. Analysis of unlabeled cyclic peptide progelator cleavage by CD (Fig. 4c) was conducted with serials additions of thermolysin (4 x 1:18,000 enzyme/substrate) over a period of 73 hr in 10 mM Tris buffer. Control samples utilized denatured enzymes under the same conditions. MMP and elastase were heat denatured with 10 min incubation at 65 °C. Thermolysin was inactivated by incubation with 10% (v/v) EDTA (0.5 M, pH 8.0).

Rheological characterization**.** All peptide samples were prepared at 10 mM peptide, except for those used to assess the effect of SAP functionalization with respect to weight (15 mg/mL). Viscous and viscoelastic properties were assessed using a stress-controlled rheometer (TA Instruments AR-G2) equipped with a Peltier plate to control temperature and a 20 mm diameter parallel plate geometry. Unless otherwise stated all measurements were taken at an angular frequency of 2.5 rad s^{-1}, strain of 0.5%, and temperature of 37 °C. Measurements were performed with a gap height of 1000 μm and repeated three times (except for step-strain and timecourse measurements) to ensure reproducibility. To prevent water evaporation, mineral oil was wrapped around the edge of the geometry at the air-sample interface. For viscoelastic measurements the apparatus was used in oscillatory mode. To ensure the measurements were made in the linear viscoelastic regime (LVR), strain sweeps were performed between 0.05-50 % strain and showed no variation in storage (*G'*) and loss (*G")* moduli up to a strain of 0.5%. The dynamic moduli of the hydrogels were measured as a function of frequency in the range 0.25–100 rad s^{-1} at a strain of 0.5%. Continuous step-strain oscillations were used to monitor hydrogel healing through disruption (3 min, 100% strain) and recovery (15 min, 0.5% strain) cycles (n=3). For viscosity measurements the apparatus was used in steady state flow mode. The viscosity of the samples was measured as a function of shear rate in the range 0.1–10 s^{-1} (5% tolerance). For timecourse measurements of enzyme activation, a stock of cyclic peptide (1 mL, 10 mM, 1x DPBS, pH 7.4) was prepared and incubated at 37 °C. A sample from this stock was applied to the rheometer for storage and loss moduli measurements (2.5 rad/s, 0.5% strain) over a 35-40 min period. This sample was removed and replaced with an identical sample mixed

via pipetting for 5 sec with thermolysin (1:4500 enz/peptide) followed by immediate addition to the rheometer. Delay time between enzyme addition and new rheology measurements was ~30 sec.

In vitro catheter injections and effect on assembly**.** *In vitro* injection of peptide systems through the 27G inner nitinol tubing of a MyoStar catheter was performed, as previously described.[60]Peptide solution (0.6-0.8 mL) was prepared at 10 mM in 1x DPBS (pH 7.4) and loaded into a 1 mL Leur Lock syringe attached to a syringe pump set to a flow rate of 0.6 mL/min. Catheters were inspected for potential clogging during injection.

Hemocompatibility analysis**.** For all measurements, peptide stocks in 1xDPBS were prepared such that the final concentration (v/v) in blood or plasma were 1:10, 1:100, 1:500,1:1000, 1:5000, 1:10000, and 1:20000 (peptide:fluid volume). Controls with collagen as a procoagulant initial platelet-adhesive surface (0.095 mg/mL as per literature[82] or 1:240 dilution) or with calcium chelated by sodium citrate utilized 1xDPBS as a vehicle to ensure consistent blood dilution in all experiments. Peptide stocks, whole human blood, isolated red blood cells (RBCs), and platelet poor plasma (PPP) were warmed to 37 °C immediately prior to use. Plate reader measurements were conducted on an EnSpire Multimode Plate Reader with 96-well tissue culture plates (TCP).

Activated clotting times (ACT) with whole human blood. A Hemochron 801 instrument calibrated with an electronic system verification (ESV) device was used to measure activated clotting time (ACT) of whole human blood. Activated clotting times (ACT) were determined using recalcified citrated whole human blood to minimize variability in starting time points for clotting in all assays.[82] To each Hemochron P214 tube with glass beads was added 4 µL $CaCl_2$ (1.1 M) and 36 µL peptide stock or additive (12.2x final blood concentration). Samples were mixed thoroughly for 30 s to soak the glass beads and incubated 30 s at 37 °C. Citrated whole human blood (400 µL) was then added (t=0 s), mixed by hand for 10 s, and added to the instrument. Time points at which the magnet was displaced by clot formation were recorded by the instrument. Collagen (0.095 mg/mL) was used as a positive control to decrease clotting time. Vehicle (1x DPBS) served as a standard for blood without additive. Samples without calcium, serving as the negative control, exceeded instrument maximum

time range (>1500 sec). Each experiment was performed n=6 times with averages and standard error of the mean (SEM) plotted.

Whole blood hemostasis kinetics. Changes to time-dependent hemostasis were monitored using a non-activated whole blood clotting assay.[83] Briefly, 100 µL of citrated whole human was mixed with 10 µL of peptide or collagen stock (11.5x final blood concentration) and 5 µL of $CaCl_2$ (230 mM). Collagen (0.095 mg/mL) and glass coverslips were used as positive controls to increase clotting rates from an additive and contact initiated perspective, respectively. Samples without calcium, where no clot was observed at any timepoint, served as negative controls. Aliquots (100 µL) were transferred to a 12-well TCP, covered, and incubated at r.t. for 5 min, 15 min, 30 min, and 45 min. Each sample was prepared in triplicate. At the end of each time point, RBCs not caught in the thrombus were lysed by gently adding 3 mL distilled H_2O and incubating for 5 min. Each well was sampled (200 µL), taking care not to disturb the clot, and transferred to a 96 well plate for analysis. Released hemoglobin from lysis was detected by measuring the absorbance at 405 nm (height 4.0 mm, 100 flashes) using a plate reader. Extent of clotting is inversely proportional to measured absorbance. Averages (n=3) and standard error of the mean (SEM) are plotted.

Hemolysis assay**.** Acute toxicity of cyclic peptide progelator was measured with a RBC hemolysis assay specific to biomacromolecular drug analysis, as previously described.[84] Averages (n=4) and standard error of the mean (SEM) for absorbance measurements (at 540 nm) were plotted.

Pro-thrombotic assays**.** The intrinsic coagulation pathway was assessed using a pro-thrombotic assay, as previously described.[83] Collagen (0.095 mg/mL), which interacts with platelets, was used to confirm proper preparation of PPP to study platelet-independent effects of our peptide. Samples without calcium, where no clot was observed at any timepoint, served as negative controls. Untreated vehicle (1x DPBS) samples were used as a standard to compare peptide dosing impacts. For each sample, n=6 repeats were conducted. Coagulation profiles were obtained by measuring well absorbance at 405 nm (height 7.0 mm, 100 flashes) at 30 sec intervals for 60 min. Onset to clotting was detected as a sharp increase in sample turbidity.

In vivo studies. All animal experiments were conducted in accordance with the guidelines established by the Institutional Animal Care and Use Committee at the University of California San Diego and the Association for the Assessment and Accreditation of Laboratory Animal Care and approved by the Institutional Animal Care and Use Committee at UCSD (A3033-01). Female Sprague Dawley rats (225 – 250 g) were used in all studies.

Intramyocardial injections of peptide into infarcted rats**.** MI was performed via 35-min ischemia-reperfusion and intramyocardial injections were performed under isoflurane, using a previously described procedure.[85,86] Briefly, cyclic peptide (75µL, 0.75 µmol, 10 mM) was administered as a single injection into the infarct with a 27 G needle at 7 days post-MI. Animals were euthanized with an overdose of pentobarbital (200 mg/kg) at 24 hours post-injection (n=5).

Cryo-sectioning, histology, and immunofluorescence imaging**.** After euthanasia, hearts were resected, fresh frozen in TissueTek OCT, and cryosectioned for histological analysis. Slides were either stained with hematoxylin and eosin (H&E) to identify the infarct region or stained for immunofluorescence analysis. H&E slides were imaged on an Aperio ScanScope CS^2 at 20x magnification. For immunofluorescence, tissue sections were permeabilized in acetone (-20 ˚C) for 1.5 min and blocked with 2% BSA and 0.3% Triton X-100 in PBS. Myocardium was labeled using mouse anti-α-actinin antibody (1:800 dilution in blocking buffer, 1 hr incubation, Sigma-Aldrich) and an Alexa Fluor 488 goat anti-mouse IgG secondary antibody (1:500 dilution in blocking buffer, 30 min incubation, Life Technologies). Nuclei were labeled using Hoechst 33342 (0.1 µg/mL in DI water, 10 min incubation, Life Technologies). Slides were then imaged using a Leica Ariol slide scanner with Ariol software at 20x magnification.

Statistical analysis. All statistical results are expressed as mean ± standard error (SEM). Ordinary one-way ANOVA tests were used for multiple comparisons of the mean in each group with that of the standard. Tukey corrections with 95% confidence intervals and significance were used. Two-way ANOVA tests without matching were used for multiple comparisons of the mean in each

group at each timepoint with that of the standard. Holm-Sidak test was used for multiple comparisons. Statistical significance was defined as follows: *ns ($p > 0.05$), *** ($p \leq 0.001$), **** ($p \leq 0.0001$).*

3.2 Acknowledgements

Chapter 3 is adapted, in part, from material currently being prepared as a revised manuscript for resubmission for publication. Carlini, Andrea; Gaetani, Roberto; Braden, Rebecca; Luo, Colin; Christman, Karen; Gianneschi, Nathan. The dissertation author is the first author of this pending manuscript.

3.3 References

1 Mozaffarian, D., Benjamin, E. J., Go, A. S., Arnett, D. K., Blaha, M. J., Cushman, M., Das, S. R., de Ferranti, S., Després, J.-P., Fullerton, H. J., Howard, V. J., Huffman, M. D., Isasi, C. R., Jiménez, M. C., Judd, S. E., Kissela, B. M., Lichtman, J. H., Lisabeth, L. D., Liu, S., Mackey, R. H., Magid, D. J., McGuire, D. K., Mohler, E. R., Moy, C. S., Muntner, P., Mussolino, M. E., Nasir, K., Neumar, R. W., Nichol, G., Palaniappan, L., Pandey, D. K., Reeves, M. J., Rodriguez, C. J., Rosamond, W., Sorlie, P. D., Stein, J., Towfighi, A., Turan, T. N., Virani, S. S., Woo, D., Yeh, R. W. & Turner, M. B. Heart Disease and Stroke Statistics—2016 Update. *Circulation* **136**, doi:10.1161/cir.0000000000000350 (2015).

2 Richardson, W. J., Clarke, S. A., Quinn, T. A. & Holmes, J. W. in *Comprehensive Physiology* (John Wiley & Sons, Inc., 2011).

3 Singelyn, J. M., DeQuach, J. A., Seif-Naraghi, S. B., Littlefield, R. B., Schup-Magoffin, P. J. & Christman, K. L. Naturally derived myocardial matrix as an injectable scaffold for cardiac tissue engineering. *Biomaterials* **30**, 5409-5416, doi:https://doi.org/10.1016/j.biomaterials.2009.06.045 (2009).

4 Yu, J., Gu, Y., Du, K. T., Mihardja, S., Sievers, R. E. & Lee, R. J. The effect of injected RGD modified alginate on angiogenesis and left ventricular function in a chronic rat infarct model. *Biomaterials* **30**, 751-756, doi:https://doi.org/10.1016/j.biomaterials.2008.09.059 (2009).

5 Dorsey, S. M., McGarvey, J. R., Wang, H., Nikou, A., Arama, L., Koomalsingh, K. J., Kondo, N., Gorman, J. H., Pilla, J. J., Gorman, R. C., Wenk, J. F. & Burdick, J. A. MRI evaluation of injectable hyaluronic acid-based hydrogel therapy to limit ventricular remodeling after myocardial infarction. *Biomaterials* **69**, 65-75, doi:https://doi.org/10.1016/j.biomaterials.2015.08.011 (2015).

6 Lee, A. S., Inayathullah, M., Lijkwan, M. A., Zhao, X., Sun, W., Park, S., Hong, W. X., Parekh, M. B., Malkovskiy, A. V., Lau, E., Qin, X., Pothineni, V. R., Sanchez-Freire, V., Zhang, W. Y., Kooreman, N. G., Ebert, A. D., Chan, C. K. F., Nguyen, P. K., Rajadas, J. & Wu, J. C. Prolonged survival of transplanted stem cells after ischaemic injury via the slow release of pro-survival peptides from a collagen matrix. *Nature Biomedical Engineering* **2**, 104-113, doi:10.1038/s41551-018-0191-4 (2018).

7 Losi, P., Briganti, E., Magera, A., Spiller, D., Ristori, C., Battolla, B., Balderi, M., Kull, S., Balbarini, A., Di Stefano, R. & Soldani, G. Tissue response to poly(ether)urethane-polydimethylsiloxane-fibrin composite scaffolds for controlled delivery of pro-angiogenic growth factors. *Biomaterials* **31**, 5336-5344, doi:https://doi.org/10.1016/j.biomaterials.2010.03.033 (2010).

8 Prokoph, S., Chavakis, E., Levental, K. R., Zieris, A., Freudenberg, U., Dimmeler, S. & Werner, C. Sustained delivery of SDF-1α from heparin-based hydrogels to attract circulating pro-angiogenic cells. *Biomaterials* **33**, 4792-4800, doi:https://doi.org/10.1016/j.biomaterials.2012.03.039 (2012).

9 Layman, H., Spiga, M.-G., Brooks, T., Pham, S., Webster, K. A. & Andreopoulos, F. M. The effect of the controlled release of basic fibroblast growth factor from ionic gelatin-based hydrogels on angiogenesis in a murine critical limb ischemic model. *Biomaterials* **28**, 2646-2654, doi:10.1016/j.biomaterials.2007.01.044 (2007).

10 Fujimoto, K. L., Ma, Z., Nelson, D. M., Hashizume, R., Guan, J., Tobita, K. & Wagner, W. R. Synthesis, characterization and therapeutic efficacy of a biodegradable, thermoresponsive hydrogel

designed for application in chronic infarcted myocardium. *Biomaterials* **30**, 4357-4368, doi:https://doi.org/10.1016/j.biomaterials.2009.04.055 (2009).

11 Bastings, M. M. C., Koudstaal, S., Kieltyka, R. E., Nakano, Y., Pape, A. C. H., Feyen, D. A. M., van Slochteren, F. J., Doevendans, P. A., Sluijter, J. P. G., Meijer, E. W., Chamuleau, S. A. J. & Dankers, P. Y. W. A Fast pH-Switchable and Self-Healing Supramolecular Hydrogel Carrier for Guided, Local Catheter Injection in the Infarcted Myocardium. *Advanced Healthcare Materials* **3**, 70-78, doi:10.1002/adhm.201300076 (2014).

12 Wang, H., Zhang, X., Li, Y., Ma, Y., Zhang, Y., Liu, Z., Zhou, J., Lin, Q., Wang, Y., Duan, C. & Wang, C. Improved myocardial performance in infarcted rat heart by co-injection of basic fibroblast growth factor with temperature-responsive Chitosan hydrogel. *The Journal of Heart and Lung Transplantation* **29**, 881-887, doi:https://doi.org/10.1016/j.healun.2010.03.016 (2010).

13 Formiga, F. R., Pelacho, B., Garbayo, E., Imbuluzqueta, I., Díaz-Herráez, P., Abizanda, G., Gavira, J. J., Simón-Yarza, T., Albiasu, E., Tamayo, E., Prósper, F. & Blanco-Prieto, M. J. Controlled delivery of fibroblast growth factor-1 and neuregulin-1 from biodegradable microparticles promotes cardiac repair in a rat myocardial infarction model through activation of endogenous regeneration. *Journal of Controlled Release* **173**, 132-139, doi:https://doi.org/10.1016/j.jconrel.2013.10.034 (2014).

14 Suarez, S. L., Muñoz, A., Mitchell, A. C., Braden, R. L., Luo, C., Cochran, J. R., Almutairi, A. & Christman, K. L. Degradable Acetalated Dextran Microparticles for Tunable Release of an Engineered Hepatocyte Growth Factor Fragment. *ACS Biomaterials Science & Engineering* **2**, 197-204, doi:10.1021/acsbiomaterials.5b00335 (2016).

15 Ungerleider, J. L. & Christman, K. L. Concise Review: Injectable Biomaterials for the Treatment of Myocardial Infarction and Peripheral Artery Disease: Translational Challenges and Progress. *Stem Cells Translational Medicine* **3**, 1090-1099, doi:10.5966/sctm.2014-0049 (2014).

16 Hernandez, M. J. & Christman, K. L. Designing Acellular Injectable Biomaterial Therapeutics for Treating Myocardial Infarction and Peripheral Artery Disease. *JACC: Basic to Translational Science* **2**, 212-226, doi:https://doi.org/10.1016/j.jacbts.2016.11.008 (2017).

17 Portnov, T., Shulimzon Tiberiu, R. & Zilberman, M. in *Rev. Chem. Eng.* Vol. 33 91 (2017).

18 Akiyama, N., Yamamoto-Fukuda, T., Takahashi, H. & Koji, T. In situ tissue engineering with synthetic self-assembling peptide nanofiber scaffolds, PuraMatrix, for mucosal regeneration in the rat middle-ear. *International Journal of Nanomedicine* **8**, 2629-2640, doi:10.2147/IJN.S47279 (2013).

19 Davis, M. E., Motion, J. P. M., Narmoneva, D. A., Takahashi, T., Hakuno, D., Kamm, R. D., Zhang, S. & Lee, R. T. Injectable Self-Assembling Peptide Nanofibers Create Intramyocardial Microenvironments for Endothelial Cells. *Circulation* **111**, 442-450, doi:10.1161/01.CIR.0000153847.47301.80 (2005).

20 French, K. M., Somasuntharam, I. & Davis, M. E. Self-assembling peptide-based delivery of therapeutics for myocardial infarction. *Advanced Drug Delivery Reviews* **96**, 40-53, doi:https://doi.org/10.1016/j.addr.2015.04.023 (2016).

21 Li, X., Chen, Y.-Y., Wang, X.-M., Gao, K., Gao, Y.-Z., Cao, J., Zhang, Z.-L., Lei, J., Jin, Z.-Y. & Wang, Y.-N. Image-guided stem cells with functionalized self-assembling peptide nanofibers for treatment of acute myocardial infarction in a mouse model. *American Journal of Translational Research* **9**, 3723-3731 (2017).

22 Yuan, X., He, B., Lv, Z. & Luo, S. Fabrication of self-assembling peptide nanofiber hydrogels for myocardial repair. *RSC Advances* **4**, 53801-53811, doi:10.1039/C4RA08582E (2014).

23 Ravichandran, R., Venugopal, J. R., Sundarrajan, S., Mukherjee, S. & Ramakrishna, S. Minimally invasive cell-seeded biomaterial systems for injectable/epicardial implantation in ischemic heart disease. *International Journal of Nanomedicine* **7**, 5969-5994, doi:10.2147/IJN.S37575 (2012).

24 Kalafatovic, D., Nobis, M., Javid, N., Frederix, P. W. J. M., Anderson, K. I., Saunders, B. R. & Ulijn, R. V. MMP-9 triggered micelle-to-fibre transitions for slow release of doxorubicin. *Biomaterials Science* **3**, 246-249, doi:10.1039/C4BM00297K (2015).

25 Zhou, J. & Xu, B. Enzyme-Instructed Self-Assembly: A Multistep Process for Potential Cancer Therapy. *Bioconjugate Chemistry* **26**, 987-999, doi:10.1021/acs.bioconjchem.5b00196 (2015).

26 Abul-Haija, Y. M. & Ulijn, R. V. in *Hydrogels in Cell-Based Therapies* 112-134 (The Royal Society of Chemistry, 2014).

27 Bowerman, C. J. & Nilsson, B. L. A Reductive Trigger for Peptide Self-Assembly and Hydrogelation. *Journal of the American Chemical Society* **132**, 9526-9527, doi:10.1021/ja1025535 (2010).

28 Chien, M.-P., Carlini, A. S., Hu, D., Barback, C. V., Rush, A. M., Hall, D. J., Orr, G. & Gianneschi, N. C. Enzyme-Directed Assembly of Nanoparticles in Tumors Monitored by in Vivo Whole Animal Imaging and ex Vivo Super-Resolution Fluorescence Imaging. *Journal of the American Chemical Society* **135**, 18710-18713, doi:10.1021/ja408182p (2013).

29 Nguyen, M. M., Carlini, A. S., Chien, M.-P., Sonnenberg, S., Luo, C., Braden, R. L., Osborn, K. G., Li, Y., Gianneschi, N. C. & Christman, K. L. Enzyme-Responsive Nanoparticles for Targeted Accumulation and Prolonged Retention in Heart Tissue after Myocardial Infarction. *Advanced Materials* **27**, 5547-5552, doi:doi:10.1002/adma.201502003 (2015).

30 Callmann, C. E., Barback, C. V., Thompson, M. P., Hall, D. J., Mattrey, R. F. & Gianneschi, N. C. Therapeutic Enzyme-Responsive Nanoparticles for Targeted Delivery and Accumulation in Tumors. *Advanced Materials* **27**, 4611-4615, doi:10.1002/adma.201501803 (2015).

31 Spinale, F. G. Myocardial Matrix Remodeling and the Matrix Metalloproteinases: Influence on Cardiac Form and Function. *Physiol. Rev.* **87**, 1285-1342, doi:10.1152/physrev.00012.2007 (2007).

32 Prabhu, S. D. & Frangogiannis, N. G. The Biological Basis for Cardiac Repair After Myocardial Infarction. *From Inflammation to Fibrosis* **119**, 91-112, doi:10.1161/circresaha.116.303577 (2016).

33 Vulesevic, B., Sirois, M. G., Allen, B., de Denus, S. & White, M. Subclinical Inflammation in Heart Failure: A Neutrophil Perspective. *Canadian Journal of Cardiology*, doi:https://doi.org/10.1016/j.cjca.2018.01.018 (2018).

34 Rad-Malekshahi, M., Lempsink, L., Amidi, M., Hennink, W. E. & Mastrobattista, E. Biomedical Applications of Self-Assembling Peptides. *Bioconjugate Chemistry* **27**, 3-18, doi:10.1021/acs.bioconjchem.5b00487 (2016).

35 Koutsopoulos, S. Self‐assembling peptide nanofiber hydrogels in tissue engineering and regenerative medicine: Progress, design guidelines, and applications. *Journal of Biomedical Materials Research Part A* **104**, 1002-1016, doi:doi:10.1002/jbm.a.35638 (2016).

36 Betush, R. J., Urban, J. M. & Nilsson, B. L. Balancing hydrophobicity and sequence pattern to influence self‐assembly of amphipathic peptides. *Peptide Science* **110**, e23099, doi:doi:10.1002/bip.23099 (2018).

37 Hamley, I. W., Dehsorkhi, A., Castelletto, V., Seitsonen, J., Ruokolainen, J. & Iatrou, H. Self-assembly of a model amphiphilic oligopeptide incorporating an arginine headgroup. *Soft Matter* **9**, 4794-4801, doi:10.1039/C3SM50303H (2013).

38 Gao, J., Tang, C., Elsawy, M. A., Smith, A. M., Miller, A. F. & Saiani, A. Controlling Self-Assembling Peptide Hydrogel Properties through Network Topology. *Biomacromolecules* **18**, 826-834, doi:10.1021/acs.biomac.6b01693 (2017).

39 Tripathi, J. K., Pal, S., Awasthi, B., Kumar, A., Tandon, A., Mitra, K., Chattopadhyay, N. & Ghosh, J. K. Variants of self-assembling peptide, KLD-12 that show both rapid fracture healing and antimicrobial properties. *Biomaterials* **56**, 92-103, doi:https://doi.org/10.1016/j.biomaterials.2015.03.046 (2015).

40 Sun, J., Zheng, Q., Wu, Y., Liu, Y., Guo, X. & Wu, W. Biocompatibility of KLD-12 peptide hydrogel as a scaffold in tissue engineering of intervertebral discs in rabbits. *Journal of Huazhong University of Science and Technology [Medical Sciences]* **30**, 173-177, doi:10.1007/s11596-010-0208-z (2010).

41 Kisiday, J., Jin, M., Kurz, B., Hung, H., Semino, C., Zhang, S. & Grodzinsky, A. J. Self-assembling peptide hydrogel fosters chondrocyte extracellular matrix production and cell division: Implications for cartilage tissue repair. *Proceedings of the National Academy of Sciences* **99**, 9996-10001, doi:10.1073/pnas.142309999 (2002).

42 Tabatabaei Ghomi, H., Topp, E. M. & Lill, M. A. Fibpredictor: a computational method for rapid prediction of amyloid fibril structures. *Journal of Molecular Modeling* **22**, 206, doi:10.1007/s00894-016-3066-1 (2016).

43 Zhang, S., Zhao, X. & Spirio, L. in *Encyclopedia of Biomedical Polymers and Polymeric Biomaterials* Vol. 11 (ed Munmaya K. Mishra) 15 (CRC Press, 2015).

44 Roeters, S. J., Iyer, A., Pletikapić, G., Kogan, V., Subramaniam, V. & Woutersen, S. Evidence for Intramolecular Antiparallel Beta-Sheet Structure in Alpha-Synuclein Fibrils from a Combination of Two-Dimensional Infrared Spectroscopy and Atomic Force Microscopy. *Scientific Reports* **7**, 41051, doi:10.1038/srep41051 (2017).

45 Bulheller, B. M. & Hirst, J. D. DichroCalc—circular and linear dichroism online. *Bioinformatics* **25**, 539-540, doi:10.1093/bioinformatics/btp016 (2009).

46 Tokunaga, M., Liu, M.-L., Nagai, T., Iwanaga, K., Matsuura, K., Takahashi, T., Kanda, M., Kondo, N., Wang, P., Naito, A. T. & Komuro, I. Implantation of cardiac progenitor cells using self-assembling peptide improves cardiac function after myocardial infarction. *J. Mol. Cell. Cardiol.* **49**, 972-983, doi:https://doi.org/10.1016/j.yjmcc.2010.09.015 (2010).

47 Boopathy, A. V., Che, P. L., Somasuntharam, I., Fiore, V. F., Cabigas, E. B., Ban, K., Brown, M. E., Narui, Y., Barker, T. H., Yoon, Y.-S., Salaita, K., García, A. J. & Davis, M. E. The modulation of cardiac progenitor cell function by hydrogel-dependent Notch1 activation. *Biomaterials* **35**, 8103-8112, doi:https://doi.org/10.1016/j.biomaterials.2014.05.082 (2014).

48 Cui, X.-J., Xie, H., Wang, H.-J., Guo, H.-D., Zhang, J.-K., Wang, C. & Tan, Y.-Z. Transplantation of Mesenchymal Stem Cells with Self-Assembling Polypeptide Scaffolds Is Conducive

to Treating Myocardial Infarction in Rats. *The Tohoku Journal of Experimental Medicine* **222**, 281-289, doi:10.1620/tjem.222.281 (2010).

49 Khakshoor, O., Demeler, B. & Nowick, J. S. Macrocyclic β-Sheet Peptides That Mimic Protein Quaternary Structure through Intermolecular β-Sheet Interactions. *Journal of the American Chemical Society* **129**, 5558-5569, doi:10.1021/ja068511u (2007).

50 Hourani, R., Zhang, C., van der Weegen, R., Ruiz, L., Li, C., Keten, S., Helms, B. A. & Xu, T. Processable Cyclic Peptide Nanotubes with Tunable Interiors. *Journal of the American Chemical Society* **133**, 15296-15299, doi:10.1021/ja2063082 (2011).

51 Montenegro, J., Ghadiri, M. R. & Granja, J. R. Ion Channel Models Based on Self-Assembling Cyclic Peptide Nanotubes. *Accounts of Chemical Research* **46**, 2955-2965, doi:10.1021/ar400061d (2013).

52 Dinerman, J. L., Mehta, J. L., Saldeen, T. G. P., Emerson, S., Wallin, R., Davda, R. & Davidson, A. Increased neutrophil elastase release in unstable angina pectoris and acute myocardial infarction. *Journal of the American College of Cardiology* **15**, 1559-1563, doi:https://doi.org/10.1016/0735-1097(90)92826-N (1990).

53 van den Burg, B. & Eijsink, V. in *Handbook of Proteolytic Enzymes* (ed Guy Salvesen) 540-553 (Academic Press, 2013).

54 Clark, R. J., Fischer, H., Dempster, L., Daly, N. L., Rosengren, K. J., Nevin, S. T., Meunier, F. A., Adams, D. J. & Craik, D. J. Engineering stable peptide toxins by means of backbone cyclization: Stabilization of the α-conotoxin MII. *Proc. Natl. Acad. Sci. U. S. A.* **102**, 13767-13772, doi:10.1073/pnas.0504613102 (2005).

55 Chen, Y., Li, T., Li, J., Cheng, S., Wang, J., Verma, C., Zhao, Y. & Wu, C. Stabilization of peptides against proteolysis through disulfide-bridged conjugation with synthetic aromatics. *Org. Biomol. Chem.* **15**, 1921-1929, doi:10.1039/C6OB02786E (2017).

56 Tian, Y. F., Hudalla, G. A., Han, H. & Collier, J. H. Controllably degradable β-sheet nanofibers and gels from self-assembling depsipeptides. *Biomaterials Science* **1**, 1037-1045, doi:10.1039/C3BM60161G (2013).

57 van den Burg, B. & Eijsink, V. in *Handbook of Proteolytic Enzymes (Third Edition)* (eds Neil D. Rawlings & Guy Salvesen) 540-553 (Academic Press, 2013).

58 Keil, B. in *Specificity of Proteolysis* Ch. Essential Substrate Residues for Action of Endopeptidases, 155-158 (Springer, Berlin, Heidelberg, 1992).

59 Habibi, N., Kamaly, N., Memic, A. & Shafiee, H. Self-assembled peptide-based nanostructures: Smart nanomaterials toward targeted drug delivery. *Nano today* **11**, 41-60, doi:10.1016/j.nantod.2016.02.004 (2016).

60 Grover, G. N., Braden, R. L. & Christman, K. L. Oxime Cross-Linked Injectable Hydrogels for Catheter Delivery. *Adv. Mater.* **25**, 2937-2942, doi:doi:10.1002/adma.201205234 (2013).

61 Seif-Naraghi, S. B., Singelyn, J. M., Salvatore, M. A., Osborn, K. G., Wang, J. J., Sampat, U., Kwan, O. L., Strachan, G. M., Wong, J., Schup-Magoffin, P. J., Braden, R. L., Bartels, K., DeQuach, J. A., Preul, M., Kinsey, A. M., DeMaria, A. N., Dib, N. & Christman, K. L. Safety and Efficacy of an Injectable Extracellular Matrix Hydrogel for Treating Myocardial Infarction. *Science Translational Medicine* **5**, 173ra125-173ra125, doi:10.1126/scitranslmed.3005503 (2013).

62 Horton, S. & Augustin, S. in *Monagle P. (eds) Haemostasis* Vol. 992 *Methods in Molecular Biology* 155-167 (Humana Press, 2013).

63 Autian, J. in *Kronenthal R.L., Oser Z., Martin E. (eds) Polymers in Medicine and Surgery* Vol. 8 *Polymer Science and Technology* 181-203 (Springer).

64 Hee, K. S., Woojune, H., Eun, K. J., Jeong, M. H., Sukwha, K., Sook, M. H., Kyu, K. B., Hyun, K. S., Hyun, C. T. & Youngmee, J. Self-Assembling Peptide Nanofibers Coupled with Neuropeptide Substance P for Bone Tissue Engineering. *Tissue Engineering Part A* **21**, 1237-1246, doi:10.1089/ten.tea.2014.0472 (2015).

65 Zhu, J. & Marchant, R. E. Design properties of hydrogel tissue-engineering scaffolds. *Expert review of medical devices* **8**, 607-626, doi:10.1586/erd.11.27 (2011).

66 Gawaz, M. Role of platelets in coronary thrombosis and reperfusion of ischemic myocardium. *Cardiovascular Research* **61**, 498-511, doi:10.1016/j.cardiores.2003.11.036 (2004).

67 Roberts, D. E., McNicol, A. & Bose, R. Mechanism of Collagen Activation in Human Platelets. *Journal of Biological Chemistry* **279**, 19421-19430, doi:10.1074/jbc.M308864200 (2004).

68 Seif-Naraghi, S. B., Singelyn, J. M., Salvatore, M. A., Osborn, K. G., Wang, J. J., Sampat, U., Kwan, O. L., Strachan, G. M., Wong, J., Schup-Magoffin, P. J., Braden, R. L., Bartels, K., DeQuach, J. A., Preul, M., Kinsey, A. M., DeMaria, A. N., Dib, N. & Christman, K. L. Safety and efficacy of an injectable extracellular matrix hydrogel for treating myocardial infarction. *Sci. Transl. Med.* **5**, 10.1126/scitranslmed.3005503, doi:10.1126/scitranslmed.3005503 (2013).

69 O'Cearbhaill, E. D., Ng, K. S. & Karp, J. M. Emerging Medical Devices for Minimally Invasive Cell Therapy. *Mayo Clin. Proc.* **89**, 259-273, doi:https://doi.org/10.1016/j.mayocp.2013.10.020 (2014).

70 Dib, N., Khawaja, H., Varner, S., McCarthy, M. & Campbell, A. Cell Therapy for Cardiovascular Disease: A Comparison of Methods of Delivery. *J. Cardiovasc. Transl. Res.* **4**, 177-181, doi:10.1007/s12265-010-9253-z (2011).

71 Kim, S. J., Kim, J. E., Kim, S. H., Kim, S. J., Jeon, S. J., Kim, S. H. & Jung, Y. Therapeutic effects of neuropeptide substance P coupled with self-assembled peptide nanofibers on the progression of osteoarthritis in a rat model. *Biomaterials* **74**, 119-130, doi:https://doi.org/10.1016/j.biomaterials.2015.09.040 (2016).

72 Lu, J., Sun, X., Yin, H., Shen, X., Yang, S., Wang, Y., Jiang, W., Sun, Y., Zhao, L., Sun, X., Lu, S., Mikos, A. G., Peng, J. & Wang, X. A neurotrophic peptide-functionalized self-assembling peptide nanofiber hydrogel enhances rat sciatic nerve regeneration. *Nano Research*, doi:10.1007/s12274-018-2041-9 (2018).

73 Wu, X., He, L., Li, W., Li, H., Wong, W.-M., Ramakrishna, S. & Wu, W. Functional self-assembling peptide nanofiber hydrogel for peripheral nerve regeneration. *Regenerative Biomaterials* **4**, 21-30, doi:10.1093/rb/rbw034 (2017).

74 Zhang, N., Luo, Y., He, L., Zhou, L. & Wu, W. A self-assembly peptide nanofibrous scaffold reduces inflammatory response and promotes functional recovery in a mouse model of intracerebral hemorrhage. *Nanomedicine: Nanotechnology, Biology and Medicine* **12**, 1205-1217, doi:https://doi.org/10.1016/j.nano.2015.12.387 (2016).

75 Yu, H., Xiao, Y. & Guo, H. From Spirolactam Mixtures to Regioisomerically Pure 5- and 6-Rhodamines: A Chemodosimeter-Inspired Strategy. *Organic Letters* **14**, 2014-2017, doi:10.1021/ol300523m (2012).

76 Reddy, K. M. B., Kumari, Y. B., Mallikharjunasarma, D., Bulliraju, K., Sreelatha, V. & Ananda, K. Large Scale Solid Phase Synthesis of Peptide Drugs: Use of Commercial Anion Exchange Resin as Quenching Agent for Removal of Iodine during Disulphide Bond Formation. *International Journal of Peptides* **2012**, 8, doi:10.1155/2012/323907 (2012).

77 Mierke, D. F., Yamazaki, T., Said-Nejad, O. E., Felder, E. R. & Goodman, M. Cis/trans isomers in cyclic peptides without N-substituted amides. *Journal of the American Chemical Society* **111**, 6847-6849, doi:10.1021/ja00199a058 (1989).

78 Nguyen, K., Iskandar, M. & Rabenstein, D. L. Kinetics and Equilibria of Cis/Trans Isomerization of Secondary Amide Peptide Bonds in Linear and Cyclic Peptides. *The Journal of Physical Chemistry B* **114**, 3387-3392, doi:10.1021/jp1000286 (2010).

79 Bhattacharyya, M., Gupta, K., Gowd, K. H. & Balaram, P. Rapid mass spectrometric determination of disulfide connectivity in peptides and proteins. *Molecular BioSystems* **9**, 1340-1350, doi:10.1039/C3MB25534D (2013).

80 Ghomi, H. T., Thompson, J. J. & Lill, M. A. Are distance-dependent statistical potentials considering three interacting bodies superior to two-body statistical potentials for protein structure prediction? *Journal of Bioinformatics and Computational Biology* **12**, 1450022, doi:10.1142/s021972001450022x %m 25212727 (2014).

81 Zhou, H. & Skolnick, J. GOAP: A Generalized Orientation-Dependent, All-Atom Statistical Potential for Protein Structure Prediction. *Biophysical Journal* **101**, 2043-2052, doi:10.1016/j.bpj.2011.09.012 (2011).

82 Girardi, L., Sudi, K. & Muntean, W. Effect of Heparin, Platelets, Activated Platelets, Platelet Fragments, and Hematocrit on Activated Clotting Time. *Artificial Organs* **24**, 507-513, doi:10.1046/j.1525-1594.2000.06552.x (2000).

83 Motlagh, D., Yang, J., Lui, K. Y., Webb, A. R. & Ameer, G. A. Hemocompatibility evaluation of poly(glycerol-sebacate) in vitro for vascular tissue engineering. *Biomaterials* **27**, 4315-4324, doi:https://doi.org/10.1016/j.biomaterials.2006.04.010 (2006).

84 Evans, B. C., Nelson, C. E., Yu, S. S., Beavers, K. R., Kim, A. J., Li, H., Nelson, H. M., Giorgio, T. D. & Duvall, C. L. Ex Vivo Red Blood Cell Hemolysis Assay for the Evaluation of pH-responsive Endosomolytic Agents for Cytosolic Delivery of Biomacromolecular Drugs. *Journal of Visualized Experiments : JoVE*, 50166, doi:10.3791/50166 (2013).

85 Seif-Naraghi, S. B., Horn, D., Schup-Magoffin, P. A. & Christman, K. L. Injectable extracellular matrix derived hydrogel provides a platform for enhanced retention and delivery of a heparin-binding growth factor. *Acta biomaterialia* **8**, 3695-3703, doi:10.1016/j.actbio.2012.06.030 (2012).

86 Johnson, T. D., DeQuach, J. A., Gaetani, R., Ungerleider, J., Elhag, D., Nigam, V., Behfar, A. & Christman, K. L. Human versus porcine tissue sourcing for an injectable myocardial matrix hydrogel. *Biomaterials science* **2014**, 60283D, doi:10.1039/C3BM60283D (2014).

Chapter 4

Charge-Conversional Peptide Progelators

4.1 Polyanionic Maleamic Acid Progelators for Minimally Invasive Delivery to Inflamed Tissue

4.1.1 Introduction

Reversible charge-conversion of proteins and polymers with maleamic acid derivatives has been used to study protein denaturation and folding pathways,[1-3] for structural disassembly of polymer films or colloidal structures,[4,5] for cellular penetration,[6-8] and for drug release.[9-11] These moieties exhibit acid-triggered amide bond hydrolysis. Furthermore, the pH sensitivity can be tuned for faster responsiveness through increasing bulkiness with aliphatic substitutions onto the alkene backbone.[12,13] Current strategies with self-assembled hydrogels utilize acidic tissue microenvironments for responsive network degradation and subsequent drug release.[14-16] To our knowledge, this strategy has not been applied to induce macromolecular hydrogel assembly, and thus targeted gelation, from a soluble precursor.

We sought to use charge-conversion chemistry as a facile method for converting inert small molecules into structurally dynamic biomaterial scaffolds at sites of tissue acidosis due to injury (e.g.

myocardial ischemia, rheumatoid arthritis, articular cartilage damage, and epidermal wounds).[17,18] Our design provides a strategy amenable to minimally invasive delivery and stimuli-responsive assembly at sites of inflammation for targeted tissue engineering (**Figure 4.1.1**).

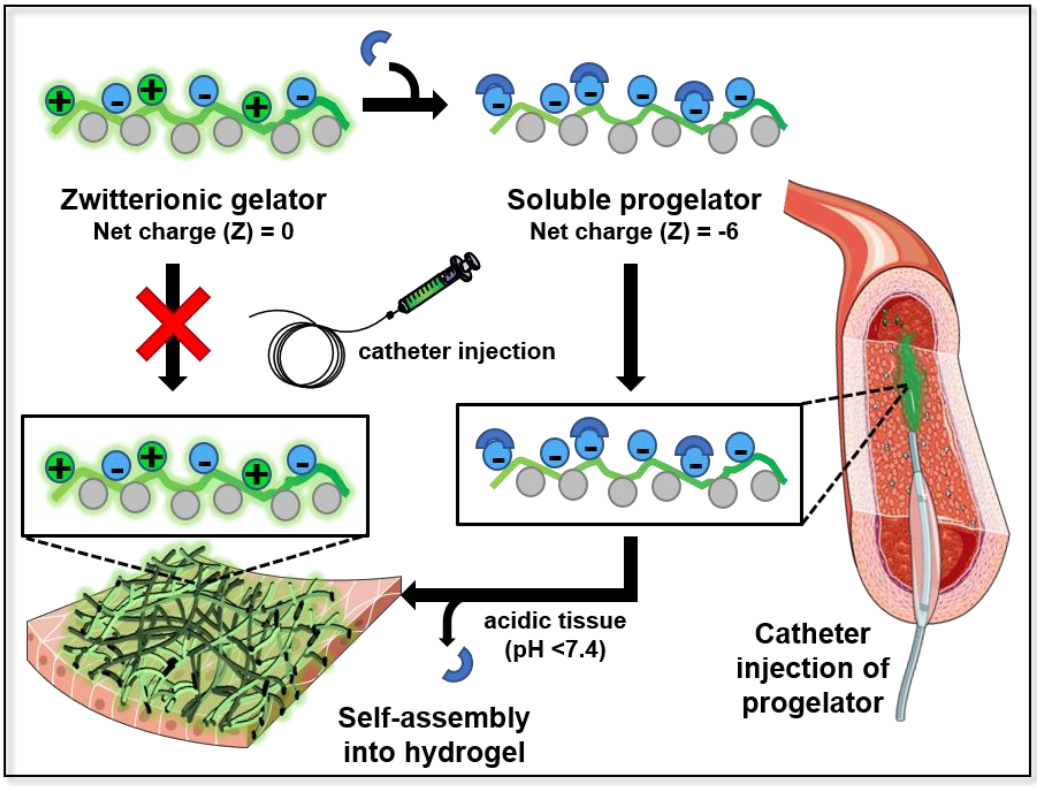


Figure 4.1.1. Schematic of charge-conversional peptide as sensors of inflammation. Soluble progelators are proposed for minimally invasive catheter delivery and stimuli-responsive gelation at the site of tissue acidosis. Structurally dynamic peptides based off of a zwitterionic self-assembling gelator are responsive to changes in pH, namely a physiologically relevant pH drop within inflamed tissues. These materials are perceived for 'smart' tissue engineering applications, especially in hard-to-reach places within the body.

During myocardial ischemia, the local pH drops below physiological conditions (~pH 6.0-6.4),[18,19] which is caused by a gradual buildup of lactic acid (pKa 3.86) and drop in plasma bicarbonate. Similar drops in pH have been observed in synovial fluid at sites of arthritis or cartilage damage (pH 6.5),[20-22] chronic metabolic acidosis due to liver failure (pH 7.1),[23] and acute (pH 6.5) and chronic (pH 5.4) epidermal wounds.[24] These forms of tissue acidosis can exacerbate inflammation, leading to further tissue damage.[17,25] Injectable hydrogels seeded with cells/growth factors or as acellular scaffolds have been used for the repair of cardiac tissue after myocardial infarction (MI),[26,27] articular

cartilage damage,[28,29] burn and epidermal wounds,[30-32] and treatment of arthritic flares from wear and tear.[33,34] Introduction of these viscoelastic scaffolds provide lubrication or act to supplement degraded extracellular matrix (ECM), which provides structural support, a niche for cellular anchoring, and biochemical communications.[35-37] Additionally, drug-loaded hydrogels provide a porous network for controlled delivery of encapsulated anti-inflammatories, growth factors, and/or cell therapies.[38,39]

Unfortunately, these injuries usually have irregular or gradated boundaries, making localized hydrogel delivery difficult. Furthermore, a balance between material spreading and solidification kinetics is a persistent challenge.[40] Excess spreading can cause material diffusion away from target tissue, and rapid gelation can preclude noninvasive delivery strategies or prevent appropriate tissue coverage. The advent of structurally dynamic materials has presented a useful strategy for controlled assembly in response to endogenous stimuli (e.g. pH, temperature, redox chemistry, metal chelation, enzymes, and mechanical stress).[41-45]

As a proof of concept, we modify the well-known KLD-12 self-assembling peptide (SAP). This peptide has already demonstrated utility as a degradable, nonimmunogenic, and nontoxic hydrogel for tissue engineering.[46-50] However, practical application in the body following traumatic injury is limited by its high viscosity, precluding the use of minimally invasive catheter delivery (see **Chapter 3**). Furthermore, lack of stimuli-responsiveness forces this material to assemble at the immediate site of application. We demonstrate that temporary charge-conversion of the self-assembling peptide KLD-12, from zwitterionic (Z=0) to polyanionic (Z=-6) is sufficient to yield soluble and low viscosity progelators. These materials are amenable to minimally invasive catheter delivery, unlike the KLD peptide. Furthermore, they exhibit pH-tunable gelation at physiologically relevant levels during injury-related tissue acidosis.

4.1.2 Results

Facile synthesis of charge-conversion progelators. For clinical translation, synthetic simplicity and reproducibility are attractive features for the design of biomaterials in biomedical

applications.[51] Also, negatively, as opposed to positively, charged biomaterials generally possess lower cytotoxicity and resist cellular internalization.[52,53] We demonstrate that KLD-12 (referred to as KLD control) were modified through the addition of either maleic anhydride, citraconic anhydride, or dimethylmaleic anhydride to yield mal-KLD, cit-KLD, and dma-KLD, respectively (**Figure 4.1.1**). The resulting polyanionic peptides persisted as soluble solutions at high concentrations (10 mM) and physiologically relevant conditions (1x DPBS, pH 7.4). Peptides were lyophilized for storage and rapidly dissolved upon resuspension. Peptide solutions were stable up to 14 days at pH 8-9 at room temperature.

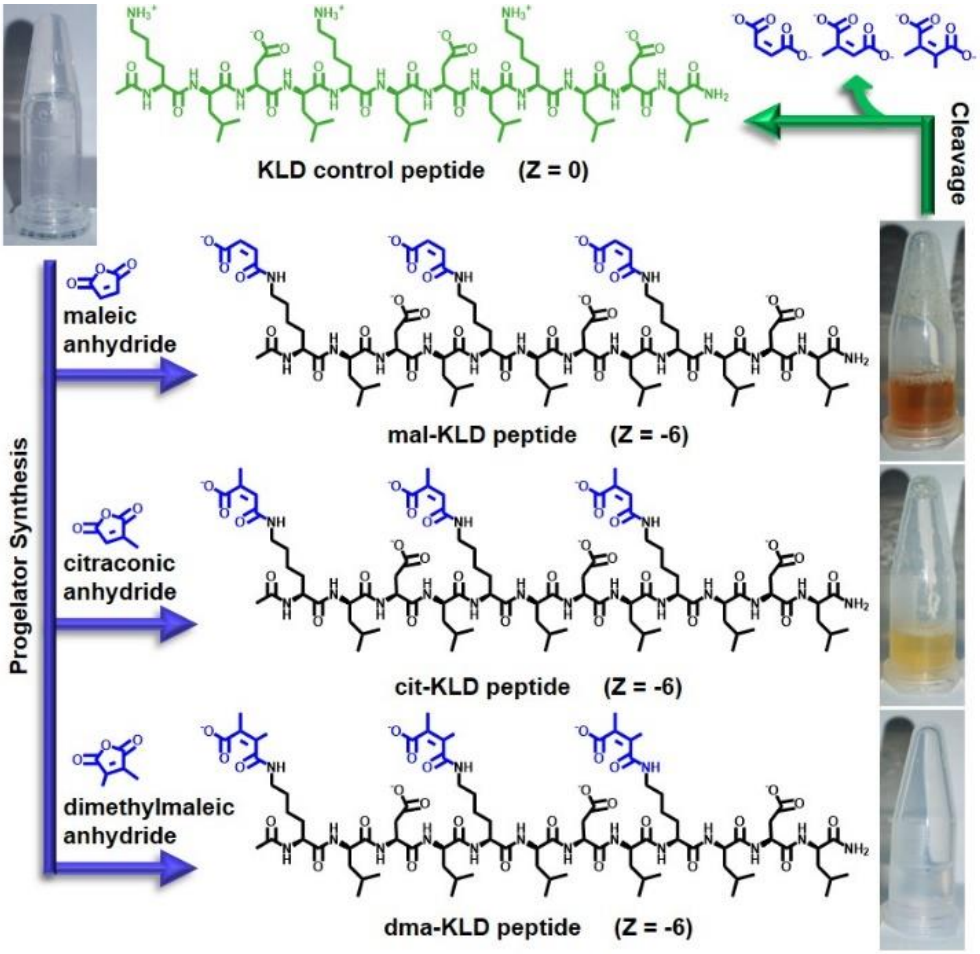


Figure 4.1.1. Facile synthesis of peptide progelators. The zwitterionic KLD self-assembling peptide is modified with maleic anhydride, citraconic anhydride, and dimethylmaleic anhydride to generate the polyanionic progelators mal-KLD, cit-KLD, and dma-KLD, respectively. Inset images of progelators at 10 mM show nonviscous solutions. Acid-treatment regenerates the starting material upon release of maleic acid derivatives.

Characterization of progelators with tunable pH-sensitivity. Synthesized progelators and KLD control peptide and were quantitatively pure by liquid chromatography mass spectrometry (LCMS) (**Figure 4.1.2**). Importantly, simple reaction workup yielded the same purity as preparatory phase HPLC (see **Experiemental Details**). Peptide precipitation in anhydrous diethyl ether followed by dialysis (1 kDa cutoff) into H_2O at pH 9.0 to remove unreacted maleic or citraconic acid and DMAP produced similar quantitative yields. Even better was the capacity to immediately separate DMA-KLD progelator from the reaction solution as a precipitation product. We observed that only peptide with all three lysine amines functionalized with dimethmaleamic acids possessed this insolubility in DMF. Filtration, and similar washing and dialysis steps yielded water soluble peptide progelators stabilized in slightly basic solution. **Table 2.2.1** shows mass spectral identities for all peptides in this study.

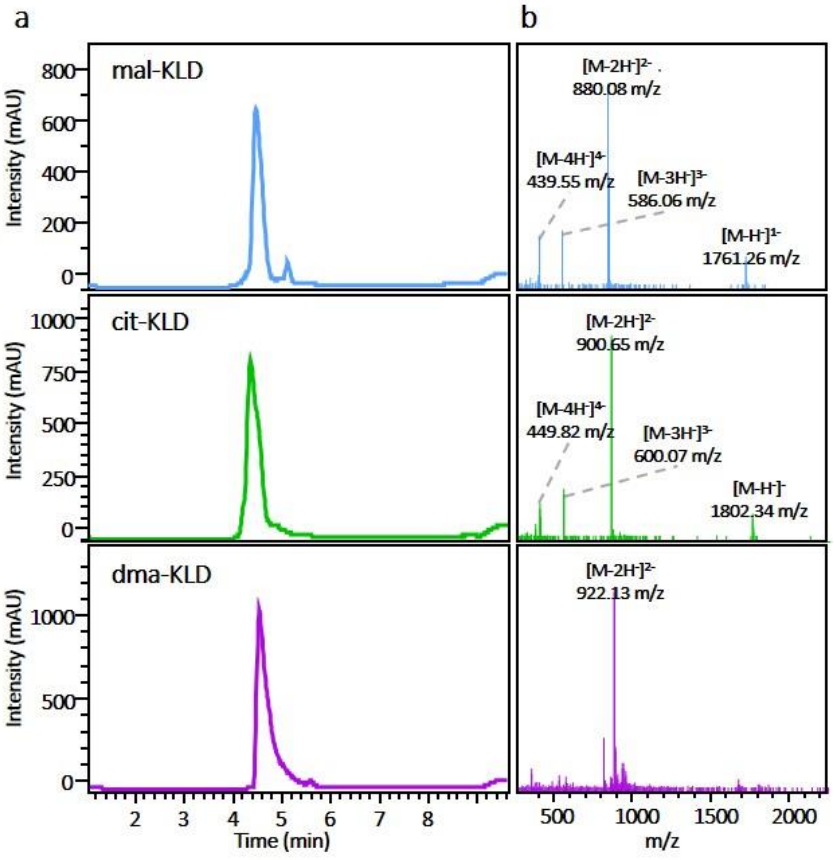


Figure 4.1.2. Characterization of progelators by LCMS. (a-b) Liquid chromatography mass spectrometry (LCMS) of mal-KLD, cit-KLD, and dma-KLD. (a) LC spectra show progelator peak (t ~4.5 min) as monitored at 214 nm and (b) corresponding mass spectral patterns with species identities. Spectra show m/z values corresponding to the progelators. Corresponds with **Table 2.2.1**

Table 4.1.5. Peptide identities by mass spectrometry and visual observation.

Peptide	Expected MW at pH 7.4 (g/mol)	Observed mass (m/z)	Observed Species	Appearance
KLD control	1467.82	734.49	$[M+2H^+]^{2+}$	clear viscoelastic hydrogel
mal-KLD	1755.94	880.08	$[M-2H^-]^{2-}$	brown transparent liquid
cit-KLD	1798.02	900.65	$[M-2H^-]^{2-}$	pale yellow transparent liquid
dma-KLD	1840.11	922.13	$[M-2H^-]^{2-}$	clear transparent liquid

Enhanced solubility of all three polyanionic peptides improved LC peak resolution in **Figure 4.1.2**, as compared to poor resolution with the KLD control peptide (**Figure 4.1.3**). Amphiphilicity and zwitterionic charges causes very pure peptide to spread on the column during analysis. Thus, future endeavors with difficult-to-purity SAPs in our lab could benefit from temporary functionalization with dimethylmaleamic acid to prevent self-assembly during peptide purification via HPLC. Acid deprotection can provide the final step in generating pure SAPs that are otherwise hampered by low yields and residual impurities due to column spreading.

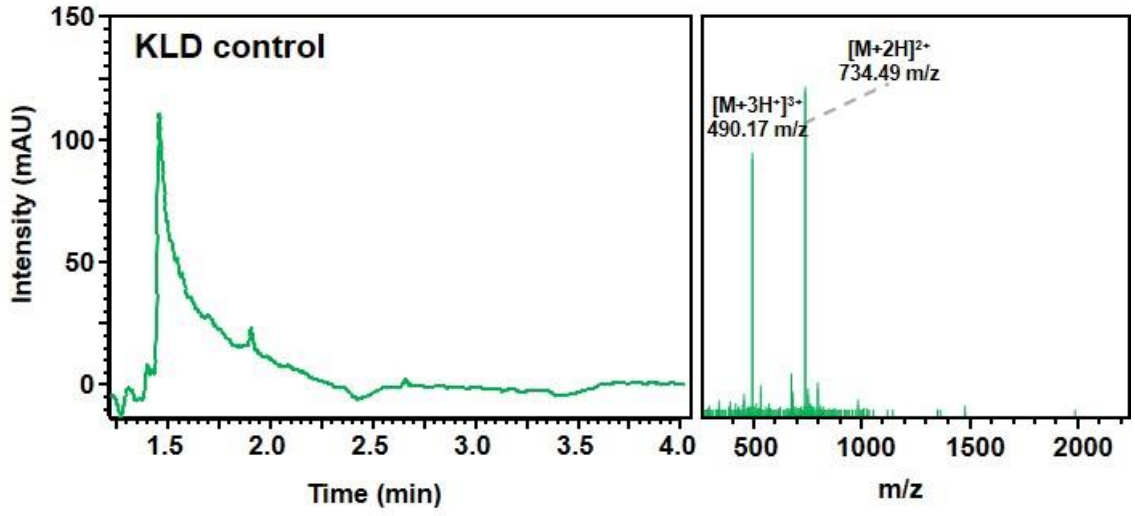


Figure 4.1.3. LCMS of KLD control peptide. Pure self-assembling peptide shows peak spreading on the column because of self-assembling properties (left). Corresponding ESI measurements (right) reveal $[M+2H^+]^{2+}$ and $[M+3H^+]^{3+}$ species. Method: 20-40% buffer B over 4 min at 0.5 mL/min. λ=214 nm. Buffer A: water (0.1% TFA). Buffer B: acetonitrile (0.1% TFA). Corresponds with **Table 2.2.1**.

Deprotection of soluble progelators initiates self-assembly. The synthesis of disperse and fully soluble biomaterials is key for reducing delivery invasiveness. We used circular dichroism (CD) to evaluate secondary structures formed by our peptides in solution before and after pH-

responsive charge-conversion (**Figure 4.1.4)**. All three progelators adopt random coil configurations, as seen by a peak minimum at ~202-205 nm (**Figure 4.1.4b-d**). The most hydrophobic progelator, dma-KLD, also absorbed at higher wavelengths indicative of weak intra-strand assembly (**Figure 4.1.4d**). Progelators were treated at pH 3.0 for 24 hr, followed by neutralization to pH 7.4 to recapitulate β-sheet assembly (minima ~215-218) observed with the KLD-12 control peptide (minimum 222 nm).

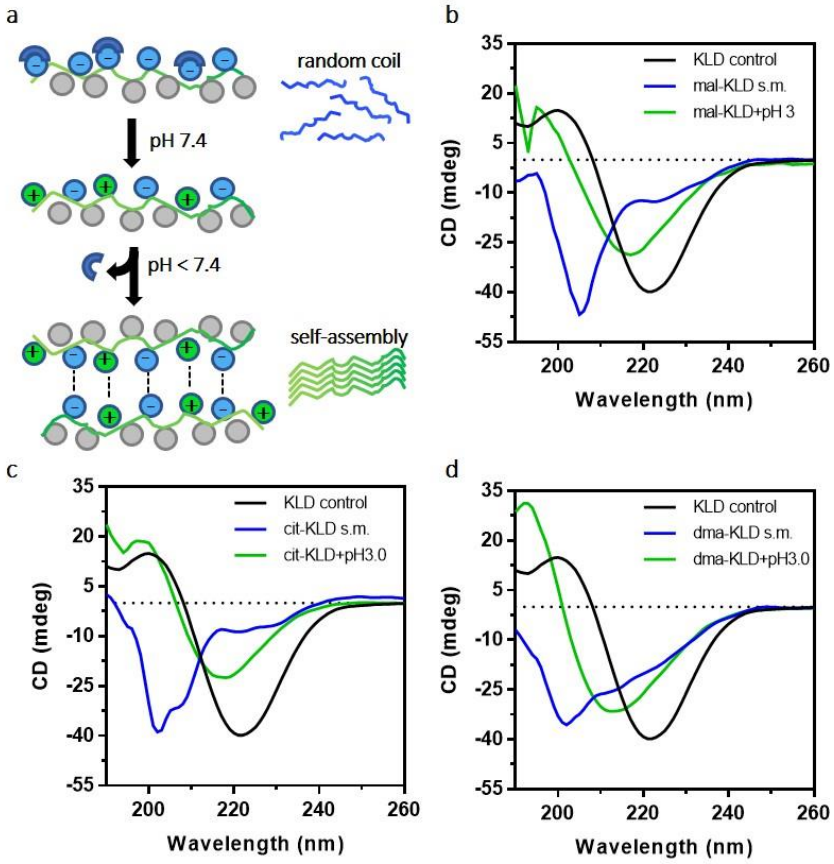


Figure 4.1.4. Circular dichroism (CD) analysis of self-assembly. (a) Schematic of polyanionic charge-conversion peptides that persist as random coils. Acid-induced lysine (+) deprotection induces self-assembly via ionic crosslinking (depicted) and hydrophobic interactions into β-sheets. (b-d) Circular dichroism of (b) mal-KLD, (c) cit-KLD, and (d) dma-KLD before and after acid treatment. KLD control peptide is shown for comparison. Progelators incubated at pH 3.0 for 24 hr, then dialyzed into 50 mM phosphate buffer (pH 7.4) for measurement at 400 μM peptide.

Strong absorbance of maleamic acids in our progelators below 200 nm, leads to near-saturation of the voltage detector (**Figure 4.1.5**). Dialysis of the deprotected solutions to remove maleic acid hydrolysis products yielded nearly identical voltage spectra to that of the KLD control.

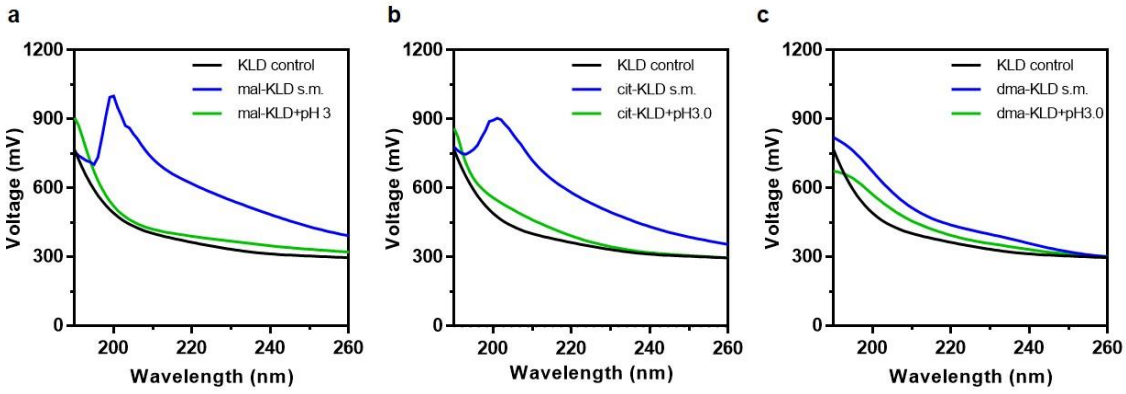


Figure 4.1.5. Voltage plots for circular dichroism measurements. Peptides were incubated at pH 3.0 for 24 hr, then dialyzed into 50 mM phosphate buffer (pH 7.4) for measurement at a final peptide concentration of 400 μM. High signal interference is caused by maleamic acids on progelators. Dialysis to remove deprotected maleic acids increases signal quality for acid-treated progelators. Corresponds with **Figure 4.1.4b-d**.

To better observe intermediate cleavage products and their secondary structure, the two less responsive peptides, mal-KLD and cit-KLD, were monitored during the timecourse of their perspective cleavages at pH 3.0 (**Figure 4.1.6**). Cleavage of dma-KLD under these dilute conditions was too fast for intermediate structural observation. Despite low signal-to-noise, cleavage intermediate structures show a gradual decrease in random coil behavior (~205 nm) and slow increase in β-sheet structure, as a new maximum at 202 nm and minimum at ~218 nm.

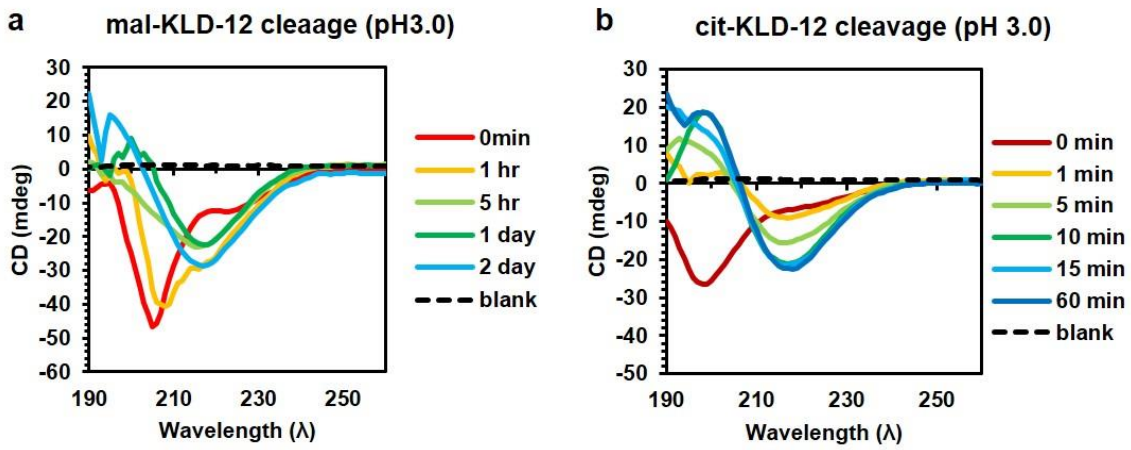


Figure 4.1.6. Circular dichroism (CD) of mal-KLD and cit-KLD deprotection over time at pH 3.0. Gradual loss of minima signal at ~205 nm, corresponding to random coils, is accompanied by an increase in signal at ~218 nm, corresponding to β-sheet structures. Progelators (400 μM) incubated at pH 3.0 for up to 2 days.

Dilute sample morphology of progelators and pH-induced SAPs was observed with stained dry state TEM (**Figure 4.1.7**). mal-KLD and cit-KLD progelators exhibited no distinct structures (**Figure 4.1.7a,b**), and dma-KLD shows low contrast staining of disordered structures (**Figure 4.1.7c**), which is likely the result of transient oligomers bound by weak hydrophobic interactions; this observation agrees with CD results. pH-induced deprotection of progelators yields elongated fibrillar networks identical to that of the KLD control peptide (**Figure 4.1.7d**). Additional images of peptide morphologies are provided in **Figure 4.1.8**.

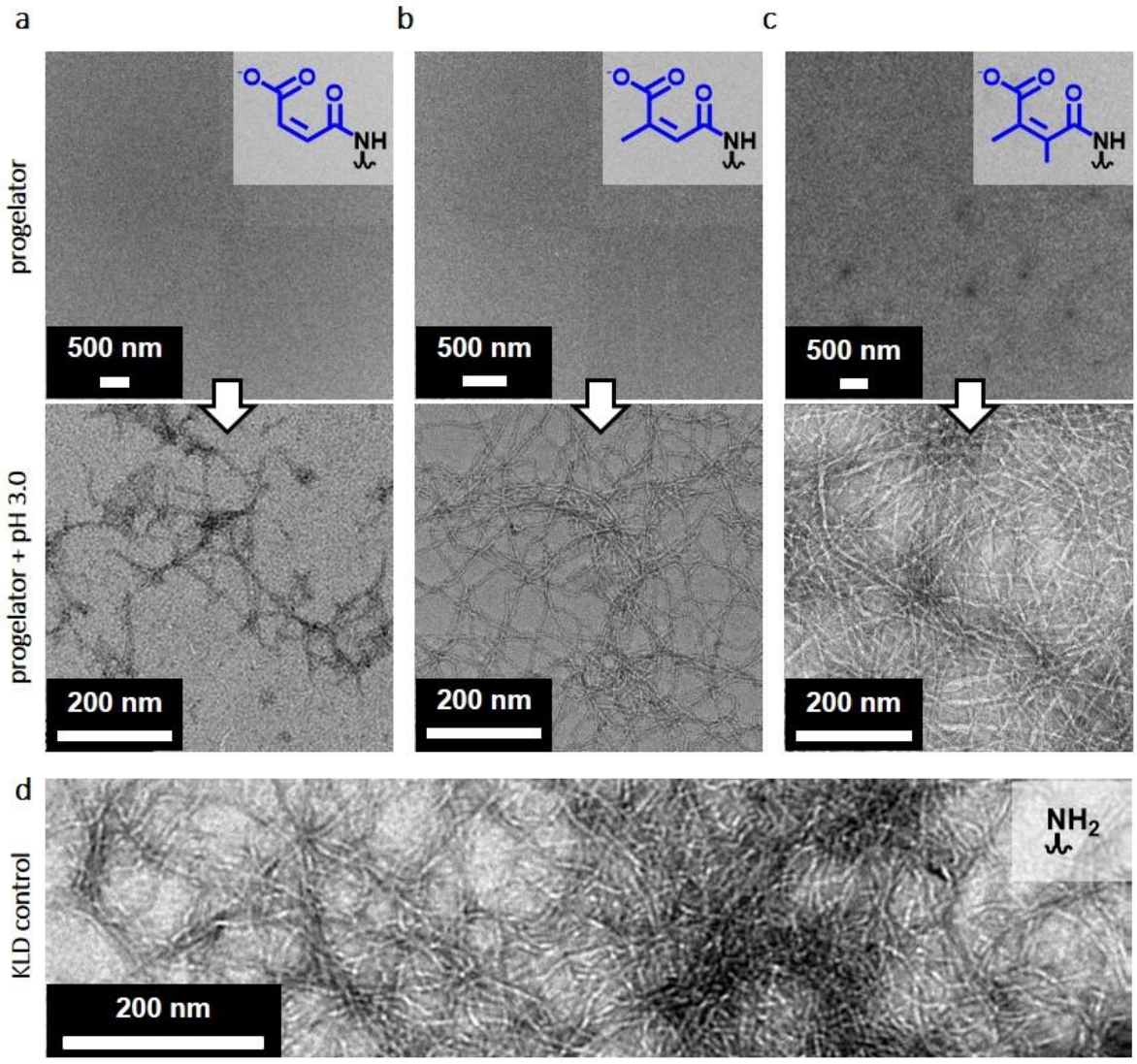


Figure 4.1.7. Transmission electron microscopy (TEM) analysis of self-assembly. (**a-d**) Dry state stained TEM of progelators and acid-treated SAPs. (a) mal-KLD, (b) cit-KLD, and (c) dma-KLD progelators with inset chemical structures of maleamic acids before (top) and after (bottom) acid treatment. (d) KLD control with inset chemical structure of deprotected lysine amine is provided as a positive control for fiber morphology. Progelators (100 μM) were treated at pH 3.0 for 12 hr, then neutralized to pH 7.4 prior to imaging.

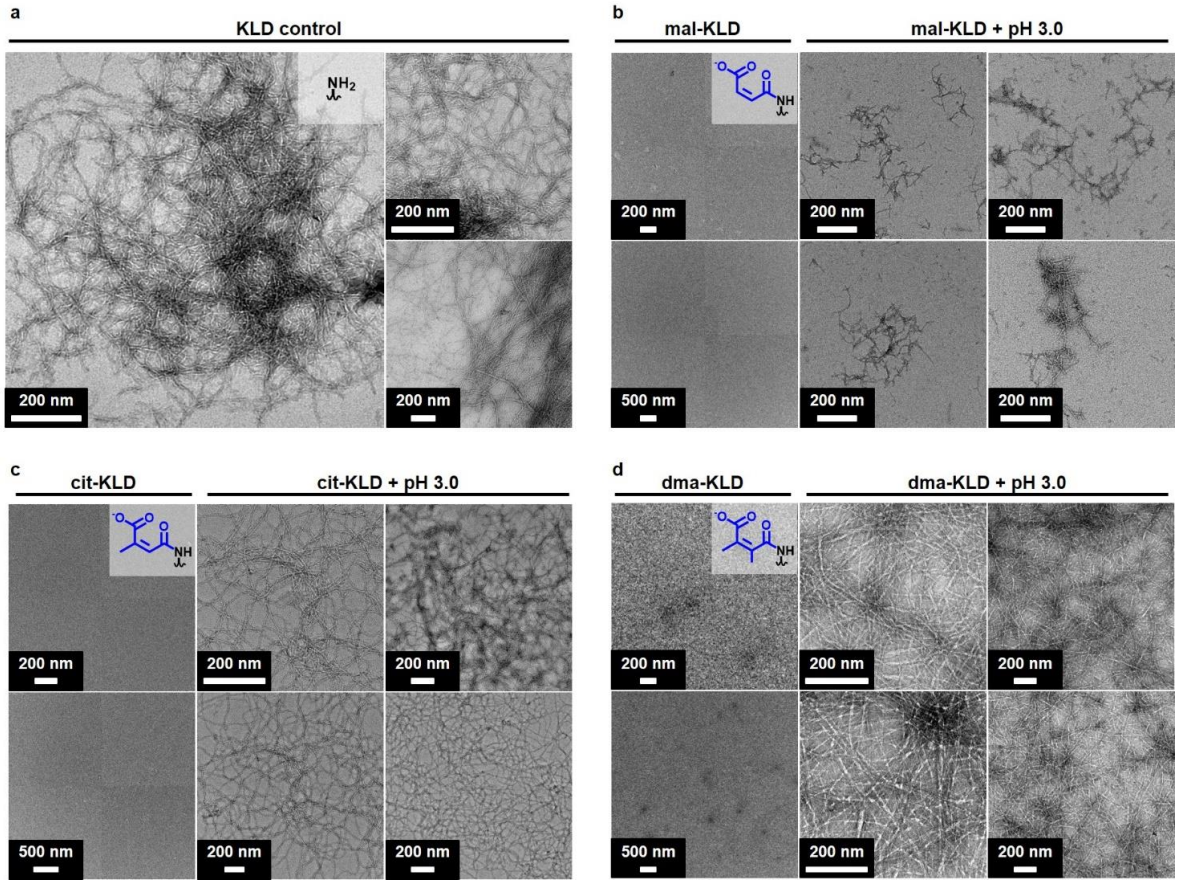


Figure 4.1.8. Additional TEM of self-assembling peptides and progelators. Extension to **Figure 4.1.7**. (a-d) Dry state stained TEM of (a) KLD control, (b) mal-KLD before (left) and after (right) acid treatment, (c) cit-KLD before (left) and after (right) acid treatment, and (d) dma-KLD before (left) and after (right) acid treatment. Inset chemical structures of maleamic acids conjugated to lysine residues prior to treatment. Peptides at 100 μM were treated at pH 3.0 for 12 hr, then neutralized to pH 7.4 prior to imaging

Bulk scale deprotection induces significant viscoelastsic changes. The KLD-12 peptide is a viscoelastic physical hydrogel with rehealable properties, as demonstrated in **Chapter 3**. We therefore, conducted tests to determine whether complete deprotection of our progelators could recapitulate native gelling behavior. Peptides were incubated at pH 7.4, 6.8, 5.5, and 3.0 for up to 24 hr then neutralized for rheological measurements (**Figure 4.1.9**). Bulk samples show solid hydrogels, similarly to the KLD control, following acid-treatment (**Figure 4.1.9a**). Incomplete deprotection or potential trapping of the maleic and citraconic acid products is suspected to cause the residual absorbance in the visible spectrum. Resulting solutions for all acid-treated progelators reveal viscoelastic hydrogels with storage moduli (G') greater than (G'') (**Figure 4.1.9b**).

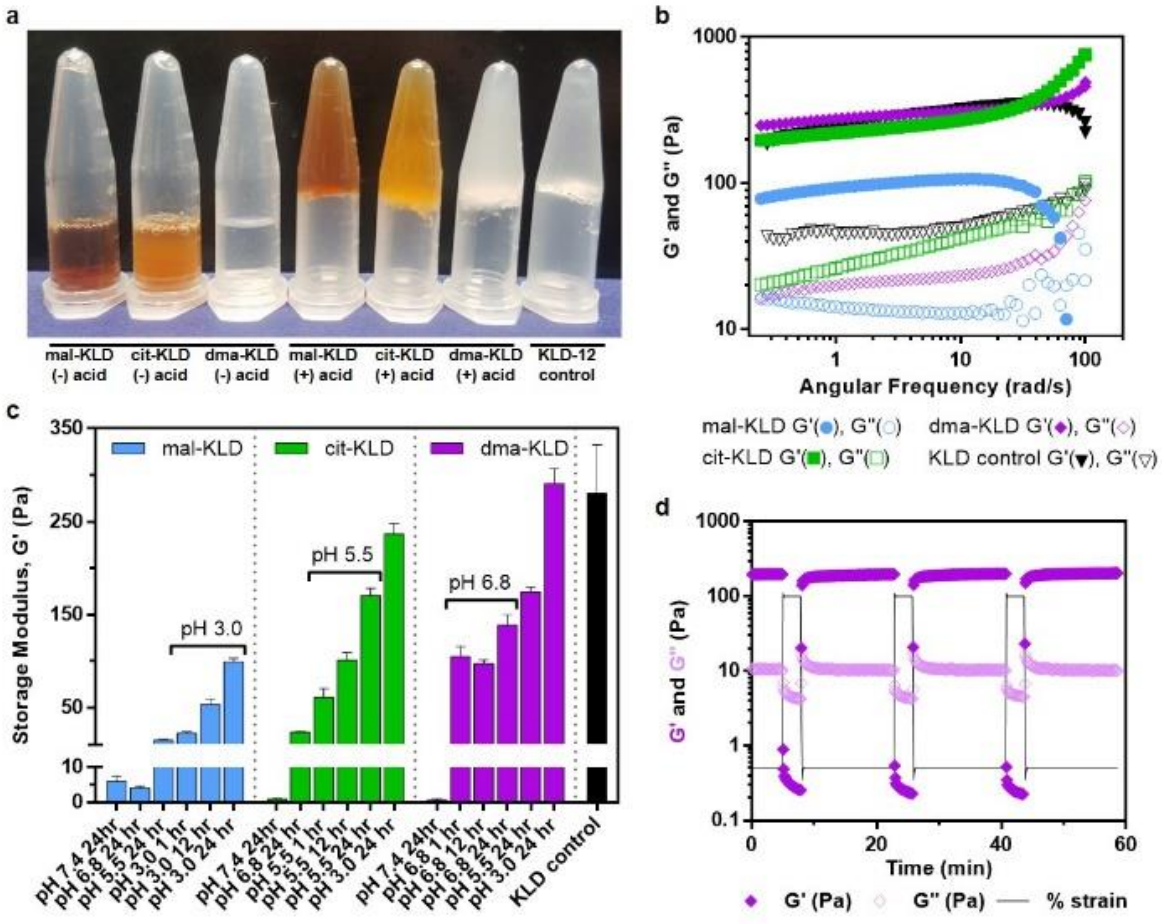
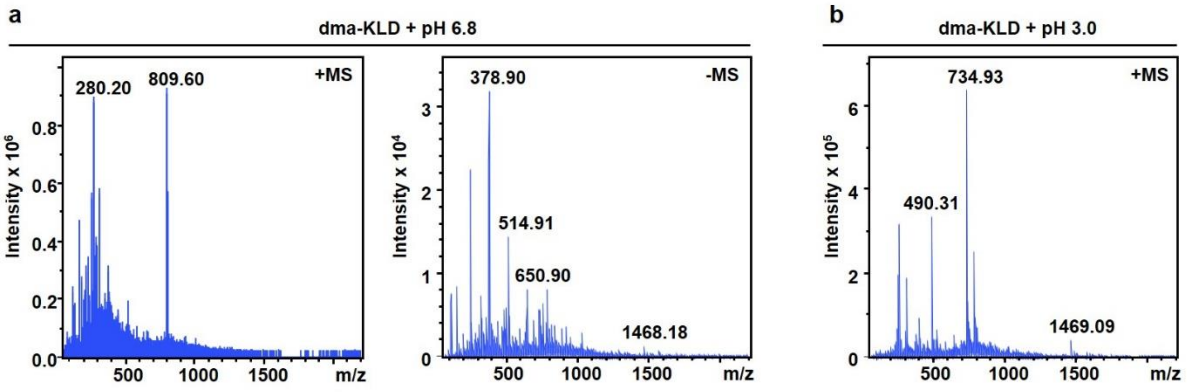


Figure 4.1.9. Bulk rheological properties of pH-activated hydrogels. (a) Image of untreated (-) progelator solutions, acid-treated (+) hydrogels, and KLD control. (b) Frequency sweeps of viscoelastic moduli, G' and G'', of KLD control and hydrogels formulated from progelators treated at pH 3.0 for 24 hr. Angular frequency 100-0.25 rad/s, 0.5% strain, n=3 repeats. (c) Storage moduli, G', of peptides treated at pH 7.4, 6.8, 5.5, or 3.0 for 1, 12, or 24 hr. Angular frequency 2.5 rad/s, 0.5% strain. (d) Representative step-strain oscillations of dma-KLD treated with pH 3.0 for 24 hr demonstrate healing capacity. Angular frequency 2.5 rad/s. Measurements conducted with destructive strain at 100% for 3 min, and then regeneration at 0.5% strain for 15 min (n=3 cycles). All measurements performed on peptide samples that were neutralized and suspended in 1x DPBS (pH 7.4) at 10 mM.

The sensitivity of each progelators under concentrated conditions, mimicking that of an injected dose, was tested at pH 7.4, 6.8, 5.5, and 3.0 for 24 hr (**Figure 4.1.9c**). Additionally, each progelator was treated for 1 and 12 hr at the pH where significant changes to responsiveness for each maleamic acid have been reported.[12,13] An increase in storage moduli, G', is observed with increasing acidity and longer treatment times. Furthermore, the stiffest hydrogels were formed by dma-KLD, which possesses the most labile maleamic acid in this study. Indeed, viscoelastic

properties for the dma-KLD treated at pH 3.0 for 24 hr resulted in viscoelastic moduli on par with the KLD control, indicative of complete maleamic acid deprotection. ESI of treated dma-KLD gels reveal partial and complete deprotection products (**Figure 4.1.10**).



c

Sample	Observed Peaks (m/z)	Peak Identities	Expected MW (g/mol)
dma-KLD + pH 6.8	1468.18 $[M\text{-}H^-]^-$	KLD	1466.81
	809.60 $[M+dma^-+Na^++2H^+]^{2+}$	KLD(w/ 1 dma)	1617.92
dma-KLD + pH 3.0	1469.09 $[M+H^+]^+$	KLD	1468.82
	734.93 $[M+2H^+]^{2+}$	KLD	1469.83
	490.31 $[M+3H^+]^{3+}$	KLD	1470.84

Figure 4.1.10. Mass spectrometry of pH-activated hydrogels. dma-KLD peptide from bulk rheological studies were analyzed by ESI as treatment at (a) pH 6.8 and (b) pH 3.0. (c) Table summarizing peak identities show cleavage products including the loss of 2 or all 3 dimethylmaleic acid protecting groups.

Furthermore, the dma-KLD responded well at physiologically relevant conditions observed in mild tissue inflammation. We note that bulk scale cleavage is likely slowed, due to decreased solvent diffusion as macromolecular self-assembly occurs. Furthermore, we suspect that *in vitro* gelation kinetics may differ from that *in vivo,*[40] as local pH gradients exist in inflamed tissues. Regardless, these experiments confirm gelation sensitivity can be tuned with simple modification of the charge-conversion moiety.

Finally, the capacity for hydrogel healing following excess strain was demonstrated through step-strain oscillations (**Figure 4.1.9d** and **Figure 4.1.11**) in which destructive strain (100 %) was applied to disrupt the hydrogels, resulting in liquid-like solutions with G'<G''. This excess strain was removed, and rapid hydrogel regeneration was observed (crossover G'=G'' occurs within seconds) over several cycles.

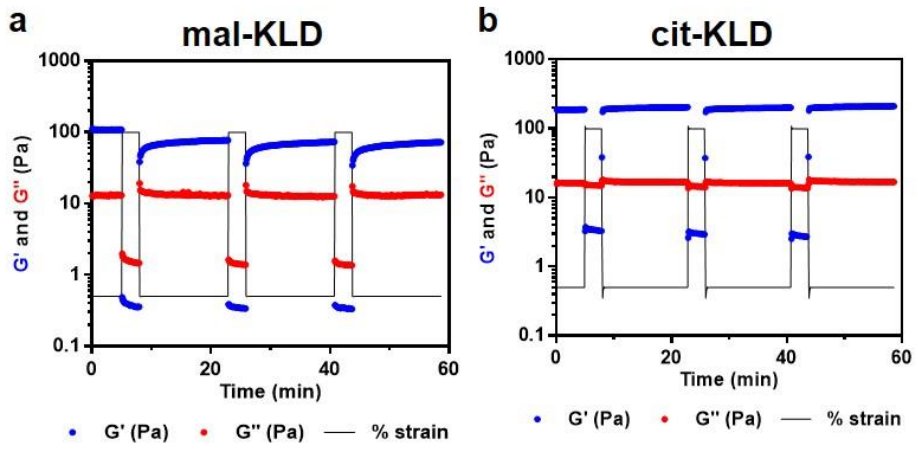


Figure 4.1.11. Step-strain oscillations for mal-KLD and cit-KLD treated with acid. Corresponds with **Figure 4.1.9d.** Progelators treated with pH 3.0 for 24 hr demonstrate healing capacity. Angular frequency 2.5 rad/s. Measurements conducted with destructive strain at 100% for 3 min, and then regeneration at 0.5% strain for 15 min (n=3 cycles). All measurements performed on peptide samples that were neutralized and suspended in 1x DPBS (pH 7.4) at 10 mM.

Strain sweeps were used to identify an appropriate measuring strain within the linear viscoelastic region (LVR) for all peptides (**Figure 4.1.12**). For mal-KLD, cit-KLD, and dma-KLD treated at pH 3.0 for 24 hr, the viscoelastic storage (G‘) and loss (G‘‘) moduli remained stable up to 1%, 4%, and 5% strain, respectively (**Figure 4.1.12a-c**). KLD control was stable up to 1% strain (**Figure 4.1.12d**).

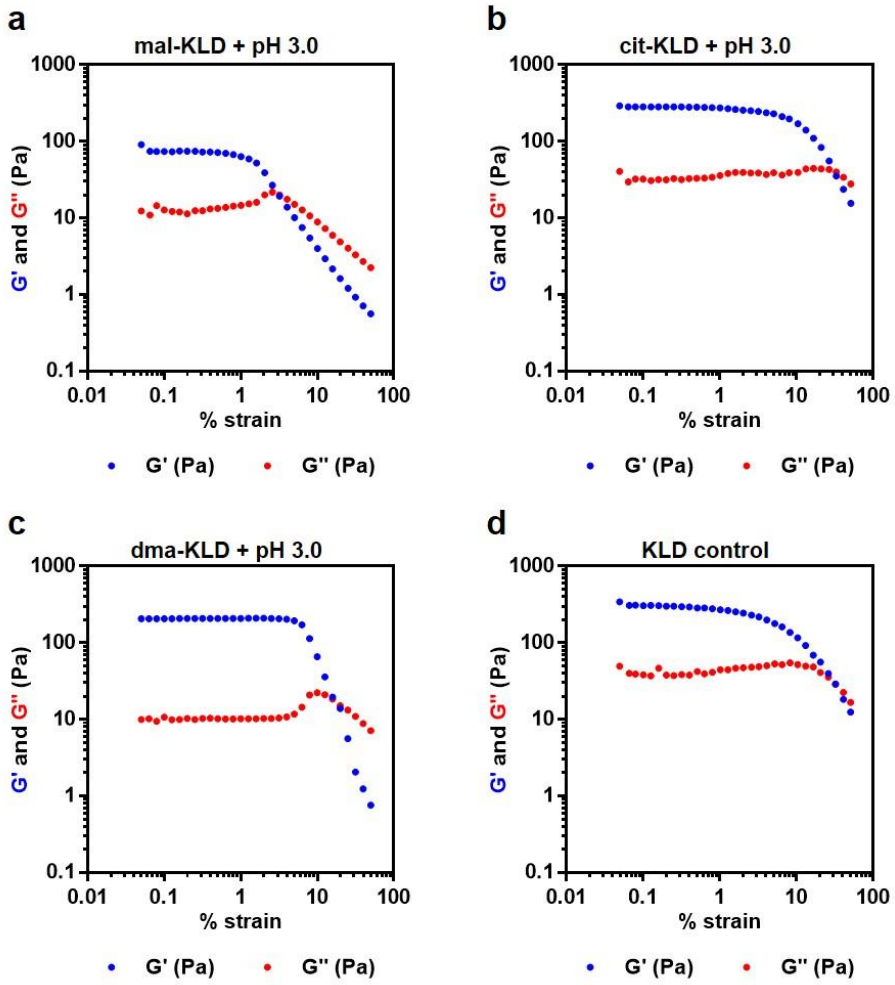


Figure 4.1.12. Strain sweeps for LVR identification of soluble progelators and pH activated hydrogels. (a-d) Storage (G') and loss (G'') moduli were measured as a function of strain (0.5–50%) to identify the linear viscoelastic region (LVR) and appropriate rheological measurement conditions for all peptides. Measurements performed on (a) mal-KLD, (b) cit-KLD, and (c) dma-KLD, treated with pH 3.0 24 hr followed by neutralization into 1x DPBS (pH 7.4). (d) KLD control in 1x DPBS (pH 7.4). Peptides at 10 mM. Strain sweep from 0.05-50 % at 2.5 rad/s and temperature of 37 °C.

Angular frequency sweeps were used to asses frequency dependent viscoelastic properties of peptide hydrogels measured in **Figure 4.1.9c**. High dependence can indicate a material that spreads easily, whereas low dependence is indicative of a low spreading, solidified material. For mal-KLD, large changes in G‘ and G‘‘ were observed for all samples at pH 7.4, 6.8, and 5.5 (**Figure 4.1.13a-c**). However, a gradual increase in frequency independence was observed with decreasing

pH and increasing incubation time (**Figure 4.1.13d-f)**, most notably after incubation at pH 3.0 for 24 hr.

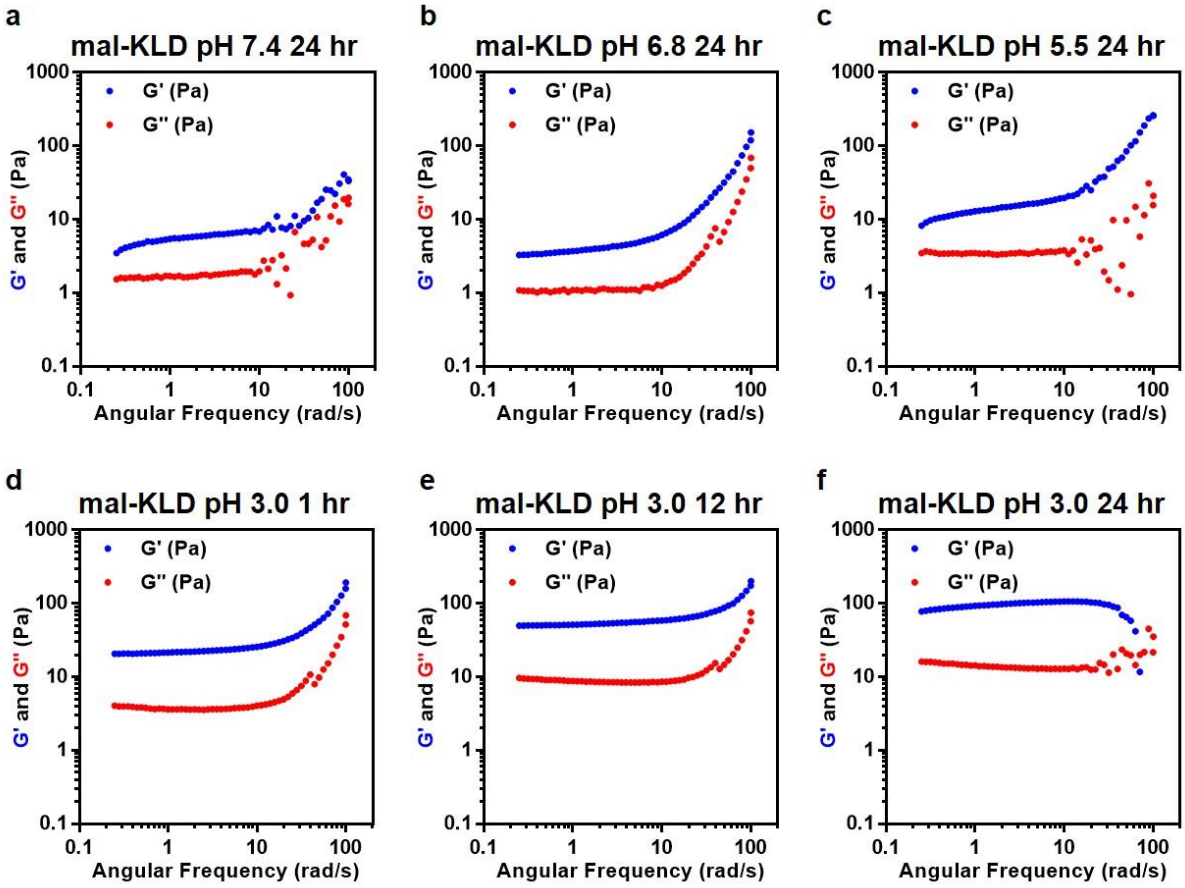


Figure 4.1.13. Frequency sweeps of mal-KLD Samples. (a-f) Angular frequency sweeps displayed for mal-KLD progelators treated at (a) pH 7.4 24 hr, (b) pH 6.8 24 hr, (c) pH 5.5 24 hr, (d) pH 3.0 1 hr, (e) pH 3.0 12 hr, and (f) pH 3.0 24 hr. Storage (G', blue traces) and loss (G'', red traces) moduli are plotted. Untreated peptides or mild-acid treated peptides demonstrate high dependence on angular frequency, indicative of a weak gel that flows over longer periods of time and behaves like a viscous liquid. Increased acidity and treatment time incurs frequency independence for assembly of a stiffer, elastic solid. Angular frequency 100-0.25 rad/s, 0.5% strain. Final peptide samples measured at 10 mM in 1xDPBS (pH 7.4). (n=3 repeats).

Frequency sweeps of treated hydrogels with cit-KLD (**Figure 4.1.14**), and to an even greater extent with dma-KLD (**Figure 4.1.15**), show this gelation-induced frequecny indenpendence as peptides solidify with continued maleamic acid deprotection. KLD control SAP shows a similar frequency independence in **Figure 4.1.16.** Thus, we conclude that acid-triggered hydrogelation induces frequency independent viscoelastic properties, indicating that self-assembled gels resist

flowing over long periods of time. This is a useful property for biomaterial implants that should stay in place within the target tissue for long periods of time. Conversely, the starting material progelators, althrough tecnically extremely weak hydrogels (because G‘>G‘‘), behaved more akin to viscous solutions prone to material spreading.

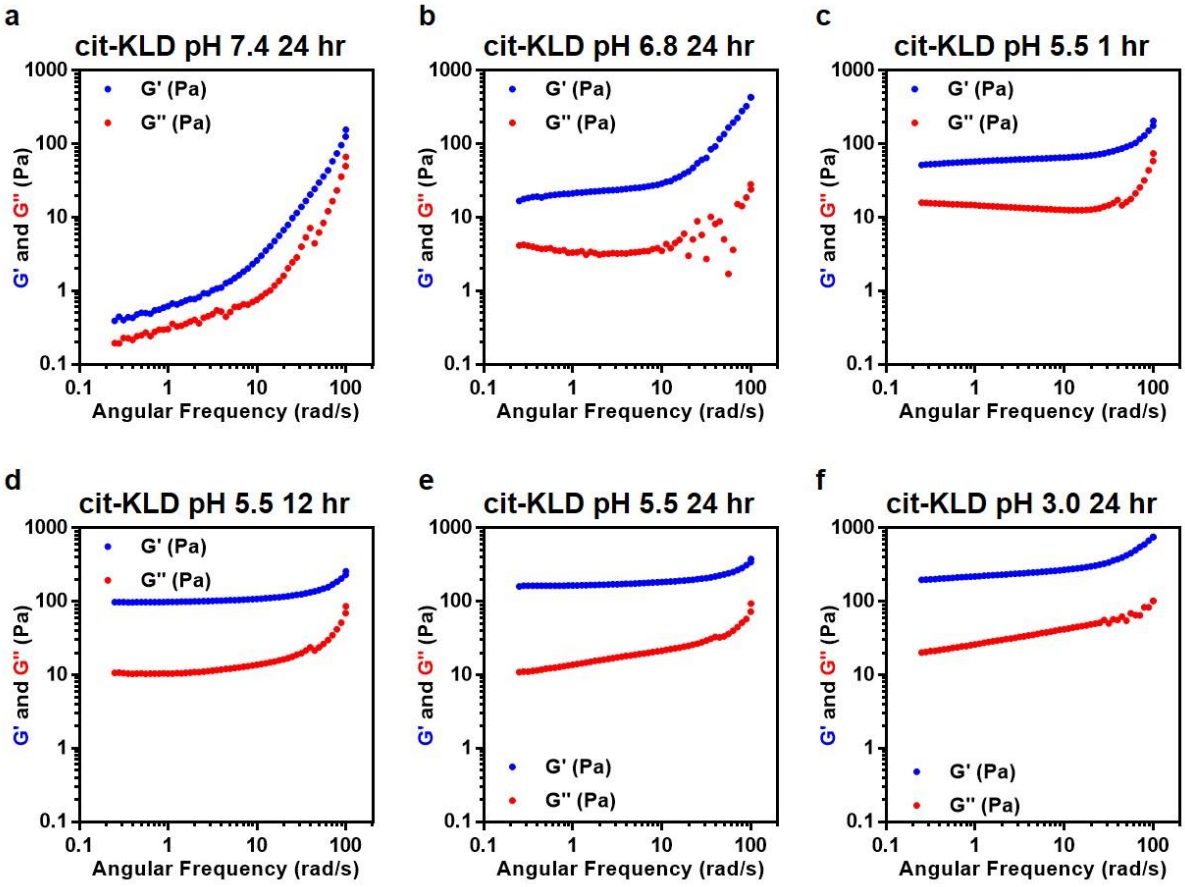


Figure 4.1.14. Frequency sweeps of cit-KLD Samples. (a-f) Angular frequency sweeps displayed for cit-KLD progelators treated at (a) pH 7.4 24 hr, (b) pH 6.8 24 hr, (c) pH 5.5 1 hr, (d) pH 5.5 12 hr, (e) pH 5.5 24 hr, and (f) pH 3.0 24 hr. Storage (G’, blue traces) and loss (G’’, red traces) moduli are plotted. Untreated peptides or mild-acid treated peptides demonstrate high dependence on angular frequency, indicative of a weak gel that flows over longer periods of time and behaves like a viscous liquid. Increased acidity and treatment time incurs frequency independence for assembly of a stiffer, elastic solid. Angular frequency 100-0.25 rad/s, 0.5% strain. Final peptide samples measured at 10 mM in 1xDPBS (pH 7.4). (n=3 repeats).

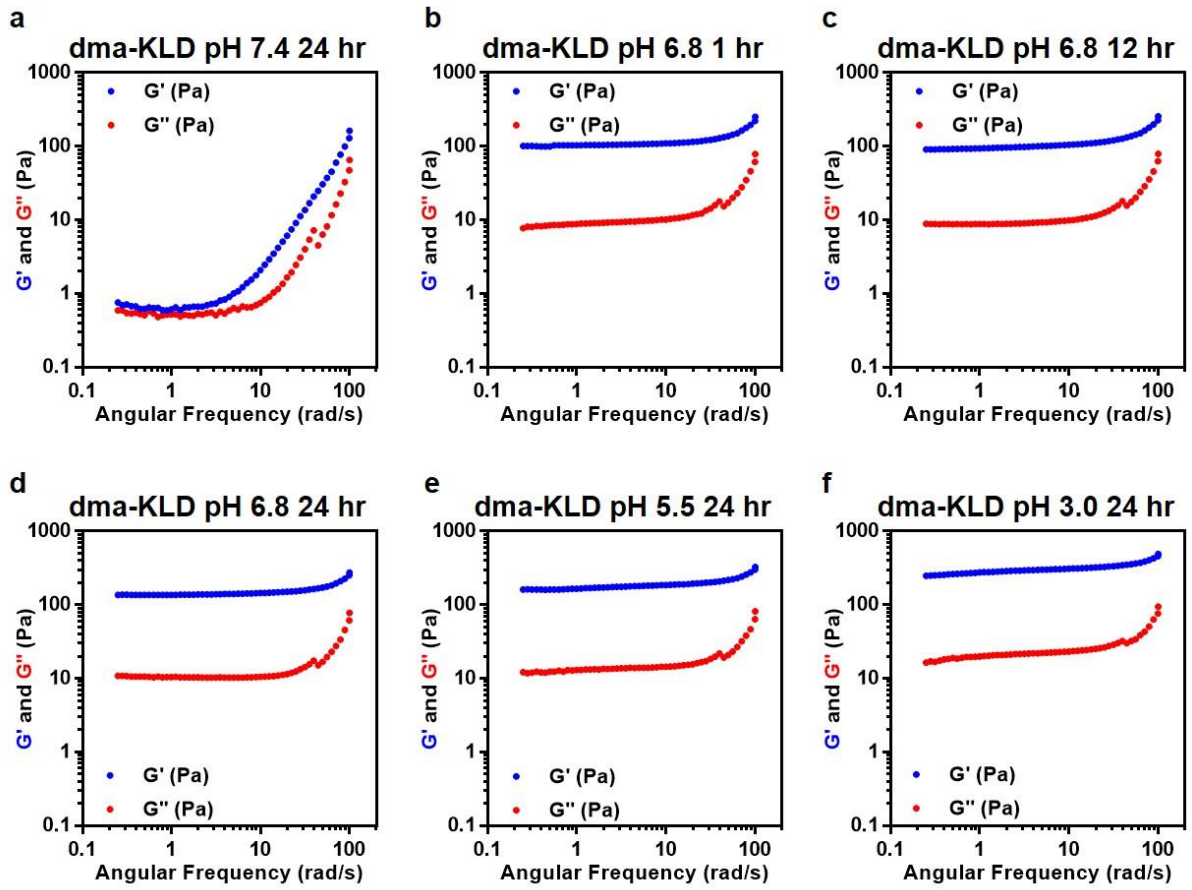


Figure 4.1.15. Frequency sweeps of dma-KLD Samples. (a-f) Angular frequency sweeps displayed for dma-KLD progelators treated at (a) pH 7.4 24 hr, (b) pH 6.8 1 hr, (c) pH 6.8 12 hr, (d) pH 6.8 24 hr, (e) pH 5.5 24 hr, and (f) pH 3.0 24 hr. Storage (G', blue traces) and loss (G'', red traces) moduli are plotted. Only untreated peptides demonstrate high dependence on angular frequency, indicative of a weak gel that flows over longer periods of time and behaves like a viscous liquid. Acid treatment incurs frequency independence for assembly of a stiffer, elastic solid. Angular frequency 100-0.25 rad/s, 0.5% strain. Final peptide samples measured at 10 mM in 1xDPBS (pH 7.4). (n=3 repeats).

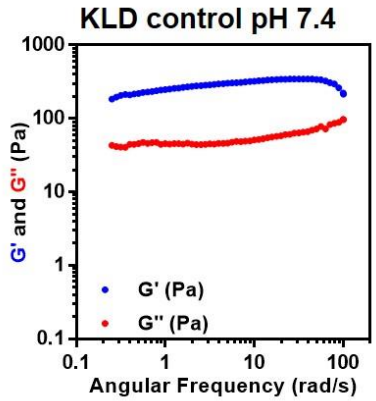


Figure 4.1.16. Frequency sweep of KLD control hydrogel. Angular frequency sweep displayed for KLD control at pH 7.4 24 hr. Storage (G', blue traces) and loss (G'', red traces) moduli are plotted. KLD control displays low frequency dependence, indicative of a stiff, elastic solid. Angular frequency 100-0.25 rad/s, 0.5% strain. Final peptide sample at 10 mM in 1xDPBS (pH 7.4). (n=3 repeats).

Low viscosity progelators are amenable to catheter injection. Needle based injections require that materials are shear-thinning. Catheter based injections further require that the material have low enough viscosity to flow through the catheter during delivery, a process which can take up to 1 hr in a clinical setting.[40,54] Many physical hydrogels are shear-thinning and rehealable, but aging time can vary from different relaxation and interpenetration properties between fractured domains.[55] Alternatively, excess viscosity from reassembly in the catheter can stop material delivery, altogether. A material that gels after delivery can bypass these issues.

As our peptide progelators in 1xDPBS are free-flowing solutions, we tested their utility for catheter-based injection (**Figure 4.1.17**). Complex viscosity of the peptides was measured as a function of shear rate (**Figure 4.1.17a,b**). Progelators were over two orders of magnitude lower in viscosity than the KLD-12 control gelator, as well as shear-thinning.

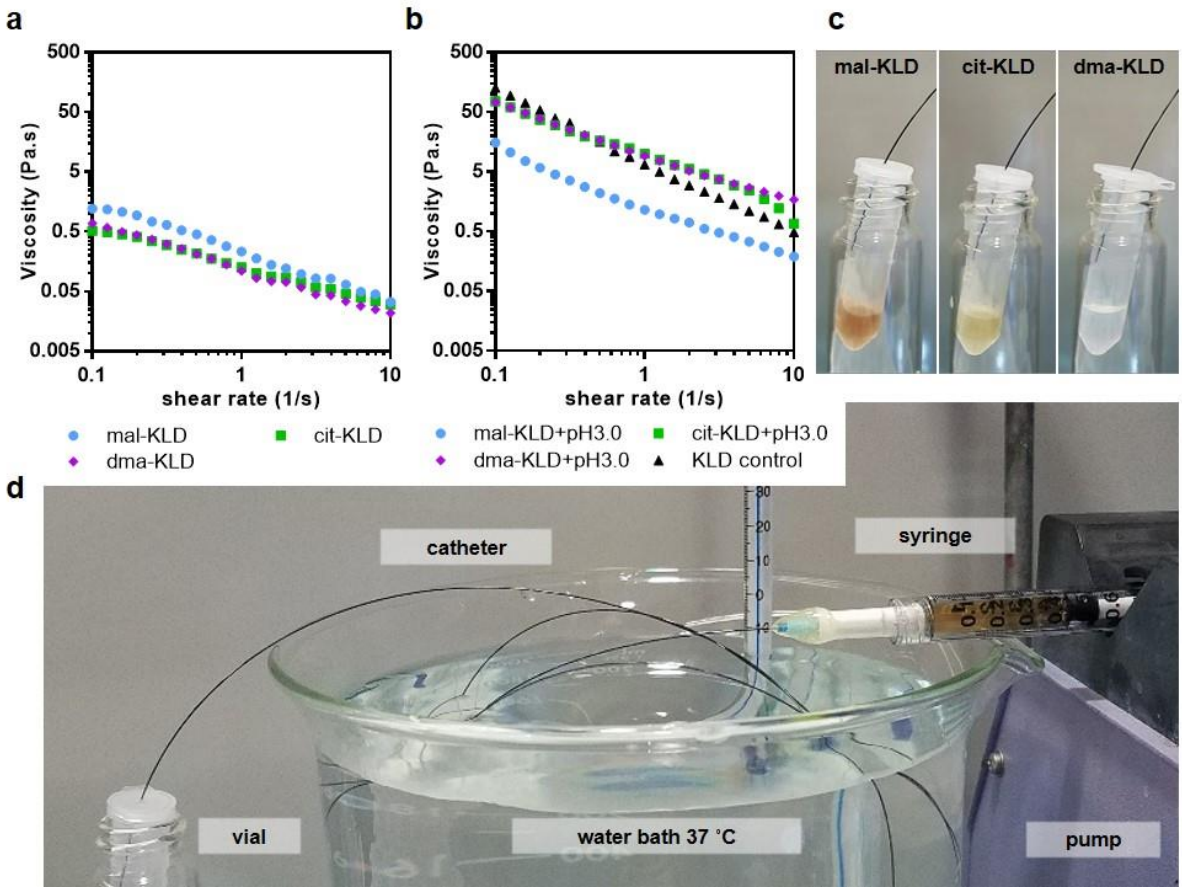


Figure 4.1.17. Progelators persist as low viscosity solutions for catheter injection. (a-b) Viscosity of (a) progelator solutions and (b) acid-treated hydrogels. (c) Progelators solutions flow smoothly through the catheter at 0.6 mL/min. (d) Catheter injection setup with loaded syringe pumping progelators through a catheter submerged in a 37 °C water bath. Peptides 10 mM in 1xDPBS (pH 7.4).

Acid-induced gelation triggered an increase in viscosity. Furthermore, no temperature dependent changes in viscoelastic properties were observed when samples were slowly heated from 21-37 °C (**Figure 4.1.18**), representative of the temperature variations generally experienced by biomaterials during catheter delivery. We reasoned that our progelators would be amenable to catheter-based injections. Progelators in this study demonstrated no resistance to delivery by hand or catheter failure when pumped at clinical relevant rates (0.6 mL/min) (**Figure 4.1.17c,d**), which excess viscosity from the KLD-12 control peptide at 10 mM in 1xDPBS caused catheter failure *in vitro*. Thus, we have successfully designed an acid-activatable material for simple formulation and noninvasive delivery. Finally, given the wider inner diameter of clinical over-the-wire infusion

catheters (e.g. EmergeTM PTCA, 0.36 mm), we reason that our low viscosity materials are amenable to both transendocardial injection and intracoronary infusion cardiac catheter delivery.

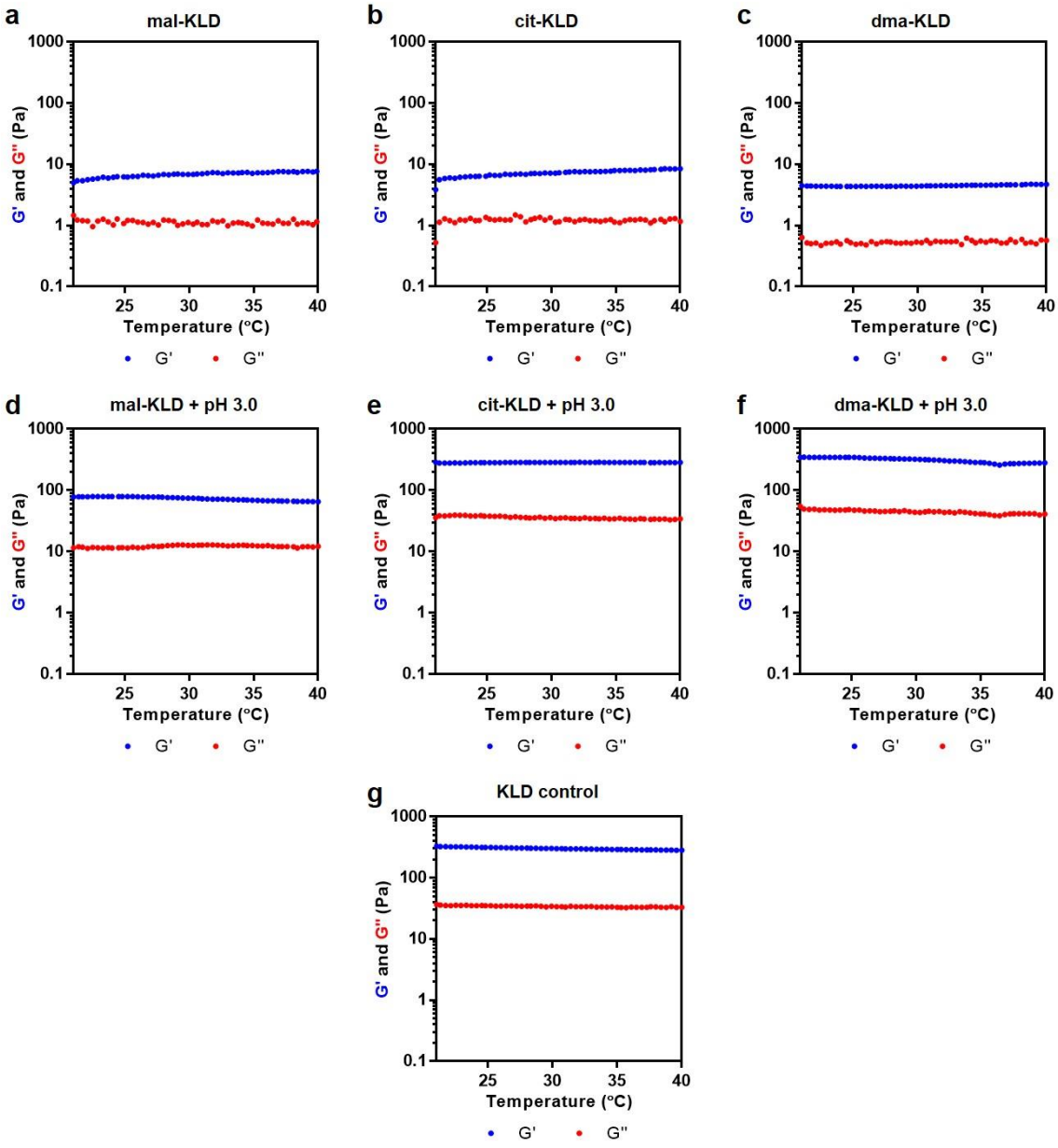


Figure 4.1.18. Temperature dependent viscoelasticity of soluble progelators and pH activated hydrogels. Progelators and acid-treated hydrogels (pH 3.0 24 hr followed by neutralization to pH 7.4 in 1x DPBS) exhibit temperature-independent viscoelastic moduli (G', G'') at conditions relevant to temperature changes experienced by injectable materials (room temperature to physiological temperature). Angular frequency of 2.5 rad/s, strain 0.5%, temperature sweep from 21-40 °C at a ramp rate of 0.5 °C/min. Peptide concentration is 10 mM

Progelators are hemocompatible in blood components. Lack of hemocompatibility can be a limiting factor for injectable biomaterials, which must demonstrate inert activity within the blood during direct (intravenous injection and catheter infusion) or indirect (subcutaneous and intramuscular injection leakage) contact with the bloodstream.[56,57] Potential blood interactions may cause thrombosis, induce hemolysis, or alter coagulation kinetics. We incubated our charge-conversion peptides in whole human blood components at increasing dosages of peptide in blood (**Figure 4.1.19** and **Figure 4.1.20**). For reference, generous estimates for clinically relevant doses from transendocardial catheter injection and intracoronary infusion are 1:830 and 1:500, respectively (see **Experimental Details**).

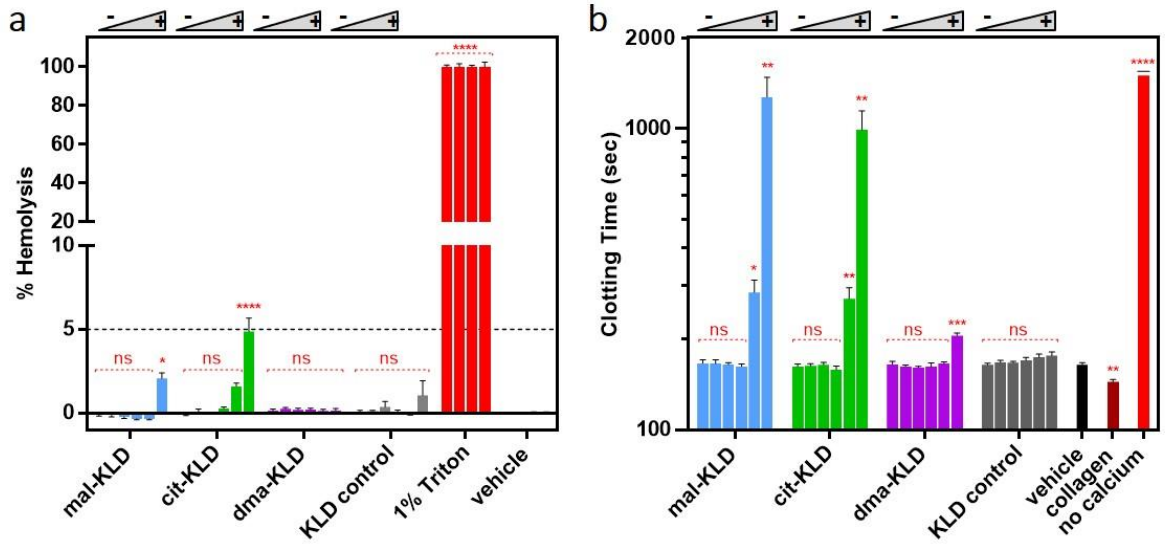


Figure 4.1.19. Hemocompatibility of peptide progelators in whole blood and red blood cells (RBCs). (a) Percent hemolysis of human red blood cells (RBCs) after incubation with different concentrations of peptide for 1 hr. Inset line defines the threshold for hemolytic response (> 5%). (n=6) (b) Activated clotting times of whole human blood in the presence of different peptide concentrations. (n=5) All peptide dilutions in biological fluid at 37 °C are provided in figures at increasing peptide in blood concentration from 1:10,000, 1:5000, 1:1000, 1:500, 1:100, and 1:10 volume ratios, given an injection concentration of 10 mM stock solution in 1xDPBS. *ns ($p > 0.05$), * ($p \leq 0.05$), ** ($p \leq 0.01$), *** ($p \leq 0.001$), and **** ($p \leq 0.0001$)*. Corresponds with **Table 4.1.6** and **Table 4.1.7**.

The hemolytic properties of our progelators and the KLD control in isolated red blood cells (RBCs) were assessed for acute toxicity (**Figure 4.1.19a** and **Table 4.1.6**). Doses up to 1:10 for all

peptides revealed <5% hemolysis, which is below the limit for consideration as a nonhemolytic biomaterial.[58]

Table 4.1.6. Hemolysis of red blood cells (RBCs). Corresponds with **Figure 4.1.19a**. Nonhemolytic biomaterials classified by < 5% hemolysis. (n=6 per group). ns ($p > 0.05$), * ($p \leq 0.05$), ** ($p \leq 0.01$), *** ($p \leq 0.001$), and **** ($p \leq 0.0001$). RM one-way ANOVA with multiple comparisons of the mean in each group with that of the vehicle standard. No correction for multiple comparisons, Values are mean ± SEM.

	peptide in blood dilutions						standard	pos control
	1:10	1:100	1:500	1:1000	1:5000	1:10000	vehicle	1% Triton
mal-KLD								
Average (%)	2.1	-0.3	-0.3	-0.2	-0.1	-0.1	0.0	100
SEM	(± 0.3)	(± 0.1)	(± 0.1)	(± 0.1)	(± 0.1)	(± 0.1)	(± 0.1)	(± 0.9)
P Value	0.0172	0.6925	0.6925	0.7830	0.8877	0.9268		< 0.0001
Summary	*	ns	ns	ns	ns	ns		****
cit-KLD								
Average (%)	4.9	1.6	0.3	0.0	0.1	-0.1	0.0	100
SEM	(± 0.8)	(± 0.2)	(± 0.1)	(± 0.0)	(± 0.2)	(± 0.1)	(± 0.0)	(± 0.9)
P Value	< 0.0001	0.0639	0.7502	0.9831	0.9267	0.9436		< 0.0001
Summary	****	ns	ns	ns	ns	ns		****
dma-KLD								
Average (%)	0.2	0.1	0.2	0.2	0.3	0.2	0.0	
SEM	(± 0.1)	(± 0.1)	(± 0.1)	(± 0.1)	(± 0.1)	(± 0.1)	(± 0.1)	(± 0.9)
P Value	0.8514	0.8786	0.8081	0.8188	0.7601	0.8459		< 0.0001
Summary	ns	ns	ns	ns	ns	ns		****
KLD control								
Average (%)	1.0	-0.1	0.1	0.4	0.1	0.1	0.0	
SEM	(± 0.9)	(± 0.0)	(± 0.1)	(± 0.3)	(± 0.1)	(± 0.1)	(± 0.1)	(± 0.9)
P Value	0.2221	0.9192	0.9134	0.6637	0.8904	0.9019		< 0.0001
Summary	ns	ns	ns	ns	ns	ns		****

Activated clotting times (ACT) were used as a general method that encompasses intrinsic and common coagulation pathways to assess thrombogenicity during delivery (**Figure 4.1.19b** and **Table 4.1.7**). This assay is the preferred test in catheterization labs and cardiac theratres.[59] Anticoagulative properties were observed at 1:100 and 1:10 blood doses for mal-KLD and cit-KLD, and to a much lesser extent at 1:10 with dma-KLD. The KLD control peptide exhibited no significant alteration to normal clotting times over that of the vehicle standard at all doses. In contrast, collagen showed a thrombogenic effect, and chelation of calcium prevented clotting altogether.

Table 4.1.7. Activated clotting times (ACT) in human blood. Corresponds to **Figure 4.1.19b**. Average times reported ± standard error of mean (n=5 per group). Analysis by RM one-way ANOVA with multiple comparisons of the mean in each group with that of the vehicle standard. No correction for multiple comparisons. ns ($p > 0.05$), * ($p \leq 0.05$), ** ($p \leq 0.01$), *** ($p \leq 0.001$), and **** ($p \leq 0.0001$). Values are mean ± SEM

	peptide in blood dilutions						standard	pos control	neg control
	1:10	1:100	1:500	1:1000	1:5000	1:10000	vehicle	collagen	no calcium
mal-KLD									
Average Time (sec)	1271	285	162	165	166	166	164	144	>1500
SEM	(± 207)	(± 28)	(± 3)	(± 2)	(±5)	(±4)	(± 3)	(± 2)	n/a
P Value	0.0058	0.0115	0.5234	0.9640	0.8129	0.7233		0.0024	< 0.0001
Summary	**	*	ns	ns	ns	ns		**	****
cit-KLD									
Average Time (sec)	989	272	159	164	163	162			
SEM	(± 155)	(± 24)	(± 4)	(± 3)	(±3)	(±3)			
P Value	0.0057	0.0081	0.1629	>0.9999	0.7222	0.2822			
Summary	**	**	ns	ns	ns	ns			
dma-KLD									
Average Time (sec)	206	166	162	161	162	165			
SEM	(± 4)	(± 2)	(± 5)	(± 1)	(±1)	(±4)			
P Value	0.0006	0.6874	0.6812	0.5498	0.9542	0.9202			
Summary	***	ns	ns	ns	ns	ns			
KLD control									
Average Time (sec)	176	174	170	167	167	164			
SEM	(± 5)	(± 4)	(± 4)	(± 2)	(±3)	(±2)			
P Value	0.1629	0.1659	0.3700	0.5083	0.9319	0.9629			
Summary	ns	ns	ns	ns	ns	ns			

Finally, plasma recalcification profiles in platelet poor plasma (PPP) were used to study the intrinsic pathway of clotting, which can reveal adverse blood-biomaterial interactions (**Figure 4.1.20** and

Table 4.1.8 **- Table 4.1.10**). Collagen, which activates platelet aggregation, showed no early onset of coagulation in the presence of platelet-poor media (**Figure 4.1.20a**). Glass coverslips, which have negatively charged and hydrophilic surfaces, were used as a positive control of contact activation, whereby coagulation onset time was reduced. As a negative control, PPP without Ca^{2+} showed no onset of coagulation.

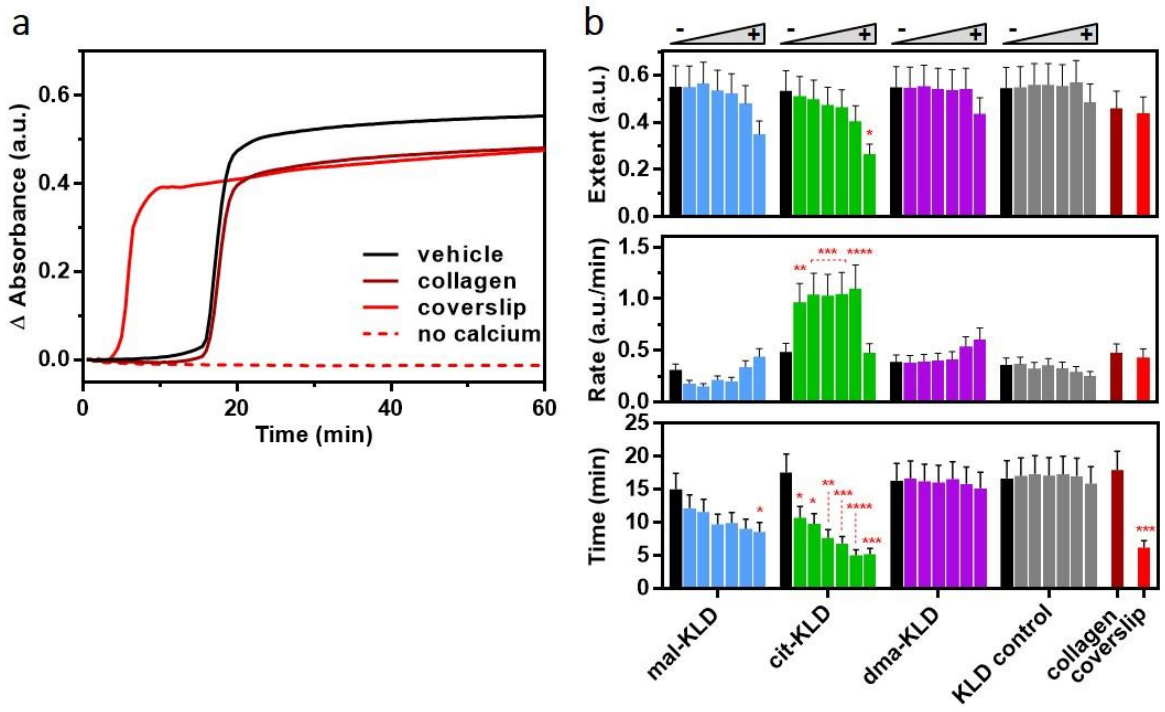


Figure 4.1.20. Hemocompatibility of peptide progelators in platelet poor plasma (PPP). (a) Plasma recalcification profiles in platelet poor plasma (PPP) for vehicle standard, and collagen, glass coverslip, and no calcium controls. (n=6) (b) Measurements of coagulation maximal extent, rate, and onset time from plasma recalcification profiles as a function of peptide concentrations. (n=6) All peptide dilutions in biological fluid at 37 °C are provided in figures at increasing peptide in blood concentration from 1:10,000, 1:5000, 1:1000, 1:500, 1:100, and 1:10 volume ratios, given an injection concentration of 10 mM stock solution in 1xDPBS. *ns ($p > 0.05$), * ($p \leq 0.05$), ** ($p \leq 0.01$), *** ($p \leq 0.001$), and **** ($p \leq 0.0001$)*. Corresponds with **Figure 4.1.21** and **Table 4.1.10** in **Experimental Details**.

Both mal-KLD and cit-KLD exhibited earlier onset times and marked decrease in extents of coagulation (**Figure 4.1.20b** and **Figure 4.1.21**). Furthermore, cit-KLD caused a faster rate of coagulation than that of the other peptides. dma-KLD and KLD control peptide, however exhibited minimal deviation from vehicle standard coagulation profiles, with no significant difference between each other at all doses.

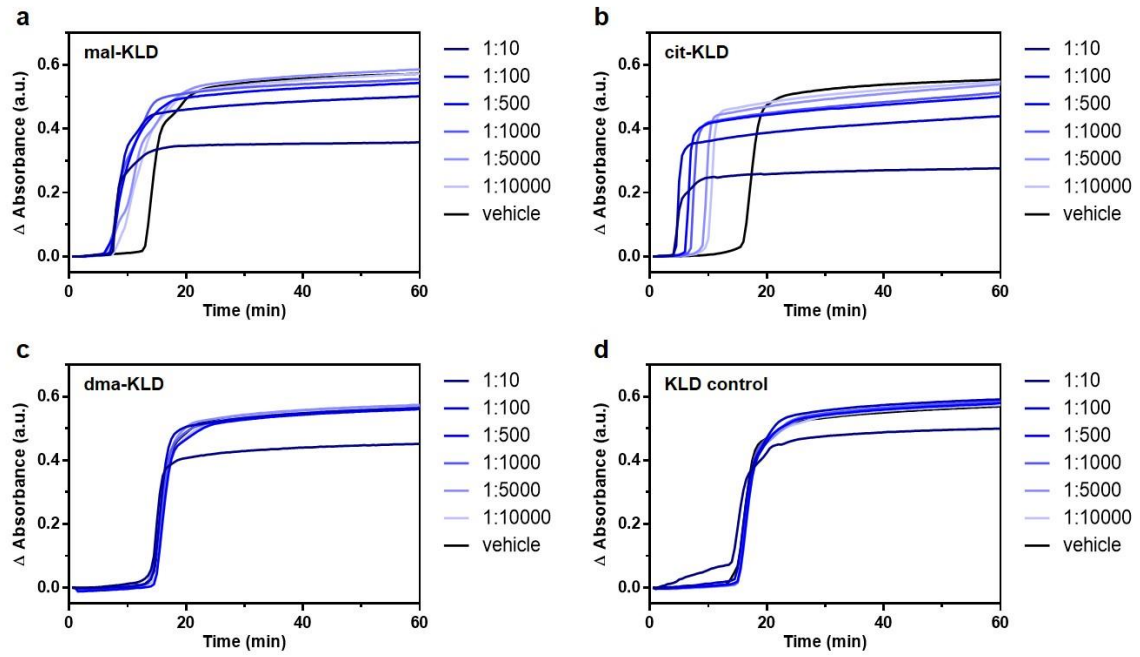


Figure 4.1.21. Plasma recalcification profiles in platelet poor plasma (PPP). Recalcified PPP was incubated with increasing concentrations of peptide to assess changes to coagulation profiles. Corresponds with **Figure 4.1.20**. Vehicle standards provided as black traces. Largest changes induced by mal-KLD and cit-KLD at increasing concentrations, whereby earlier onset of coagulation and reduced extent of coagulation are observed. All peptide dilutions in PPP at 37 °C are 1:10, 1:100, 1:500, 1:1000, 1:5000, and 1:10,000 from a 10 mM stock solution in 1xDPBS (n=6)

Self-assembly induced encapsulation of model drug. We reason that acid-induced deprotection and simultaneous self-assembly imbues our progelators with the capacity for activatable drug encapsulation. Thioflavin T (ThT) was chosen as a model drug for its fluorogenic capacity to quantitatively detect fiber formation and its stability to acidic pH.[60-63] Serial dilution of KLD in ThT revealed a critical aggregation concentration (CAC) at pH 5.5, 6.8, and 7.4 of 80.0 (± 3.1) μM peptide (**Figure 4.1.22**). Corresponding emission spectra at each pH value are provided in **Figure 4.1.23**. Future studies with acid-induced progelatos will study kinetics of self-assembly induced encapsulation of this model drug after exceeding the CAC.

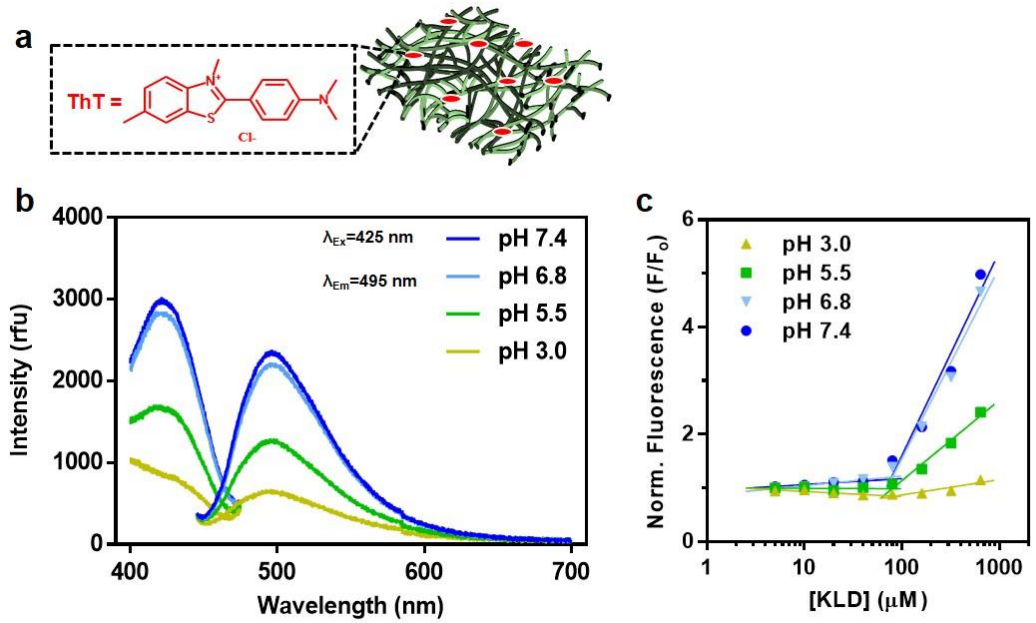


Figure 4.1.22. Excitation and Emission Spectra of ThT in preformed hydrogel. Schematic showing the chemical structure of ThT embedded in pre-formed hydrogel. (b) Excitation (400-475 nm, λ_{Em} = 495 nm) and emission (445-700 nm, λ_{Ex} = 425 nm) spectra for ThT (10 μM) incubated in KLD control peptide (1000 μM) at pH 3.0, 5.5, 6.8, and 7.4. Different pH values induce no spectroscopic absorbance shifts with respect to pH. Reduction in signal with increased acidity is directly proportional to lack of self-assembled peptide fiber stability. (c) The critical aggregation concentration (CAC) for KLD control at pH 5.5, 6.8, and 7.4 is 80.0 (± 3.1) μM peptide. No CAC was detected at pH 3.0 up to 640 μM. Signal reported in units of F/F_o, or fluorescence of ThT (50 μM) in KLD (5 - 640 μM) normalized to fluorescence of ThT only. CMC plot corresponds with raw data in **Figure 4.1.23**. Buffers were prepared at pH 3.0 (200 mM glycine-HCl buffer), pH 5.5 (200 mM acetate buffer), pH 6.8 (200 mM phosphate buffer), and pH 7.4 (200 mM phosphate buffer). Samples (n=4 repeats) were measured in black 96 well clear-bottom plates (V_{total} = 100 μL). Spectra collected at 37 ˚C with step size of 0.2 nm, 100 flashes, height of 3 mm from bottom, with n=3 accumulations.

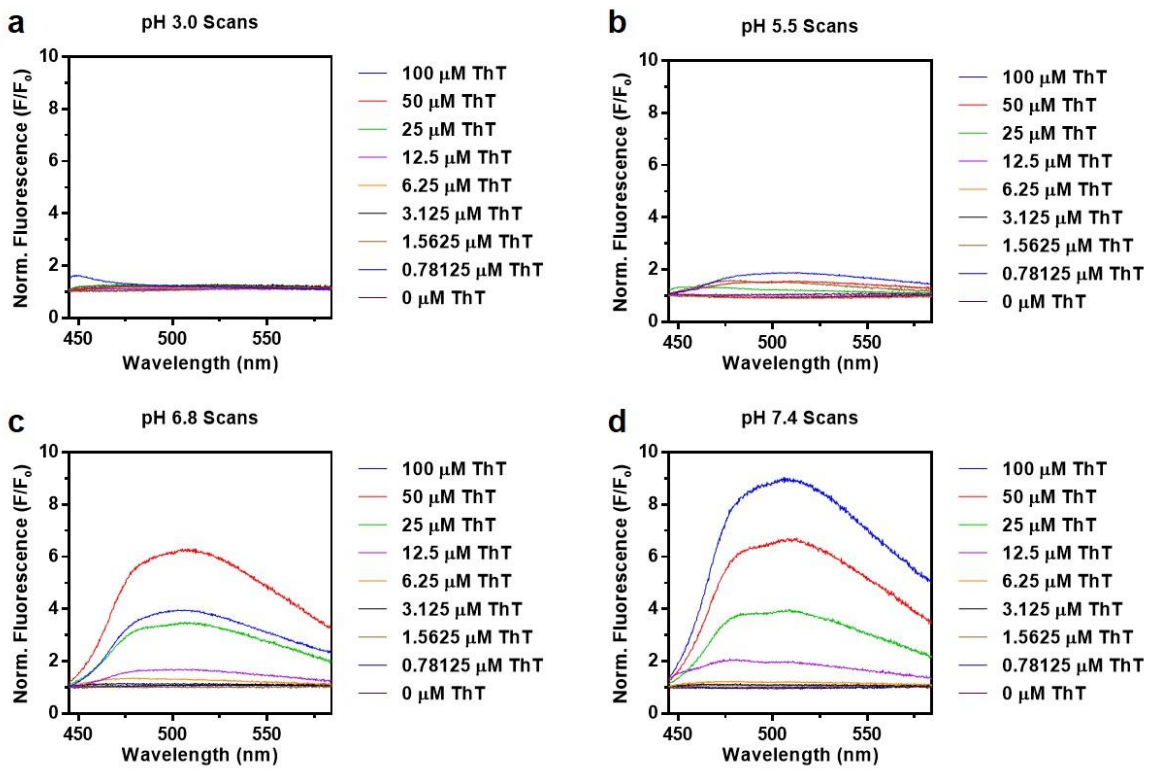


Figure 4.1.23. Serial Addition of ThT to KLD Control at Different pH Values. Emission spectra (445-700 nm, λ_{Ex} = 425 nm) spectra for ThT (50 μM) incubated in KLD control peptide (ranging from 0-100 μM) at pH 3.0, 5.5, 6.8, and 7.4. Buffers were prepared at pH 3.0 (200 mM glycine-HCl buffer), pH 5.5 (200 mM acetate buffer), pH 6.8 (200 mM phosphate buffer), and pH 7.4 (200 mM phosphate buffer). Samples measured in black 96 well clear-bottom plates (V_{total} = 100 μL). Spectra collected at 37 ˚C with step size of 0.2 nm, 100 flashes, height of 3 mm from bottom, with n=3 accumulations. Spectra correspond to **Figure 4.1.22c.**

4.1.3 Discussion and Conclusions

There is a need for synthetically simple tissue engineering scaffolds that can be delivered non-invasively to injury sites. In many extreme cases, inflammation is not localized (e.g. arthritis, myocardial ischemia, traumatic injury), so single injections of a preformed hydrogel to the site of interest may not be practical. Our design strategy enables a stimuli-responsive solution that flows freely until activated by inflammation-associated extracellular acidosis.

We present a simplistic approach to reversible modification of a self-assembling peptide using a one-step synthesis with quantitative yields. The pH-sensitivity of these progelators is readily tuned with substituted maleamic acids moiety, enabling assembly at physiologically relevant tissue acidities (pH ~ranging from 5.4-7.1). Thus, our platform utilizes unique advantages of both soluble small

molecules (injectability and tissue perfusion) and macromolecular hydrogels (stationary support, prolonged retention, and drug encapsulation).

We reason that our materials have the capacity to spread unhindered until activated by the acidic extracellular microenvironment of inflamed tissue. This structurally dynamic behavior is especially useful in wound-healing applications where the in vivo architectures are tortuous, and in some instances require navigation through narrow pathways prior to self-assembly as a stationary hydrogel. A distinct advantage that many soft injectable hydrogels have is the capacity to repeatedly heal after strain-induced network disassembly. We showed that our acid-treated progelators were able to recapitulate this important property as well as increased spreading resistance during solidification.

Both mal-KLD and cit-KLD progelators exhibit significant anticoagulative properties, whereas dma-KLD dosing was nearly indistinguishable from that of hemocompatible KLD control peptide. The extent of coagulation for dma-KLD was only altered at the highest dose (1:10 peptide:blood), which indicates that local high concentrations of peptide have a minor anticoagulative effect on the intrinsic coagulation (contact-based) pathway. It is important to note that the two highest blood doses (1:10 and 1:100) are higher than would theoretically be present in the blood after 1 min of circulation, and assumes all material entered into the bloodstream and not the intended tissue. We therefore reason that maleamic acid modified peptides induce no relevant impact on hemocompatibility. Finally, a general trend presented itself as improved hemocompatibility with increasing progelator hydrophobicity in all clotting and coagulation assays. Additionally, no acute cytotoxicity was observed with RBCs with all four peptides.

Finally, we provide a simple strategy for targeted drug accumulation without the need for complex synthetic modifications, as activation of peptide self-assembly was shown to trap a model drug in the hydrogel network. Ultimately, co-injection of progelators with any number of therapeutics (e.g. small drugs, growth factors, cell therapies) could allow for targeted accumulation and localized

drug release from a stationary scaffold. This work provides a glimpse into the future of tissue engineering with simple chemistries that exhibit complex behavior.

4.1.1 Experimental Details

General Information: Amino acids used in Fmoc SPPS were purchased from AAPPTec, ChemPep and NovaBiochem. All other synthetic materials were obtained from Sigma-Aldrich and used without further purification unless otherwise noted.

KLD Control Peptide Synthesis: KLD control peptide was synthesized by standard Fmoc SPPS in an AAPPTec Focus XC peptide synthesizer on rink amide MBHA resin. HBTU (N,N,N′,N′-tetramethyl-O-(1H-benzotriazol-1-yl) uronium hexafluorophosphate) was used as the general coupling agent. Peptide cleavage and deprotection was performed in 95:2.5:2.5 (%v/v) trifluoroacetic acid (TFA), triisopropyl silane (TIPS), and H2O, respectively, for 2 hr. TFA was removed from the filtrate via rotary evaporation and the remaining residue was precipitated with cold anhydrous diethyl ether (3x) and sonication to yield a white solid product.

KLD Control Peptide Purification: KLD control peptide was prepared for purification in 5:20:75 acetic acid/water (0.1% TFA)/ acetonitrile (0.1% TFA) via initial dissolution in acetic acid with sonication, followed by addition of acetonitrile then water (final concentration 10 mg/mL). Peptide was purified on a Jupiter Proteo90A Phenomenex column (2050 x 25.0 mm) on an Armen Glider CPC preparatory phase HPLC to yield 95% purity. KLD control peptide was purified using an acidic mobile phase consisting of H2O with 0.1% TFA (Buffer A) and acetonitrile with 0.1% TFA (Buffer B). Gradient: 20-40% over 43 min at 214 nm. KLD control peptide was dialyzed into basic H2O (pH 8-9) prior to lyophilization.

Progelator Peptide Synthesis: Charge-conversion peptide progelators, mal-KLD, cit-KLD, and dma-KLD were synthesized in a one-pot step. To a solution of pure KLD peptide in DMF (40 mg/mL) was added maleic, citraconic, or dimetylmaleic anhydride (30 eq), and dimethylaminopyridine (DMAP) (30 eq). The reaction was stirred 48 hr to yield a black (mal-KLD) or brown (cit-KLD) solution

or white precipitate (dma-KLD). mal-KLD and cit-KLD were precipitated with anhydrous diethyl ether (2x) to yield brown and pale-yellow powders, respectively. dma-KLD reactions were decanted and washed with anhydrous diethyl ether (2x) to yield a white powder. We suspect that observed coloration with mal-KLD and cit-KLD is caused by intramolecular charge transfer complexes between the maleamic acid amide protons with carboxylic acids on the peptide, which increases the molar absorptivity and lowers the absorbance energy barrier.64 Increased steric hindrance with pendant methyl groups likely limits this interaction leading to decreased sample coloration.

Dry peptides were dissolved into basic H2O (pH 10) and dialyzed into H2O at pH 8 with 1kDa cut-off dialysis tubes for 24 hr prior to lyophilization. This procedure yields quantitatively pure peptide and requires no additional purification steps. Peptides were lyophilized for prolonged storage. All stock solutions of progelator peptides were freshly prepared by reconstitution of lyophilized powder into 1x DPBS (pH 7.4) and sterilized through a 0.2 μm PES filter.

Peptide Purity and Mass Spectrometric Characterization: General mass spectra were analyzed on Bruker AmaZon SL quadrupole ion trap mass analyzer configured with an electrospray ionization (ESI) source. Peptide purity was analyzed via LCMS on an Bruker AmaZon X, which couples an Agilent 1200 Series LC system with a quadrupole ion trap mass analyzer configured with an electrospray ionization (ESI) source. mal-KLD, cit-KLD, and dma-KLD progelator peptides were run on a Thermo ScientificTM HyPURITYTM C18 HPLC column (3μm particle size), using a slightly basic mobile phase consisting of 0.05% (v/v) NH4OH in H2O, pH 8 (Buffer A) and acetonitrile (Buffer B). Gradient: 0-30% over 10 min at 214 nm. Peptide masses and identities are provided in Figure 4.1.2.

Circular Dichroism (CD) of Peptides: Progelator peptides were incubated for 24 hr at pH 3.0 to deprotect lysine residues, and dialyzed into H2O at pH 7 to neutralize and remove excess salt, buffer, and maleic acids. Peptides were lyophilized and re-dissolved at 400 μM in 50 mM phosphate buffer (pH 7.4). Secondary structure of peptide progelators before and after acid treatment were measured on a JASCO 815 Circular Dichroism Spectropolarimeter using the following settings:

temperature=21 ˚C, pathlength=2 mm, scanning speed=50 nm/min, response time=2 s, bandwidth=1 nm, accumulations=3, and scan range=260-190 nm. Spectra are presented as an average of all accumulations.

Transmission electron microscopy (TEM): Formvar/Carbon-coated 400 mesh Cu grids (Ted Paella, Inc.) were glow discharged for 90 s and spotted with 5 µL peptide sample (100 µM) and set for 5 min. Grids were rinsed with distilled H2O (5 drops), stained with 1% (w/w) uranyl acetate (3 drops), and wicked dry with filter paper. TEM images were acquired on an FEI Tecnai G2 Sphera TEM or Joel ARM200CF Aberration-Corrected TEM at 200 kV. Acid-treated samples were prepared by incubated at pH 3.0 for 12 hr followed by neutralization.

Rheology of Bulk Peptide Solutions at Various Extents of Deprotection: KLD control hydrogel was suspended at 10 mM in 1xDPBS (pH 7.4). Peptide progelators were dissolved at 13.9 mM peptide in H2O at pH 8.0 and diluted with 5x stock solutions of glycine buffer (1M, pH 3.0), acetate buffer (1M, pH 5.5), or phosphate buffer (1M, pH 6.8 and 7.4) to initiate cleavage (peptide concentration 11.1 mM and buffer concentration 200 mM). Solutions were vortexed for 20 sec, then incubated at 37 °C for 1, 12, or 24 hr. Resulting gels were neutralized with concentrated NaOH, and diluted with 10x DPBS to a final concentration of 10 mM for rheological measurements.

All peptide samples were prepared at 10 mM peptide. Viscous and viscoelastic properties were assessed using a stress-controlled rheometer (Anton Paar MCR 302) equipped with a 25 mm diameter parallel plate geometry (PP25). Unless otherwise stated all measurements were taken at an angular frequency of 2.5 rad/s, strain of 0.5%, and temperature of 37 °C. Measurements were performed with a gap height of 1000 µm. To prevent water evaporation, mineral oil was wrapped around the edge of the geometry at the air-sample interface. For viscoelastic measurements the apparatus was used in oscillatory mode. To ensure that measurements were made within the linear viscoelastic regime (LVR), strain sweeps were performed between 0.05-50 % strain at 2.5 rad/s. The dynamic moduli of the hydrogels were measured as a function of angular frequency in the range of 0.25–100 rad/s at a strain of 0.5% (n=3 accumulations). Continuous step-strain oscillations were used

to monitor hydrogel healing through disruption (3 min, 100% strain) and recovery (15 min, 0.5% strain) cycles (n=3). Temperature sweeps were measured by increasing the apparatus temperatures from 21-40 °C at a ramp rate of 0.5 °C/min. For viscosity measurements the apparatus was used in steady state flow mode. The viscosity of samples was measured as a function of shear rate in the range 0.1–10 s–1 (5% tolerance).

In Vitro Catheter Injections of Progelators: In vitro injection of peptide progelators through the 27G inner nitinol tubing of a MyoStar catheter was performed, as previously described.65Peptide solutions (0.6 mL) were prepared at 10 mM in 1x DPBS (pH 7.4) and loaded into a 1 mL Luer Lock syringe attached to a syringe pump set to a flow rate of 0.6 mL/min. Catheters were inspected for potential clogging during and after injection.

Blood Dilutions for Hemocompatibility: Peptide in blood dilutions were performed at volume ratios of 1:10000, 1:5000, 1:1000, 1:500, 1:100, and 1:10. These doses indicate peptide dilution in blood given a 10 mM injected dose. Assuming an average cardiac output of 5 L/min at 5 L of blood total, the maximal dosing from a high volume transendocardial catheter injection (6 mL) or intracoronary infusion (10 m) after 1 min of circulation would be 1:830 and 1:500, respectively. This generous estimate assumes that all injected material leaks into the bloodstream and none reaches its intended target tissue. Furthermore, injection via catheter is generally performed over a period of many minutes, which enables further dilution in the blood during delivery.

Activated Clotting Time (ACT) Assay with Whole Human Blood: Activated clotting times (ACT) with whole human blood. A Hemochron 801 instrument calibrated with an electronic system verification (ESV) device was used to measure activated clotting time (ACT) of whole human blood. Activated clotting times (ACT) were determined using recalcified citrated whole human blood to minimize variability in starting time points for clotting in all assays.66 To each Hemochron P214 tube with glass beads was added 4 µL CaCl2 (1.1 M) and 36 µL peptide stock or additive (12.2x final blood concentration). Samples were mixed thoroughly for 30 s to soak the glass beads and incubated 30 s at 37 °C. Citrated whole human blood (400 µL) was then added (t=0 s), mixed by hand for 10 s, and

added to the instrument. Time points at which the magnet was displaced by clot formation were recorded by the instrument. Type I soluble collagen (0.095 mg/mL) was used as a positive control to decrease clotting time. Vehicle (1x DPBS) served as a standard for blood without additive. Samples without calcium, serving as the negative control, exceeded instrument maximum time range (>1500 sec). Each experiment was performed n=5 times with averages and standard error of the mean (SEM) plotted.

Hemolysis of Red Blood Cells (RBCs): Acute toxicity of peptide progelators was measured with a RBC hemolysis assay specific to biomacromolecular drug analysis.67 RBCs were isolated by centrifugation of 40 mL citrated whole human blood at 500 x rcf for 10 min, followed by gentle aspiration of plasma and refilling with 150 mM NaCl solution. After gentle mixing through tube inversion, these steps were repeated 3 x (using 1x DPBS instead of NaCl solution for the last two repeats). To a 49 mL of 1x DPBS (pH 7.4) was added 1 mL of isolated RBCs for a 1:50 dilution. RBCs were lightly agitated prior to use to prevent settling. Briefly, 190 µL of dilute RBCs and 10 µL of peptide stock or additive (20x final concentration) were mixed and added to a clear, flat-bottomed 96-well plate, covered, and incubated at 37 °C for 1 hr. 1% Triton X-100 was used to lyse RBCs as a positive control and untreated vehicle (1x DPBS) was used as a negative control. For each sample, n=6 repeats were prepared. Following incubation, plates were centrifuged at 500 rcf to pellet intact RBCs using a centrifuge equipped with a microplate rotor. Supernatant (100 µL) was transferred to a new 96-well plate, taking care not to disturb the pellet. Absorbance of the supernatant was measured at via plate reader at 540 nm (height 7.5 mm, 100 flashes) to detect released hemoglobin from RBC lysis. To calculate % hemolysis, absorbances were corrected for background absorbance from untreated vehicle and then normalized to 1% Triton X-100 treated RBCs to represent 100% hemolysis. %Hemolysis was calculated according to the following equation:

$$\%Hemolysis = \frac{(Abs_{experiemental}) - (Abs_{negative\ control})}{(Abs_{positive\ control}) - (Abs_{negative}\ control)}\ x\ 100$$

, where Absexperiemental is the average well absorbance pertaining to RBCs pertaining to the additive sample being analyzed, Absnegative control is the average well absorbance for RBCs

incubated with vehicle (1x DPBS), and Abspositive control is the average well absorbance for RBCs containing 1% Triton X-100. Averages (n=6) and standard error of the mean (SEM) are plotted.

Plasma Recalcification Profiles: The intrinsic coagulation pathway was assessed using a plasma recalcification assay. Platelet poor plasma (PPP) was isolated from citrated whole human blood through centrifugation at 2000 rcf for 10 min and collection of the upper 2/3 layer of PPP. The collected plasma was spun again at 2000 rcf for 10 min and the upper 3/4 layer. Briefly, 100 µL of PPP, 50 µL of peptide stock or additive (4x final concentration), and 50 µL of CaCl2 (50 mM) were added to a clear, flat-bottomed 96-well plate, covered, and loaded into a plate reader incubated at 37 °C for kinetics measurements. Collagen (0.095 mg/mL) which interacts with platelets to decrease coagulation time, was used to confirm proper preparation of PPP to study platelet-independent effects of our peptide. Glass coverslips were used as positive controls for altered coagulation kinetics. Samples without calcium, where no coagulation was observed, served as negative controls. Untreated vehicle (1x DPBS) samples were used as a standard to compare peptide dosing impacts. For each sample, n=6 repeats were conducted. Coagulation profiles were obtained by measuring well absorbance at 540 nm (height 7.0 mm, 100 flashes) at 30 sec intervals for 60 min. Onset to clotting was detected as a sharp increase in sample turbidity. Measurements were all baseline corrected to account for variable turbidity from peptides at different concentrations. The onset of coagulation is indicated by a steep rise in the absorbance vs time curve. A plateau in absorbance was reached within a few minutes and maintained over time, indicating a fully formed, stable clot.

Table 4.1.8. Plasma recalcification clotting extent. Corresponds to **Figure 4.1.20b**. Average times reported ± standard error of mean (n=6 per group). Analysis by regular two-way ANOVA with multiple comparisons of the mean in each group with that of the vehicle standard. No correction for multiple comparisons. ns ($p > 0.05$), * ($p \leq 0.05$), ** ($p \leq 0.01$), *** ($p \leq 0.001$), and **** ($p \leq 0.0001$). Values are mean ± SEM.

	peptide in blood dilutions						standard	pos control	pos control
	1:10	1:100	1:500	1:1000	1:5000	1:10000	vehicle	collagen	coverslip
mal-KLD									
Average (Δ Abs)	0.35	0.48	0.52	0.54	0.56	0.55	0.55	0.46	0.44
SEM	(± 0.06)	(± 0.08)	(± 0.08)	(± 0.09)	(±0.09)	(± 0.09)	(± 0.09)	(± 0.07)	(± 0.07)
P Value	0.0760	0.5290	0.8000	0.8898	0.9065	0.9901		0.3977	0.5059
Summary	ns	ns	ns	ns	ns	ns		ns	ns
cit-KLD									
Average (Δ Abs)	0.27	0.40	0.46	0.47	0.50	0.51	0.53		
SEM	(± 0.04)	(± 0.07)	(± 0.07)	(± 0.08)	(± 0.08)	(± 0.08)	(± 0.09)		
P Value	0.0185	0.2538	0.5363	0.5867	0.7574	0.8453			
Summary	*	ns	ns	ns	ns	ns		ns	ns
dma-KLD									
Average (Δ Abs)	0.44	0.54	0.54	0.54	0.55	0.55	0.55		
SEM	(± 0.07)	(± 0.09)	(± 0.09)	(± 0.09)	(± 0.09)	(± 0.09)	(± 0.09)		
P Value	0.3149	0.9535	0.9177	0.9542	0.9669	0.9789			
Summary	ns	ns	ns	ns	ns	ns		ns	ns
KLD control									
Average (Δ Abs)	0.49	0.57	0.56	0.56	0.56	0.55	0.55		
SEM	(± 0.08)	(± 0.09)	(± 0.09)	(± 0.09)	(± 0.09)	(± 0.09)	(± 0.09)		
P Value	0.5959	0.8260	0.9304	0.8995	0.9030	0.9782			
Summary	ns	ns	ns	ns	ns	ns		ns	ns

Table 4.1.9. Plasma recalcification clotting rate. Corresponds to **Figure 4.1.20b**. Average times reported ± standard error of mean (n=6 per group). Analysis by regular two-way ANOVA with multiple comparisons of the mean in each group with that of the vehicle standard. No correction for multiple comparisons. ns ($p > 0.05$), * ($p \leq 0.05$), ** ($p \leq 0.01$), *** ($p \leq 0.001$), and **** ($p \leq 0.0001$). Values are mean ± SEM.

	peptide in blood dilutions						standard	pos control	pos control
	1:10	1:100	1:500	1:1000	1:5000	1:10000	vehicle	collagen	coverslip
mal-KLD									
Average (a.u./min)	0.4	0.3	0.2	0.2	0.2	0.2	0.3	0.5	0.4
SEM	(± 0.1)	(± 0.1)	(± 0.0)	(± 0.0)	(±0.0)	(± 0.0)	(± 0.1)	(± 0.1)	(± 0.1)
P Value	0.3827	0.8573	0.4472	0.4980	0.2673	0.3569		0.9707	0.7120
Summary	ns	ns	ns	ns	ns	ns		ns	ns
cit-KLD									
Average (a.u./min)	0.5	1.1	1.0	1.0	1.0	1.0	0.5		
SEM	(± 0.1)	(± 0.2)	(± 0.2)	(± 0.2)	(± 0.2)	(± 0.2)	(± 0.1)		
P Value	0.9629	< 0.0001	0.0001	0.0002	0.0001	0.0010			
Summary	ns	****	***	***	***	**		ns	ns
dma-KLD									
Average (a.u./min)	0.6	0.5	0.4	0.4	0.4	0.4	0.4		
SEM	(± 0.1)	(± 0.1)	(± 0.1)	(± 0.1)	(± 0.1)	(± 0.1)	(± 0.1)		
P Value	0.1268	0.2963	0.8497	0.9187	0.9707	0.9773			
Summary	ns	ns	ns	ns	ns	ns		ns	ns
KLD control									
Average (a.u./min)	0.3	0.3	0.3	0.4	0.3	0.4	0.4		
SEM	(± 0.0)	(± 0.1)	(± 0.1)	(± 0.1)	(± 0.1)	(± 0.1)	(± 0.1)		
P Value	0.4468	0.6361	0.8178	0.9790	0.7979	0.9579			
Summary	ns	ns	ns	ns	ns	ns		ns	ns

Table 4.1.10. Plasma recalcification clotting time. Corresponds to **Figure 4.1.20b**. Average times reported ± standard error of mean (n=6 per group). Analysis by regular two-way ANOVA with multiple comparisons of the mean in each group with that of the vehicle standard. No correction for multiple comparisons. ns ($p > 0.05$), * ($p \leq 0.05$), ** ($p \leq 0.01$), *** ($p \leq 0.001$), and **** ($p \leq 0.0001$). Values are mean ± SEM.

	peptide in blood dilutions						standard	pos control	pos control
	1:10	1:100	1:500	1:1000	1:5000	1:10000	vehicle	collagen	coverslip
mal-KLD									
Average Time (min)	9	9	10	10	12	12	15	18	6
SEM	(± 1)	(± 1)	(± 2)	(± 2)	(±2)	(± 2)	(± 2)	(± 3)	(± 1)
P Value	0.0419	0.0583	0.1043	0.0913	0.2785	0.3688		0.9108	0.0003
Summary	ns	ns	ns	ns	ns	ns		ns	ns
cit-KLD									
Average Time (min)	5	5	7	8	10	11	18		
SEM	(± 1)	(± 1)	(± 1)	(± 1)	(± 2)	(± 2)	(± 3)		
P Value	0.0001	< 0.0001	0.0007	0.0018	0.0135	0.0291			
Summary	ns	****	***	***	***	**		ns	ns
dma-KLD									
Average Time (min)	15	16	17	16	16	17	16		
SEM	(± 2)	(± 3)	(± 3)	(± 3)	(± 3)	(± 3)	(± 3)		
P Value	0.7080	0.8753	0.9464	0.9286	0.9693	0.9184			
Summary	ns	ns	ns	ns	ns	ns		ns	ns
KLD control									
Average Time (min)	16	17	17	17	17	17	17		
SEM	(± 3)	(± 3)	(± 3)	(± 3)	(± 3)	(± 3)	(± 3)		
P Value	0.7954	0.9133	0.8426	0.8905	0.8301	0.9006			
Summary	ns	ns	ns	ns	ns	ns		ns	ns

Stimuli-Induced Drug Encapsulation with Thioflavin T (ThT): ThT stock solutions were sterile filtered through a 0.22 μm PES membrane prior to use. Peptide stock was predissolved in water at 1 mM. ThT stocks were prepared in either glycine buffer (200 mM, pH 3.0), acetate buffer (200 mM, pH 5.5), or phosphate buffer (200 mM, pH 6.8 and 7.4). Peptide and ThT were added to black 96-well clear-bottom plates (n=4 sample repeats) for Plate Reader analyses. Spectra collected at 37 ˚C with step size of 0.2 nm, 100 flashes, height of 3 mm from bottom, with n=3 accumulation

Statistical Analysis: All statistical results are expressed as mean ± standard error (SEM) and all analyses were conducted in Prism. RM one-way ANOVA with multiple comparisons of the mean in each group with that of the vehicle standard was used for analysis of red blood cell (RBC) hemolysis and activated clotting times (ACT) in whole human blood. No correction for multiple comparisons was performed. Statistics for plasma recalcification profiles were calculated using a “Sigmoidal, 4PL, X is log(concentration)” interpolation function with no handling of outliers and reported with 95% confidence intervals (CI). The Top, HillSlope, and LogIC50 were used as values for coagulation maximal extent, rate, and onset time. Regular two-way ANOVA with multiple comparisons of the mean in each group with that of the standard was used. No correction for multiple comparisons was performed. Statistical significance was defined as follows: ns ($p > 0.05$), * ($p \leq 0.05$), ** ($p \leq 0.01$), *** ($p \leq 0.001$), and **** ($p \leq 0.0001$).

4.2 Perspectives and Future Outlooks

4.1.4 pH Responsiveness by NMR

Synthesized progelators and KLD control peptide were characterized for pH-responsive deprotection. NMR was used to monitor peptide deprotection kinetics in real time at pH 7.4, 6.8, 5.5, and 3.0 for all charge-conversion progelators. Deprotected KLD control peptide possesses Hydrogen bonding between deprotected peptides caused proton peak broadening and signal loss, which limited analysis of the deprotected peptide. In contrast, deprotected maleic acid products participate in minimal hydrogen bonding once expunged from the peptide into the surrounding solvent. Thus, we are monitoring kinetics as a function of increasing signal from maleic acid olefin and methyl protons. Progelators are incubated in deuterated buffers at pH 7.4, 6.8, 5.5, and 3.0 for up to 48 hr.

4.1.5 Cell Viability of Progelators and Deprotection Products

For biomedical considerations, any released product should be nontoxic and nonimmunogenic. Once the peptide has reached its intended acidic tissue target, deprotected KLD-12 peptide can self-assemble as a local tissue scaffold. This peptide is known to be biocompatible, but it is unclear what cytotoxicity our new chemistries may present. We are performing cell viability assays by incubating progelators (mal-KLD, cit-KLD, and dma-KLD) and deprotected caps (maleic, citraconic, and dimethylmaleic acid) with L929 epithelial cells to understand their cytotoxicity.

4.3 Acknowledgements

Chapter 4 is adapted, in part, from material currently being prepared for submission for publication. Carlini, Andrea; Choi, Wonmin; McCallum, Naneki; Gianneschi, Nathan. The dissertation author is the first author of this pending manuscript.

4.4 References

1 Palacián, E., González, P. J., Piñeiro, M. & Hernández, F. Dicarboxylic acid anhydrides as dissociating agents of protein-containing structures. *Mol. Cell. Biochem.* **97**, 101-111, doi:10.1007/bf00221051 (1990).

2 Goto, Y., Takahashi, N. & Fink, A. L. Mechanism of acid-induced folding of proteins. *Biochemistry* **29**, 3480-3488, doi:10.1021/bi00466a009 (1990).

3 Butler, P. J. G., Harris, J. I., Hartley, B. S. & Leberman, R. The use of maleic anhydride for the reversible blocking of amino groups on polypeptide chains. *Biochem. J.* **112**, 679-689 (1969).

4 Liu, X., Zhang, J. & Lynn, D. M. Polyelectrolyte multilayers fabricated from 'charge-shifting' anionic polymers: a new approach to controlled film disruption and the release of cationic agents from surfaces. *Soft Matter* **4**, 1688-1695, doi:10.1039/B804953J (2008).

5 Lee, E. S., Na, K. & Bae, Y. H. Super pH-Sensitive Multifunctional Polymeric Micelle. *Nano Lett.* **5**, 325-329, doi:10.1021/nl0479987 (2005).

6 Lee, Y., Fukushima, S., Bae, Y., Hiki, S., Ishii, T. & Kataoka, K. A Protein Nanocarrier from Charge-Conversion Polymer in Response to Endosomal pH. *J. Am. Chem. Soc.* **129**, 5362-5363, doi:10.1021/ja071090b (2007).

7 Takemoto, H., Miyata, K., Hattori, S., Ishii, T., Suma, T., Uchida, S., Nishiyama, N. & Kataoka, K. Acidic pH-Responsive siRNA Conjugate for Reversible Carrier Stability and Accelerated Endosomal Escape with Reduced IFNα-Associated Immune Response. *Angew. Chem. Int. Ed.* **52**, 6218-6221, doi:doi:10.1002/anie.201300178 (2013).

8 Deng, H., Liu, J., Zhao, X., Zhang, Y., Liu, J., Xu, S., Deng, L., Dong, A. & Zhang, J. PEG-b-PCL Copolymer Micelles with the Ability of pH-Controlled Negative-to-Positive Charge Reversal for Intracellular Delivery of Doxorubicin. *Biomacromolecules* **15**, 4281-4292, doi:10.1021/bm501290t (2014).

9 Luo, G.-F., Chen, W.-H., Liu, Y., Lei, Q., Zhuo, R.-X. & Zhang, X.-Z. Multifunctional Enveloped Mesoporous Silica Nanoparticles for Subcellular Co-delivery of Drug and Therapeutic Peptide. *Sci. Rep.* **4**, 6064, doi:10.1038/srep06064 (2014).

10 Huo, Q., Zhu, J., Niu, Y., Shi, H., Gong, Y., Li, Y., Song, H. & Liu, Y. pH-triggered surface charge-switchable polymer micelles for the co-delivery of paclitaxel/disulfiram and overcoming multidrug resistance in cancer. *International Journal of Nanomedicine* **12**, 8631-8647, doi:10.2147/IJN.S144452 (2017).

11 Zhou, Q., Hou, Y., Zhang, L., Wang, J., Qiao, Y., Guo, S., Fan, L., Yang, T., Zhu, L. & Wu, H. Dual-pH Sensitive Charge-reversal Nanocomplex for Tumor-targeted Drug Delivery with Enhanced Anticancer Activity. *Theranostics* **7**, 1806-1819, doi:10.7150/thno.18607 (2017).

12 Su, S., Du, F.-S. & Li, Z.-C. Synthesis and pH-dependent hydrolysis profiles of mono- and dialkyl substituted maleamic acids. *Organic & Biomolecular Chemistry* **15**, 8384-8392, doi:10.1039/C7OB02188G (2017).

13 Kang, S., Kim, Y., Song, Y., Choi, J. U., Park, E., Choi, W., Park, J. & Lee, Y. Comparison of pH-sensitive degradability of maleic acid amide derivatives. *Bioorg. Med. Chem. Lett.* **24**, 2364-2367, doi:https://doi.org/10.1016/j.bmcl.2014.03.057 (2014).

14 Rizwan, M., Yahya, R., Hassan, A., Yar, M., Azzahari, A., Selvanathan, V., Sonsudin, F. & Abouloula, C. pH Sensitive Hydrogels in Drug Delivery: Brief History, Properties, Swelling, and Release Mechanism, Material Selection and Applications. *Polymers* **9**, 137 (2017).

15 Chassenieux, C. & Tsitsilianis, C. Recent trends in pH/thermo-responsive self-assembling hydrogels: from polyions to peptide-based polymeric gelators. *Soft Matter* **12**, 1344-1359, doi:10.1039/C5SM02710A (2016).

16 Wang, L., Shi, X., Zhang, J., Zhu, Y. & Wang, J. Self-assembled pH-responsive supramolecular hydrogel for hydrophobic drug delivery. *RSC Advances* **8**, 31581-31587, doi:10.1039/C8RA06064A (2018).

17 Kellum, J. A., Song, M. & Li, J. Science review: Extracellular acidosis and the immune response: clinical and physiologic implications. *Critical Care* **8**, 331-336, doi:10.1186/cc2900 (2004).

18 Inserte, J., Barba, I., Hernando, V. & Garcia-Dorado, D. Delayed recovery of intracellular acidosis during reperfusion prevents calpain activation and determines protection in postconditioned myocardium. *Cardiovascular Research* **81**, 116-122, doi:10.1093/cvr/cvn260 (2009).

19 Kitakaze, M., Takashima, S., Funaya, H., Minamino, T., Node, K., Shinozaki, Y., Mori, H. & Hori, M. Temporary acidosis during reperfusion limits myocardial infarct size in dogs. *American Journal of Physiology-Heart and Circulatory Physiology* **272**, H2071-H2078, doi:10.1152/ajpheart.1997.272.5.H2071 (1997).

20 Goldie, I. & Nachemson, A. Synovial pH in Rheumatoid Knee-Joints I. The Effect of Synovectomy. *Acta Orthop. Scand.* **40**, 634-641, doi:10.3109/17453676908989529 (1969).

21 Treuhaft, P. S. & McCarty, D. J. Synovial fluid pH, lactate, oxygen and carbon dioxide partial pressure in various joint diseases. *Arthritis Rheum.* **14**, 475-484, doi:doi:10.1002/art.1780140407 (1971).

22 Stevens, C. R., Williams, R. B., Farrell, A. J. & Blake, D. R. Hypoxia and inflammatory synovitis: observations and speculation. *Ann. Rheum. Dis.* **50**, 124-132 (1991).

23 Green, J. & Maor, G. Effect of metabolic acidosis on the growth hormone/IGF-I endocrine axis in skeletal growth centers. *Kidney Int.* **57**, 2258-2267, doi:https://doi.org/10.1046/j.1523-1755.2000.00086.x (2000).

24 Dissemond, J., Witthoff, M., Brauns, T. C., Haberer, D. & Goos, M. pH-Wert des Milieus chronischer Wunden. *Der Hautarzt* **54**, 959-965, doi:10.1007/s00105-003-0554-x (2003).

25 Rajamäki, K., Nordström, T., Nurmi, K., Åkerman, K. E. O., Kovanen, P. T., Öörni, K. & Eklund, K. K. Extracellular Acidosis Is a Novel Danger Signal Alerting Innate Immunity via the NLRP3 Inflammasome. *The Journal of Biological Chemistry* **288**, 13410-13419, doi:10.1074/jbc.M112.426254 (2013).

26 Seif-Naraghi, S. B., Singelyn, J. M., Salvatore, M. A., Osborn, K. G., Wang, J. J., Sampat, U., Kwan, O. L., Strachan, G. M., Wong, J., Schup-Magoffin, P. J., Braden, R. L., Bartels, K., DeQuach, J. A., Preul, M., Kinsey, A. M., DeMaria, A. N., Dib, N. & Christman, K. L. Safety and efficacy of an

injectable extracellular matrix hydrogel for treating myocardial infarction. *Sci. Transl. Med.* **5**, 10.1126/scitranslmed.3005503, doi:10.1126/scitranslmed.3005503 (2013).

27 Peña, B., Laughter, M., Jett, S., Rowland, T. J., Taylor, M. R. G., Mestroni, L. & Park, D. Injectable Hydrogels for Cardiac Tissue Engineering. *Macromol. Biosci.* **18**, 1800079, doi:doi:10.1002/mabi.201800079 (2018).

28 Spiller, K. L., Maher, S. A. & Lowman, A. M. Hydrogels for the Repair of Articular Cartilage Defects. *Tissue Engineering. Part B, Reviews* **17**, 281-299, doi:10.1089/ten.teb.2011.0077 (2011).

29 Rey-Rico, A., Madry, H. & Cucchiarini, M. Hydrogel-Based Controlled Delivery Systems for Articular Cartilage Repair. *BioMed Research International* **2016**, 12, doi:10.1155/2016/1215263 (2016).

30 Li, Z., Yuan, B., Dong, X., Duan, L., Tian, H., He, C. & Chen, X. Injectable polysaccharide hybrid hydrogels as scaffolds for burn wound healing. *RSC Advances* **5**, 94248-94256, doi:10.1039/C5RA16912G (2015).

31 Griffin, D. R., Weaver, W. M., Scumpia, P., Di Carlo, D. & Segura, T. Accelerated wound healing by injectable microporous gel scaffolds assembled from annealed building blocks. *Nature materials* **14**, 737-744, doi:10.1038/nmat4294 (2015).

32 Li, Z., Zhou, F., Li, Z., Lin, S., Chen, L., Liu, L. & Chen, Y. Hydrogel Cross-Linked with Dynamic Covalent Bonding and Micellization for Promoting Burn Wound Healing. *ACS Applied Materials & Interfaces* **10**, 25194-25202, doi:10.1021/acsami.8b08165 (2018).

33 Bell, C. J., Carrick, L. M., Katta, J., Jin, Z., Ingham, E., Aggeli, A., Boden, N., Waigh, T. A. & Fisher, J. Self-assembling peptides as injectable lubricants for osteoarthritis. *Journal of Biomedical Materials Research Part A* **78A**, 236-246, doi:doi:10.1002/jbm.a.30672 (2006).

34 Joshi, N., Yan, J., Levy, S., Bhagchandani, S., Slaughter, K. V., Sherman, N. E., Amirault, J., Wang, Y., Riegel, L., He, X., Rui, T. S., Valic, M., Vemula, P. K., Miranda, O. R., Levy, O., Gravallese, E. M., Aliprantis, A. O., Ermann, J. & Karp, J. M. Towards an arthritis flare-responsive drug delivery system. *Nature Communications* **9**, 1275, doi:10.1038/s41467-018-03691-1 (2018).

35 El-Sherbiny, I. M. & Yacoub, M. H. Hydrogel scaffolds for tissue engineering: Progress and challenges. *Global Cardiology Science & Practice* **2013**, 316-342, doi:10.5339/gcsp.2013.38 (2013).

36 Zhu, J. & Marchant, R. E. Design properties of hydrogel tissue-engineering scaffolds. *Expert review of medical devices* **8**, 607-626, doi:10.1586/erd.11.27 (2011).

37 Chuang, E.-Y., Chiang, C.-W., Wong, P.-C. & Chen, C.-H. Hydrogels for the Application of Articular Cartilage Tissue Engineering: A Review of Hydrogels. *Advances in Materials Science and Engineering* **2018**, 13, doi:10.1155/2018/4368910 (2018).

38 Li, J. & Mooney, D. J. Designing hydrogels for controlled drug delivery. *Nature Reviews Materials* **1**, 16071, doi:10.1038/natrevmats.2016.71

https://www.nature.com/articles/natrevmats201671#supplementary-information (2016).

39 Burdick, J. A. & Murphy, W. L. Moving from static to dynamic complexity in hydrogel design. *Nature Communications* **3**, 1269, doi:10.1038/ncomms2271 (2012).

40 Portnov, T., Shulimzon Tiberiu, R. & Zilberman, M. in *Rev. Chem. Eng.* Vol. 33 91 (2017).

41 Nguyen, M. M., Carlini, A. S., Chien, M.-P., Sonnenberg, S., Luo, C., Braden, R. L., Osborn, K. G., Li, Y., Gianneschi, N. C. & Christman, K. L. Enzyme-Responsive Nanoparticles for Targeted Accumulation and Prolonged Retention in Heart Tissue after Myocardial Infarction. *Advanced Materials* **27**, 5547-5552, doi:doi:10.1002/adma.201502003 (2015).

42 Wojtecki, R. J., Meador, M. A. & Rowan, S. J. Using the dynamic bond to access macroscopically responsive structurally dynamic polymers. *Nature Materials* **10**, 14, doi:10.1038/nmat2891 (2010).

43 Webber, M. J., Appel, E. A., Meijer, E. W. & Langer, R. Supramolecular biomaterials. *Nature Materials* **15**, 13, doi:10.1038/nmat4474 (2015).

44 Selegård, R., Aronsson, C., Brommesson, C., Dånmark, S. & Aili, D. Folding driven self-assembly of a stimuli-responsive peptide-hyaluronan hybrid hydrogel. *Scientific Reports* **7**, 7013, doi:10.1038/s41598-017-06457-9 (2017).

45 Guilbaud, J.-B., Vey, E., Boothroyd, S., Smith, A. M., Ulijn, R. V., Saiani, A. & Miller, A. F. Enzymatic Catalyzed Synthesis and Triggered Gelation of Ionic Peptides. *Langmuir* **26**, 11297-11303, doi:10.1021/la100623y (2010).

46 Sun, J., Zheng, Q., Wu, Y., Liu, Y., Guo, X. & Wu, W. Biocompatibility of KLD-12 peptide hydrogel as a scaffold in tissue engineering of intervertebral discs in rabbits. *Journal of Huazhong University of Science and Technology* **30**, 173-177 (2010).

47 Tripathi, J. K., Pal, S., Awasthi, B., Kumar, A., Tandon, A., Mitra, K., Chattopadhyay, N. & Ghosh, J. K. Variants of self-assembling peptide, KLD-12 that show both rapid fracture healing and antimicrobial properties. *Biomaterials* **56**, 92-103, doi:https://doi.org/10.1016/j.biomaterials.2015.03.046 (2015).

48 Bian, Z. & Sun, J. Development of a KLD-12 polypeptide/TGF-β1-tissue scaffold promoting the differentiation of mesenchymal stem cell into nucleus pulposus-like cells for treatment of intervertebral disc degeneration. *International Journal of Clinical and Experimental Pathology* **8**, 1093-1103 (2015).

49 Sun, J. & Zheng, Q. Experimental study on self-assembly of KLD-12 peptide hydrogel and 3-D culture of MSC encapsulated within hydrogel in vitro. *Journal of Huazhong University of Science and Technology* **29**, 512-516 (2009).

50 Wan, S., Borland, S., Richardson, S. M., Merry, C. L. R., Saiani, A. & Gough, J. E. Self-assembling peptide hydrogel for intervertebral disc tissue engineering. *Acta Biomater.* **46**, 29-40, doi:https://doi.org/10.1016/j.actbio.2016.09.033 (2016).

51 Raghavendra, G. M., Varaprasad, K. & Jayaramudu, T. in *Nanotechnology Applications for Tissue Engineering* (eds Sabu Thomas, Yves Grohens, & Neethu Ninan) 21-44 (William Andrew Publishing, 2015).

52 Fröhlich, E. The role of surface charge in cellular uptake and cytotoxicity of medical nanoparticles. *International Journal of Nanomedicine* **7**, 5577-5591, doi:10.2147/IJN.S36111 (2012).

53 Jiang, Z., Vasil, A. I., Hale, J. D., Hancock, R. E. W., Vasil, M. L. & Hodges, R. S. Effects of Net Charge and the Number of Positively Charged Residues on the Biological Activity of Amphipathic α-Helical Cationic Antimicrobial Peptides. *Biopolymers* **90**, 369-383, doi:10.1002/bip.20911 (2008).

54 Grover, G. N., Braden, R. L. & Christman, K. L. Oxime Cross-Linked Injectable Hydrogels for Catheter Delivery. *Advanced materials (Deerfield Beach, Fla.)* **25**, 2937-2942, doi:10.1002/adma.201205234 (2013).

55 Yan, C., Altunbas, A., Yucel, T., Nagarkar, R. P., Schneider, J. P. & Pochan, D. J. Injectable solid hydrogel: mechanism of shear-thinning and immediate recovery of injectable β-hairpin peptide hydrogels. *Soft matter* **6**, 5143-5156, doi:10.1039/C0SM00642D (2010).

56 Hernandez, M. J. & Christman, K. L. Designing Acellular Injectable Biomaterial Therapeutics for Treating Myocardial Infarction and Peripheral Artery Disease. *JACC: Basic to Translational Science* **2**, 212-226, doi:https://doi.org/10.1016/j.jacbts.2016.11.008 (2017).

57 Weber, M., Steinle, H., Golombek, S., Hann, L., Schlensak, C., Wendel, H. P. & Avci-Adali, M. Blood-Contacting Biomaterials: In Vitro Evaluation of the Hemocompatibility. *Frontiers in Bioengineering and Biotechnology* **6**, 99, doi:10.3389/fbioe.2018.00099 (2018).

58 Autian, J. in *Kronenthal R.L., Oser Z., Martin E. (eds) Polymers in Medicine and Surgery* Vol. 8 *Polymer Science and Technology* 181-203 (Springer).

59 Horton, S. & Augustin, S. in *Monagle P. (eds) Haemostasis* Vol. 992 *Methods in Molecular Biology* 155-167 (Humana Press, 2013).

60 Xue, C., Lin, T. Y., Chang, D. & Guo, Z. Thioflavin T as an amyloid dye: fibril quantification, optimal concentration and effect on aggregation. *Royal Society Open Science* **4**, 160696, doi:10.1098/rsos.160696 (2017).

61 Hackl, E. V., Darkwah, J., Smith, G. & Ermolina, I. Effect of acidic and basic pH on Thioflavin T absorbance and fluorescence. *Eur. Biophys. J.* **44**, 249-261, doi:10.1007/s00249-015-1019-8 (2015).

62 Groenning, M. Binding mode of Thioflavin T and other molecular probes in the context of amyloid fibrils—current status. *J. Chem. Biol.* **3**, 1-18, doi:10.1007/s12154-009-0027-5 (2010).

63 Chen, Y., Hua, Y., Zhang, W., Tang, C., Wang, Y., Zhang, Y. & Qiu, F. Amyloid-like staining property of RADA16-I nanofibers and its potential application in detecting and imaging the nanomaterial. *International Journal of Nanomedicine* **13**, 2477-2489, doi:10.2147/IJN.S159785 (2018).

64 Karaca, E., Kaplan Can, H., Bozkaya, U. & Özçiçek Pekmez, N. Charge-Transfer Complex of p-Aminodiphenylamine with Maleic Anhydride: Spectroscopic, Electrochemical, and Physical Properties. *Chemphyschem* **17**, 2056-2065, doi:doi:10.1002/cphc.201600161 (2016).

65 Grover, G. N., Braden, R. L. & Christman, K. L. Oxime Cross-Linked Injectable Hydrogels for Catheter Delivery. *Adv. Mater.* **25**, 2937-2942, doi:doi:10.1002/adma.201205234 (2013).

66 Girardi, L., Sudi, K. & Muntean, W. Effect of Heparin, Platelets, Activated Platelets, Platelet Fragments, and Hematocrit on Activated Clotting Time. *Artificial Organs* **24**, 507-513, doi:doi:10.1046/j.1525-1594.2000.06552.x (2000).

67 Evans, B. C., Nelson, C. E., Yu, S. S., Beavers, K. R., Kim, A. J., Li, H., Nelson, H. M., Giorgio, T. D. & Duvall, C. L. Ex Vivo Red Blood Cell Hemolysis Assay for the Evaluation of pH-responsive Endosomolytic Agents for Cytosolic Delivery of Biomacromolecular Drugs. *Journal of Visualized Experiments : JoVE*, 50166, doi:10.3791/50166 (2013).

Chapter 5

Biomimetic Polymer Hydrogel

5.1. Architectural Influence on Biosynthetic Polymer Analogues to a Peptide Hydrogel

5.1.1 Introduction

Hydrogels assembled through physical cross-linking of soluble structures are an intriguing class of materials that have been applied as tissue engineering scaffolds and drug delivery vehicles, and in biotechnology as stabilizing scaffolds for labile biomolecules (e.g. growth factors and nucleic acids) and adhesive surfaces.[1,2] For feasible application as a soft tissue scaffold, the bulk mechanical properties of a biomimetic polymer hydrogel must be complementary to that of native tissue and compatible with current delivery strategies. For instance, hydrogel rigidity and elasticity must be appropriately tuned to the target tissue.[3] Furthermore, minimally invasive hydrogel delivery can lower the barrier to clinical translation when formulated for injection. However, injectable hydrogels which possess shear-thinning capacity as well as the ability to reassemble after cessation of shearing,[4,5] can be technically challenging to generate. Either sufficient mechanical strength or rapid rehealing

kinetics are required to resist structural disassembly and elimination from target tissue within a biological environment.

Self-assembling peptides (SAPs) represent a major class of soft hydrogels that have been successfully used for repair of inflamed heart tissue, cartilage wear and tear, nerve damage, and acute brain injury.[6-8] This is strongly influenced by their unique morphological properties as fibrous and porous networks, as well as complementary mechanical properties that mimic native tissue ECM.[9-11] One such peptide, KLD-12, is comprised of three amphipathic Lys-Leu-Asp-Leu repeats that enable unimers to stack as antiparallel β-sheets and further self-assemble into highly crosslinked fibrous hydrogels via a combination of electrostatic and hydrophobic interactions.[9] Studies of the KLD-12 peptide have demonstrated desirable qualities for *in-vivo* application such as non-immunogenicity,[12] antimicrobial properties,[13] and the capacity to provide a template for cellular proliferation and extracellular matrix (ECM) acccumulation.[14,15]

Unfortunately, peptide materials are susceptible to proteolytic degradation[16,17] and subsequent disassembly,[18,19] which precludes their use as long-term (e.g. months-years) or permanent implants. Furthermore, synthesis of these biopolymers involves step-wise addition of amino acids followed by deprotection steps, increasing production costs. Sequence modification in search of SAPs with improved mechanical or bioactivity properties can be arduous and synthetically involved.[13,20] Despite high yields (> 98%) for solid phase peptide synthesis (SPPS), the synthetic range is limited to only 70 amino acids.[21] Based on the discussed limitations, we were inspired to prepare analogues of the KLD-12 peptide in which the amide backbone is replaced with a proteolytic-resistant biosynthetic polymer framework. Furthermore, we aimed to mimic bulk morphological and viscoelastic properties of KLD-12 hydrogels using the three-amino acid sequence as a template.iving radical polymerizations can incorporate a diverse array of functionalities, including targeting, therapeutic or imaging agents, into a single polymer via graft-through techniques without the need for complicated protecting group strategies.[22-24] Amongst these strategies, ring-opening metathesis polymerization (ROMP) offers a high degree of synthetic control, allowing for the rapid preparation of

polymers with varying block lengths and sizes in low dispersity.[25-28] This polymerization strategy utilizes a highly functional group tolerant initiator making possible polymerizing directly sugars,[29,30] peptides,[31,32] drugs,[33-35] nucleobases,[36,37] and contrast agents.[38,39] To this end, we chose ROMP to generate proteolytically resistant polynorbornene backbones,[40,41] for the synthesis of all biosynthetic polymers in this study. Moreover, we reasoned that these polymeric systems would have unique properties based on the rigidity of the polynorbornene backbone and the high density of the polymer side chains, which could influence the viscoelastic properties of our biomimetic system.

Herein the design and characterization of novel polymeric analogues to the KLD-12 SAP prepared by ROMP, is reported (**Figure 5.1.1**). A diverse array of physical and mechanical properties was accessed through polymerization of three monomers analogues of the KLD-12 amino acids. With this strategy, diverse polymer architectures (e.g. blend vs block copolymers) were prepared with simple changes to monomer additions during ROMP. This strategy offers a key advantage over traditionally labile and short-lived self-assembling peptides used in tissue engineering., while providing complementary bulk scale behavior. Moreover, we demonstrate a facile method for searching phase space for new and dynamic self-assembling morphologies. Ultimately, these insights may provide simple design parameters for other biomimetic polymers used in medicine and technology.

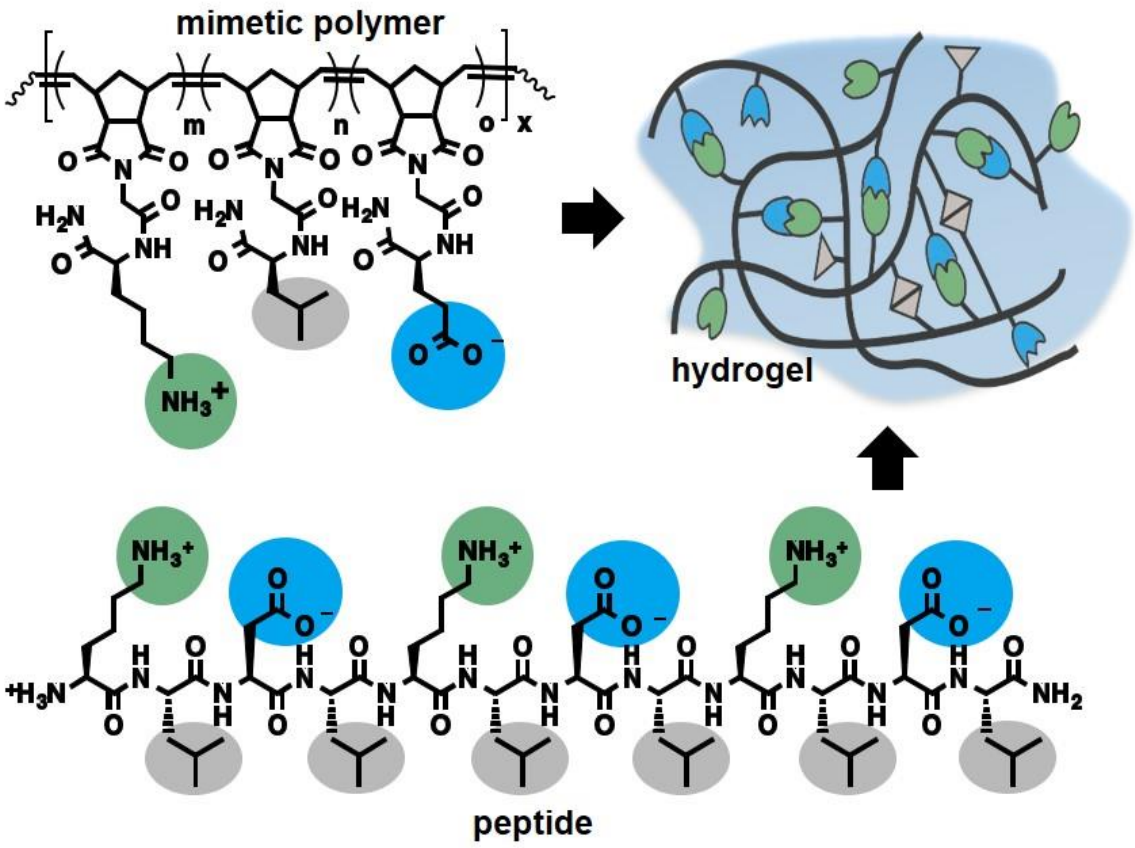


Figure 5.1.1. Diagram of biomimetic polymer analogue to the KLD-12 peptide hydrogel.

5.1.2 Results and Discussion

Design of polymers. Three norbornene-amino acid conjugates (NACs) were synthesized as protected monomers K', L', and E', to mimic canonical amino acids in KLD-12 SAP (**Supplementary Fig. XX**). A mimetic glutamic acid, which contains one additional carbon linkage, was used instead of aspartic acid to extend the functional moiety reach and range of motion for our peptide mimics. This we found was an important modification to account for the larger and more rigid polynorborne backbone. A library of statistical and block copolymers was generated to explore the influence of primary sequence, degree of polymerization (DP), and hydrophobic content on self-assembly behavior (**Figure 5.1.2** and **Table 2.2.1**).

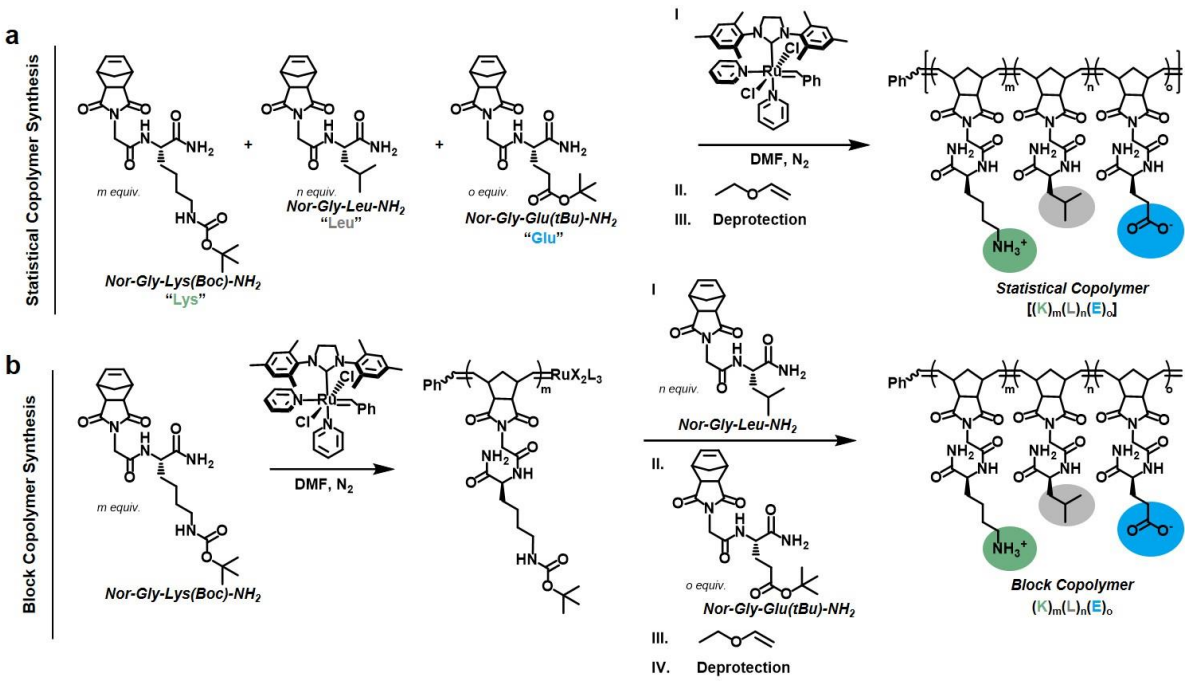


Figure 5.1.2. Synthetic routes for ring-opening metathesis polymerization (ROMP) of self-assembling polymers using norbornene-amino acid conjugates (NACs). Protected NAC monomers Nor-Gly-Lys(Boc)-NH_2, Nor-Gly-Leu-NH_2, and Nor-Gly-Glu(tBu)-NH_2, are referred to as Lys, Leu, and Glu. respectively. (a-b) Routes to the preparation of (a) statistical copolymers, and (b) block copolymers with Ru initiator. Deprotection with 95% TFA yields copolymers bearing cationic lysine, hydrophobic leucine, and anionic glutamate residues. For each polymer, *m*, *n*, and *o* are the degrees of polymerization (DP) given in **Table 1.** See the Experimental Section and Supporting Information for synthetic details.

Increasing the number of repeats within an SAP sequence, thereby increasing peptide length, enhances inter-strand overlap and improves hydrogel stiffness.[42] We reasoned this modification could similarly affect our polymer constructs. The polymers introduced in this study were readily synthesized at various block lengths (degree of polymerization 20, 40, 90, and 300) by tuning the ratio of initiator to monomer. This range of lengths was also explored to accommodate for inherent backbone atacticity of these polymers,[43,44] which we suspected could have a detrimental impact on self-assembly for lower DP polymers. A range from 3-9 blocks were explored for block copolymers architectures. We note that synthesis of block copolymers with total DPs of 20 and 40 was not feasible, as some blocks would need to be only 2 and 4 monomers in length, respectively. In contrast, synthesis of statistical copolymers at these lower DPs was possible with premixed monomers. Finally, hydrophobicity was varied between 33% Leu content, as is in the KLD-12 peptide, and 50% Leu

content. This increased hydrophobicity was explored to increase solid-like behavior of assembled hydrogels.

Table 5.1.11. Polymers prepared with varying primary sequence, degree of polymerization (DP), and hydrophobic content. The sequence nomenclature for statistical copolymers (e.g. $[KLE]_m$) was simplified from the IUPAC nomenclature given as [K-*stat*-L-*stat*-E]$_m$. The sequence nomenclature for block copolymers (e.g. $(K)_m(L)_m(E)_m$) was simplified from the IUPAC nomenclature given as $(K)_m$-*block*-$(L)_m$-*block*-$(E)_m$. Polymers were synthesized by D. Crystal and F. Hidalgo.

Statistical Copolymers					
Polymer Name	Sequence	Total DP	Number of Blocks	Leucine Content	Charged Units
statistical 20mer [KLE]	$[KLE]_m$	20	n/a	33%	13
statistical 40mer[KLE]	$[KLE]_m$	40	n/a	33%	27
statistical 90mer [KLE]	$[KLE]_m$	90	n/a	33%	60
statistical 300mer [KLE]	$[KLE]_m$	300	n/a	33%	200
statistical 20mer [KLEL]	$[KLEL]_m$	20	n/a	50%	13
statistical 40mer [KLEL]	$[KLEL]_m$	40	n/a	50%	27
statistical 90mer [KLEL]	$[KLEL]_m$	90	n/a	50%	60
statistical 300mer [KLEL]	$[KLEL]_m$	300	n/a	50%	200
Block Copolymer					
Polymer Name	Sequence	Total DP	Number of Blocks	Leucine Content	Charged Units
block 90mer KLE	$(K)_m(L)_m(E)_m$	90	3	33%	13
block 90mer KLEKLEKLE	$((K)_m(L)_m(E)_m)_3$	90	9	33%	27
block 300mer KLE	$(K)_m(L)_m(E)_m$	300	3	33%	60
block 300mer KLEKLEKLE	$((K)_m(L)_m(E)_m)_3$	300	9	33%	200
block 90mer KLEL	$(K)_m(L)_m(E)_m(L)_m$	90	4	50%	13
block 90mer KLELKLEL	$((K)_m(L)_m(E)_m(L)_m)_2$	90	8	50%	27
block 300mer KLEL	$(K)_m(L)_m(E)_m(L)_m$	300	4	50%	60
block 300mer KLELKLEL	$((K)_m(L)_m(E)_m(L)_m)_2$	300	8	50%	200

Polymerization kinetics and polymer block lengths were monitored by ^{1}H NMR and size exclusion chromatography multi-angle light scattering (SEC-MALS) (**Figure 5.1.3**). Polymerizations were monitored by the disappearance of norbornene olefinic hydrogens, which accompanies the appearance of polynorbornene hydrogens. Nearly 100% conversion for all three monomers was observed by 1 hr (**Figure 5.1.3a**). For polymerization of Lys, Leu, and Glu monomers, no significant difference in the rates of initiation was detected (**Figure 5.1.3b**). Thus, we reasoned that statistical copolymers could be prepared by premixing all monomers prior to initiator addition. For block copolymers, sequential aliquots of individual monomers were made. Size distribution of statistical copolymers were analyzed by SEC-MALS (**Figure 5.1.3c**). Block sizes in block copolymers were determined by measurement of sample aliquots taken before addition of new monomer (**Figure**

5.1.3d). The growth in polymer block length is observed as a decrease in elution time. Importantly, the dispersity of polymers was not adversely affected by incorporation of successive block.

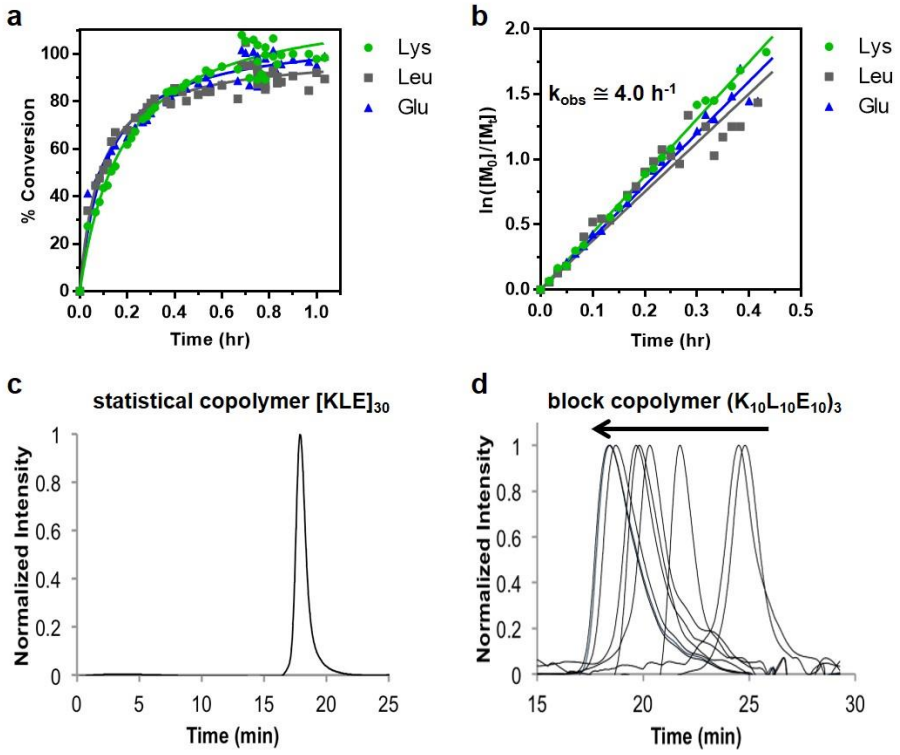


Figure 5.1.3. Representative examples of polymerization kinetics by NMR and characterization of polymer sizes by SEC-MALS after monomer additions. (a) Percent conversion of monomers. (b) Plot of initiation rates for each monomer (k_{obs} .≅ 4.0 h^{-1}). (c-d) Representative SEC-MALS traces for a statistical (c) and block (d) copolymer polymerizations. Polymers were characterized by D. Crystal and F. Hidalgo.

Characterization of polymer structure and nano-structure assembly characteristics in water. Polymers and peptide were studied at the same concentrations with respect to total charged units. This accounted for the high variability in total DP as well as the relative ratio of charged monomers capable of ionic crosslinking within these polymers.

The KLD-12 peptide self-assembles via β-sheet stacking along the amino acid faces with intermolecular electrostatic crosslinking and hydrophobic interactions of the Leu residues.[13,45] These structures further assemble to form entangled nanofibrils. Circular dichroism (CD) was used to evaluate the propensity for polymer self-assembly (**Figure 5.1.4**). The KLD-12 peptide exhibits a molar ellipticity minimum at 215 nm, characteristic of β-sheets. For both statistical and block

copolymers, however, secondary structure more closely resembled that of α-helices. In peptides, this structure is observed by CD as two characteristic minima at 208 nm (n→π* transition) and 222 nm (π-π* transition).[46] With our norbornene-based polymers, these minima were red-shifted to lower energies at 230 nm and 247 nm, which has been observed with helical materials that possess larger pitch length, interhelical distances, and/or helical thickness.[47-51] The larger and more rigid polynorbornene backbone is suspected to create longer helix turns than that of peptide amide backbones. Signal smoothing between both minima with the statistical copolymer might be caused by inhomogeneity of helical structures from lack of sequence control. Regardless, consistent evidence of secondary structure was found for disparate statistical and block copolymer architectures indicating potential for further self-assembly.

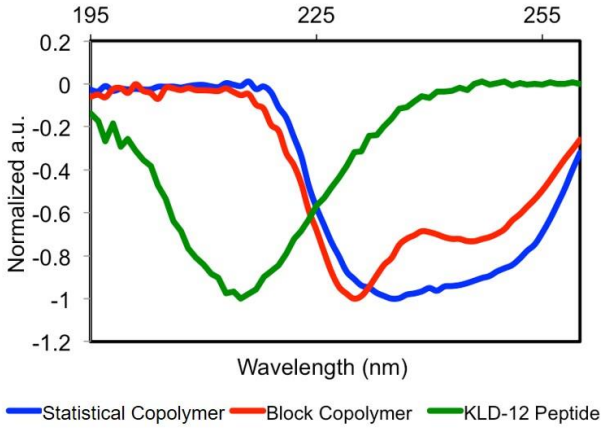


Figure 5.1.4. Circular dichroism (CD)of representative copolymers and KLD-12 peptide. Normalized CD Spectra of KLD-12 peptide, statistical 90mer [KLE], and block 90mer KLEKLEKLE at 100 μM with respect to charged moieties (pH 6.4).

An experiment with one gel-forming polymer, block 300mer KLEKLEKLE, showed that gelation occurred around pH 5.5-7.0 (see **Supplementary Fig XX**), which agrees with the calculated isoelectric point (pI = 6.42) for KLD-12. At this pH, ideal polymers in this study are expected to have no net electrical charge, because every cationic lysine amine is matched by an anionic glutamate carboxylate. The resulting drop in solubility causes solidification as a gel to occur.

Structural morphology of this polymer was investigated with dry state transmission electron microscopy (TEM) (**Figure 5.1.5**). Analysis showed that assemblies were structurally dynamic, with morphological switches observed when pH and salt content were adjusted. This manifests as discrete spherical particles under neutral conditions (**Figure 5.1.5a**). When the acidity is increased to pH 5.0 or decreased to pH 8.5, the morphology become large loosely packed sheets (**Figure 5.1.5b-c**). Finally, salt concentrations can have an effect on SAP fiber density and bulk viscosity,[52-54] hence these effects were briefly explored in our polymeric systems. Addition of NaCl to nongelling acidic samples up to 100 mM induced structural rearrangement into aggregated needle-like structures (**Figure 5.1.5d**). At bulk scale concentrations, this resulted in a noticeable increase in solution viscosity but did not alter the propensity for polymer samples to gel. Higher salt concentrations at any pH had no added effect on morphology. These morphological observations were consistent with the rest of our gel-forming polymers. Together, CD and TEM data show that the mimetic polymers designed in this study exhibit strong pH dependence with minor influence from NaCl content. This contrasts with a much larger geling range (pH 3-9) exhibited by KLD-12 peptide.

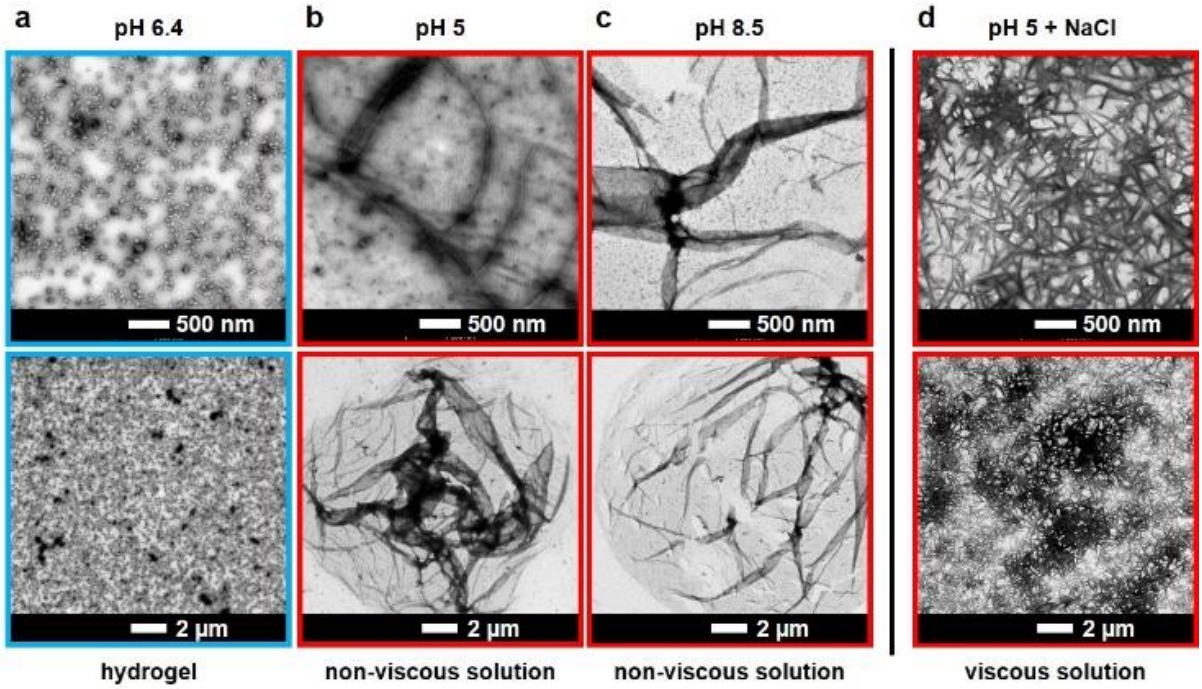


Figure 5.1.5. The effect of pH and salt on polymer morphology. Block 300mer KLEKLEKLE at (a) pH 6.4 assembles into micellar particles. These assemblies rearrange into large, loosely packed sheets at (b) pH 5.0 and (c) pH 8.5. Sample drying causes folding and collapse of sheets on the TEM grids. (d) Polymer at pH 5.0 with 100 mM NaCl shows needle-like structures. Images are outlined with blue and red, to indicate pH conditions at which bulk gelation does and does not occur, respectively. Polymer samples at 200 μM with respect to charged moieties.

For comparative analyses of all polymer morphologies in aqueous solvent, we analyzed samples with 100 mM NaCl at pH 6.4 (**Figure 5.1.6**). It is interesting to note that gel-forming polymers in this study adopted micellar structures (**Figure 5.1.6a-b**), whereas the KLD-12 peptide adopts elongated fibrillar structures (**Figure 5.1.6c**). This has been observed with polymeric micellar particles comprised of helical structures.[55-58] Most striking is the influence that statistical vs block architectures have on polymer morphology, even when comparing polymers with similar DP and hydrophobicity (**Figure 5.1.6a-b**). Statistical copolymers were less likely to form micellar structures than their block copolymer analogues. For these polymers, lower DP and decreased hydrophobicity caused preferential assembly into large sheets and fibers, as seen with statistical [KLE] 40mer, statistical

[KLE] 90mer, and statistical [KLE] 300mer (**Figure 5.1.6a**). Increasing hydrophobicity favored spherical morphology, as has been reported.[59]

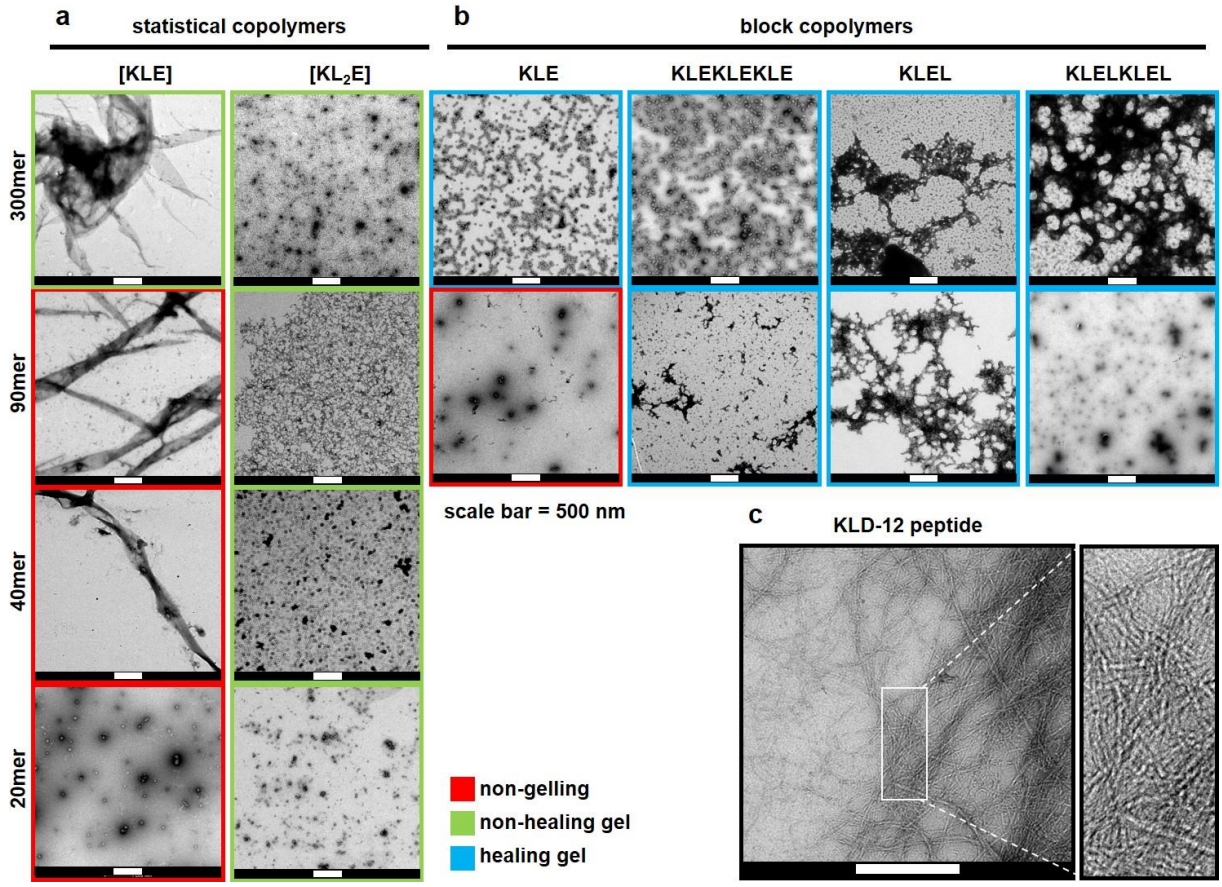


Figure 5.1.6. TEM morphology of polymers. (a-b) Micrographs of (a) statistical and (b) block copolymers organized horizontally by sequence and vertically by DP. Color coding with red, green, and blue, identifies polymers that are non-gelling, non-healing gels, and healing gels, respectively. (c) Micrograph of the KLD-12 peptide with magnified region Scale bar 500 nm. Peptide and polymer at 200 μM with respect to charged moieties with 100 mM NaCl (pH 6.4). Some TEM images were collected by S. Sahu.

Increasing hydrophobicity and DP within block copolymer samples caused particles to transition into lamellar networks, as shown in **Figure 5.1.6b** with block 90mer KL_2E, block 300mer KLEL, and block 300mer KLELKLEL. Finally, TEM images were color coded red, green, and blue to identify polymers that formed non-gelling solutions, non-healing hydrogels, and rehealable hydrogels when concentrated. Notably, gelling polymers preferentially formed spherical nanoparticles and fused lamellar networks, whereas non-gelling solutions were comprised of sheets and fibers. Together, these results highlight the potential to manipulate morphology through control of polymer architecture. We note that the polymers generated in this study adopted different secondary and tertiary structures

than the model KLD-12 peptide under dilute conditions. Regardless of these differences, we observed bulk scale gelation with several polymer architectures.

Characterization of bulk hydrogel morphology. The impact of polymer architecture on bulk scale morphology and viscoelastic properties was investigated. Regardless of individual differences in dilute-phase morphology by TEM, polymer architectures that supported bulk phase hydrogelation produced swollen and porous 3D networks by SEM (**Figure 5.1.7**). Notably, the KLD-12 peptide appears to be interconnected fibers whereas the block copolymer forms a lamellar network. We suspect that micellar particles from block 90mer KLE (**Figure 5.1.7b**) – at sufficiently high enough concentrations – fuse to generate these features. Finally, the statistical copolymer hydrogel appears less ordered with much smaller pore sizes than that of the block copolymer hydrogel. For this polymer, statistical 90mer [KLE], the dilute phase morphology in **Figure 5.1.6a** was that of sheets and fibers. Physical entanglement, rather than molecular rearrangement of polymers under concentrated conditions, might explain the rough texture observed with this network. Such. differences in bulk scale morphology have a profound impact upon mechanical properties, as shown by rheological studies below.

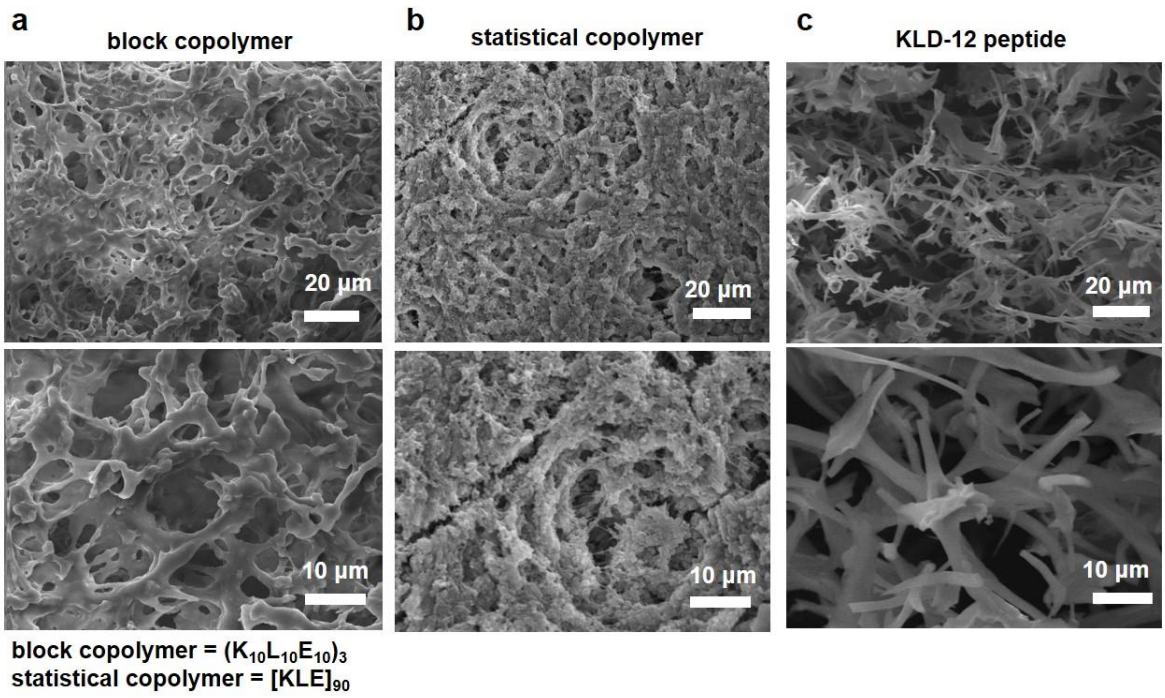


Figure 5.1.7. Scanning Electron Microscopy (SEM) of peptide and representative polymer hydrogels. (a) KLD-12 peptide, (b) block 90mer KLEKLEKLE copolymer, and (c) statistical 90mer [KLE] copolymer. Scale bars 20 μm (top) and 10 μm (bottom). Hydrogels were imaged by D. Crystal.

Characterization of bulk hydrogel mechanical properties. The bulk mechanical properties of self-assembled polymers was investigated to assess which architectures produce viscoelastic, shear-thinning, and rehealable hydrogels, as discussed in the introduction. Hydrogels were prepared by dissolving polymers at 108 mM with respect to charged moieties in 100 mM (pH 6.4) and submitted to rheological analysis. Initial strain sweep analyses were used to identify % strain tolerance of self-assembled hydrogels (**Figure 5.1.8**). The end of the linear viscoelastic region (LVR) is denoted by a rapid convergence of G'' and G' as the hydrogel structure breaks down. Samples possessed a stable G' and G'' up to 1 % strain, which was used as the applied strain for subsequent rheological measurements.

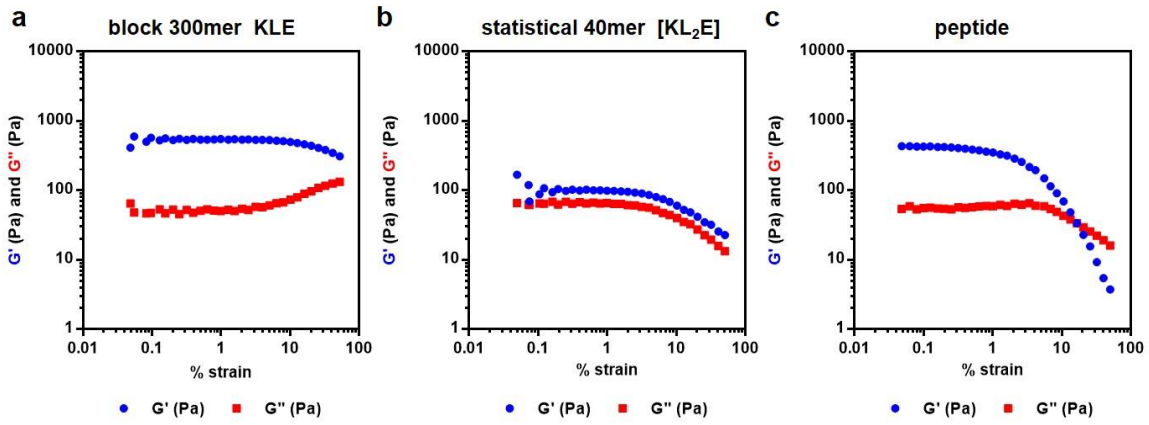


Figure 5.1.8. Representative strain sweep plots of polymer and peptide hydrogels. (a) block 300mer KLE copolymer, (b) statistical 40mer [KLEL] copolymer, and (c) KLD-12 peptide hydrogel control are shown. Storage (G') and loss (G'') moduli measured as a function of increasing % strain. Angular frequency 1 rad/s.

Polymers were assessed for their capacity to form hydrogels through analysis of storage (G') and loss (G'') moduli (**Figure 5.1.9**). Polymer identities in these plots are displayed with statistical copolymers in the first two groups, block copolymers in the second two groups, and the control peptide as the last group. Within each group, further separation highlights less (33% Lue) and more (50% Leu) hydrophobic content. Finally, each subgroup is arranged by increasing DP. Bars are colorized to indicate polymer architectures that gel (light/dark blue) or do not gel (light/dark red). Light-colored bars correspond to statistical copolymers, whereas dark-color bars correspond to block copolymers. The black bar corresponds to gel-forming KLD peptide control.

Figure 5.1.9a shows G', which provides a measure of the bulk elastic behavior and is proportional to hydrogel stiffness. **Figure 5.1.9b** shows tan δ, which is calculated as the ratio of loss (G'') and storage (G') moduli. This loss tangent is a measure of the internal friction (material damping) and is proportional to the strength of colloidal forces in a physical hydrogel.[60] When tan δ > 1, the sample is considered more viscous than elastic, behaving as a viscous fluid rather than an elastic solid. Therefore, all polymer samples that satisfy G' >1 Pa (minimal instrument tolerance) and tanδ <1 were classified as viable hydrogels for this study and were color-coded accordingly.

A wide range of viscoelastic moduli were access with different polymer architectures. Notably, all but one block copolymer (block 90mer KLE) formed a hydrogel. By increasing the number of blocks

without changing total DP, a weak hydrogel was achieved with block 90mer KLEKLEKLE. Even stiffer hydrogels were achieved when the total DP was increased up to 300 and hydrophobic content was increased to 50% Leu. We suspect these modifications increase the density of physical crosslink within these systems. In contrast, several statistical copolymer architectures did not form hydrogels, and those that did possessed lower gel stability, as exhibited by tan δ approaching 1. Increasing tanδ, likely correlated to increasing crosslink density,[60,61] was achieved with more hydrophobic architectures.

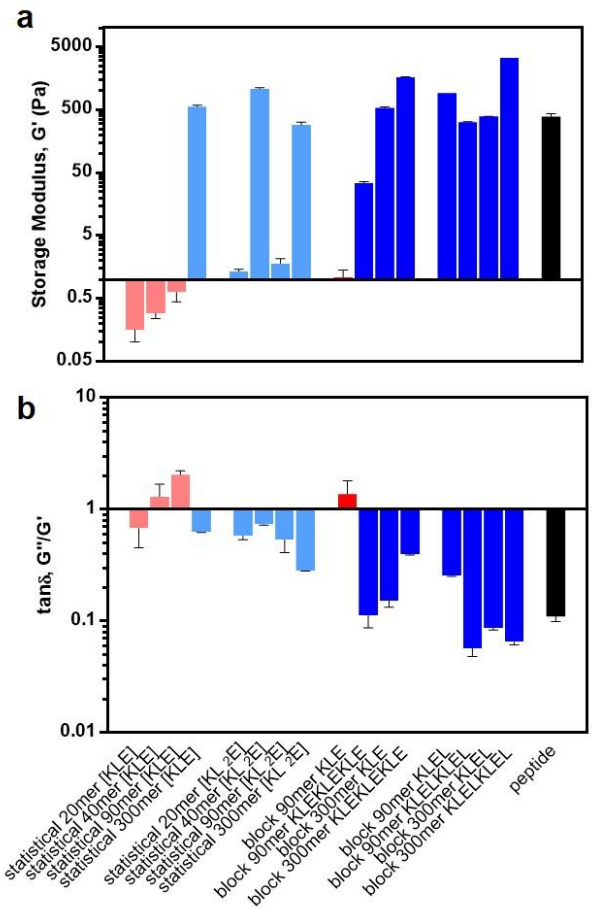


Figure 5.1.9. Viscoelastic properties of bulk polymer assemblies. (**a**) Hydrogel stiffness is measured as the storage modulus (G') of each polymer in the presence of water. (**b**) The strength of the colloidal forces is displayed as tan δ = (G''/G'), the ratio of the storage (G') and loss (G'') moduli. The x-axis at tan δ = 1 represents the crossover point at which samples with tan δ < 1 are considered hydrogels. Samples in light and dark blue are statistical and block copolymer, respectively, that have formed a hydrogel. Samples in light and dark red are statistical and block copolymers, respectively, that possess viscoelastic stiffness values below the instrument tolerance of 1 Pa, and not considered as viable hydrogels. The positive control peptide is shown in black. Data is plotted on a logarithmic scale with standard deviation (n=3 measurements). Polymer at 108 mM with respect to charged moieties with 100 mM NaCl (pH 6.4).

Angular frequency sweeps were conducted on each polymer sample (**Figure 5.1.10Figure 5.1.12**). G' values for the KLD-12 peptide were frequency independent within a range of 0.1-100 rad/s, indicating a rigid network that resists flowing (**Figure 5.1.10**).[62] Furthermore, G'>G'' at all frequencies, indicating that the peptide hydrogel displays a predominantly elastic behavior. Conversely, all but one statistical polymer sample exhibited frequency dependent behavior, and in some cases showed crossover between G' and G'' (**Figure 5.1.11**). This architecture causes polymers to behave more like viscous fluids rather than solid gels. Block copolymer architectures show increased frequency independence with higher DP (300mer) and hydrophobic content, resembling that of the KLD-12 peptide (**Figure 5.1.12**).

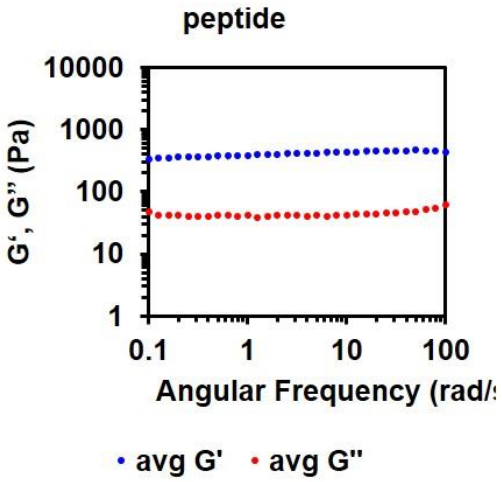


Figure 5.1.10. Frequency sweep plot of KLD peptide prepared at 108 mM with respect to charged moieties (100 mM NaCl, pH 6.4). Storage (G', blue) and loss (G'', red) moduli plotted as a function of angular frequency (100-0.1 rad/s). Measurements made at 1% strain. (n=3).

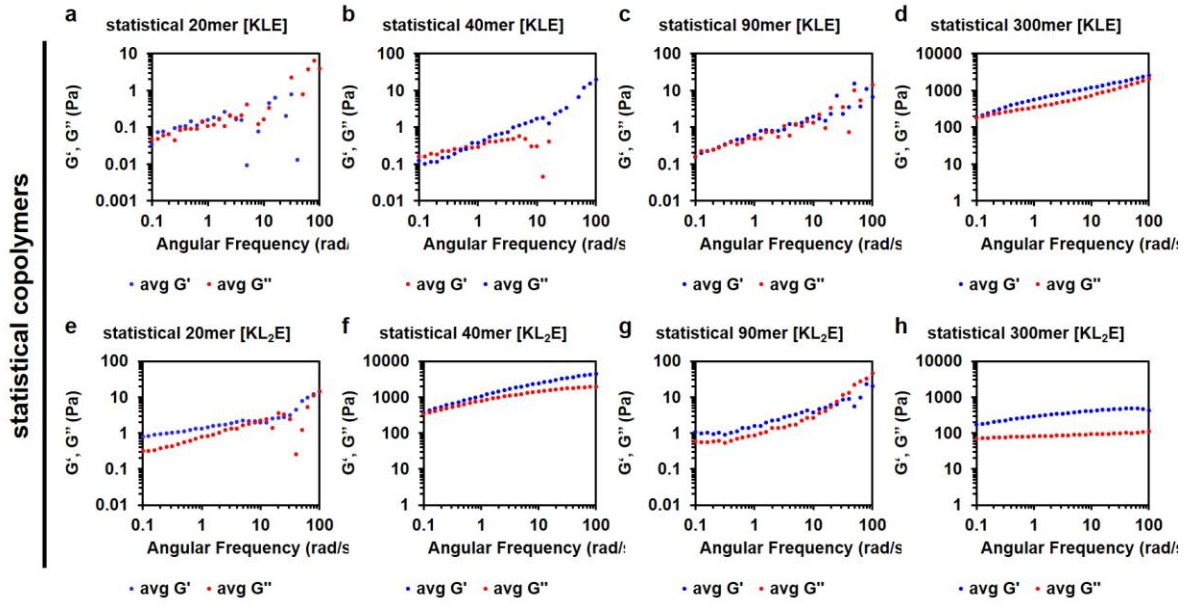


Figure 5.1.11. Frequency sweep plots of statistical copolymer samples. (a-h) Measurements of (a) statistical 20mer [KLE], (b) statistical 40mer [KLE], (c) statistical 90mer [KLE], (d) statistical 300mer [KLE], (e) statistical 20mer [KL_2E], (f) statistical 40mer [KL_2E], (g) statistical 90mer [KL_2E], and (h) statistical 300mer [KL_2E]. Polymers prepared at 108 mM with respect to charged moieties (100 mM NaCl, pH 6.4). Storage (G', blue) and loss (G'', red) moduli plotted as a function of angular frequency (100-0.1 rad/s). Measurements made at 1% strain. (n=3).

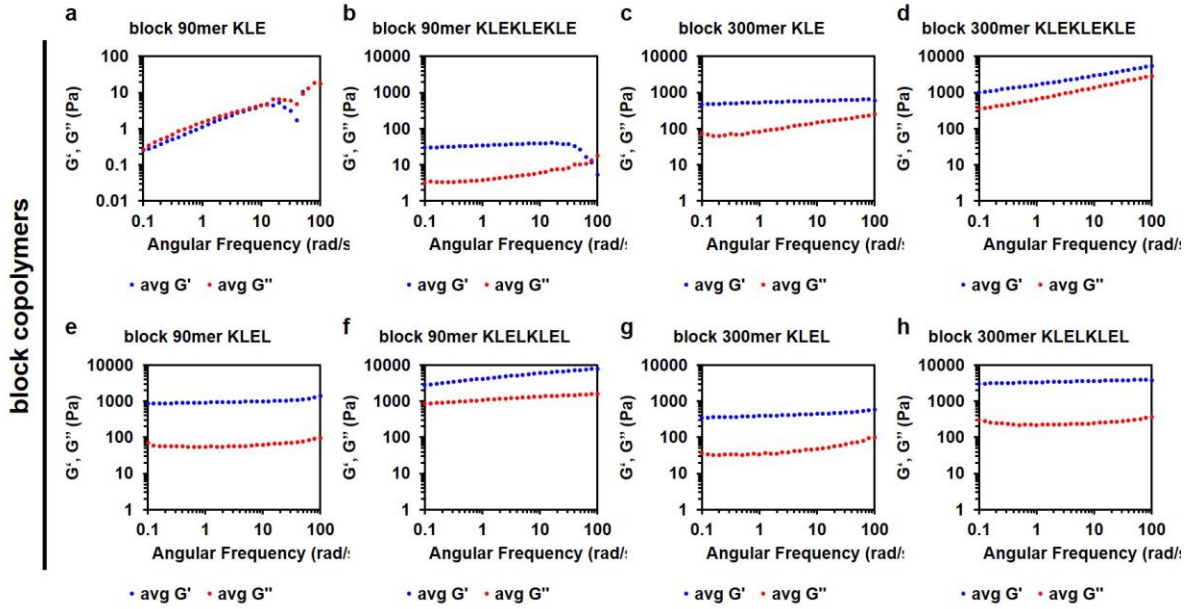


Figure 5.1.12. Frequency sweep plots of block copolymer samples. (a-h) Measurements of (a) block 90mer KLE, (b) block 90mer KLEKLEKLE, (c) block 300mer KLE, (d) block 300mer KLEKLEKLE, (e) block 90mer KLEL, (f) block 90mer KLELKLEL, (g) block 300mer KLEL, and (h) block 300mer KLELKLELKLEL. Polymers prepared at 108 mM with respect to charged moieties (100 mM NaCl, pH 6.4). Storage (G', blue) and loss (G'', red) moduli plotted as a function of angular frequency (100-0.1 rad/s). Measurements made at 1% strain. (n=3).

Practical Analysis of Hydrogel Injectability and Healing. Hydrogels for biomedical applications are surgically implanted in the form of patches[63] or as injectable formulations.[64] While patches are static pre-molded scaffolds, injectables are required to be shear thinning during delivery. Injectables have the advantage over patches in that their application can be used in minimally or non-invasive procedures, which is a current requirement with many translational procedures.[65-67] Furthermore, injectable hydrogels can fill irregular defects for tailored shape-fitting *in vivo*. To investigate injectability, the complex viscosity (η*) of polymer and peptide formulations was measured as a function of shear stress (**Figure 5.1.13**). All samples measured exhibited shear thinning behavior similar to that of the control peptide (black), regardless of polymer architecture. The relative viscosities with respect to polymer varied greatly (> 4 orders of magnitude), however, which influences the type of delivery strategies these hydrogels may be amenable to. Architectures that adopted lower viscosities than the KLD-12 peptide, such as **1** in **Figure 5.1.13**, might be amenable to minimally invasive deep-tissue injections such as transendocardial catheter injection and intracoronary infusion for cardiac repair. In Chapter 3 and 4, it was reported that the KLD-12 peptide induced catheter clogging, however, decreasing the viscosity of peptide progelators by over an order of magnitude enabled their use for minimally invasive catheter injection. Many samples, such as **2** and **3** in **Figure 5.1.13** exhibited much higher viscosities than the KLD-12 peptide, which likely precludes their use in a catheter. Subsequently, these higher viscosity and shear-thinning materials could be useful for delivery by needle-based subcutaneous and intramuscular injection.

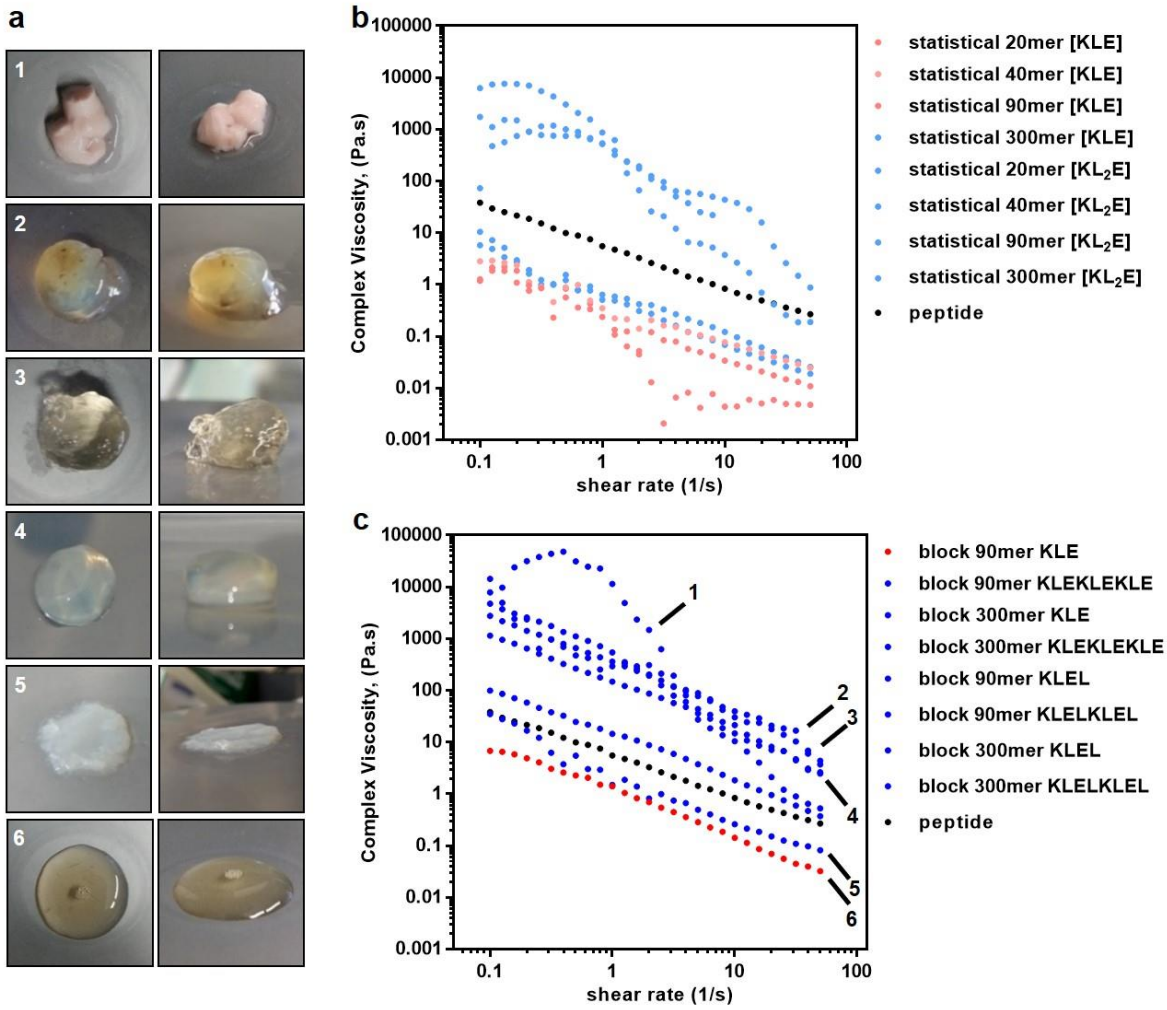


Figure 5.1.13. Shear thinning behavior of formulated hydrogels and non-gelling solutions. (**a**) Hydrogels and non-gelling solutions of selected block copolymer formulations. Hydrogel identities are (**1**) block 300mer KLEKLEKLE, (**2**) block 300mer KLEL (**3**) block 300mer KLE, (**4**) block 300mer KLELKLEL, (**5**) block 90mer KLELKLEL, and (**6**) block 90meer KLE. (**b-c**) Complex viscosity (η*) of polymer and peptide formulations as a function of shear rate (0.1 - 100 1/s). Compiled (**b**) statistical and (**c**) block copolymers are displayed. Data from (**a**) are labeled.

A vital property for injectable hydrogels is that they can still gel after exposure to excess shearing forces during needle-based or catheter delivery. Polymer and peptide hydrogels were analyzed for healing capacity after network disruption from excess strain (**Figure 5.1.14**). At high strain (100% strain), all hydrogels yielded causing a steep drop in G' and G'' as well as crossover of both viscoelastic moduli (G''>G'). This strain breaks physical crosslinks that contribute to solid-like behavior, causing the network to behavior predominantly as a viscous liquid. Cessation of yield level

strains after 3 min was accompanied by rapid hydrogel recovery by block copolymers or little to no recovery with statistical copolymers.

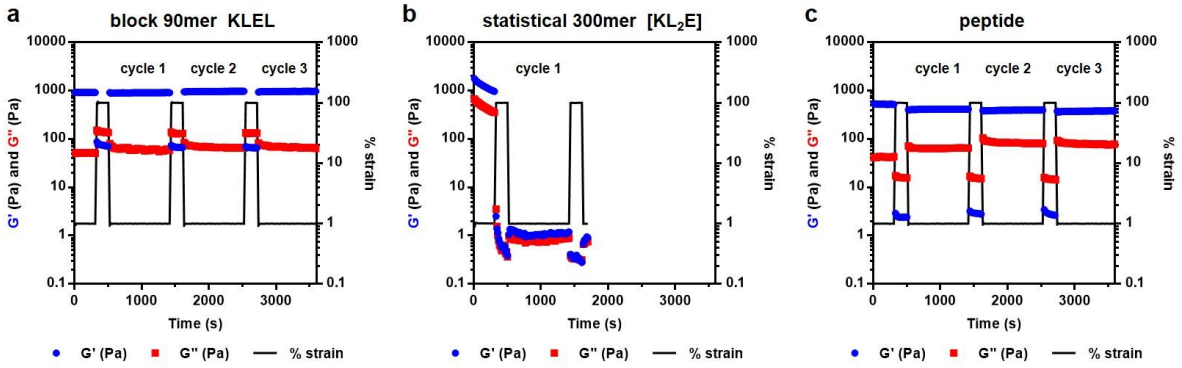


Figure 5.1.14. Representative step-strain oscillation profiles. (a-c) Hydrogel samples comprising the (a) block 90mer KLEL copolymer, (b) statistical 300mer [KLEL] copolymer, and (c) KLD-12 peptide control were subjected to repeat rounds of excess strain (100%) for 3 min to disrupt the hydrogel network and allowed to recover for 5 min (1% strain). Measurements for the statistical copolymer were not continued past two rounds of excess strain as no measurable hydrogel persisted (G'>G''). Angular frequency 1 rad/s. 1% strain (n=3).

Repeat healing capacity of all hydrogels is summarized in **Figure 5.1.15**. Normalized healing efficiency was calculated according to the following equation:

$$Normalized\ Healing\ (\%) = {G'}_n / {G'}_{pristine} * 100$$

, where G'_n is the storage modulus during the recovery period after a strain cycle (n=0, 1, 2, 3) and $G'_{pristine}$ is the storage modulus under pristine conditions (n=0). Notably, all block copolymer demonstrated nearly complete hydrogel recovery for up to 3 cycles of high and low strain. Recovery was observed for only two statistical copolymer architectures, which in both cases was incomplete and nonrecoverable after the first cycle of high strain. As a control, KLD-12 peptide displayed repeat healing capacity like block copolymers, however, healing after cycle 1 led to ~80% recovery. Thus, we show that many of our biomimetic block copolymer architectures display superior healing capacity over that of the model peptide.

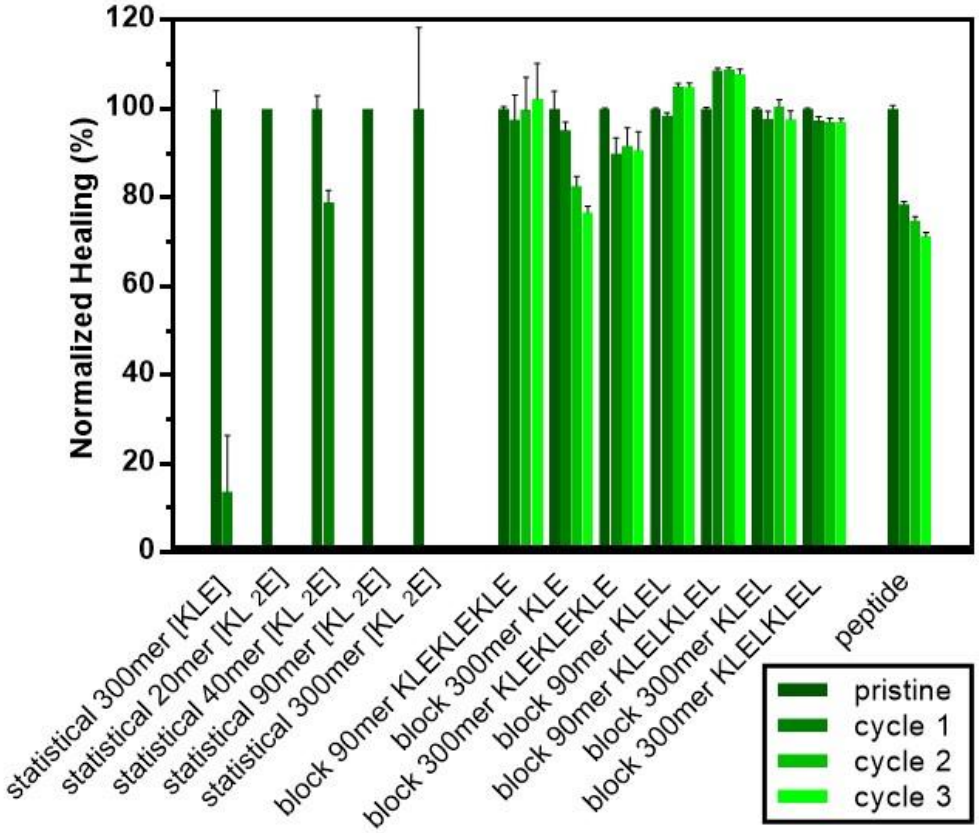


Figure 5.1.15. Strain recovery healing of hydrogels following repeat cycles of excess strain. Shown are the normalized healing efficiency (%) of polymer and peptide hydrogels from pristine condition and recovery after 3 repeat cycles of disruptive strain. Healing efficiency is normalized to pristine hydrogel conditions, calculated according to the equation above. Error bars represent standard deviation measured over 5 minutes of recovery.

In several biomedical applications, hydrogels experience a change in environmental conditions, such as change in temperature when administered *in vivo*. To assess this sensitivity, storage modulus (G') and tan δ (G''/G') were measured with respect to increasing temperature (21 – 40°C) to represent the transition from room to physiological temperature experienced by hydrogels during delivery (**Figure 5.1.16**). When heated to 37 °C, the highest resistance to viscoelastic deviations was displayed by block copolymers containing higher hydrophobic content (block 90mer KLEL, block 90mer KLELKLEL, block 300mer KLEL, and block 300mer KLELKLEL). Interestingly, these four polymer architectures were even less effected by temperature changes than the model peptide. Peptides with lower hydrophobic content or statistical copolymer architectures exhibited

higher deviations in viscoelastic moduli; in some instances, hydrogel disassembly during these temperature sweeps occurred.

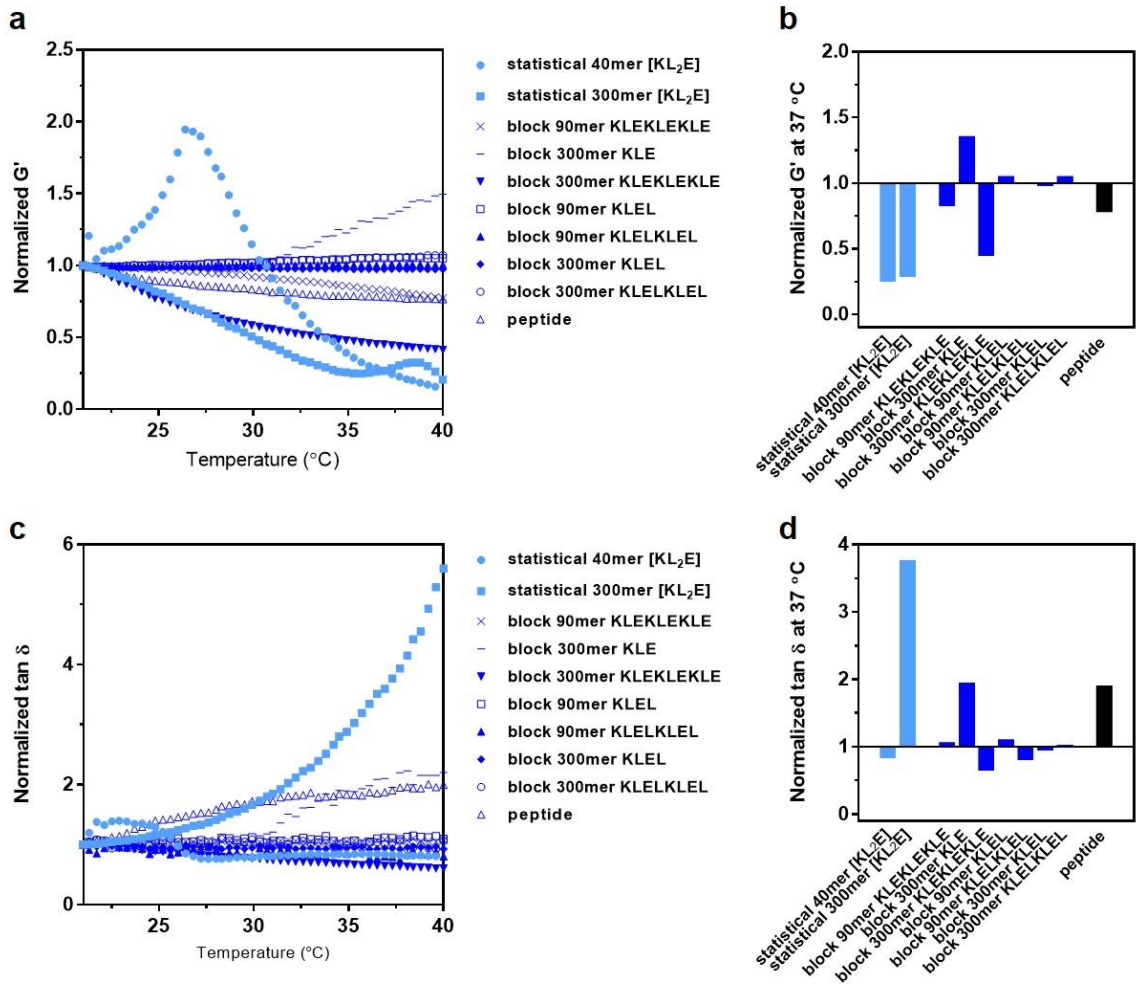
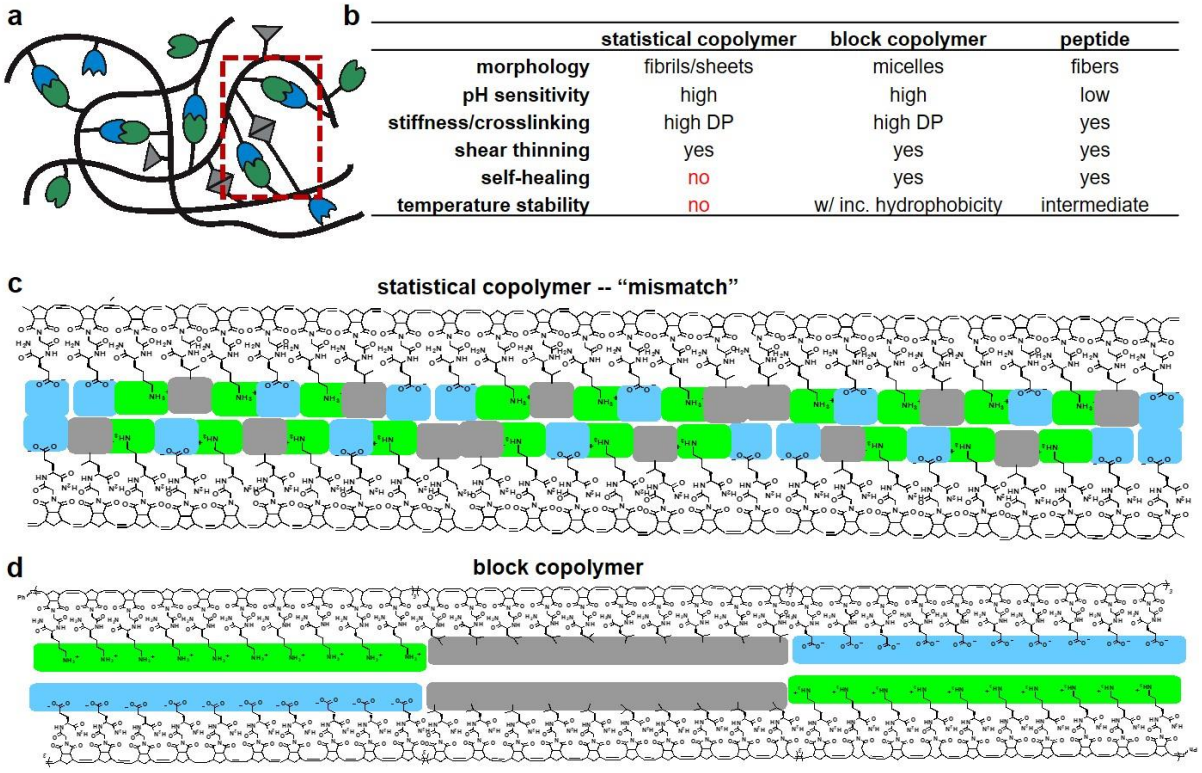


Figure 5.1.16. Hydrogel stability to clinically relevant temperature changes. (a-b) (a) Normalized storage modulus (G') as a function of increasing temperature (21-40 ˚C), depicting deviations in hydrogel stiffness when warmed to physiologically relevant temperatures. (b) Bar graph for hydrogels depicting G' at 37 ˚C as normalized to initial G' at formulation temperature (21 ˚C). (c-d) (c) Normalized tan δ (G''/G') as a function of increasing temperature (21-40 ˚C), depicting deviations in internal friction of the material and relative crosslinking density when warmed to physiologically relevant temperatures. (d) Bar graph for hydrogels depicting G''/G' at 37 ˚C as normalized to initial G''/G' at formulation temperature (21 ˚C).

5.1.3 Overall Influence of Architecture

A summary of self-assembly properties for peptide, block copolymers, and statistical copolymers is provided in **Figure 5.1.17.** To assess all of these results in comparison within the model template, we scrutinized the KLD-12 peptide architecture and its impact on self-assembly through

alignment of ionic charges and hydrophobic residues (**Figure 5.1.17a**). The KLD-12 peptide could either be considered a sequence-controlled blend copolymer or block copolymer consisting of 12 evenly sized units. This order is sufficient to promote self-assembly between neighboring strands. Thus, these two major architectures were critically assessed with respect to our mimetic polymers (**Figure 10b**).



	statistical copolymer	block copolymer	peptide
morphology	fibrils/sheets	micelles	fibers
pH sensitivity	high	high	low
stiffness/crosslinking	high DP	high DP	yes
shear thinning	yes	yes	yes
self-healing	no	yes	yes
temperature stability	no	w/ inc. hydrophobicity	intermediate

Figure 5.1.17. Summary schematic depicting statistical versus block copolymers. (a) Schematic of hydrogel assembly via ionic crosslinks and hydrophobic interactions. (b) Summary of physical properties observed with polymers and peptide analyzed throughout this study. (c) Schematic of statistical copolymer alignment with mismatches. (d) Schematic of block copolymer alignment of domains.

Despite efforts to generate statistical copolymers as a mimic of the KLD-12 peptide's alternating hydrophobic, cationic, and anionic residues, lack of sequence control limited their self-assembly (**Figure 5.1.17c**). Furthermore, individual statistical copolymers were not identical to their neighbor strands, so a large degree of mismatch and transient network defects during self-assembly inevitably prevented gelation of several architectures. Increasing statistical copolymer DP did enable gelation, which is largely attributed to increasing entanglement opportunities.[68] However, none of

these hydrogels were rehealable. Chain detangling with excess strain permanently disrupted these networks. Thus, statistical sequence architecture are non-ideal for injectable and rehealable systems.

Block copolymers in this study were able to compensate for interstrand mismatches with large regions devoted entirely to a single functional group (e.g. cationic amine, anionic carboxylate, or aliphatic hydrophobe) (**Figure 5.1.17d**). Thus, slight misalignments within self-assembled polymer networks were well tolerated. Furthermore, longer polymers (e.g. 300mer) with these evenly spaced blocks significantly increased viscoelastic stiffness and frequency independent moduli. We suspect that covalent tethering of more domains promotes physical interactions between several polymers, thus increasing bulk crosslink density.

5.1.4 Conclusions

Success with the use of peptidic biomaterials *in vivo* has been historically thwarted by errant proteolysis. Advances with functional biosynthetic polymers provides robust polymer backbones that can be used as proteolytic resistant mimics of nature's polymer templates. Despite significant improvements in biocompatible and functionally diverse polymers, our success in the field is constrained by a limited understanding of how polymer architectures can induce responsive and structurally dynamic behavior.

Within this study, the near-neutral pI for all polymers introduced strong pH responsiveness for gelation at physiologically relevant conditions. These materials experience morphological transitions from disperse sheets in solution (6>pH>8) to lamellar particles (pH 6-8) that further fuse into porous macromolecular hydrogels. One might envision responsive tissue scaffolds which are easily injected as low viscosity slightly basic solutions (pH 8.5); rapid neutralization within biological fluids (pH 7.4) would then be the trigger for gelation. Acidosis from tissue inflammation[69,70] could be a secondary trigger for hydrogel disassembly and potential cargo release.

Much work is needed to demonstrate the practical application and biocompatibility of our materials *in vivo.* What has been demonstrated is an in-depth investigation into the influence of

polymer architecture on hydrogel self-assembly characteristics. Critically, we provide a simple set of design criteria to access various morphological and mechanical properties for physically crosslinked hydrogels. Ultimately, these trends can be taken into considerations for future designs of injectable biosynthetic tissue scaffolds. Finally, we posit that these design criteria are not limited to a polynorbornene backbone, as has been demonstrated by transitioning from ROMP[71,72] to RAFT[73] based polymers for the synthesis of structurally dynamic nanomaterials.

5.1.5 Experimental Details

General Considerations: N-(Glycine)-cis-5-norbornene-exo-dicarboximide was purchased from TCI. Amino acids used in the monomer synthesis were purchased from Bachem. The polymerization initiator, $(H_2IMES)(pyr)_2$-$(Cl)_2Ru$=CHPh was prepared as previously published.[26] Unless otherwise noted, all other compounds and materials were purchased from Sigma Aldrich and used without further purification. ^1H (400 MHz) and ^{13}C (125 MHz) NMR spectra were recorded on a Varian Mercury Plus spectrometer. Chemical shifts are reported in ppm relative to residual solvent peaks from DMF-d_7 or $CDCl_3$. Mass spectra were obtained at the UCSD Chemistry and Biochemistry Molecular Mass Spectrometry Facility.

Nor-Gly-Glu(OtBu)-NH_2 Monomer Synthesis**:** A 100 mL round-bottom flask equipped with a stir bar was charged with N-(Glycine)-*cis*-5-norbornene-*exo*-dicarboximide (1.974 g, 8.9 mmol, 1.1 equiv.), which was prepared as described previously[74] and dissolved in 20 mL of DMF. To this was added HBTU (3.076 g, 8.1 mmol, 1 equiv) and diisopropylethylamine (5.65 ML, 32.4 mmol, 4 equiv). The mixture was stirred at room temperature for 1 h. To this mixture was added H-Glu(OtBu)-NH_2 (1.936 g, 8.1 mmol, 1 equiv.), and the reaction was stirred at room temperature for 72 h. The solution was then concentrated to dryness. The resulting solid was resuspended in CH_2Cl_2 (70 mL) and subsequently washed with HCl (aq) (1M, 30 mL) (×3), $NaHCO_3$ (aq) (5%, 30 mL) (×3) and brine (30 mL) (×3). The organic layer was collected, dried over Na_2SO_4 (s) and concentrated to dryness. The material was then purified by flash column chromatography on silica gel (5% MeOH in CH_2Cl_2) to

yield a white powder in 77% yield (2.570 g, 6.33 mmol) R_f = 0.33 (5% MeOH in CH_2Cl_2). ^{1}H NMR (400MHz, $CDCl_3$, 298 K) δ 7.68 ppm (1H, d, J = 7.3 Hz), 6.62 (1H, s), 6.35 (2H, s), 5.65 (1H, s), 4.43 (1H, m), 4.20 (2H, q, J = 15.7 Hz, 17.6 Hz), 3.28 (2H, s), 2.75 (2H, m), 2.35 (2H, m), 2.01 (2H, m), 1.70 (2H, d, J = 10.0 Hz), 1.51 (1H, d, J = 10.1 Hz), 1.43 (9H, s);^{13}C NMR (125 MHz, $CDCl_3$, 298 K) δ 177.88, 177.53, 173.87, 173.32, 166.14, 138.10 81.53, 52.93, 48.26, 48.16, 45.52, 43.13, 41.26, 31.95, 28.19, 27.31; HRMS analysis (ESI-TOFMS) m/z calculated for $[C_{20}H_{27}N_3O_6Na]^+$ 428.1792, found 428.1789.

Nor-Gly-Leu-NH_2 Monomer Synthesis**:** Nor-Gly-Leu-NH_2 monomer was synthesized as described for Nor-Gly-Glu(OtBu)-NH_2. A white powder in 51% yield (2.027 g, 6.08 mmol) R_f = 0.44 (5% MeOH in CH_2Cl_2). ^{1}H NMR (400MHz, CDCl3, 298 K) δ 6.83-6.81 (1H, d, J = 8.3 Hz), 6.48 (1H, s), 6.29 (2H, m), 5.85 (1H, s), 4.50-4.44 (1H, m), 4.24-4.09 (2H, q, J = 15.7 Hz, 26.7 Hz), 3.30 (2H, s,), 2.75 (2H, m), 1.72-1.51 (6H, dd, J = 11.1 Hz, 5.7 Hz), 0.95-0.90 (6H, m,).^{13}C NMR (125 MHz, DMF, 298 K) δ 177.96, 177.62, 175.50, 166.58, 137.96, 137.90, 55.15, 51.81, 48.06, 47.97, 45.33, 45.31, 43.17, 42.94, 40.78, 40.70, 24.70, 22.95, 21.70; High resolution MS analysis (ESI-TOFMS) m/z calculated for $[C_{17}H_{23}N_3O_4Na]^+$, 356.1581, found 356.1579.

Nor-Gly-Lys(Boc)-NH_2 Monomer Synthesis**:** Nor-Gly-Lys(Boc)-NH_2 monomer was synthesized as described for Nor-Gly-Glu(OtBu)-NH_2. A white powder in 62% yield (2.118 g, 4.70 mmol) R_f = 0.29 (5% MeOH in CH_2Cl_2). ^{1}H NMR (400MHz, $CDCl_3$, 298 K) δ 7.69 ppm (1H, d, J = 7.3 Hz), 6.98 (1H, s), 6.28 (2H, s), 5.85 (1H, s), 4.90 (1H, s), 4.39 (1H, m), 4.23-4.14 (2H, q, J = 25.9 Hz, 16.0 Hz), 3.26 (2H, s), 3.06 (2H, s), 2.74 (2H, s), 1.81 (3H, m), 1.70 (2H, m), 1.50-1.35 (15H, m); ^{13}C NMR (100 MHz, $CDCl_3$, 298 K) δ 177.91, 177.70, 174.07, 166.32, 156.62, 138.10, 79.50, 53.17, 48.22, 45.54, 43.11, 41.12, 40.23, 31.34, 29.68, 28.61, 22.44; High resolution MS analysis (ESI-TOFMS) m/z calculated for $[C_{22}H_{32}N_4O_6Na]^+$, 471.2214, found 471.2212.

Polymerization Kinetics**:** ^{1}H NMR spectroscopy was used to follow the time course of polymerization of the three monomers by monitoring the resonances corresponding to the protons of the reacting olefin, which shift upfield once polymerized from ~ 6.3 to 5.9 ppm. To ascertain rate

constants, polymerizations of each of the three monomers were carried out under identical conditions to a desired degree of polymerization of 50 ($[M_0]/[I]=50$). To this end, the monomers (0.0125 mmol, 50 equiv.) dissolved in 380 uL of DMF-d7 were placed in a J-Young tube in a glove box under N_2 (g). The polymerization initiator (0.00025 mmol, 1 equiv.) dissolved in 20 uL of DMF-d7 was then added to the tube. ^{1}H NMR spectra were then acquired at 1 min intervals. The rate constants found were: $k_{Lys} = 1.58 \bullet 10^4\ s^{-1}$, $k_{Leu} = 1.35 \bullet 10^4\ s^{-1}$, $k_{Glu} = 1.44 \bullet 10^4\ s^{-1}$. Given that nearly identical rates are observed for the polymerization of all three monomers, we reasoned that statistical of copolymers can be prepared by mixing the three monomers in a single pot.

Statistical Copolymerization**:** All statistical copolymerizations were carried out in a glove box under N_2 (g). Given that each of the three monomers polymerize at equivalent rates, the protocol for these polymerizations simply involved mixing together each monomer in DMF-d7 at the concentration specified in Table S1 for 5 h. The polymerizations were then terminated by ethyl vinyl ether and then characterized by SEC-MALS (Table S2) to obtain the polymer molecular weight (M_n) and dispersity (M_w/M_n). The polymers were then precipitated from solution by the addition of cold ether, collected by centrifugation and dried. Side-chain protecting groups were removed by dissolving the resulting powder in a 5 mL of a mixture of TFA/H_2O/TIPS (95:2.5:2.5) and stirring the resulting mixture for 4 hours at room temperature (**Figure Sxxx**). The polymers were then precipitated with cold ether, collected by centrifugation and dried. ^{1}H NMR analysis of the polymers prior to side-chain deprotection was used to determine the relative ratio of each of the three peptide monomers present in the polymers. Given that the three monomers have the same scaffold, only differing in the side chain identity, each polymer ^{1}H NMR spectrum contains many overlapping signals for the three monomers, but fortunately, each monomer has at least one side-chain hydrogens with a distinctive NMR shift. The ratio between the distinctive signals and the overlapping signals can be used to estimate the percentage of each monomer in the final blend copolymer.

Block Copolymerization**:** All block copolymerizations were carried out in a glove box under N_2 (g). To a stirred solution of a Lys monomer in dry, degassed DMF at the concentration specified in

Table S3, was added a solution of the polymerization initiator. The reaction was left to stir for 1 h, after which an aliquot (20 µL) was removed for SEC-MALS characterization. The second monomer was added, and the reaction was left stir for 1h. An aliquot (20 µL) was set aside. This sequential process was repeated until each block had been polymerized. The polymerizations were then terminated with ethyl vinyl ether. The polymers were then precipitated with cold ether, collected by centrifugation and dried. Side-chain deprotection was carried out as described for the statistical copolymers.

Degree of Polymerization and Block Length Analysis**:** Size-exclusion chromatography coupled with multiangle light scattering (SEC-MALS) was used to determine polymer dispersity and molecular weights. SEC was performed on a Phenomenex Phenogel 5 u 10, 1K-75K, 300 × 7.80 mm column in series with a Phenomenex Phenogel 5 u 10, 10K-1000K, 300 × 7.80 mm column, which ran with 0.05 M LiBr in DMF as the running buffer (flow rate of 0.75 mL/min) using a Shimadzu pump. The instrument was also equipped with a MALS detector (DAWN-HELIO, Wyatt Technology) and a refractive index (RI) detector (Wyatt Optilab T-rEX dectector). All detectors were normalized with a 30,000 MW polystyrene standard.

Slow Titration Assembly Screening**:** A dialysis-based screen for polymer self-assembly was performed to assess pH and salt tolerance. Polymers were pre-dissolved in H_2O (54 mM wrt charge, pH > 9) and transferred to pressure-sealed dialysis cups with 4.5k MW cutoff, to prevent excess dilution during solvent exchanges. Polymer solutions were dialyzed into stirred phosphate buffered solution (pH 9.0), then incrementally dialyzed into stirred phosphate buffered solutions at decreasing pH (pH 9, 7, 5, and 3) and increasing NaCl concentrations (0, 100, 200, and 300 mM). Visible observation of increased turbidity or apparent viscosity was recorded. The 2D screen is represented below with arrows depicting incremental transitions. Equilibration time between transitions was 1hr.

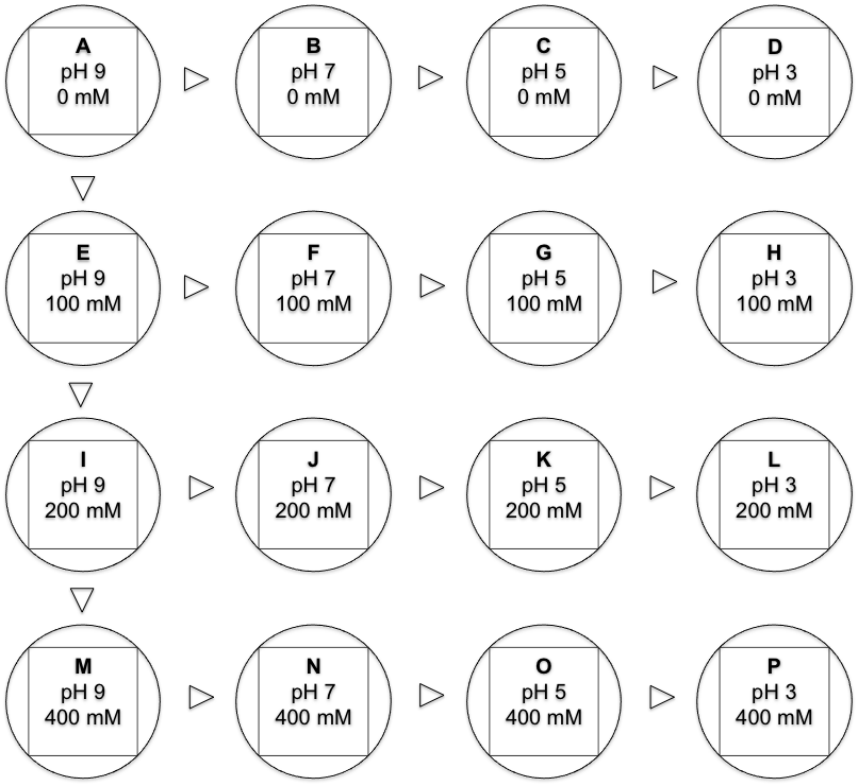


Figure 5.1.18. Assembly screen setup. Samples in dialysis cups (16 total) at pH 9 with 0 mM NaCl were sequentially solvent-exchanged into solutions with decreasing pH and increasing NaCl concentration, according to arrows in the schematic. Ultimately, polymer samples in 16 different pH and salt concentrations were assessed for gelation.

Hydrogel Formulation Protocol**:** Polymers were pre-dialyzed into H_2O at pH 9 to remove excess salts and disassemble aggregates. Samples were slowly neutralized with HCl (1M) to induce assembly and diluted to achieve a final polymer concentration of 108 mM with respect to charge (pH 6.4). Resulting hydrogels were incubated undisturbed at 25 °C overnight. HPLC purified $(KLDL)_3$ peptide was prepared similarly without pre-dialysis.

SEM General Sample Preparation Protocol**:** SEM images were collected on an FEI XL30-SFEG UHR SEM. Hydrogels were prepared from the KLD-12 peptide and two representative copolymers with identical DP and hydrophobic content: block 90mer KLEKLEKLE and statistical 90mer [KLE]. A solution of the peptide (14 mg/mL, 80 mM with respect to charge) and block copolymer (23.5 mg/mL, 45 mM with respect to charge) in H_2O (pH 6.4) was prepared. Following an incubation period of 1 hour, a portion of the hydrogel was removed and placed onto a silicon SEM

wafer. The sample was gently blot-dried and frozen in liquid nitrogen. The sample was lyophilized directly onto the SEM chip for imaging. Prior to imaging, the sample was sputter coated with iridium metal for 7 seconds at 85 milliAmps. A solution of the statistical copolymer (20 mg/ml, 40 mM with respect to charge) in H_2O (pH 6.4) was prepared. An aliquot of this solution was transferred onto a silicon SEM wafer. To this aliquot, NaCl(aq) was added dropwise to a final concentration of 200 mM, to seed hydrogel formation. Following an incubation period of 1 hour, the sample was blot dried, and put into a sealed apparatus containing calcium sulfate anhydrous. After 24 hours of drying, the sample was imaged via SEM. Prior to imaging, the sample was sputter coated with iridium metal for 7 seconds at 85 milliAmps.

TEM General Sample Preparation Protocol**:** Formvar/Carbon-coated 400 mesh Cu grids (Ted Paella, Inc.) were glow discharged for 90 s and spotted with 5 µL peptide or polymer sample (200 µM with respect to charged moieties) and set for 5 min. Grids were rinsed with distilled H2O (5 drops), stained with 1% (w/w) uranyl acetate (3 drops), and wicked dry with filter paper. TEM images were acquired on an FEI Tecnai G2 Sphera TEM at 200 kV.

Circular Dichroism**:** UV-Vis circular dichroism (CD) was used to evaluate the secondary structure of KLD-12 peptide and representative block and statistical copolymers. The peptide and polymers were dissolved in H_2O to a final concentration of 100 µM (with respect to charged moieties). CD spectra were measured using an Aviv 215 spectrometer and each sample was measured from 190 to 260 nm with a slit width of 1 nm, scanning at 1 nm intervals with a 1s integration time. Measurements were taken 3× at 25°C, averaged, and normalized.

Rheological Characterization**:** Viscous and viscoelastic properties were assessed using a stress-controlled rheometer (TA Instruments AR-G2) equipped with a Peltier plate to control temperature. A parallel plate geometry was used with a diameter of 20 mm. For viscosity measurements the apparatus was used in flow mode. The viscosity of the samples was measured as a function of shear rate in the range 0.1–50 s^{-1}. For viscoelastic measurements the apparatus was used in an oscillatory mode. To ensure the measurements were made in the linear viscoelastic regime

(LVR), amplitude sweeps were performed between 0.05-50 % strain at 1 rad s^{-1} and showed no variation in storage (*G'*) and loss (*G")* moduli up to a strain of 1%. The dynamic moduli of the hydrogels were therefore measured as a function of frequency in the range 0.1–100 rad s^{-1} at a strain of 1%. Temperature sweeps were by increasing temperature from 21-40 °C at a ramp rate of 1 °C/min. Step-strain tests were used to monitor gel recovery following disruption for 3 min at 100% strain and recovery 15 min at 1% strain over 3 cycles. Calculations of % normalized healing were made from averages of G' over the first 5 min under nondestructive (1% strain) conditions. All experiments were performed at 25 °C, with a gap height of 650 μm, and repeated at least three times (with the exception of step-strain tests) to ensure reproducibility. Unless otherwise stated all moduli mentioned in the text are taken at an angular frequency of 1rad/s and strain of 1%.

5.2. Acknowledgements

Chapter 5 is adapted, in part, from material currently being prepared for submission for publication. Crystal, Dustin; Carlini, Andrea; Sahu, Swagat; Hidalgo, Francisco; Blum, Angela; Gianneschi, Nathan. The dissertation author is a co-author of this pending manuscript

5.3. References

1 Zhu, J. & Marchant, R. E. Design properties of hydrogel tissue-engineering scaffolds. *Expert Rev. Med. Devices* **8**, 607-626, doi:10.1586/erd.11.27 (2011).

2 Carlini, A. S., Adamiak, L. & Gianneschi, N. C. Biosynthetic Polymers as Functional Materials. *Macromolecules* **49**, 4379-4394, doi:10.1021/acs.macromol.6b00439 (2016).

3 Nair, L. S. *Injectable Hydrogels for Regenerative Engineering*.

4 Chen, M. H., Wang, L. L., Chung, J. J., Kim, Y.-H., Atluri, P. & Burdick, J. A. Methods To Assess Shear-Thinning Hydrogels for Application As Injectable Biomaterials. *ACS Biomaterials Science & Engineering* **3**, 3146-3160, doi:10.1021/acsbiomaterials.7b00734 (2017).

5 Yan, C., Altunbas, A., Yucel, T., Nagarkar, R. P., Schneider, J. P. & Pochan, D. J. Injectable solid hydrogel: mechanism of shear-thinning and immediate recovery of injectable β-hairpin peptide hydrogels. *Soft matter* **6**, 5143-5156, doi:10.1039/C0SM00642D (2010).

6 Pugliese, R. & Gelain, F. Peptidic Biomaterials: From Self-Assembling to Regenerative Medicine. *Trends Biotechnol.* **35**, 145-158, doi:10.1016/j.tibtech.2016.09.004 (2017).

7 Maude, S., Ingham, E. & Aggeli, A. Biomimetic self-assembling peptides as scaffolds for soft tissue engineering. *Nanomedicine* **8**, 823-847, doi:10.2217/nnm.13.65 (2013).

8 Koutsopoulos, S. Self-assembling peptide nanofiber hydrogels in tissue engineering and regenerative medicine: Progress, design guidelines, and applications. *Journal of Biomedical Materials Research Part A* **104**, 1002-1016, doi:doi:10.1002/jbm.a.35638 (2016).

9 Sieminski, A. L., Semino, C. E., Gong, H. & Kamm, R. D. Primary sequence of ionic self-assembling peptide gels affects endothelial cell adhesion and capillary morphogenesis. *Journal of Biomedical Materials Research Part A* **87A**, 494-504, doi:doi:10.1002/jbm.a.31785 (2008).

10 Johnson, T. D., DeQuach, J. A., Gaetani, R., Ungerleider, J., Elhag, D., Nigam, V., Behfar, A. & Christman, K. L. Human versus porcine tissue sourcing for an injectable myocardial matrix hydrogel. *Biomaterials science* **2014**, 60283D, doi:10.1039/C3BM60283D (2014).

11 Firth, A., Aggeli, A., Burke, J. L., Yang, X. & Kirkham, J. Biomimetic self-assembling peptides as injectable scaffolds for hard tissue engineering. *Nanomedicine* **1**, 189-199, doi:10.2217/17435889.1.2.189 (2006).

12 Sun, J., Zheng, Q., Wu, Y., Liu, Y., Guo, X. & Wu, W. Biocompatibility of KLD-12 peptide hydrogel as a scaffold in tissue engineering of intervertebral discs in rabbits. *Journal of Huazhong University of Science and Technology Medical Sciences* **30**, 173-177 (2010).

13 Tripathi, J. K., Pal, S., Awasthi, B., Kumar, A., Tandon, A., Mitra, K., Chattopadhyay, N. & Ghosh, J. K. Variants of self-assembling peptide, KLD-12 that show both rapid fracture healing and antimicrobial properties. *Biomaterials* **56**, 92-103, doi:https://doi.org/10.1016/j.biomaterials.2015.03.046 (2015).

14 Bian, Z. & Sun, J. Development of a KLD-12 polypeptide/TGF-β1-tissue scaffold promoting the differentiation of mesenchymal stem cell into nucleus pulposus-like cells for treatment of intervertebral disc degeneration. *Int. J. Clin. Exp. Pathol.* **8**, 1093-1103 (2015).

15 Kisiday, J., Jin, M., Kurz, B., Hung, H., Semino, C., Zhang, S. & Grodzinsky, A. J. Self-assembling peptide hydrogel fosters chondrocyte extracellular matrix production and cell division: Implications for cartilage tissue repair. *Proc. Natl. Acad. Sci. U. S. A.* **99**, 9996-10001, doi:10.1073/pnas.142309999 (2002).

16 Werner, H. M., Cabalteja, C. C. & Horne, W. S. Peptide Backbone Composition and Protease Susceptibility: Impact of Modification Type, Position, and Tandem Substitution. *Chembiochem : a European journal of chemical biology* **17**, 712-718, doi:10.1002/cbic.201500312 (2016).

17 Böttger, R., Hoffmann, R. & Knappe, D. Differential stability of therapeutic peptides with different proteolytic cleavage sites in blood, plasma and serum. *PLoS One* **12**, e0178943, doi:10.1371/journal.pone.0178943 (2017).

18 Giano, M. C., Pochan, D. J. & Schneider, J. P. Controlled Biodegradation of Self-Assembling β-hairpin Peptide Hydrogels by Proteolysis with Matrix Metalloproteinase-13. *Biomaterials* **32**, 6471-6477, doi:10.1016/j.biomaterials.2011.05.052 (2011).

19 Selegård, R., Aronsson, C., Brommesson, C., Dånmark, S. & Aili, D. Folding driven self-assembly of a stimuli-responsive peptide-hyaluronan hybrid hydrogel. *Sci. Rep.* **7**, 7013, doi:10.1038/s41598-017-06457-9 (2017).

20 Paradís-Bas, M., Tulla-Puche, J. & Albericio, F. The road to the synthesis of “difficult peptides”. *Chem. Soc. Rev.* **45**, 631-654, doi:10.1039/C5CS00680E (2016).

21 Sun, L., Zheng, C. & Webster, T. J. Self-assembled peptide nanomaterials for biomedical applications: promises and pitfalls. *International Journal of Nanomedicine* **12**, 73-86, doi:10.2147/IJN.S117501 (2017).

22 Nicolas, J., Mantovani, G. & Haddleton, D. M. Living Radical Polymerization as a Tool for the Synthesis of Polymer-Protein/Peptide Bioconjugates. *Macromol. Rapid Commun.* **28**, 1083-1111, doi:doi:10.1002/marc.200700112 (2007).

23 Matyjaszewski, K. & Spanswick, J. Controlled/living radical polymerization. *Mater. Today* **8**, 26-33, doi:https://doi.org/10.1016/S1369-7021(05)00745-5 (2005).

24 Bhattacharya, A. & Misra, B. N. Grafting: a versatile means to modify polymers: Techniques, factors and applications. *Prog. Polym. Sci.* **29**, 767-814, doi:https://doi.org/10.1016/j.progpolymsci.2004.05.002 (2004).

25 Trnka, T. M. & Grubbs, R. H. The Development of L2X2RuCHR Olefin Metathesis Catalysts: An Organometallic Success Story. *Acc. Chem. Res.* **34**, 18-29, doi:10.1021/ar000114f (2001).

26 Sanford, M. S., Love, J. A. & Grubbs, R. H. A Versatile Precursor for the Synthesis of New Ruthenium Olefin Metathesis Catalysts. *Organometallics* **20**, 5314-5318, doi:10.1021/om010599r (2001).

27 Matson, J. B., Virgil, S. C. & Grubbs, R. H. Pulsed-Addition Ring-Opening Metathesis Polymerization: Catalyst-Economical Syntheses of Homopolymers and Block Copolymers. *J. Am. Chem. Soc.* **131**, 3355-3362, doi:10.1021/ja809081h (2009).

28 Matson, J. B. & Grubbs, R. H. Monotelechelic Poly(oxa)norbornenes by Ring-Opening Metathesis Polymerization Using Direct End-Capping and Cross-Metathesis. *Macromolecules* **43**, 213-221, doi:10.1021/ma9019366 (2010).

29 Oh, Y. I., Sheng, G. J., Chang, S.-K. & Hsieh-Wilson, L. C. Tailored Glycopolymers as Anticoagulant Heparin Mimetics. *Angewandte Chemie (International ed. in English)* **52**, 11796-11799, doi:10.1002/anie.201306968 (2013).

30 Sletten, E. T., Svec, R. L. & Nguyen, H. M. Synthesis of a polymerizable, bivalent glycan mimetic of the HIV envelope spike gp120. *Tetrahedron Lett.* **56**, 3473-3476, doi:10.1016/j.tetlet.2015.01.016 (2015).

31 Hahn, M. E., Randolph, L. M., Adamiak, L., Thompson, M. P. & Gianneschi, N. C. Polymerization of a peptide-based enzyme substrate. *Chem. Commun.* **49**, 2873-2875, doi:10.1039/C3CC40472B (2013).

32 Kammeyer, J. K., Blum, A. P., Adamiak, L., Hahn, M. E. & Gianneschi, N. C. Polymerization of protecting-group-free peptides via ROMP. *Polymer Chemistry* **4**, 3929-3933, doi:10.1039/C3PY00526G (2013).

33 Callmann, C. E., Barback, C. V., Thompson, M. P., Hall, D. J., Mattrey, R. F. & Gianneschi, N. C. Therapeutic Enzyme-Responsive Nanoparticles for Targeted Delivery and Accumulation in Tumors. *Adv. Mater.* **27**, 4611-4615, doi:10.1002/adma.201501803 (2015).

34 Liao, L., Liu, J., Dreaden, E. C., Morton, S. W., Shopsowitz, K. E., Hammond, P. T. & Johnson, J. A. A Convergent Synthetic Platform for Single-Nanoparticle Combination Cancer Therapy: Ratiometric Loading and Controlled Release of Cisplatin, Doxorubicin, and Camptothecin. *J. Am. Chem. Soc.* **136**, 5896-5899, doi:10.1021/ja502011g (2014).

35 Johnson, J. A., Lu, Y. Y., Burts, A. O., Xia, Y., Durrell, A. C., Tirrell, D. A. & Grubbs, R. H. Drug-Loaded, Bivalent-Bottle-Brush Polymers by Graft-through ROMP. *Macromolecules* **43**, 10326-10335, doi:10.1021/ma1021506 (2010).

36 James, C. R., Rush, A. M., Insley, T., Vuković, L., Adamiak, L., Král, P. & Gianneschi, N. C. Poly(oligonucleotide). *J. Am. Chem. Soc.* **136**, 11216-11219, doi:10.1021/ja503142s (2014).

37 Lo, P. K. & Sleiman, H. F. Nucleobase-Templated Polymerization: Copying the Chain Length and Polydispersity of Living Polymers into Conjugated Polymers. *J. Am. Chem. Soc.* **131**, 4182-4183, doi:10.1021/ja809613n (2009).

38 Thompson, M. P., Randolph, L. M., James, C. R., Davalos, A. N., Hahn, M. E. & Gianneschi, N. C. Labelling Polymers and Micellar Nanoparticles via Initiation, Propagation and Termination with ROMP. *Polymer chemistry* **5**, 1954-1964, doi:10.1039/C3PY01338C (2014).

39 Sowers, M. A., McCombs, J. R., Wang, Y., Paletta, J. T., Morton, S. W., Dreaden, E. C., Boska, M. D., Ottaviani, M. F., Hammond, P. T., Rajca, A. & Johnson, J. A. Redox-responsive branched-bottlebrush polymers for in vivo MRI and fluorescence imaging. *Nature Communications* **5**, 5460, doi:10.1038/ncomms6460

https://www.nature.com/articles/ncomms6460#supplementary-information (2014).

40 Fishman, J. M. & Kiessling, L. L. Synthesis of Functionalizable and Degradable Polymers by ROMP. *Angewandte Chemie (International ed. in English)* **52**, 10.1002/anie.201300293, doi:10.1002/anie.201300293 (2013).

41 Blum, A. P., Kammeyer, J. K., Yin, J., Crystal, D. T., Rush, A. M., Gilson, M. K. & Gianneschi, N. C. Peptides Displayed as High Density Brush Polymers Resist Proteolysis and Retain Bioactivity. *J. Am. Chem. Soc.* **136**, 15422-15437, doi:10.1021/ja5088216 (2014).

42 Caplan, M. R., Schwartzfarb, E. M., Zhang, S., Kamm, R. D. & Lauffenburger, D. A. Control of self-assembling oligopeptide matrix formation through systematic variation of amino acid sequence. *Biomaterials* **23**, 219-227, doi:https://doi.org/10.1016/S0142-9612(01)00099-0 (2002).

43 Rosebrugh, L. E., Marx, V. M., Keitz, B. K. & Grubbs, R. H. Synthesis of Highly Cis, Syndiotactic ROMP Polymers Using Ruthenium Metathesis Catalysts. *J. Am. Chem. Soc.* **135**, 10032-10035, doi:10.1021/ja405559y (2013).

44 Song, A., Lee, J. C., Parker, K. A. & Sampson, N. S. Scope of the Ring Opening Metathesis Polymerization (ROMP) Reaction of 1-Substituted Cyclobutenes. *J. Am. Chem. Soc.* **132**, 10513-10520, doi:10.1021/ja1037098 (2010).

45 Kim, J. E., Kim, S. H. & Jung, Y. In situ chondrogenic differentiation of bone marrow stromal cells in bioactive self-assembled peptide gels. *J. Biosci. Bioeng.* **120**, 91-98, doi:https://doi.org/10.1016/j.jbiosc.2014.11.012 (2015).

46 Greenfield, N. J. Using circular dichroism spectra to estimate protein secondary structure. *Nat. Protoc.* **1**, 2876-2890, doi:10.1038/nprot.2006.202 (2006).

47 Song, C., Blaber, M. G., Zhao, G., Zhang, P., Fry, H. C., Schatz, G. C. & Rosi, N. L. Tailorable Plasmonic Circular Dichroism Properties of Helical Nanoparticle Superstructures. *Nano Lett.* **13**, 3256-3261, doi:10.1021/nl4013776 (2013).

48 Feng, W., Kim, J.-Y., Wang, X., Calcaterra, H. A., Qu, Z., Meshi, L. & Kotov, N. A. Assembly of mesoscale helices with near-unity enantiomeric excess and light-matter interactions for chiral semiconductors. *Science Advances* **3**, doi:10.1126/sciadv.1601159 (2017).

49 Miyahara, T., Nakatsuji, H. & Sugiyama, H. Helical Structure and Circular Dichroism Spectra of DNA: A Theoretical Study. *The Journal of Physical Chemistry A* **117**, 42-55, doi:10.1021/jp3085556 (2013).

50 Kuzyk, A., Schreiber, R., Fan, Z., Pardatscher, G., Roller, E.-M., Högele, A., Simmel, F. C., Govorov, A. O. & Liedl, T. DNA-based self-assembly of chiral plasmonic nanostructures with tailored optical response. *Nature* **483**, 311, doi:10.1038/nature10889

https://www.nature.com/articles/nature10889#supplementary-information (2012).

51 Amornthep, S. & Nantakan, W. Mid-infrared circular polarization switching in helical metamaterials. *Journal of Optics* **18**, 115102 (2016).

52 Otsuka, T., Maeda, T. & Hotta, A. Effects of Salt Concentrations of the Aqueous Peptide-Amphiphile Solutions on the Sol–Gel Transitions, the Gelation Speed, and the Gel Characteristics. *The Journal of Physical Chemistry B* **118**, 11537-11545, doi:10.1021/jp5031569 (2014).

53 Hong, Y., Pritzker, M. D., Legge, R. L. & Chen, P. Effect of NaCl and peptide concentration on the self-assembly of an ionic-complementary peptide EAK16-II. *Colloids Surf. B. Biointerfaces* **46**, 152-161, doi:https://doi.org/10.1016/j.colsurfb.2005.11.004 (2005).

54 Feng, Y., Taraban, M. & Yu, Y. B. The effect of ionic strength on the mechanical, structural and transport properties of peptide hydrogels. *Soft Matter* **8**, 11723-11731, doi:10.1039/C2SM26572A (2012).

55 Mochida, Y., Cabral, H., Miura, Y., Albertini, F., Fukushima, S., Osada, K., Nishiyama, N. & Kataoka, K. Bundled Assembly of Helical Nanostructures in Polymeric Micelles Loaded with Platinum Drugs Enhancing Therapeutic Efficiency against Pancreatic Tumor. *ACS Nano* **8**, 6724-6738, doi:10.1021/nn500498t (2014).

56 Dong, H., Shu, J. Y., Dube, N., Ma, Y., Tirrell, M. V., Downing, K. H. & Xu, T. 3-Helix Micelles Stabilized by Polymer Springs. *J. Am. Chem. Soc.* **134**, 11807-11814, doi:10.1021/ja3048128 (2012).

57 Therien, A. G. & Deber, C. M. Interhelical Packing in Detergent Micelles: FOLDING OF A CYSTIC FIBROSIS TRANSMEMBRANE CONDUCTANCE REGULATOR CONSTRUCT. *J. Biol. Chem.* **277**, 6067-6072, doi:10.1074/jbc.M110264200 (2002).

58 Shi, S., Liu, Y., Chen, Y., Zhang, Z., Ding, Y., Wu, Z., Yin, J. & Nie, L. Versatile pH-response Micelles with High Cell-Penetrating Helical Diblock Copolymers for Photoacoustic Imaging Guided Synergistic Chemo-Photothermal Therapy. *Theranostics* **6**, 2170-2182, doi:10.7150/thno.16633 (2016).

59 Figg, C. A., Carmean, R. N., Bentz, K. C., Mukherjee, S., Savin, D. A. & Sumerlin, B. S. Tuning Hydrophobicity To Program Block Copolymer Assemblies from the Inside Out. *Macromolecules* **50**, 935-943, doi:10.1021/acs.macromol.6b02754 (2017).

60 Gradin, P., Howgate, P. G., Seldén, R. & Brown, R. A. in *Comprehensive Polymer Science and Supplements* (eds Geoffrey Allen & John C. Bevington) 533-569 (Pergamon, 1989).

61 Cauich-Rodriguez, J. V., Deb, S. & Smith, R. Effect of cross-linking agents on the dynamic mechanical properties of hydrogel blends of poly(acrylic acid)-poly(vinyl alcohol-vinyl acetate). *Biomaterials* **17**, 2259-2264, doi:https://doi.org/10.1016/0142-9612(96)00058-0 (1996).

62 Chen, F., Yu, S., Liu, B., Ni, Y., Yu, C., Su, Y., Zhu, X., Yu, X., Zhou, Y. & Yan, D. An Injectable Enzymatically Crosslinked Carboxymethylated Pullulan/Chondroitin Sulfate Hydrogel for Cartilage Tissue Engineering. *Sci. Rep.* **6**, 20014, doi:10.1038/srep20014

https://www.nature.com/articles/srep20014#supplementary-information (2016).

63 Caló, E. & Khutoryanskiy, V. V. Biomedical applications of hydrogels: A review of patents and commercial products. *Eur. Polym. J.* **65**, 252-267, doi:https://doi.org/10.1016/j.eurpolymj.2014.11.024 (2015).

64 Sivashanmugam, A., Arun Kumar, R., Vishnu Priya, M., Nair, S. V. & Jayakumar, R. An overview of injectable polymeric hydrogels for tissue engineering. *Eur. Polym. J.* **72**, 543-565, doi:https://doi.org/10.1016/j.eurpolymj.2015.05.014 (2015).

65 Mukherjee, S., Hill, M. R. & Sumerlin, B. S. Self-healing hydrogels containing reversible oxime crosslinks. *Soft Matter* **11**, 6152-6161, doi:10.1039/C5SM00865D (2015).

66 Grover, G. N., Braden, R. L. & Christman, K. L. Oxime Cross-Linked Injectable Hydrogels for Catheter Delivery. *Adv. Mater.* **25**, 2937-2942, doi:doi:10.1002/adma.201205234 (2013).

67 Nguyen, M. M., Gianneschi, N. C. & Christman, K. L. Developing injectable nanomaterials to repair the heart. *Curr. Opin. Biotechnol.* **34**, 225-231, doi:https://doi.org/10.1016/j.copbio.2015.03.016 (2015).

68 Hoffman, A. S. Hydrogels for biomedical applications. *Adv. Drug Del. Rev.* **64**, 18-23, doi:https://doi.org/10.1016/j.addr.2012.09.010 (2012).

69 Kellum, J. A., Song, M. & Li, J. Science review: Extracellular acidosis and the immune response: clinical and physiologic implications. *Critical Care* **8**, 331-336, doi:10.1186/cc2900 (2004).

70 Inserte, J., Barba, I., Hernando, V. & Garcia-Dorado, D. Delayed recovery of intracellular acidosis during reperfusion prevents calpain activation and determines protection in postconditioned myocardium. *Cardiovasc. Res.* **81**, 116-122, doi:10.1093/cvr/cvn260 (2009).

71 Chien, M.-P., Thompson, M. P., Barback, C. V., Ku, T.-H., Hall, D. J. & Gianneschi, N. C. Enzyme-Directed Assembly of a Nanoparticle Probe in Tumor Tissue. *Adv. Mater.* **25**, 3599-3604, doi:10.1002/adma.201300823 (2013).

72 Nguyen, M. M., Carlini, A. S., Chien, M.-P., Sonnenberg, S., Luo, C., Braden, R. L., Osborn, K. G., Li, Y., Gianneschi, N. C. & Christman, K. L. Enzyme-Responsive Nanoparticles for Targeted Accumulation and Prolonged Retention in Heart Tissue after Myocardial Infarction. *Adv. Mater.* **27**, 5547-5552, doi:10.1002/adma.201502003 (2015).

73 Wright, D. B., Thompson, M. P., Touve, M. A., Carlini, A. S. & Gianneschi, N. C. Enzyme-Responsive Polymer Nanoparticles via Ring-Opening Metathesis Polymerization-Induced Self-Assembly. *Macromol. Rapid Commun.* **0**, 1800467, doi:doi:10.1002/marc.201800467.

74 Ku, T.-H., Chien, M.-P., Thompson, M. P., Sinkovits, R. S., Olson, N. H., Baker, T. S. & Gianneschi, N. C. Controlling and Switching the Morphology of Micellar Nanoparticles with Enzymes. *J. Am. Chem. Soc.* **133**, 8392-8395, doi:10.1021/ja2004736 (2011).